Investigating G-protein-coupled receptor structure and function using novel nano-encapsulation strategies

by

Rachael L. Grime

A thesis submitted to the University of Birmingham for the degree of

DOCTOR OF PHILOSOPHY

School of Biosciences
College of Life and Environmental Sciences
University of Birmingham, UK
February 2021

Abstract

Nano-encapsulation of membrane proteins using the archetypical polymer poly(styrene-*co*-maleic acid) (SMA) is well established. In this study, fluorescence correlation spectroscopy (FCS) was employed to characterise binding at the G-protein-coupled receptor (GPCR), adenosine 2A receptor, solubilised with SMA to form SMA lipid particles (SMALPs). Optimal conditions were systematically ascertained and FCS was validated for the biophysical study of GPCR-SMALPs. A novel fluorescent parathyroid hormone 1 receptor (PTH1R) agonist was characterised and is ready for use in fluorescent studies with purified PTH1R-SMALP.

The rapid adoption of nanodisc technology has resulted in demand for a 'polymer tool kit' to provide alternatives where SMA presents limitations. Emerging polymers, poly(styrene-*co*-maleimide) (SMI) and poly(diisobutylene-*alt*-maleic acid) (DIBMA) were used alongside SMA to solubilise rhodopsin from rod outer segments (ROS) and characterised. SMA, SMI and DIBMA were efficient at extracting rhodopsin from ROS. Isomerisation of 11-*cis*-retinal was evident upon photobleaching, however SMA and SMI restrained rhodopsin in inactive meta I conformation, whereas DIBMA supported transition to fully-active meta II.

Finally, the role of extracellular loop one (ECL1) of calcitonin receptor-like receptor was probed via systematic residue deletion. A functional role was established for several ECL1 residues and loop length, with differences between the calcitonin gene-related peptide receptor and adrenomedullin 1 receptor. This study provides insight into GPCR pharmacology and the utility of SMA-like polymers.

Acknowledgements

"For a long-time it seemed to me that life was about to begin - real life. But there was always some obstacle in the way, something to be gotten through first, some unfinished business, time still to be served, a debt to be paid. At last it dawned on me that these obstacles were my life. This perspective has helped me to see there is no way to happiness. Happiness is the way. So, treasure every moment you have and remember that time waits for no one." - Alfred D. Souza

First and foremost, I would not be where I am today, if in 2016 Professor Mark Wheatley had not agreed to take me on in his laboratory. So, Mark, thank you for the opportunity, the supervision, guidance, faith, curries and pints. I am grateful to have had the pleasure of learning from you. I am also extremely grateful to Professor Tim Dafforn, whose supervision, knowledge and enthusiasm was always enlightening and motivating. Of course, I must also extend my gratitude to Reverend Professor David Poyner whose supervision, advice and chocolate teacakes were always warmly welcomed. Having such an expert and supportive team of professors behind me has been a great experience, so thank you all.

Thank you to all my collaborators, I have been lucky to spend time at several outstanding institutions. Thank you to Dr. Stephen J. Briddon and Dr. Joelle Goulding who made me feel extremely welcome at University of Nottingham and taught me everything I know about fluorescence correlation spectroscopy. Thank you to Dr. Phillip J. Reeves; returning to University of Essex as a PhD student was a great experience. I remain a proud University of Essex alumnus.

I also thank my funding body, the BBSRC and by extension, Midlands Integrative Biosciences Training Partnership for making this project possible. I would also like to

thank everyone at The Centre of Membrane Proteins and Receptors and Team Science, who helped to fund my visits to University of Nottingham.

I must extend my gratitude to Professor Mark Wheatley's team. Firstly, Dr. Richard T. Logan, thank you for all your help and guidance in the very beginning. Dr. Romez Uddin, thank you for hosting me at Aston University and teaching me many techniques. Dr. Hoor Ayub, it has been great working with you over the last couple of years.

I was unsure what I would find when I moved to Birmingham, but I have made some of the best, life-long friendships one could ever ask for. Dr. Elizabeth Connolly, where would I be without your continued advice, support and craic? You were the first person I met on induction day and since then I have had the honour of living with you for the last three years, thank you. Hannah Pugh, without you I would have never moved into the Woodleigh Avenue house and I am so happy I did. You have been a great friend and your humour, love and capacity for pints have been so welcomed after long lab days, I am lucky to call you a friend. Dr. Carys Howell, you have brought me friendship, tea, smart advice, tea, laughter and of course more tea. Your rational advice always kept me calm, it is a pleasure to call you my friend. Dr. Laurie Cazalé-Debat, merci pour ton soutien et ton amitié lors de la dernière ligne droite de ce travail.

I must of course acknowledge the seventh-floor team – my 'lab family'. Without their help, support, advice and encouragement none of this would have been possible, so thank you all:

Dr. Naomi Pollock and Dr. Sarah Lee you have provided me with two great scientific role models. Stephanie Nestorow, I am in awe of your scientific skill. Khaled Ali you have a truly kind and generous soul, I appreciate your support and friendship.

Dr. Simon Caulton, thank you for the advice and laughter. Dr. Ian Cadby, thanks for your help early on. Hannah Walters-Morgan, thanks for camaraderie and of course, baked goods. Amber Wilson, you are one of the most generous people I know, thanks for

helping get me through my PhD. Rebecca Parr, thanks for the friendship, but I am not going to miss the Disney songs! Mauricio Valdivia Delgado, thank you for your calming lab presence and good company.

Dr. Tim J. Knowles, thank you for the office laughter and guidance when needed. Pooja Sridhar, thank you for answering so many of my questions and always being willing to lend a helping hand. Dr. David Hardy, finally someone to share the woes of cell culture with! Thank you for being a good climbing buddy too. Peter Wotherspoon, you have been great company and a great friend in times of need (six pints is plenty...). I am in awe of your genius and capacity to learn.

There are just too many people to thank and acknowledge, you have all been the best colleagues someone could ask for and I am going to miss you all terribly. I would like to extend thanks to many more colleagues, old, current and new: Dr. Zoe Stroud, Dr. Gareth Hughes, Dr. Deborah Ricci, Liam Riley, Jake Carter, Ben Cooper, Liam Mead, Giedre Ratkeviciute...And everyone else in Biosciences with whom I have crossed paths, grabbed coffee, gone for a pint, or talked science.

Finally, I must thank my family for their continued support throughout my life and my PhD. Thank you for housing and feeding me during my visits to Essex, thank you for keeping me motivated and thank you for offering welcome breaks when they were needed.

- Ad majora natus sum -

Contents

List of Figures

List of abbreviations

Throughout this thesis, abbreviations have been used as recommended by the Journal of Biological Chemistry style guide. The International System of Units (SI) (Système International d'Unités) has been followed. The following abbreviations have also been used:

$A_{2A}R$	adenosine 2A receptor
AM	adrenomedullin
AM_1R	adrenomedullin 1 receptor
AM_2R	adrenomedullin 2 receptor
AUC	analytical ultracentrifugation
AVP	[arginine^8]vasopressin
β_2AR	beta$_2$-adrenoreceptor
βarr	beta-arrestin
BRET	bioluminescence resonance energy transfer
cDNA	complementary deoxyribonucleic acid
CGRP	calcitonin gene-related peptide
CLR	calcitonin receptor-like receptor
$C_{(S)}$	continuous distribution model
COS-7	CV-1 (simian) in Origin, carrying SV40 gene
CRFR1	corticotropin releasing hormone receptor 1
CRFR1	corticotropin releasing hormone receptor 1

Cryo-EM	Cryogenic electron microscopy
DAG	diacylglycerol
DDM	n-dodecyl-β-D-maltoside
DIBMA	poly(diisobutylene-*alt*-maleic acid)
DLS	dynamic light scattering
DPM	disintegrations per minute
ECD	extracellular domain
ECL	extracellular loop
FCS	fluorescence correlation spectroscopy
FRET	Förster resonance energy transfer
G-protein	guanine nucleotide binding protein
GLP1R	glucagon-like peptide 1 receptor
GPCR	G-protein-coupled receptor
GRK	G-protein-coupled receptor kinase
G(τ)	autocorrelation analysis
$\mathbf{G}_{(t)}$	transducin
HA	haemagluttinin
HEK	human embryonic kidney
HRP	horseraddish peroxidase
ICL	intracellular loop
IMAC	immobilised metal affinity chromatography

$InsP_3$	inositol 1,4,5-trisphosphate
MSP	membrane scaffold protein
NIHF	nonimmune hydrops fetalis
NLP	nano-lipoprotein particle
OT	oxytocin
OTR	oxytocin receptor
PBS	phosphate buffered saline
PDB	protein data bank
PEI	polyethylenimine
PIP2	phosphatidylinositol 4,5-bisphosphate
PKC	protein kinase C
PTH	parathyroid hormone
PTH1R	parathyroid hormone 1 receptor
PTHrP	parathyroid hormone-related protein
RAMP	receptor activity modifying protein
Rho	rhodopsin
Rhodopsin-LP	rhodopsin-lipid particle
ROS	rod outer segments
S*f*9	clonal isolate of *Spodoptera frugiperda*
SMA	poly(styrene-*co*-maleic acid); styrene maleic acid
SMAd-A	dehydrated SMA-ED

SMA-ED	styrene maleic acid-ethylene diamine
SMA-SH	styrene maleic acid derivative with solvent-exposed sulfhydrils
SMALP	styrene maleic acid lipid particle
SMI	poly(styrene-*co*-(N-(3-N',N'-dimethylaminopropyl)maleimide)); poly(styrene-*co*-maleimide); styrene maleimide
SMILP	styrene maleimide lipid particle
SPR	surface plasmon resonance
τ_D	dwell time
tetO	tetracycline-operator sequence
tetR	tetracycline-repressor
TM	transmembrane
TMD	transmembrane domain
$\mathbf{V_{1a}R}$	vasopressin $_{1a}$ receptor

Chapter 1: Introduction

1.1 G-protein-coupled receptors: An overview

G-protein-coupled receptors (GPCRs) are expressed at the cell surface and transmit extracellular signals from a variety of ligands. GPCR ligands differ in respect to physical class, size and property, they range from biogenic amines, to peptides and large glycoproteins (Hill, 2006). Their role is central to many biological processes such as hormonal and nervous system homeostasis (Hanlon and Andrew, 2015). Their name derives from their ability to signal via guanine nucleotide-binding proteins (G-proteins). Signalling ability is highly complex, acting through numerous pathways, both G-protein dependent and G-protein independent (Pavlos and Friedman, 2017).

Approximately 35 % of clinically-approved drugs target GPCRs or act through GPCR mediated pathways (Sriram and Insel, 2018). Given this clinical significance, a detailed understanding of GPCR structure and function is essential in driving forward pharmacological innovation. Coded for by approximately 4 % of the human genome, these seven-transmembrane receptors have approximately 800 different subtypes, making them the largest family of eukaryotic membrane proteins (Fredriksson *et al.*, 2003; Matthews and Sunde, 2012).

Advances in structural biology, molecular modelling, protein engineering and biophysical techniques, mean there are many new pharmacological paradigms to explore with regard to GPCRs including, but not limited to; anti-GPCR antibodies, allosteric modulation, biased signalling and GPCR heterodimer-targeting (Jacobson, 2015).

1.2 GPCR classification

GPCRs share a common characteristic architecture of seven transmembrane helices (TM 1–7) linked by intracellular loops (ICL) and extracellular loops (ECL); along with

an extracellular amino (N-) terminus and intracellular carboxyl (C-) terminus (figure 1.1). Despite this conserved overall structure, sequence conservation among the superfamily is poor however, sequence analysis has revealed homology and conserved motifs that appear throughout the family, meaning sub-classes are identifiable. There are two, overlapping schemes of classification for GPCRs, the first classifies receptors into six subfamilies (A–F) based on sequence homology (Kolakowski, 1994). These subfamilies are: family A (rhodopsin/β2-adreno-like), family B (secretin/adhesion), family C (metabotropic glutamate), family D (fungal mating pheromone receptors), family E (cyclic AMP receptors in slime moulds) and family F (frizzled/smoothened). Of these, families A, B and C are the most pharmacologically relevant, containing receptors found within vertebrates. The second scheme of classification, known as GRAFS nomenclature, is based on phylogenetic analysis and specifically divides vertebrate GPCRs into five sub-categories: glutamate (C), rhodopsin-like (A), adhesion (B), frizzled/smoothened and secretin-like (B) (Schioth and Fredriksson, 2005).

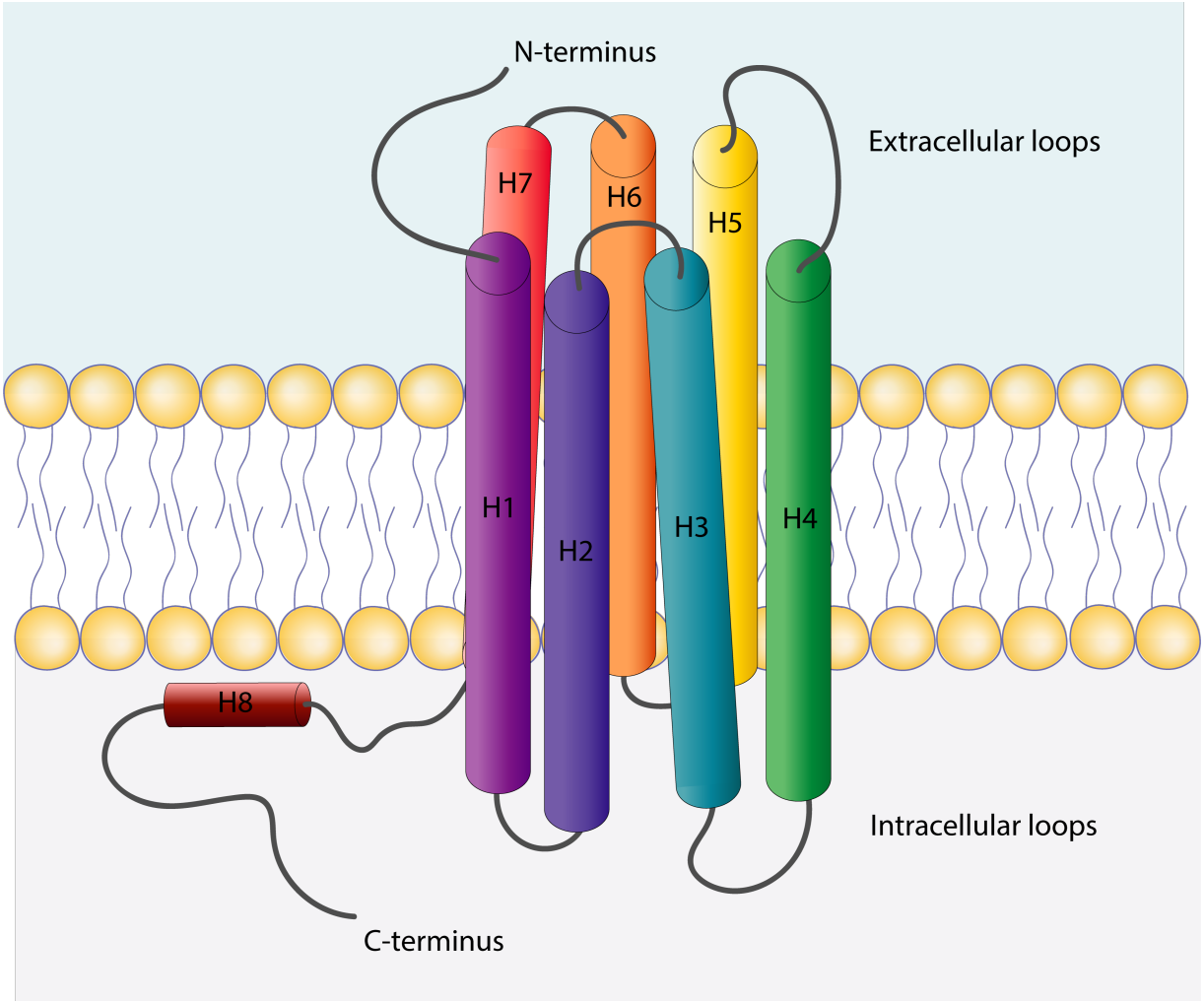

Figure 1.1: **Schematic demonstrating overall GPCR structure.** Seven transmembrane (TM) helices are represented as rainbow-coloured cylinders. Intracellular and extracellular loops connect the helices. An eighth helix (H8) is also present.

Family A represents the largest and most researched subfamily of GPCRs, accounting for 719 of all known receptors (Alexander *et al.*, 2017). As a whole, they have low sequence homology however, there are conserved residues and motifs that have vital roles for receptor function and structural integrity (Rosenbaum *et al.*, 2009) (figure 1.2). To permit comparison amongst family A GPCRs, a common numbering system has been devised in which the most highly conserved residue in each TM-helix is a reference point, denoted as $X.^{50}$ (where X is TM number). Residues following $X.^{50}$ are denoted as an increase from 50, and preceding residues as a decrease from 50 (Ballesteros and Weinstein, 1995). A similar numbering system exists for family B GPCRs (Wootten *et al.*, 2013).

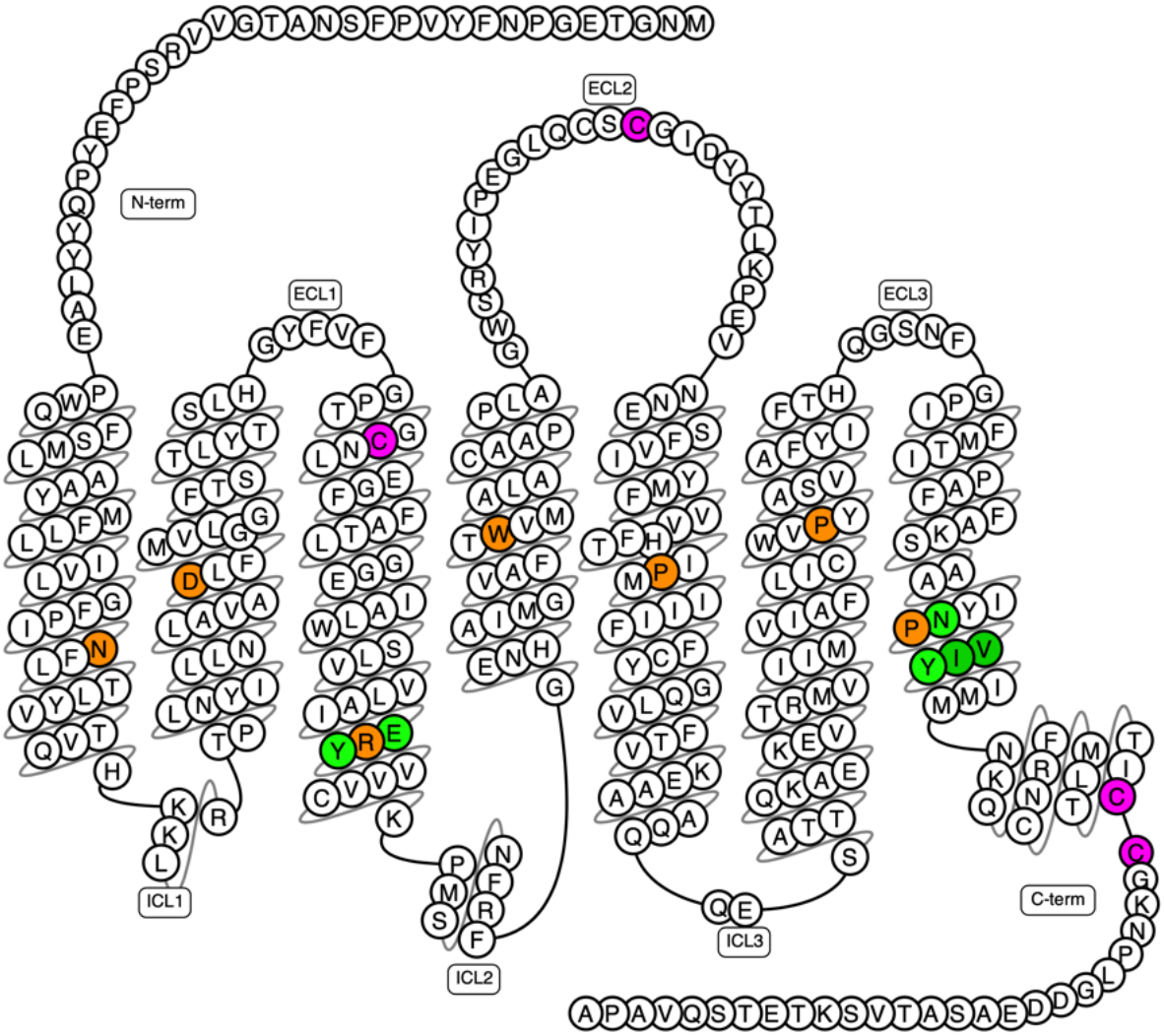

Figure 1.2: **'Snake plot' diagram of a family A GPCR, human rhodopsin.** Orange: Ballesteros residues (x.^{50}), where 'x is helix number, for example, Asn (N) in helix 1 is denoted Asn$^{1.50}$. Pink: Conserved cysteines for di-sulphide bonds, or palmitoylation at the end of helix 8. Green: Conserved motifs within family A GPCRs.

Conserved motifs within family A include an Asp/Glu$^{3.49}$ - Arg$^{3.50}$ - Tyr$^{3.51}$ (D/ERY) motif at the cytoplasmic face of TM3, which maintains the receptor in an inactive state. Mutation at Asp/Glu$^{3.49}$ commonly leads to receptor constitutive activation (Rovati *et al.*, 2007). Arg$^{3.50}$ is almost totally conserved within family A receptors (Probst *et al.*, 1992), and has been functionally linked to the also highly conserved, Asp/Glu$^{6.30}$. Together, Arg$^{3.50}$ and Asp/Glu$^{6.30}$ form an ionic lock, stabilising inactive receptor state (Audet and

Bouvier, 2012). Furthermore, two conserved cysteine residues form a disulphide bridge between the top of TM3 ($Cys^{3.25}$) and ECL2, essential for structural stability (Gether, 2000). Another well-conserved motif is the $Asn^{7.49}$ - $Pro^{7.50}$ - X - X - $Tyr^{7.53}$ (NPXXY) in TM7. $Asn^{7.49}$ acts as an activation switch (Govaerts *et al.*, 2001). Conserved proline residues are also present throughout transmembrane helices 4, 5, 6, and 7 which are structurally important for the correct folding of receptors by causing kinks in the transmembrane α-helices (Wess *et al.*, 1993). Many class A GPCRs also have conserved cysteine residues at the C-terminus, which allow for palmitoylation and formation of an eighth, intracellular, α-helix (Hawtin *et al.*, 2001b). Palmitoylation of helix 8 is thought to anchor this region into the membrane bilayer, and provide a target for partitioning into cholesterol-rich rafts and caveolae (Oddi *et al.*, 2012).

Similar to family A GPCRs, family B and family C GPCRs both share the conserved cysteine residues at the top of TM3 and within ECL2, essential for structural stability however, there are notable differences in homology. Family B GPCRs have an amino-terminal signal peptide (Oddi *et al.*, 2012), while family C GPCRs undergo mandatory dimerisation, either as homo- or hetero- dimers (Chun *et al.*, 2012). Family B and C members also have a larger extracellular N-terminus, assisting in the recognition and binding of their much larger peptide ligands (Hollenstein *et al.*, 2014). Family B GPCRs also have their own highly conserved motifs, including the $YLH^{3.51}$ motif in TM3. The $YLH^{3.51}$ motif is considered functionally similar to the E/DRY motif found in class A GPCRs (Vohra *et al.*, 2013). Family B receptors also have a VS/AxxY motif located in TM7 (*cf.* NPXXY, family A) (Barwell *et al.*, 2012).

Despite this extensive classification based on sequence homology, there are approximately 110 receptors that have orphan status, meaning their natural ligand is not known (Pandy-Szekeres *et al.*, 2018) (correct as of February 2021). Many orphan receptors are associated with diseases such as diabetes, cancer, psychiatric disorders, inflammatory disorders and obesity (Dorsam and Gutkind, 2007; Valtcheva *et al.*, 2013; Komatsu, 2015).

1.3 G-proteins and G-protein dependent signalling

G-proteins are heterotrimeric GTPases composed of three subunits, α, β and γ, which functionally couple to specific GPCRs. There are 21 Gα, 6 Gβ and 12 Gγ subunits that have been identified in the human genome (Baltoumas *et al.*, 2013). Gα is the largest G-protein subunit and is typically divided into four main classes based on primary sequence similarity: Gα_s, Gα_i, Gα_q and Gα_{12} (Baltoumas *et al.*, 2013). Gα_s and Gα_i function to stimulate and inhibit adenylyl cyclase activity respectively. Adenylyl cyclase produces the second messenger, cyclic-adenosine 3'-5'-monophosphate (cAMP). This activates cAMP-dependent protein kinases (PKA) and some guanine nucleotide exchange factors. Gα_q induces phospholipase Cβ to cleave phosphatidylinositol 4,5-bisphosphate (PIP2) to form inositol 1,4,5-trisphosphate ($InsP_3$), stimulating calcium release from the endoplasmic reticulum (ER), and diacylglycerol (DAG) which activates protein kinase C (PKC) (Litosch, 2016). Gα_{12} targets Rho-GEFs which can regulate a wide variety of cellular functions from migration to transformation (Suzuki *et al.*, 2009) (figure 1.3).

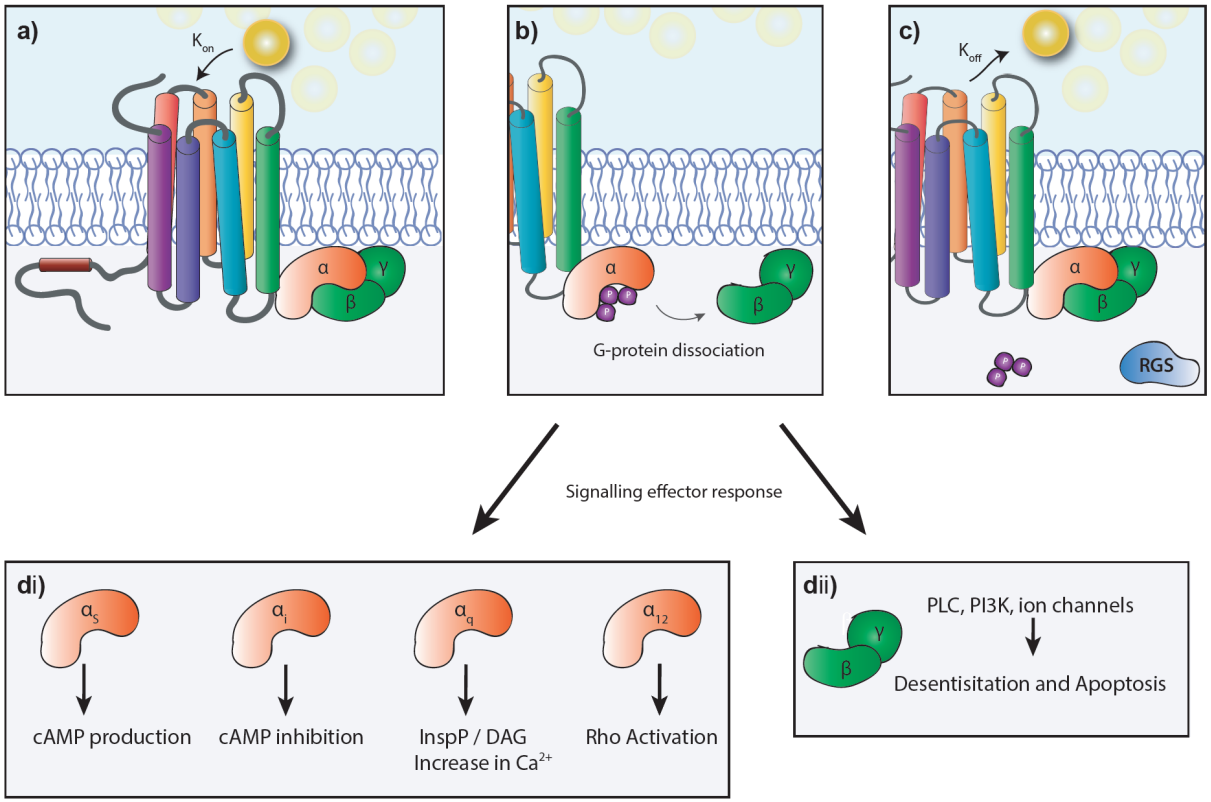

Figure 1.3: **G-protein dependent signalling.** **(a)** Upon agonist binding, conformational changes occur within the GPCR. **(b)** The Gα subunit exchanges GDP for GTP and the Gα and G$\beta\gamma$ subunits dissociate. **(c)** Hydrolysis of GTP to GDP is controlled by regulator of G-protein signalling complexes (RGS), resulting in the reformation of the G$\alpha\beta\gamma$ complex. **(di)** Different Gα subtypes activate different signalling pathways, resulting in a variety of second messengers and cellular responses. **(dii)** The G$\beta\gamma$ subunit stays associated and is capable of regulating PLC, and ion channels.

Solved crystal structures of the Gα subunit reveal that it comprises two sub-domains, a conserved GTPase domain and a six α-helical domain, which forms a lid over the nucleotide-binding pocket and differentiates the Gα proteins from the monomeric, small G-proteins (small G-proteins belong to the RAS family of GTPases) (Lambright *et al.*, 1996; Sprang, 1997). The GTPase domain is responsible for hydrolysing guanosine triphosphate (GTP) and binding the G$\beta\gamma$ dimer (Coleman *et al.*, 1994). Gα binds guanosine diphosphate (GDP) in its inactive conformation; once the preceding GPCR has been activated, conformational changes result in GDP exchange for GTP and dissociation of the trimeric complex. The GTP-bound conformation and the G$\beta\gamma$ dimer can then activate downstream effectors. The signal is terminated upon hydrolysis of GTP to GDP, by Gα GTPase domain which is regulated by several mechanisms including proteins such as regulator of G protein signalling (RGS) (Oldham and Hamm, 2008).

1.4 G-protein independent signalling

GPCR signalling is incredibly complex; going far beyond simple agonism or antagonism; and beyond interactions with orthosteric binding sites (Milligan *et al.*, 2017). Increasingly, concepts of allosteric modulation, signalling bias, constitutive activity, and inverse agonism are being explored and have potential for great pharmacological impact (Flordellis, 2012). Further to this, it has been acknowledged that GPCRs are able to signal not only at the plasma membrane, but within endosomes too (Irannejad *et al.*, 2013).

Broadly speaking, signalling is categorised into G-protein-dependent, and G-protein-independent pathways with the latter being identified and understood in the recent decade. Upon GPCR stimulation, interactions occur not only with heterotrimeric G-proteins (discussed above), but also with GPCR kinases (GRKs), which phosphorylate C-terminal serine/threonine residues, inducing the recruitment of beta-arrestin (βarr) (Pierce and Lefkowitz, 2001; Moore *et al.*, 2007). βarr is known to be involved in the desensitisation and internalisation of many membrane receptors (Goodman *et al.*, 1996). Recently, they have been appreciated as independent signalling units by virtue of their crucial role

as both adaptors and scaffolds for an increasing number of signalling pathways, including non-receptor tyrosine kinase 'Src' and mitogen-activated protein kinase (Pierce *et al.*, 2002; Shukla *et al.*, 2011). The significance of these G-protein-independent signalling pathways opens up extraordinary therapeutic potential for 'biased agonists' (figure 1.4). Biased agonism is the phenomenon whereby different ligands acting at the same receptor, can stabilise distinct receptor conformations. This leads to only a subset of signalling pathways being activated. Examples of biased agonist research can be seen in the ongoing investigations regarding the widely used drug morphine; which acts via the μ-opioid receptor (MOR, family A GPCR) (DeWire *et al.*, 2013). The drug side-effects of constipation, vomiting, respiratory suppression, and physical dependence were lessened in the absence of βarr3 in mice models, suggesting that MOR-βarr3 signalling may underpin some of these physiological responses (Raehal *et al.*, 2005). Subsequently, this has led to the development of several drug-candidates, in which animal studies have shown analgesic efficacy, with significantly reduced unwanted side effects. Many of these candidates are in early clinical trials (Schmid *et al.*, 2017; Conibear *et al.*, 2020; Grim *et al.*, 2020). Potent biased agonists which signal through one pathway while antagonising others, have huge potential to revolutionise drug specificity.

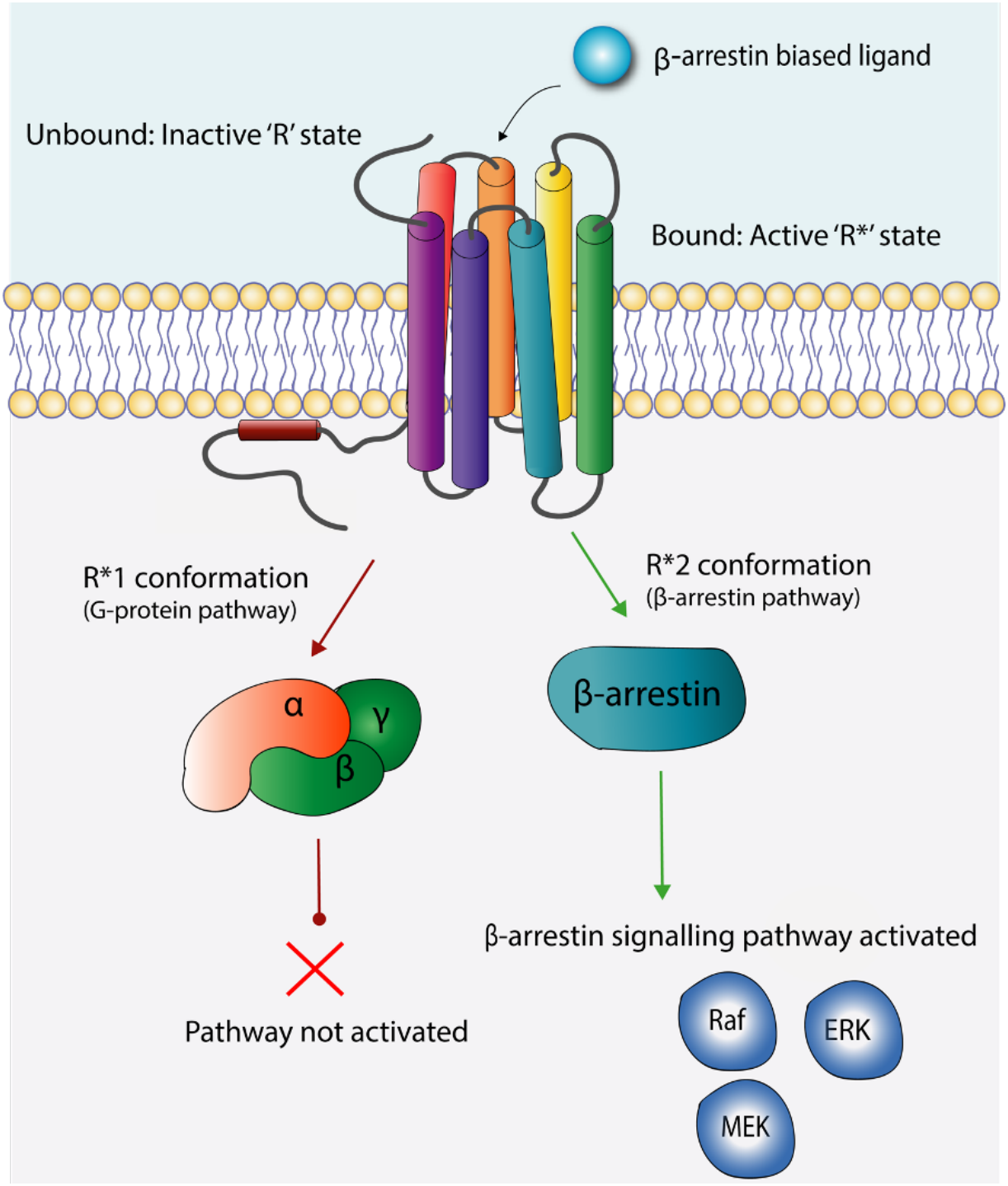

Figure 1.4: **The concept of biased agonism.** A biased agonist preferentially signals through one pathway over another by stabilising specific active receptor conformations (R^*).

1.5 Termination of receptor signalling and desensitisation

Regulation of GPCR signalling is essential, and receptor inactivation is mediated through complex mechanisms. Desensitisation refers to a decrease in response to repeated or continuous stimulation, and is a phenomenon observed in GPCR signalling. Upon agonist binding and activation, responses from second messengers peak anywhere from a few milliseconds to a few minutes post agonist binding, depending on the specific GPCR-ligand complex (Lefkowitz, 2013). The response then plateaus and declines rapidly, even in the continued presence of agonist. Furthermore, repeated binding of agonist over minutes, results in further decreased GPCR responses. This process is of great importance from a pharmacological standpoint, in that a given dose of a drug may give rise to distinctly different responses, depending on the prior sensitisation state of the system (Gainetdinov *et al.*, 2004). Once desensitised, the GPCR either remains at the cell surface, refractory to stimuli, or, is internalised and either degraded or recycled back up to the membrane at a later time (figure 1.5) (Ferguson *et al.*, 1996). Receptor desensitisation is initialised by a family of GRKs which are comprised of three domains; an RGS homology domain at the amino-terminus, a catalytic domain and a membrane-targeting domain at the carboxyl-terminus (Magalhaes *et al.*, 2012). Indeed, much of our understanding of desensitisation can be attributed to experiments from the Lefkowitz group, whom observed that catecholamine-induced desensitisation of adenylyl cyclase was associated with phosphorylation of the beta$_2$-adrenoreceptor (β_2AR) (Stadel *et al.*, 1983). Once phosphorylated, the receptor has increased affinity for scaffold proteins such as βarr. βarr binding to the GPCR prevents G-protein coupling, therefore inhibiting G-protein dependent signalling. βarr also interacts with clathrin and its adaptor AP2 to promote receptor endocytosis (Goodman *et al.*, 1996).

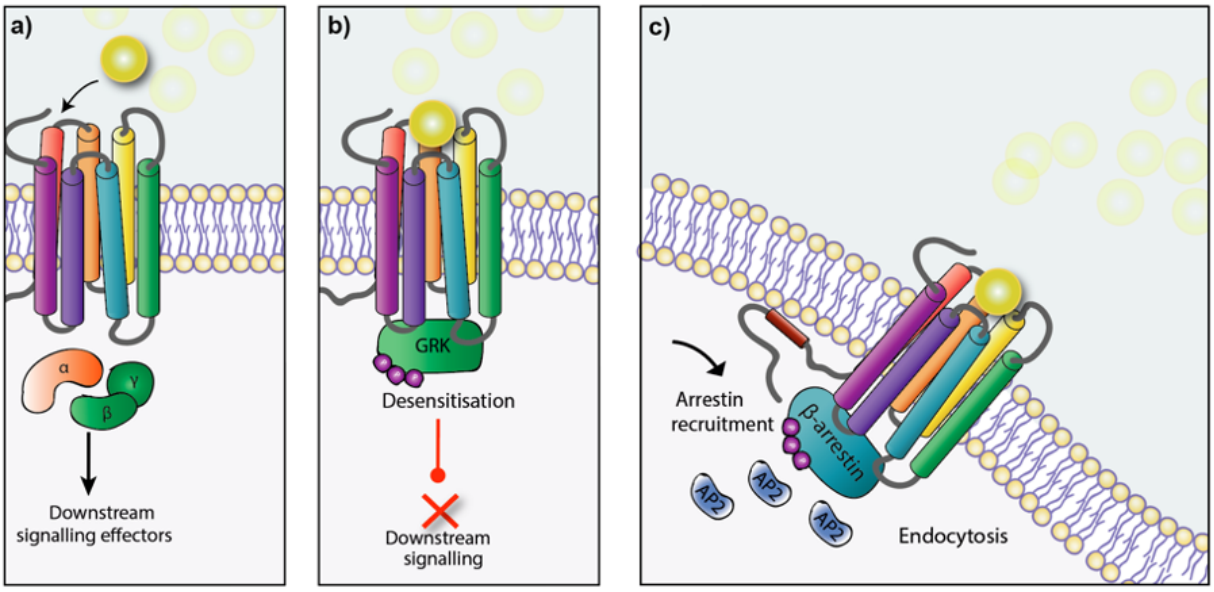

Figure 1.5: **Beta-arrestin (βarr) mediated endocytosis.(A)** Following receptor activation (ligand in yellow), downstream signalling pathways are activated. **(B)** Ligand activated GPCRs are phosphorylated by GRKs, which results in; **(C)** The recruitment of βarr. βarr recruits further proteins such as AP2 and clathrin to initiate endocytosis. The encapsulated receptor and ligand can be degraded in the endosome.

1.6 GPCR structural revolution

Structural studies of GPCRs have made tremendous progress over the last two decades. The elucidation of structures has provided valuable insights into molecular mechanisms of ligand recognition, receptor activation, and signalling transduction, while also providing a structural basis for drug development. The understanding of the overall 7TM topology of GPCRs was first solved in 1993, from two-dimensional crystals of rhodopsin (Schertler *et al.*, 1993). It wasn't until the turn of the millennium when the first, high-resolution GPCR structure, bovine rhodopsin (bRho), was solved at a 2.8 angstrom (Å) (figure 1.6a) (Palczewski *et al.*, 2000). It would then take another seven years for the second GPCR structure to be solved, β_2AR at 2.4 Å (Cherezov *et al.*, 2007), which was the first GPCR structure bound to a diffusible ligand. Since these milestone events, GPCR structural information has seen enormous growth, to date, 90 unique receptor complexes have been solved, 53 of these being published in the last 5 years (correct as of February 2021) (Pandy-Szekeres *et al.*, 2018). Many of the structures result from crystallographic studies, however, it would be remiss not to mention the 'resolution revolution' of cryo-EM, which is contributing to the growing number of GPCR structures being deposited in the Protein Data Bank (PDB) (figure 1.6b) (Kuhlbrandt, 2014). In 2017, the first two unique cryo-EM GPCR structures were solved for family B receptors, calcitonin receptor (CTR) (Liang *et al.*, 2017) and glucagon-like peptide 1 receptor (GLP1R) (Zhang *et al.*, 2017). Since then, 98 GPCR structures have been solved via cryo-EM and deposited into the Protein Data Bank (correct as of February 2021).

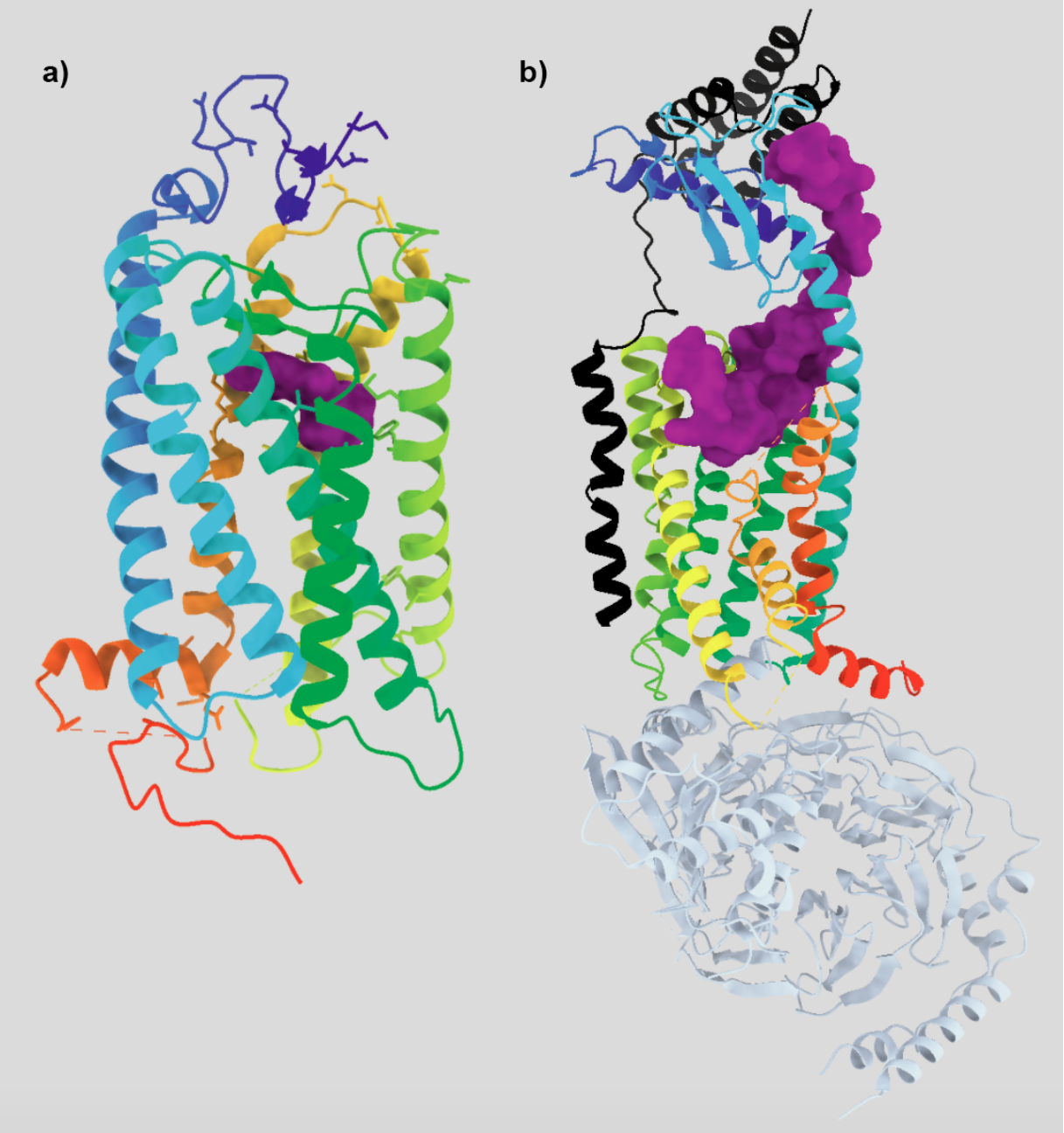

Figure 1.6: **Twenty years of GPCR structural biology. (a)** The first GPCR crystal structure, bovine rhodopsin solved in 2000. The covalently bound ligand, 11-*cis*-retinal is shown (purple) (PDB 1F88) (Schertler *et al.*, 1993). **(b)** The human calcitonin receptor-like receptor in complex with RAMP2 (black), adrenomedullin$_{13-52}$ (purple) and heterotrimeric G_s (pastel blue/grey). Solved via cryo-EM in 2020 (PDB 6UUN) (Liang *et al.*, 2017). Protein images modified in UCSF ChimeraX v0.91 from PDB files (Goddard *et al.*, 2018).

These structural breakthroughs have contributed to the understanding of receptor activation. Of the 90 available unique structures, 42 of these are active-state, permitting direct observational assessment of conformational changes that occur during receptor activation. While family A and family B GPCRs show low sequence identity, the overall architectural changes upon activation appear to be preserved throughout the GPCR superfamily (Katritch *et al.*, 2013). Upon ligand binding, the orthosteric site contracts, even in the absence of G-protein (Weis and Kobilka, 2018). Most prominently, a large outward movement of TM6 (approximately 10–15 Å) has been observed in active structures, as well as an approximate 2 Å inward shift of TM7 in Gα_s and Gα_i -coupled structures (Cherezov *et al.*, 2007; Liu *et al.*, 2012; Siu *et al.*, 2013; Hausch, 2017). The degree of these movements is receptor-specific and are a pre-requisite for the rotation and extension of the α5 helix of the Gα subunit, into the receptor core. The α5 helix can adopt a variety of tilt angles relative to the Gα core, which again are receptor-specific (Glukhova *et al.*, 2018; Weis and Kobilka, 2018). An example of the valuable insights structural information has yielded is of the potent, selective, and orally efficacious 1,2,4-triazine derivatives that have been identified as antagonists of the adenosine $_{2A}$ receptor (Congreve *et al.*, 2012). The increasing amounts of structural information available are due to advancements in expression, stabilisation and solubilisation methods combined with advancements in crystallisation, and cryo-EM techniques.

1.7 GPCRs in drug discovery

Many of the therapeutics now known to act on GPCRs were developed long before actual knowledge of their target, demonstrating the important physiological roles GPCRs play and their inherent tractability as drug targets. Traditionally, GPCRs have been targeted with small molecules or low-molecular-weight peptides that mimic a natural agonist. Obtaining suitable small molecules is a vastly challenging process, owing to the complex and dynamic nature of GPCRs. Small molecules generally demonstrate poor selectivity owing to their relatively high lipophilicity and low molecular weight, meaning *in-vivo* side-effects can be difficult to regulate (Leeson and Springthorpe, 2007). These hurdles have meant that up to 75 % of the 'GPCRome' remains 'un-drugged'. Approximately 80 receptors are targeted by small molecules and a further 30 by peptides (Santos *et al.*, 2017). An alternative and growing approach to developing GPCR-based drugs is with monoclonal antibodies (mAbs), which demonstrate a number of key benefits over small molecules and peptide mimetics.

1.8 Monoclonal antibodies (mAbs) in GPCR drug discovery

mAbs demonstrate significant therapeutic and commercial opportunity with growing approvals and marketed therapies in recent years. Out of a total of approximately 150 approved mAb drugs (FDA, 2018), just two of these are anti-GPCR mAbs, both receiving approval for use in the UK in 2019. Erenumab is a calcitonin gene-related peptide receptor (CGRPR) antagonist used for the treatment of migraine (SMC, 2019). Mogamulizumab is an anti-CCR4 mAb, approved for use in cases of T-cell lymphoma (NHS, 2019). The apparent delay in the generation of anti-GPCR antibodies is due to inherent GPCR characteristics that present hurdles to overcome with regards to understanding GPCR structure and function. Inherent GPCR flexibility and multiple conformational states mean that obtaining a homogenous, functional, and clinically-relevant sample of GPCR is difficult (Ayoub *et al.*, 2017). Further to this, a relatively small portion of the receptor is avail-

able, the extracellular domains (N-terminus and ECLs), for antigen-epitope recognition. Despite these hurdles, advances in expression systems, novel solubilisation methods and innovative antibody generating platform technologies, mean it is now more accessible than ever to generate anti-GPCR antibodies, and reap the benefits of mAb associated drugs, as well as to aid further research.

Compared to small molecules, while still more expensive to produce, mAbs can demonstrate a markedly improved specificity for receptors, being able to bind specifically to a single receptor type, even if it has closely related subtypes. This is because small molecules tend to target the receptor binding site, which, due to evolutionary selection pressures, tends to remain conserved within sub-types. For example, the small molecule, anti-psychotic drug clozapine has been shown to have activity at seven different receptors (Bymaster *et al.*, 1996). The markedly increased specificity of mAbs mean antibody drugs generally demonstrate less inter-patient variability. Producing a uniquely specific mAb is still challenging, as highly similar three-dimensional structures between subtypes means cross-reactivity can still occur (Michel *et al.*, 2009). mAb drug-conjugates can be engineered to have limited central nervous system (CNS) penetration, giving significant advantage for targeting peripheral receptors. Furthermore, antibodies demonstrate a longer duration of action compared to small molecules or peptide mimetics, which can mean preferential dosing regimens and improved patient compliance. Finally, the attrition rate of biologics is less than small molecules, with ∼25 % biologics being approved after pre-clinical testing, compared with ∼7 % for small molecules (Muller, 2013). mAbs generally interact with the extracellular domain (ECD) of the receptor, whereas small molecules tend to act at the transmembrane domain (TMD), meaning mAbs may stabilise different conformational states. Furthermore, the recent application of camelid nanobodies which are small (12–15 kDa) antibody-like binding structures, allow for penetration deep into the TM helical bundle and small TMD cavities (figure 1.7). Nanobody-based medicines are beginning to make their way into the clinic. The first therapeutic nanobody, caplacizumab, was approved for use in the UK in February 2020 (NHS, 2020). Caplacizumab

is a bivalent anti-von Willebrand Factor humanised nanobody, used in indications of acquired thrombotic thrombocytopenic purpura. Whilst not a GPCR-targeting therapeutic, many nanobodies are in clinical trials at present, including two chemokine receptor targeting nanobodies (Jovcevska and Muyldermans, 2020). Their specific binding capability represents a potential to influence GPCR signalling in a number of ways. The antibody may block the binding site of the natural ligand, either by orthosteric modulation or by causing a conformational change when binding to an allosteric site. The binding of the antibody may stabilise an inactive state of the receptor, terminating all signalling pathways. The antibody may stabilise an active form of the receptor, in the absence of the natural ligand, and as it is recognised that there are multiple active conformations, an antibody has the potential to influence any one of these, which could lead to biased signalling. The antibody may stabilise the agonist-bound state, reducing dissociation of ligand to the receptor. The antibody may induce internalisation, reduce cell-surface signalling, and this could have implications for endosomal signalling. Finally, the antibody may promote hetero or homo-dimerisation.

With such therapeutic potential for anti-GPCR antibodies, the delay in lead generation is frustrating for researchers and the medical field alike. Next to be discussed will be some of these hurdles and frustrations to GPCR research, and how recent advances are overcoming such issues.

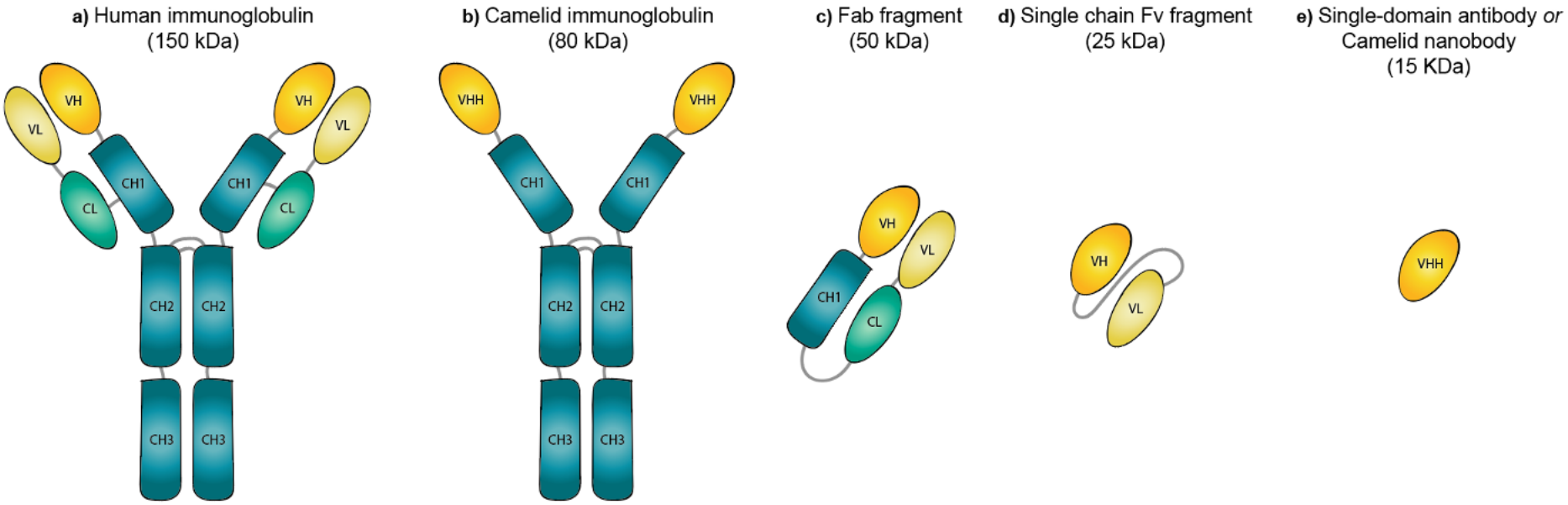

Figure 1.7: **Comparison of different types of antibody.** **(a)** Human IgG, comprised of two heavy chains (H) and two light chains (L). The Fab region contains constant (C) and variable (V) domains. **(b)** A camelid antibody, or heavy chain antibody, consists of only heavy chains (H) and one variable domain (VHH). Disulphide bonds found in both antibody types stabilise chain conformation (indicated by the double line). **(c)** The antigen-binding fragment (Fab) is the region that binds the antigens. It contains both a heavy and variable light domain. **(d)** A single-chain Fv fragment, technically a fusion protein of both heavy and light variable chains **(e)** Camelid nanobody, which consists of a single VHH domain.

1.9 Challenges of GPCR study

The major hurdles to generating samples suitable for structural analysis include; *(i)* Inherent flexibility of GPCRs, especially in loop regions and extracellular domains, which make obtaining receptors in a homogenous conformation extremely challenging. Attempts to overcome this have involved generating truncated receptors (Jaakola *et al.*, 2008), fusing them with T4 lysozymes (Cherezov *et al.*, 2007), incorporating thermo-stabilising mutations (Serrano-Vega *et al.*, 2008), or more recently, camelid nanobodies are being utilised to aid GPCR crystallography (Ayoub *et al.*, 2017). *(ii)* The fact they are membrane proteins, therefore obtaining a solubilised sample without denaturing the receptor is technically challenging, owing to the need for detergents. This is a problem which may be overcome by the addition of lipids during purification and crystallisation (Congreve and Marshall, 2010). More recently, detergent-free extraction using nanodiscs has been achieved using amphipathic polymers (discussed in next section) (Jamshad *et al.*, 2015a). *(iii)* Most GPCRs are expressed at relatively low levels, requiring a suitable recombinant expression system to yield adequate amounts of sample (Kesidis *et al.*, 2020). Recent advances in expression systems have enabled multiple improvements, allowing for many milligrams of purified protein to be obtained (He *et al.*, 2014). There has been success with yeast expression systems, in particular *Pichia pastoris* (*P. pastoris*) and *Saccharomyces cerevisiae* (*S. cerevisiae*). For example, the human adenosine A_2 receptor ($A_{2A}R$) is well characterised for expression in yeast (Butz *et al.*, 2003; Wedekind *et al.*, 2006). Structures of the histamine H_1 receptor have also been determined using *P. pastoris* (Shiroishi *et al.*, 2011). Yeast endogenously express accessory proteins such as receptor activity modifying proteins (RAMPs) and heat-shock proteins which have been shown to promote folding of rhodopsin (Chapple and Cheetham, 2003), as well as known to interact with other GPCRs to influence expression and function (Hay *et al.*, 2006). However, yeast cell membranes are lacking in cholesterol which is essential for effective oxytocin receptor (OTR) function (Gimpl and Farenholz, 2000). Furthermore, yeast performs high-mannose type N-linked

glycosylation which is heterogeneous and causes 'bottlenecks' during crystallisation studies (Yurugi-Kobayashi *et al.*, 2009) however, this is dependent on the exact GPCR in question. This hurdle may also be overcome by using specific engineered strains that have 'humanised' glycosylation properties (Laukens *et al.*, 2015). It is also worth noting that yeasts have a cell wall which requires extra lysing steps which may hinder protein recovery, or require additional equipment (Massotte, 2003).

Insect cells represent an alternative expression system that can be used for GPCR expression, capable of performing complex post-translation modifications such as phosphorylation, fatty-acid acylation and glycosylation (Massotte, 2003) however, N-glycosylation is bound by similar limitations as with yeasts (Jarvis and Finn, 1995). The most widely used cell lines derive from *Spodoptera frugiperda* ovarian tissue known as $Sf9$, or $Sf21$ cells. Many crystal structures have been solved utilising insect cells including, but not limited to, several $A_{2A}R$, β_2AR, chemokine, muscarinic and opioid receptors (Maeda and Schertler, 2013; Zhang *et al.*, 2015; Wang *et al.*, 2018; Kumar *et al.*, 2019; Liu *et al.*, 2019).

Mammalian cells represent an ideal expression environment for human GPCRs, owing to the fact they are capable of performing the complex post-translation modifications and protein processing required for correct receptor folding, trafficking and function. Mammalian cells also mimic the natural lipid environment, which can be essential for ensuring correct function. The major limitation to mammalian cell expression appears to be generating adequate amounts of protein, often requiring stably-transfected, inducible cell lines which are rarely commercially-available (Reeves *et al.*, 2002; Chaudhary *et al.*, 2012). Other tactics to increase expression levels within mammalian cells include codon optimisation (Babcock *et al.*, 2001) and expression export tags (Krautwurst *et al.*, 1998).

1.10 Solubilisation of GPCRs

Understanding the structure, function and behaviour of a receptor and its ligand(s) is an essential pre-requisite for rational drug design. Various biophysical, pharmacological and molecular techniques exist that enable detailed information about protein interactions, structure and dynamics to be obtained. However, almost all of these require a sample of solubilised protein in aqueous solution. Traditionally, proteins are solubilised with detergents, which are amphipathic molecules that possess hydrophobic and hydrophilic groups (Seddon *et al.*, 2004; Prive, 2007). In aqueous solution, they form micellar structures in which the polar head groups confer solubility on the micelle, while the hydrophobic hydrocarbon chains are shielded from solution (figure 1.8a). Membrane proteins are frequently soluble in micelles formed by amphiphilic detergents however, denaturing may occur. This denaturing is a result of the loss of the native lipid bilayer (de-lipidation) and subsequent loss of the lateral pressure that normally exerts on the membrane protein, allowing it to lose its native folded shape (Marsh, 2007; Harvey and Wysocki, 2015). Indeed, this de-lipidation may be the most common cause of membrane protein inactivation during solubilisation (Popot, 2010). Much work has been done in attempting to optimise detergent solubilisation of membrane proteins, for example, to reduce detergent contact time, the application of non-conventional surfactants, such as amphipathic polymers (amphipols) or fluorinated surfactants have been successfully applied (Nehme *et al.*, 2010) (figure 1.8b). Amphipol polymers associate with the TMD with high affinity, which confers stability on the membrane protein. Amphipols have been proven to be efficient at stabilising GPCRs and are well suited for NMR studies (Mary *et al.*, 2014). Despite improved protein stability, limitations remain with amphipol usage, perhaps most significant is the dependency on initial detergent contact. The latter also holds for a bicelle (bilayered micelles) approach, whereby a substituted lipid-rich medium mimics the phospholipid bilayer and is edge-stabilised by detergent (Vold *et al.*, 1997) (figure 1.8c). This dependency on detergents despite the universal acknowledgement that receptor stability and functionality

are compromised has resulted in significant research efforts in the hunt for other membrane mimetic systems. Ideally, GPCR samples should be generated in a native-like state, complete with annular lipid, without any exposure to detergent. One approach utilises nanodiscs that provide a defined lipid bilayer, surrounded by a belt of apolipoproteins (termed membrane scaffold proteins, MSPs) with resultant diameters between 10–20 nm (Nath *et al.*, 2007) (figure 1.8d). This approach has demonstrated success in the purification of functional GPCRs, and detergent contact time is significantly reduced (Leitz *et al.*, 2006; Mitra *et al.*, 2013; Dijkman and Watts, 2015). Despite the useful application of MSP nanodiscs, the ultimate requirement for detergent contact means limitations remain.

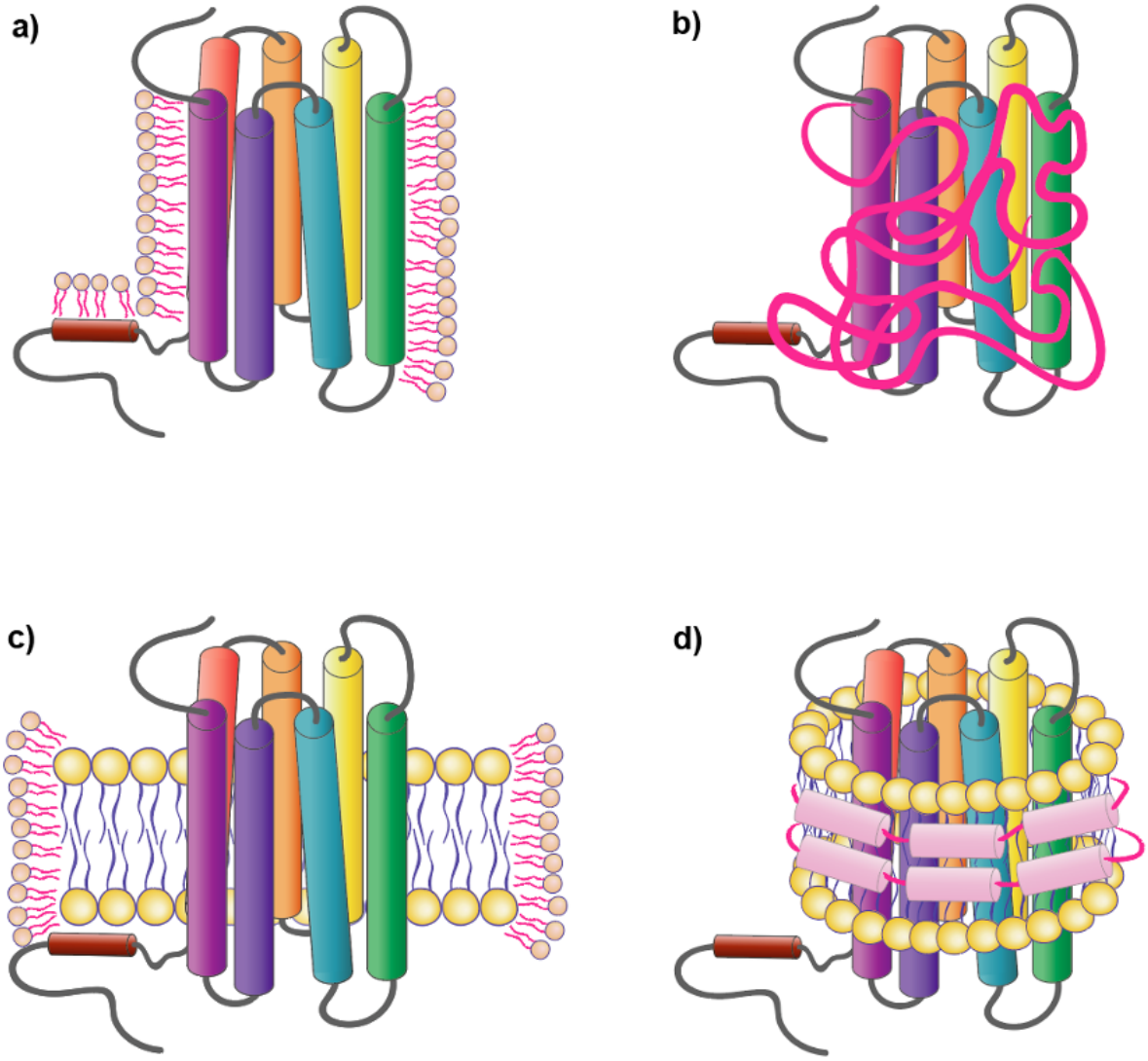

Figure 1.8: **Schematic representation of GPCR environments following extraction from the native membrane environment.(a)** Detergents; **(b)** Amphipol, or fluorinated surfactants; **(c)** Bicelles; **(d)** Protein-stabilised nanodiscs (membrane scaffold protein, MSPs)

Building on the nanodisc approach, the first solubilisation and purification of a functional GPCR, the human $A_{2A}R$, without the use of detergent at any stage, was reported in 2015 (Jamshad *et al.*, 2015a). This was achieved by exploiting spontaneous encapsulation of a GPCR direct from a membrane using poly(styrene-*co*-maleic acid) (SMA) to form a **s**tyrene **m**aleic **a**cid **l**ipid **p**article (SMALP). This generates a nano-section of the native membrane excised and stabilised by a ring of SMA polymer (Knowles *et al.*, 2009) (figure 1.9). Proof of concept was initially demonstrated via efficient extraction of

functionally intact proteins including PagP, a palmitoyl transferase and bacteriorhodopsin (Knowles *et al.*, 2009). SMA-solubilised membrane proteins have since been widely published upon and utilised in biophysical analysis, structural studies and as a platform for drug discovery (Sarkar *et al.*, 2019; Su *et al.*, 2019; Horsey *et al.*, 2020; Routledge *et al.*, 2020) (http://smalp.net/publications.html).

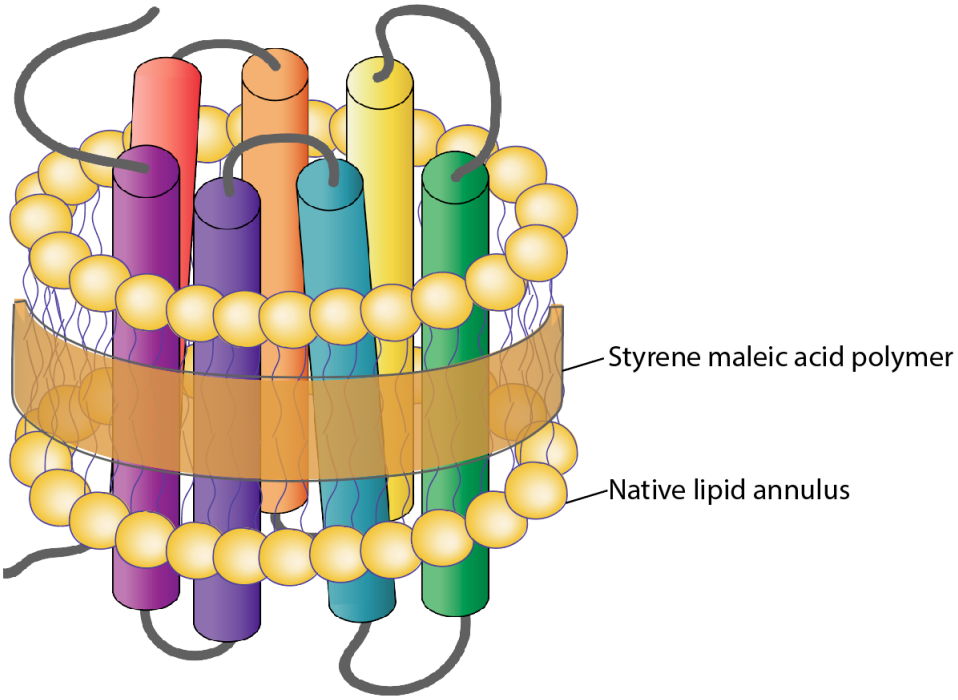

Figure 1.9: **Schematic of a styrene maleic acid lipid particle (SMALP).** SMA polymer 'wraps' around a membrane protein to generate an encapsulated SMALP, whereby native lipids are retained.

1.11 Styrene maleic acid

Styrene maleic acid is the hydrolysed form of commercially-available **s**tyrene **m**aleic **a**nhydride (SMAnh) copolymer, which is synthesised from hydrophobic styrene and hydrophilic maleic acid moieties (figure 1.10). The ratio of styrene to maleic acid can be varied, as can polymer chain length. These alterations result in polymers that provide different chemical properties such as, variation in disc size and solubilisation efficacy (Stroud *et al.*, 2018). Work reported in this thesis utilised a 2:1 (styrene/maleic anhydride) ratio. As well its more recent use in detergent-free solubilisation of membrane proteins, SMAnh has long-standing applications in the plastics industry, as it confers heat resistance and increases impact strength. It also has uses in the production of glossed paper, as well as paint emulsifiers. Away from this, SMA polymers have uses in the medical field, for example in long-term male contraceptive investigations (Lohiya *et al.*, 2014), as well as ongoing investigations and applications for its use in oral drug delivery systems (Parayath *et al.*, 2015).

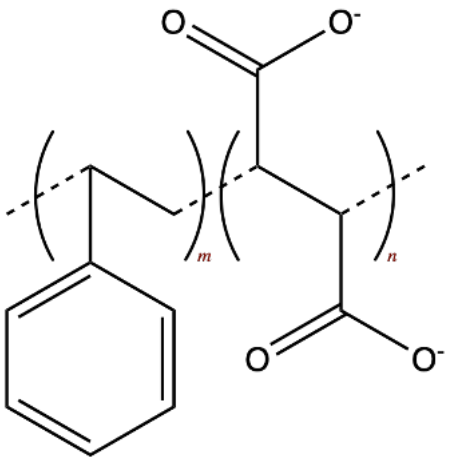

Figure 1.10: **Chemical structure of poly(styrene-*co*-maleic acid), SMA.** SMA is comprised of repeating units of styrene *(m)* and maleic acid *(n)*. The ratio of styrene to maleic acid can be altered, as well as chain length.

In 2001, it was first published that SMA forms discoidal structures that are capable of incorporating hydrophobic molecules upon interaction with phospholipids (Tonge and Tighe, 2001). While the exact mechanism is still not fully understood, it is believed that in the membrane, SMA chains undergo spontaneous polymerisation to form longer chains (Tonge and Tighe, 2001). This spontaneous polymerisation allows discs of varying sizes to form. SMA at a 2:1 (styrene/maleic acid) ratio consistently forms disc sizes approximately 10 nm in diameter. Once a disc has formed the styrene and maleic acid groups re-orientate around the highly flexible, carbon-carbon single bond, backbone. This allows the lipophilic styrene groups to interact with lipids and membrane proteins (Parmar *et al.*, 2017), while hydrophilic maleic acid groups orientate to the outside of the disc conferring a strong negative charge, and solubility in aqueous solution (Dominguez-Pardo *et al.*, 2017). The fact that SMA is able to solubilise directly from the membrane presents a major advantage over other approaches, as a detergent is not required at any stage. Hydrolysis of SMAnh to form SMA is also inexpensive and the solubilisation method is technically very simple. Post-solubilisation, there is no need to supplement buffers with additional SMA, and excess polymer can be removed by dialysis or other size-exclusion techniques. Furthermore, when compared to MSPs, due to SMA being non-proteinaceous, spectroscopic techniques (such as circular dichroism) and fluorescence methods can be performed.

1.12 Second-generation polymers

Detergent-free solubilisation has been dominated by SMALPs however, SMA is not without limitations. The disc-scaffold of a membrane protein embedded in SMALP has high UV absorption, which hinders UV-spectroscopic studies, meaning the quantification of protein yield by SMA cannot be reliably determined using absorbance at 280 nm, especially in the presence of excess polymer. Furthermore, the SMALP structure is sensitive to divalent cations (such as Mg^{2+}), which above a certain concentration ($\sim$4 mM), will cause the SMA to precipitate (Morrison *et al.*, 2016). The negative charge surrounding the SMALP could interact with positively charged ligands, which has been shown to increase non-specific binding (Charlton, 2015), which limits the pharmacological characterisation of certain SMALP-membrane proteins. SMALP nanodiscs also have a specific diameter $\sim$10 nm, meaning large complexes, densely packed and highly ordered membranes do not solubilise effectively in SMALPs (Swainsbury *et al.*, 2017).

The described limitations have resulted in a small arsenal of emerging, alternative copolymers with differing characteristics ('polymer tool kit'), however many of these are yet to be widely characterised, especially in a cell-based context. SMA-based derivatives that maintain the ability to self-assemble into nanodiscs appear a logical progression in the development of a 'polymer tool kit'. To achieve customised functionality, SMAnh has been modified to contain cysteamine maleic anhydride. This is cleaved to acid form under slight-alkaline conditions to produce SMA containing solvent-exposed reactive sulfhydryl groups (SMA-SH) (Lindhoud *et al.*, 2016). These sulfhydryl groups allow a wide range of bio-conjugation chemistries, such as the addition of functional groups including fluorophores and biotin. Furthermore, this can allow for the immobilisation of SMALPs on surface plasmon resonance (SPR) chips, as a drug discovery aid (Trahey *et al.*, 2015).

In a similar strategy to SMA-SH, the carboxylic acid groups on each maleic acid moiety have been substituted with N-(2-aminoethyl)amide to yield SMA-ED. SMA-ED may be dehydrated, producing SMAd-A (dehydrated SMA-ED) which is positively charged

at acidic pH. Both SMA-ED and SMAd-A are functional at acidic pH, as opposed to 'standard' SMA which is functional at neutral to mildly alkaline pH (Ravula *et al.*, 2017).

In another approach, the carboxyl acids of SMA were replaced with zwitterionic phosphatidylcholine (PC) groups to yield zwitterionic SMA's (zSMA). zSMA's present wider buffer compatibility than SMA and do not precipitate at neutral to low pH, due to the omission of carboxyl groups (Fiori *et al.*, 2017). Finally, another example of an emerging copolymer is poly(**s**tyrene-*co*-(N-(3-N',N'-dimethylaminopropyl)**m**ale**i**mide)) (SMI), similar to SMA, except the **s**tyrene **m**ale**i**mide **l**ipid **p**article (SMILP) is positively charged (figure 1.11) (table 1.1). SMI has been validated as capable of solubilising phospholipids by self-assembling in the same way as seen for SMA (Hall *et al.*, 2018). Furthermore, SMI exhibits tolerance to divalent cations, which proves useful in the study of ATPases and ion channels. SMI is also capable of solubilising biological membranes, with functional encapsulation of membrane proteins from *E. coli* and HEK 293T cells (Hall *et al.*, 2018). Notably, two GPCRs have been shown to maintain ligand binding capability upon SMILP-extraction (Charlton, 2015; Hall *et al.*, 2018). SMI is an emergent, promising alternative to SMA, functional at acidic to physiological pH, providing an alternative working range.

There are a number of other SMA-based derivative polymers, thoroughly reviewed in (Stroud *et al.*, 2018). Overall, the introduction of different hydrophobic groups emphasises the robustness of the SMA solubilisation strategy. This has allowed a toolbox of polymers to be developed where SMA reaches its limitations. Many of these SMA-like polymers are yet to be extensively tested in biological membranes, therefore it will be some time before larger-scale polymer-screening becomes routine, as is current with detergents. As an alternative to modifying existing SMAnh to generate derivatives, a number of non-SMA polymers have also been developed and shown to be functional in nanodisc generation. One emergent example is poly(**d**i**i**so**b**utylene *alt*-**m**aleic **a**cid) (DIBMA) (figure 1.12). In contrast to SMA, DIBMA contains aliphatic diisobutylene in place of aromatic styrene groups. The omission of the styrene ring means DIBMA does not interfere with UV-spectroscopic studies. DIBMA is also more tolerable of low millimolar concentrations

of divalent cations than SMA. DIBMA-lipid particles (DIBMALPs) have a tunable size range from approximately 20–50 nm, depending on the polymer to lipid ratio (table 1.1). Therefore, DIBMA has the potential to encapsulate larger membrane complexes than SMA (Oluwole *et al.*, 2017b). Furthermore, from a thermodynamic perspective, DIBMA is less perturbing than SMA. Calorimetry and Raman spectroscopy experiments demonstrated that the inclusion of diisobutylene chains from DIBMA into the encapsulated lipid bilayer led to less perturbation of the lipids than the phenyl ring from SMA (Oluwole *et al.*, 2017a).

Table 1.1: **Summary of solubilisation polymers used within this thesis.**

Polymer name	Hydrophobic moiety	Hydrophilic moiety	Disc size (nm)	Polymer solubility (pH)	Ion tolerance
SMA2000	Styrene	Maleic acid	10	> 5.8	< 4 mM Mg^{2+} < 4 mM Ca^{2+} *(1)*
SMA2000i	Styrene	Maleimide	10	< 7.8	> 100 mM Mg^{2+} > 100 mM Ca^{2+} *(2)*
DIBMA *(Sokalan CP9®)*	Diisobutylene	Maleic acid	20	> 6.5	< 50 mM Mg^{2+} < 20 mM Ca^{2+} *(3)*

*(1)*Stroud *et al.* (2018) *(2)*Hall *et al.* (2018) *(3)*Oluwole *et al.* (2017)

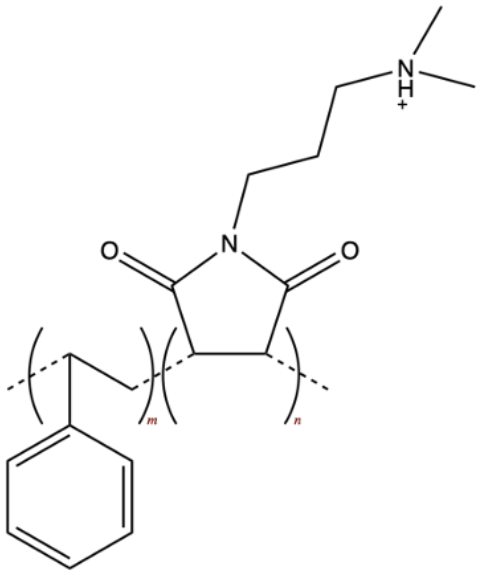

Figure 1.11: **Chemical structure of poly(styrene-*co*-maleimide), SMI.** The carboxyl groups of SMA are replaced with a maleimide moiety.

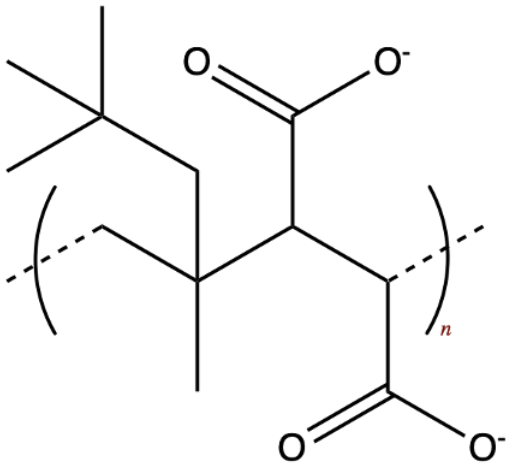

Figure 1.12: **Chemical structure of alternative solubilisation polymer, poly(diisobutylene-*alt*-maleic acid), DIBMA.** Aliphatic diisobutylene chains replace the styrene ring from SMA.

1.13 Aims and scope of thesis

This chapter has described and introduced GPCR structure, function, pharmacology and relevance to medicine, furthermore, associated challenges with their study have been discussed. The overall aim of this work was to elucidate novel insights into GPCR pharmacology utilising a variety of techniques, as well as validate the application of SMA and SMA-like polymers for the extraction of functionally active GPCRs.

The use of SMALPs has become well-established and widely validated however, there is still relatively little published work with regards to GPCR-SMALPs, particularly in a mammalian-cell context. Previous work from the Wheatley lab established optimal experimental procedures for SMALP-solubilising GPCRs from mammalian cell membranes, in particular with $A_{2A}R$. This study builds on that work by probing other GPCR-targets (family A and family B), and explores use of downstream biophysical techniques, such as fluorescence correlation spectroscopy (FCS) to quantify ligand binding, alongside traditional methods such as radioligand binding. With the limitations of SMA in terms of pH stability and sensitivity to divalent cations (discussed above), the demand for alternative, biologically validated, commercially-available polymers is increasing. To this end, the conformational dynamics of polymer-extracted rhodopsin were investigated using SMA, SMI and DIBMA, and compared to the behaviour of rhodopsin in classically utilised detergent, *n*-dodecyl β-*D*-maltoside (DDM). The rhodopsin-lipid particles (rhodopsin-LPs) were also biophysically characterised via stability assays, dynamic light scattering (DLS) and analytical ultracentrifugation (AUC).

Finally, another relatively unexplored field of GPCR research is their interaction with accessory proteins known as RAMPs. It is known that most family-B GPCRs form interaction with at least one RAMP and that RAMPs have the ability to dramatically alter receptor phenotype. A recently discovered in-frame deletion of Val^{205} in the extracellular loop of the calcitonin receptor-like receptor (CLR) has been implicated in a human disease (Mackie *et al.*, 2018). The CLR is known to interact with all known RAMPs, and this

study probed the CLR-RAMP interaction at the WT, Val^{205} deletion and other deletion mutations generated along the extracellular loop. Deletions along the loop were generated in order to investigate if Val^{205} is particularly important for receptor function, or if there is a wider functional importance of ECL1.

Chapter 2: Materials and Methods

2.1 Materials and Suppliers

2.1.1 AlphaScreen™ cAMP detection assay

AlphaScreen™ cAMP Detection Kit (cat. 6760635D) and 96-well, white, half-area plates (cat. 6005560) were bought from Perkin Elmer (Beaconsfield, UK). Forskolin (cat. 1099) was purchased from Tocris (Abingdon, UK) and dissolved in di-methyl-sulphoxide (DMSO) to form a 1 mM stock. 3-Isobutyl-1-methylxanthine (IBMX) (cat. 15879) was purchased from Sigma-Aldrich (Dorset, UK) and dissolved in DMSO to form a 500 mM stock.

2.1.2 Antibodies

Mouse monoclonal anti-haemagglutinin (HA) (cat. H9658) and mouse anti-FLAG monoclonal M2 clone (cat. F1804) were purchased from Sigma-Aldrich. Monoclonal horse anti-mouse horseradish peroxidase (HRP) linked-IgG (cat. 7076S) and mouse monoclonal anti-His (cat. 27E8) were purchased from New England Biolabs (Hitchin, UK).

2.1.3 Cell tissue culture

Plastic-ware for cell tissue culture was purchased from Greiner Bio One (Gloucestershire, UK). Dulbeccos Modified Eagle Medium (DMEM) with 4.5 g/L glucose and L-glutamine (cat. LZBE12-604F) was obtained from Scientific Laboratory Supplies (Northumberland, UK). DMEM F12 with HEPES (cat. 11559716) and G418 sulphate (cat. 15393671) were purchased from Fisher Scientific Ltd (Leicestershire, UK). Foetal Bovine Serum (FBS) (cat. F9665), trypsin solution (0.25 % w/v) (cat. T4424) and N,N-bis(2-hydroxyethyl)-2-aminoethanesulfonic acid (BES) (cat. B9879) were purchased from Sigma-Aldrich.

2.1.4 Inositol phosphates (InsP-InsP$_3$) accumulation assay

Inositol-free DMEM was custom made and purchased from Thermo-Fisher Scientific (New York, USA). UltimaFlo AF scintillation cocktail was procured from Perkin Elmer. Resin AG1-X8 was purchased from Bio-Rad (Hemel Hempstead, UK).

2.1.5 Membrane harvesting and competition binding assays

Phosphate-buffered saline (PBS) tablets (137 mM NaCl, 2.7 mM KCl and 10 mM phosphate buffer solution, pH 7.4) were obtained from Oxoid (Basingstoke, UK). Bovine serum albumin (BSA), ethylene glycol-bis(2-aminoethylether)-*N,N,N,N*-tetraacetic acid (EGTA), and magnesium acetate were purchased from Sigma-Aldrich. Bacitracin was purchased from Acros Organics (Geel, Belgium). Soluene®-350 and OptiPhase HiSafe3 scintillant were purchased from Perkin Elmer.

2.1.6 Molecular biology reagents

Pfu Turbo DNA polymerase (2.5 U/µl) (cat. 600252) was purchased from Agilent Technologies (Cheadle, UK). Deoxynucleotide mix (10 mM) (cat. D7295) was purchased from Sigma-Aldrich. *Dpn*I (cat. R6231) was purchased from Promega (Southampton, UK). Apyrase (cat. M0398S) was purchased from New England Biolabs.

2.1.7 Peptides

Human parathyroid hormone (1-34) (PTH_{1-34}) was purchased from Generon (cat. A12790) (Berkshire, UK). Oxytocin (cat. H-2510) and [Arg^8]vasopressin (AVP) (cat. H1780) were acquired from Cambridge Bioscience (Cambridge, UK). Human adrenomedullin 13-52 (AM_{13-52}) (cat. J66619) and calcitonin gene-related peptide (CGRP) (cat. J65667) were purchased from Alfa Aesar (Lancaster, UK). All peptide ligands were dissolved in 0.02% sterile acetic acid to form a stock of 1 mM.

Mini-G_o was a kind gift from Dr. Christopher G. Tate (Medical Research Council Laboratory of Molecular Biology, Francis Crick Avenue, Cambridge, UK). The peptide analogue derived from the α-subunit of transducin, $G_{(t)}$-peptide, (VLEDLKSCGLF) (cat.

S3605-1) was synthesised by Severn Biotech (Kidderminster, UK).

PTH_{1-34} conjugated to a BODIPY 630/650 fluorophore was custom synthesised by Cambridge Research Biochemicals (quotation reference CP17210) (Cambridge, UK).

2.1.8 Plasmid preparation

The pCMV-tetR plasmid was a kind gift from Dr. Phillip J. Reeves (University of Essex, UK). Parathyroid hormone receptor 1 and oxytocin receptor Avi-tagged™ constructs were synthesised and cloned into pCMV-tetR by Genscript (New Jersey, USA). pcDNA3.1(+) was purchased originally from Thermo Fisher Scientific (Loughborough, UK).

Plasmid DNA was isolated and purified using either QIAprep Spin Miniprep (cat. 12155) or Maxiprep (cat. 12163) kit from QIAGEN (Manchester, UK), or PureYieldTM Plasmid Maxiprep System from Promega.

2.1.9 SDS-PAGE and Western blotting

NuPAGE™ LDS Sample Buffer (4X) (cat. NP0007) and NuPAGE™ Sample Reducing Agent (10X) (cat. NP0004) were from Novex®, Thermo Fisher Scientific. InstantBlue® Protein Stain (cat. ISB1L) was purchased from Sigma-Aldrich.

2.1.10 Solubilisation reagents

Styrene maleic anhydride (SMAnh) (SMA2000P) was purchased from Cray Valley (Pennsylvania, U.S.A). Sokalan® CP9 was purchased from BASF (Maastricht, Netherlands).

2.1.11 Substrates

SIGMAFAST™ O-phenyenediamine dihydrochloride (OPD) tablets (cat. P9187) were purchased from Sigma-Aldrich.

2.1.12 Transfection reagents

Lipofectamine® 3000 kit (cat. L3000008) was purchased from Thermo Fisher Scientific. Linear polyethyleneimine (PEI) (cat. 9002-98-6) was obtained from Polysciences Inc. (Eppelheim, Germany).

2.2 Methods

2.2.1 QuikChange™ PCR

The QuikChange™ method for mutagenesis (Stratgene, Cambridge, UK) was utilised to engineer in specific point mutations into the wildtype (WT) calcitonin receptor-like receptor (CLR) construct. Mutagenic primers were designed containing the desired mutation along with flanking, complementary template DNA, WT CLR in pcDNA3.1(+).

Reaction mixtures: 1x *Pfu* buffer; 100–200 ng template DNA; 10 pmol sense and antisense primer; 0.4 mM each of nucleotides dATP, dCTP, dGTP and dTTP; 0.5–2 units *Pfu* DNA polymerase in a final reaction volume of 50 µl.

PCR was carried out in a Biometra T3000 Thermocycler with the following reaction conditions: Initial 95 °C for 1 min; Followed by 11 cycles of 95 °C for 30 s (denaturation), 55 °C for 1 min (annealing), 68 °C for 14 min (elongation). Methylated template DNA was digested with *Dpn*I at 37 °C for 90 min. (*n.b.*: Most commonly used annealing temperature stated).

2.2.2 Agarose gel electrophoresis

DNA products were mixed with a 6x loading dye and separated on 1 % (w/v) TBE agarose gels containing 0.5 µg/ml ethidium bromide. UVItec Cambridge Alliance System (Cambridge, U.K.) was used to image the gels.

2.2.3 Transformation

Chemically competent XL10-Gold cells were transformed aseptically using heat-shock methodology. 1 µl of QuikChange™ product was mixed with 15 µl competent cells and incubated on ice for 30 min. Heat-shock was carried out for 30–45 s at 42 °C, followed by recovery on ice for 2 min. Incubation with 800 µl sterile LB for 1 h at 37 °C was then performed. Cells were then centrifuged (9,500 g, 10 min). All but ∼50 µl of the supernatant was removed and cells were resuspended in the remaining volume. Transformants were inoculated on LB plates containing 100 µg/ml ampicillin and incubated overnight at

37 °C.

2.2.4 Plasmid cDNA purification

QIAGEN Plasmid Mini kit was used as per manufacturer's instructions to isolate and purify between 1–10 μg of cDNA from *E. coli* culture. QIAGEN Plasmid Maxi kit was used as per manufacturer's instructions to isolate and purify between 0.5–2 mg cDNA from *E. coli* culture. cDNA concentration was determined by absorbance at 260 nm using a DeNovix DS-11+ spectrophotometer. Sample purity was determined by measuring the absorbance ratio at 260/280 nm.

2.2.5 Automated fluorescence DNA sequencing

All DNA sequences were confirmed by automated fluorescence DNA sequencing, carried out by Sanger Sequencing Services at Source Biosciences (Nottingham, UK).

2.2.6 Cell culture

HEK 293T, HEK 293S-tetR and COS-7 cells were incubated at 37 °C, 5 % CO_2 in a humidified incubator and passaged twice-weekly. HEK 293T and COS-7 cells were maintained in DMEM supplemented with FBS (10 % v/v). HEK 293S-tetR cells were maintained in DMEM-F12 with HEPES, supplemented with FBS (10 % v/v) and 2 mg/ml G418 (selection media) as appropriate during stable cell generation and routine passage of stable cell lines.

2.2.7 Calcium chloride ($CaCl_2$) transfection

HEK 293S-tetR cells were stably-transfected exactly as described in (Reeves *et al.*, 2002). The transfection solution composed of DNA, $CaCl_2$ and BES buffer (2x BES buffer: 50 mM BES, 250 mM NaCl, 1.5 mM Na_2HPO_4, pH 7.02).

For each dish, 30 μg of relevant tetO-DNA was made up to a volume of 450 μl sterile-distilled H_2O and vortexed. Next, 50 μl of 2.5 M $CaCl_2$ was slowly added and vortexed for 30 s. Finally, 500 μl of 2x BES buffer was added drop-wise over 60 s and mixed by vortex. The transfection solution was then added drop-wise to the cell medium and dishes gently

swirled. The dish was then transferred to a humidified incubator set at 1 % (v/v) CO_2, 37 °C. 16 h post-transfection the medium was removed by aspiration and cells were gently rinsed with un-supplemented DMEM-F12. Cells were fed with 10 ml of supplemented DMEM-F12 and incubated at 37 °C, 5 % CO_2 (v/v) for a further 24 h. After this, the cells were split 1:2, 1:5, 1:10 and 1:20 into new dishes, and pairs of dishes were incubated as above in DMEM-F12 for a further 24 h. After which, medium was removed and cells were fed with selection media. Selection media was refreshed every 3–4 days. Cells that had successfully incorporated the tetO-plasmid into their genome grew as colonies, visible after 2–3 weeks.

2.2.8 Lipofectamine® transfection

Lipofectamine® transfection was carried out exactly as per manufacturer's protocol.

2.2.9 PEI transfection

PEI transfection solutions composed of sterile 5 % (w/v) glucose solution, sterile 0.8 mg/ml PEI solution and relevant DNA samples (table 2.1). The solutions were incubated for 30 min at room temperature before addition of fresh DMEM and applied to cells.

Table 2.1: Composition of PEI transfection solutions, according to plate-size.

	per well			
Plate type	**Glucose solution 5 % (w/v)** (µl)	**PEI** (µg)	**DNA** (µg)	**DMEM** (ml)
92 mm	1000	48	5–12	6
6-well	120	8	2	2
12-well	60	4	1	1
24-well	30	2	0.5	0.5
96-well	7.5	0.6	0.125	0.125

2.2.10 Mammalian-cell membrane harvesting

The following buffers were used in mammalian-cell membrane harvesting and competition radioligand binding assays:

Harvest buffer: 20 mM HEPES, 10 mM magnesium acetate, 1mM EGTA

Solution one: Harvest buffer, bacitracin 0.1 mg/ml, 250 mM sucrose

Solution two: Harvest buffer, bacitracin 0.1 mg/ml

Solution three: Harvest buffer, 250 mM sucrose

Binding buffer: Harvest buffer, BSA 0.1 % (w/v)

Cell membranes were harvested 48 h post-induction or post-transfection as described previously (Wheatley *et al.*, 1997). All steps are carried out at 4 °C. Cells were washed with ice-cold PBS and scraped from dishes with 1 ml per plate of solution one. Cells were centrifuged at 2700 g for 10 min. Supernatant was discarded and pellet was resuspended in 1 ml per plate solution two, and incubated for 20 min, to allow lysis to occur. The solution was centrifuged for 10 min and resuspended in 0.5 ml per plate solution three. Extracts were stored at -20 °C.

2.2.11 Yeast-cell membrane harvesting

A de-glycosylated human adenosine 2A receptor construct was originally designed by Dr. Niall J. Fraser (University of Glasgow, UK) and optimised for expression in *Pichia pastoris* (*P. pastoris*) (appendix E; appendix F) (Fraser, 2006). Heterologous expression of $A_{2A}R$ in *P. pastoris* was achieved exactly as described previously (Singh *et al.*, 2008). Membranes were generated by suspension of induced culture in breaking buffer (50 mM sodium phosphate buffer, 100 mM NaCl, 5 % glycerol, EDTA-free protease inhibitor, pH 7.5, 4 °C) and poured into an Avestin-C3 cell-disrupter and passage performed three-to-five times, with ice kept around the cell to keep solutions cool. Unbroken cells and debris were removed from the suspension by low-speed centrifugation (5000 g, 10 min, 4 °C). Membrane fraction was then collected via ultracentrifuge (100,000 g, 60 min, 4 °C) and re-suspended to 80 mg/ml (wet-weight) in extraction buffer (300 mM NaCl, 20 mM

HEPES, pH 7.5). Extracted membranes were stored at -80 °C.

2.2.12 Preparation of amphipathic copolymers

SMA, and SMI were prepared from SMAnh exactly as described previously (Lee *et al.*, 2016; Hall *et al.*, 2018).

SMI was prepared from SMA2000I resin (purchased from Cray Valley, UK). Concentrated HCl was added dropwise to 10 % (w/v) SMA2000I in ultra-pure water to yield a 1 M solution. The solution was heated under reflux at 125 °C for 2–4 h, until clarification. Solubilised SMI was then precipitated by addition of 5 M NaOH to pH 9.0 and washed three times in ultrapure water. The precipitated SMI was then re-dissolved in a minimal volume of 0.6 M HCl, and pH adjusted to pH 6.0 before lyophilisation.

For SMA preparation, a 10 % (w/v) solution of SMAnh was dissolved in 1 M NaOH, and heated under reflux at 125 °C for 2–4 h, until the solution clarified. Solubilised SMA was then precipitated by drop-wise addition of concentrated HCl, and washed three times in ultrapure water. The SMA was then re-dissolved in 0.6 M NaOH and wash steps were repeated. Finally, SMA was re-dissolved in 0.6 M NaOH, pH adjusted to pH 8.0 and lyophilised.

DIBMA was prepared from Sokalan® CP9. Briefly, 10 ml of Sokalan was pipetted into 40 cm of dialysis tubing (1000 MWCO) and dialysed for 24 h in dH_2O water, with a water change at 12 h. A second dialysis stage was then performed, for a further 24 h (with water change at 12 h), with 200 ml solution being placed into 80 cm fresh dialysis tubing (1000 MWCO). After 24 h, the solution was pH adjusted to pH 8.0, then frozen at -80 °C for 48 h and subsequently lyophilised.

2.2.13 Solubilisation of mammalian cell lines with SMA

The following buffers were used in during SMA-solubilisation:

SMA 1x buffer: 20 mM HEPES, 300 mM NaCl, 2.5 % (w/v) SMA, pH 7.5

SMA 2x buffer: 20 mM HEPES, 300 mM NaCl, 5 % (w/v) SMA, pH 7.5

Crude membranes preparations were thawed on ice and equal volumes of 2x solubilisa-

tion buffer added. If buffer exchange was required, samples were centrifuged for 15 min at 5000 g, 4 °C and resuspended in 1x solubilisation buffer. Samples were incubated for 1–2 h, room temperature (RT), with gentle mixing. Centrifugation at 100,000 g was carried out for 1 h, 4 °C. Supernatant was saved and insoluble pellet was re-suspended in equal volume of storage buffer, for analysis purposes (20 mM HEPES, 300 mM NaCl, pH 7.5). Samples were stored at 4 °C.

2.2.14 Solubilisation of rod outer segments with SMA, SMI or DIBMA

Bovine rod outer segment (ROS) membranes were prepared via sucrose-density gradient centrifugation previously by Dr. Phillip J. Reeves (University of Essex, UK), exactly as described in (Papermaster, 1982). ROS membrane preparations were thawed on ice and approximately 100 µg protein was added to relevant extraction buffer. The DDM extraction buffer consisted of 1 % (w/v) DDM in 1x PBS, pH 7.8. The SMA extraction buffer consisted of 2.5 % (w/v) SMA in 1x PBS, pH 7.8. The SMI extraction buffer consisted of 2.5 % (w/v) SMI in 1x PBS, pH 6.8. The DIBMA extraction buffer consisted of 5 % (w/v) DIBMA in 1x PBS, pH 7.8. Samples were incubated on an end-over-end rotator for 1 h, RT, before centrifugation at 100,000 g, 1 h, 4 °C. Supernatant containing solubilised rhodopsin was collected and stored at 4 °C. Insoluble pellets were resuspended in equal volume of 1x PBS, and stored at 4 °C.

2.2.15 Ni^{2+}-NTA affinity purification

All purification steps were carried out at 4 °C. The supernatant fraction obtained from SMA solubilisation was incubated with ∼1 ml Ni^{2+}-NTA resin, overnight on an end-over-end rotator. The column was washed with 20 column volumes (cv) of wash buffer (300 mM NaCl, 20 mM HEPES, 20 mM imidazole, EDTA-free protease inhibitor, pH 7.5). Elution of GPCR-SMALP was achieved with 10 cv of elution buffer ($A_{2A}R$ and PTH1R: 300 mM NaCl, 20 mM HEPES, 250 mM imidazole, EDTA-free protease inhibitor pH 7.5) (OTR: 300 mM NaCl, 20 mM HEPES, 300 mM imidazole, EDTA-free protease inhibitor pH 7.5). Elution fractions were pooled, buffer-exchanged and concentrated using size-exclusion spin

columns (10,000 MWCO) into assay buffer (300 mM NaCl, 20 mM HEPES, pH 7.5).

2.2.16 SDS-PAGE and Coomassie staining

Samples were incubated for 10 min, RT with NuPAGE™ LDS Sample Buffer, and NuPAGE® sample reducing agent (1x). Samples were loaded into 12 % (w/v) polyacrylamide gel with a 4 % (w/v) polyacrylamide stacking gel. Gels were run at 100 V until samples were beyond the stacking gel, and thereafter at 180 V until the dye-front reached the bottom of the gel.

Coomassie visualisation of protein bands was performed using InstantBlue®, exactly as per manufacturer's instructions.

2.2.17 Western blotting

Gels were washed in transfer buffer (25 mM tris, 25 mM glycine, 10 % [v/v] methanol) for 10 min, shaking at RT. Proteins were transferred to nitrocellulose membrane at 100 V for 1 h in pre-cooled transfer buffer. Nitrocellulose was blocked in 5 % (w/v) milk in PBS (blocking buffer) for 1 h, RT. Primary antibody (1:5000) was added to fresh blocking buffer and incubated overnight, shaking, 4 °C. Nitrocellulose was then washed thrice in wash buffer (PBS, 0.1 % [v/v] TWEEN20) for 5 min, shaking at RT. HRP-linked secondary antibody was then added (1:5000) to fresh blocking buffer and incubated at RT, shaking, 1 h. Nitrocellulose was washed thrice more, as before. Antibody was detected using EZ-ECL detection kit (as per manufacturer's instructions; purchased from Gene Flow, cat. K1-0170). Image was captured using a Uvitec alliance chemiluminescent detection system.

2.2.18 Enzyme-linked-immunosorbent assay

48 h post-transfection cells for internalisation investigation were stimulated with 10^{-6} M appropriate ligand for the time stated. After this, cells were fixed in 3.7 % (v/v) formaldehyde for 15 min before washing three-times with PBS. Nonspecific binding was blocked with 0.1 % (w/v) BSA in PBS for 45 min. Incubation with mouse monoclonal anti-haemagglutinin (HA) (diluted 1:2500) in PBS with 0.1 % (w/v) BSA was carried

out for 1 h at room temperature, shaking. Cells were then washed three-times with PBS, before a repeat blocking step for 15 min. This was followed by incubation with the secondary antibody, monoclonal horse anti-mouse horseradish peroxidase (HRP) linked IgG, (diluted 1:2500) in PBS with 0.1 % (w/v) BSA incubation for 60 min at room temperature, shaking. Cells were washed three times with PBS before addition of 250 µl peroxidase substrate SIGMAFAST^{TM} o-phenylenediamine (0.4 mg/ml OPD, 0.4 mg/ml urea hydrogen peroxide, and 0.05 M phosphate-citrate, pH 5.0). Reaction was developed in the dark and 100 µl sample was added to 100 µl 1M sulphuric acid to halt the reaction. Absorbance was read at 492 nm on an Anthos, Zenyth 340 rt plate reader.

2.2.19 Radioligand binding assay for membrane-bound receptors

Radioligand binding assays were performed on crude membranes, prepared as described above. A 500 µl reaction mixture composed of tritiated ligand; competing ligand at final stated concentration; membrane-bound protein sample containing (50–300 µg) in assay buffer (20 mM HEPES, 1 mM EGTA, 10 mM magnesium acetate, pH 7.4), also containing: 0.1 % (w/v) BSA for peptide ligands, or 0.1 U of adenosine deaminase for A_{2A}R constructs. Nonspecific binding was determined with a saturating concentration of unlabelled ligand. Samples were incubated for 30–90 min at 30 °C, to establish equilibrium. Centrifugation (5000 g, 10 min) separated bound and free ligand. Membrane pellet were superficially washed twice in water and solubilised with 50 µl Soluene®-350. HiSafe3 liquid (1 ml) scintillation cocktail was added to solubilised membrane pellets and samples counted using Tri-carb® 2810 TR liquid scintillation analyser (Perkin Elmer) for 3 min.

2.2.20 Radioligand binding assay for solubilised receptors

Radioligand binding assays were performed on SMALP-solubilised receptors, prepared as described above. A 100 µl reaction mixture composed of tritiated ligand; competing ligand at final stated concentration; SMALP-solubilised membranes (50–100 µg) in assay buffer (20 mM HEPES, 1 mM EGTA, 1 mM magnesium acetate, 0.1 % [w/v] BSA, pH 7.4). Samples were incubated for 30–90 min at 30 C, to establish equilibrium. Separation

of bound from free ligand was achieved by centrifugation (1000 g, 4 min) of 50 µl reaction mixture through Sephadex® G-25 or G-50 packed spin columns (purchased from Sigma-Aldrich). Void volumes were collected and 1 ml of Hisafe3 liquid scintillation cocktail was added to samples. Counting was performed on Tri-carb® 2810 TR liquid scintillation analyser for 3 min.

2.2.21 cAMP detection assay

Performed as previously described (Simms *et al.*, 2009). 48 h post-induction, or post-transfection, medium was removed and cells incubated in DMEM (without phenol red), containing 1 mM isobutyl methylxanthine (IBMX) and 0.1 % (w/v) BSA for 45 min. Appropriate ligand was added in the range of 10^{-6} M to 10^{-12} M and incubated for 30 min. Reaction was terminated by aspiration of stimulation buffer. Cells were then washed once in PBS, and ice-cold 100 % ethanol was added and allowed to dry for ∼1 h at 37 °C. Lysis buffer was then added and incubated for 10 min. Cell lysate was transferred to a 96-well (half-area) plate and addition of acceptor beads (1.0 % AlphaScreen™ cAMP acceptor beads diluted in lysis buffer) and donor beads (0.3 % AlphaScreen™ cAMP donor beads, 0.025 % AlphaScreen™ cAMP biotinylated cAMP [133 U/µl] diluted in lysis buffer, and preincubated for a minimum of 30 min) in reduced light. Plates were incubated in the dark, at room temperature for ∼16 h. Fluorescence signal was read on a Mithras LB 940 (excitation 680 nm, emission 520–620 nm).

2.2.22 Inositol phosphates (InsP-InsP$_3$) accumulation assay

Inositol phosphates accumulation was assessed post agonist stimulation as previously described (Hawtin *et al.*, 2001b). 48 h post-transfection cells were radiolabelled with 1 µCi/ml myo-[2-^{3}H] inositol, prepared in inositol-free DMEM. After 24 h, cells were washed twice with 500 µl PBS and 1 ml inositol-free DMEM with 10 mM LiCl was added to each well, and incubated for 30 min. Appropriate ligand was then added to wells, and basal signalling was determined in the absence of ligand. Ligand stimulation was 30 min, unless stated otherwise. Post-stimulation, media was rapidly aspirated and 500 µl perchloric

acid solution (5 % [v/v] $HClO_4$, 1 mM EDTA and 1 mg/ml phytic acid hydrolysate) was applied to each well and left for 15 min at RT. Well contents were then transferred to a microfuge tube and neutralised with the addition of KOH buffer (1.2 M KOH, 10 mM EDTA, 50 mM HEPES), pH was monitored with universal indicator. Samples were frozen for at least 2 h (allowing for precipitation of $KClO_4$). Samples were defrosted and sedimented via centrifugation at 9,500 g for 10 min and loaded onto columns containing 10 ml dH_2O and 1 ml AG1-X8 resin. Columns were washed with 10 ml 60 mM ammonium formate and 0.1 M formic acid to elute free inositol and glycerolphosphoinositol. $InsP_3$ were eluted and collected in clean vials, using 10 ml 850 mM ammonium formate and 0.1 M formic acid. UltimaFlo AF scintillation cocktail was added and solutions mixed by vortex. Samples were counted using 3 min counts, performed in triplicate on the Tri-Carb® 2810TR liquid scintillation analyser.

2.2.23 UV-visible absorption spectroscopy of rhodopsin, and photobleaching

UV-visible (UV-vis) absorption spectroscopy was performed using a Perkin-Elmer γ35 UV-vis spectrophotometer equipped with water-jacketed cell holder. All scans were carried out at 20 °C, unless otherwise stated and temperatures in the quartz cuvettes were confirmed using a thermocouple probe. Temperature was regulated with a water bath. A scan speed of 480 nm^{-1} min^{-1} was set, as well as a data interval of 2 nm bandwidth, with a response time of 1 s. All spectra obtained were subject to normalisation to correct for baseline-drift, whereby absorbance at 650 nm (A_{650}) was corrected to exactly zero.

For photobleaching, all samples were illuminated directly in the spectrophotometer quartz cuvette using a fibre-optic light guide (SCHOTT KL1500 Compact) fitted with a >495 nm long-pass filter. Full dark-state spectra were obtained before manually photobleaching the samples for 30 s intervals, up to 150 s.

The molar extinction coefficient value used for WT-bRho at 500 nm was 40,600 M^{-1} cm^{-1} (Wald and Brown, 1953). Rhodopsin yields were determined using the Beer-Lambert Law (equation 2.1); where ε is molar extinction coefficient (M^{-1} cm^{-1}); c is concentration (M); and l is the path length (cm). Molar concentration (c) was then converted to mass

using (equation 2.2) (relative formula mass of bovine rhodopsin = 39010 Da).

$$c = \frac{A_{500}}{\varepsilon \cdot l} \tag{2.1}$$

$$Mass = c \cdot M_r \tag{2.2}$$

2.2.24 Thermal stability assay for solubilised rhodopsin

Thermal stability of the solubilised rhodopsin was determined by monitoring A_{500} over time, at a given temperature. A_{500} was monitored via UV-vis absorption spectroscopy as described above. The temperature regulating water bath was set to yield an in-cuvette temperature of either 37 °C, or 55 °C. Cuvettes were pre-heated prior to addition of rho-polymer sample, and then allowed to equilibrate in the spectrophotometer for 90 s, before absorbance between 650 nm and 250 nm was recorded over time. For experiments at 37 °C, spectra were recorded every 30 min for a period of 960 min. Data were normalised to allow for plotting of relative A_{500} (%). A_{500} at 0-min was corrected to 100 %, and 0 % was set to the A_{500} value of the buffer blank (*circa* exactly 0).

2.2.25 Thermal melt experiments for solubilised rhodopsin

Solubilised rhodopsin samples were incubated at a set temperature for 30 min and then analysed by UV-vis absorption spectroscopy at 20 °C, as described above.

2.2.26 Addition of transducin $G_{(t)}$-peptide or mini-G_o protein to solubilised rhodopsin

Binding assays for both $G_{(t)}$-peptide (VLEDLKSCGLF) and mini-G_o were performed in buffer containing 20 mM HEPES, 10 mM $MgCl_2$, 1 mM EGTA, pH 7.5. Solubilised rhodopsin was incubated with mini-G_o (final molar ratios of 1:1.2, 1:5 and 1:50) and

apyrase (25 mU/ml) for 30 min (Tsai *et al.*, 2018). For the $G_{(t)}$-peptide, rhodopsin samples were incubated with 500 μM $G_{(t)}$-peptide for 30 min (Kisselev *et al.*, 1999). The complexed solutions were then analysed by UV-vis absorption spectroscopy and photobleaching experiments, as described above.

2.2.27 Analytical ultracentrifugation (AUC)

Sedimentation velocity experiments were performed by Pooja Sridhar at the Birmingham Biophysical Characterisation Facility, University of Birmingham, UK. Experiments were performed in a Beckman Coulter Proteome Lab XL-I Analytical Ultracentrifuge with a Ti50 rotor at 20 °C, 40,000 rpm (129,000 g). Absorbance at 280 nm was monitored. Data were analysed using SEDFIT (Schuck *et al.*, 2014) applying the continuous c(s) distribution model. Buffer density and viscosity were calculated with SEDNTERP (Laue *et al.*, 1992). Frictional ratio was permitted to float.

2.2.28 Dynamic light scattering (DLS)

Dynamic light scattering (DLS) experiments were preformed using a DynaPro® Plate Reader III and DYNAMICS software (Wyatt Technology, Haverhill, UK), using the laser wavelength of 825.4 nm with a detector angle of 150°. Each sample (40 μl) was loaded into a 384-well glass bottom SensoPlate™ (Greiner Bio-One, Germany) in triplicate. Each measurement consisted of 5 scans of 5 s. Scans were carried out initially at 25 °C. The attenuator position and laser power automatically optimised for size determination (nm). For stability experiments, discrete 5 °C temperature increases, up to 60 °C were carried out. Samples were subject to a 30 min incubation at the given temperature, before scanning.

2.2.29 Fluorescence correlation spectroscopy (FCS)

Solution-based FCS was performed essentially as described in (Briddon *et al.*, 2011). FCS measurements were carried out on Nunc Lab-Tek 8-well chambered cover-glass, using a ZEISS LSM510 Confocor3 using 633 nm excitation (0.5–1 kW/cm^2), with emission

collected through a long-pass 650 filter. The confocal volume was placed 200 μm above the surface of the coverslip. Confocal volume dimensions were calculated using 500 nM and 1 μM Cy-5 (D = 3.16x10^{-10} m^2/s) (Amersham Pharmacia Bioscience) prepared in high performance liquid chromatography grade water. FCS measurements were performed in a final 200 μl assay buffer. A_{2A}R-SMALPs were incubated with CA200645 (25 nM), in the presence or absence of stated concentrations of ZM241385. Equilibrium was established at 30 min and read times of 4 x 10 s were employed to record time-dependent fluctuations in fluorescent intensity.

Autocorrelation analysis was performed and fitted using Zeiss AIM 4.2 software (equation 2.3). Data were fitted to an appropriate 1-component or 2-component 3-D diffusion model, incorporating a triplet state component. Fit quality was assessed on residuals. The concentrations of free and bound components were then calculated directly from the autocorrelation amplitude. Specific binding was determined using equation 2.4. Total binding was defined as N(τ_{D2}) (nM) as calculated via autocorrelative analysis for A_{2A}R-SMALPs in the absence of saturating competing ligand. Nonspecific binding was defined as N(τ_{D2}) (nM) via autocorrelative analysis for in the presence of saturating competing ligand.

The Stokes-Einstein formula (equation 2.5) was utilised to probe the relationship between the hydrodynamic radii of the nanoparticle and its diffusion time. Where; D = Diffusion coefficient (m^2/s); KB is the Boltzmann constant (1.3806488e^{-23} J K^{-1}); T = Temperature (K); n = dynamic viscosity (Pa*s); r = radius of spherical particle (m).

$$G(\tau) = 1 + \frac{1}{N} \cdot \sigma_{i=0}^{N} \cdot f_i \cdot \left(1 + \frac{\tau}{\tau_{Di}}\right)^{-1} \cdot \left(1 + \frac{\tau}{S^2 \cdot \tau_{Di}}\right)^{-\frac{1}{2}} \tag{2.3}$$

$$Specific\ binding = Total\ binding - Nonspecific\ binding \tag{2.4}$$

n.b.: Nonspecific binding is defined as N(τ_{D2}) (nM) calculated via autocorrelative analysis in the presence of saturating competing ligand.

$$\frac{k_b\ T}{6\ \pi\ r\ \eta} \tag{2.5}$$

2.2.30 Data analysis

Unless stated otherwise, data analysis was performed using GraphPad Prism 8 for macOS (GraphPad Software LLC, San Diego, CA).

For ELISA, cAMP and InsP-$InsP_3$ assays mock-transfected cells (empty pcDNA3.1(+)) were used to determine background signal, and data were normalised to obtain a 0 % value. For 100 % values, ELISA data were normalised to maximum expression of stated receptor. cAMP data were normalised to maximal forskolin response (100 μM). InsP-$InsP_3$ data were normalised to maximal signalling response of the stated ligand. For cAMP and InsP-$InsP_3$ assay, the non-linear regression one-site competition equation (equation 2.6) was used to fit theoretical curves to the experimental data and derive E_{max} and EC_{50} values.

For radioligand binding experiments, specific binding was determined with equation 2.7, where nonspecific binding is defined as radioactive counts detected in the presence of saturating concentration of stated ligand. Total binding was normalised to 100 %, and nonspecific binding was normalised to 0 %. The non-linear regression one-site competition equation (equation 2.8) was used to fit theoretical curves to the experimental data and derive an IC_{50} value. K_i values were subsequently calculated using the Cheng and Prusoff equation to correct for radioligand occupancy (equation 2.9) (Cheng and Prusoff, 1973). All data presented are the mean ± s.e.m of a minimum of three individual experiments performed in triplicate, unless otherwise stated.

$$Y = \frac{Bottom + (Top - Bottom)}{(1 + 10^{(X - LogEC_{50})})} \tag{2.6}$$

n.b.: Bottom and top refer to the bottom and top of the dose response curve respectively.

$$Specific\ binding = Total\ binding - Nonspecific\ binding \tag{2.7}$$

n.b.: Nonspecific binding is defined as radioactive counts detected in the presence of saturating

concentration of stated ligand.

$$Y = \frac{Bottom + (Top - Bottom)}{(1 + 10^{(X - LogIC_{50})})} \tag{2.8}$$

n.b.: Bottom and top refer to the bottom and top of the dose response curve respectively.

$$K_i = \frac{IC_{50}}{(1 + (\frac{[L]}{K_d}))} \tag{2.9}$$

Chapter 3: The use of fluorescence correlation spectroscopy (FCS) to study binding at GPCR-SMALPs

---

The work presented within this chapter resulted in a first author publication (appendix A) and was awarded a 'Flash Poster Prize' at The British Pharmacological Society's flagship annual meeting; Pharmacology 2018, London, UK (appendix B):

Grime, R. L *et al.* (2020) Single molecule binding of a ligand to a G-protein-coupled receptor in real time using fluorescence correlation spectroscopy, rendered possible by nano-encapsulation in styrene maleic acid lipid particles. *Nanoscale*, **12**, 11518-11525, DOI: https://doi.org/10.1039/D0NR01060J

3.1 Introduction

Detergent-free membrane protein solubilisation and purification is becoming increasingly well-established (Lee and Pollock, 2016). GPCR-SMALPs have potential downstream utility to support; biophysical and structural studies (Parmar *et al.*, 2017); to be used as a platform for discovery of GPCR-targeted therapeutic antibodies using phage display libraries; and for high-throughput screening in drug discovery following immobilisation on surface plasmon resonance (SPR) chips (Wheatley *et al.*, 2016). A pre-requisite to all of these applications is establishing that ligand binding capability of the encapsulated GPCR is preserved. Traditionally, radioligand binding experiments are the method of choice for probing GPCR binding kinetics (Flanagan, 2016). In recent years however, the number of commercially-available radioligands has depleted. Coinciding with this is an increase in the design of fluorescently-labelled ligands which can be used to quantify GPCR binding (Vernall *et al.*, 2014; Stoddart *et al.*, 2015a, 2016). The advances in

fluorescent technologies and increase in fluorescent ligand technology has enabled fluorescence correlation spectroscopy (FCS) to be applied to GPCR research. FCS is a powerful confocal-based approach that is based on monitoring temporal and spatial changes in fluorescence intensity as fluorescent molecules move through a defined, precisely positioned detection volume (∼0.25 fl). First conceptualised in the 1970s (Magde *et al.*, 1974), computing and optical advances led to its practical applications being realised in the late-90s and early-00s (Elson, 2013). Further advances, such as the explosion in development of fluorescent probes, mean FCS is now routinely used as a complementary method for investigating receptor dynamics, receptor-ligand interactions and oligomeric states (Ciruela *et al.*, 2014; Vernall *et al.*, 2014; Wu *et al.*, 2017).

FCS utilises basic confocal optics, a high numerical aperture objective and a confocal pinhole to generate a small, defined illumination volume (∼1 x 0.3 μm). When fluorescent species move through this detection volume, fluctuations in fluorescent intensity are detected and temporally monitored. Autocorrelation analysis [G(τ)] probes the time dependency of these fluctuations to gleam quantitative information such as dwell time (τ_D) of the fluorescent species and average number of particles within the detection volume during the measurement (N). This enables calculation of concentration of fluorescent species and diffusion coefficient (D).

FCS is able to detect a range of diffusion coefficients (0.02–200 $\mu m^2/s$), meaning fluorescent molecules with a large range of sizes, from small molecules to large proteins, can be examined. FCS is able to exploit the fact that free ligand will move rapidly through the detection volume (τ_{D1} ∼40–60 μs) and ligand-receptor complexes, being much larger, diffuse slower through the detection volume (τ_{D2} ∼300–700 μs). This gives FCS sensitivity that allows very low concentrations of receptor to be studied, sensitive enough to detect endogenous, low-level expression. Indeed, FCS has been widely used to probe interactions in live cells (Meissner and Haberlein, 2003; Briddon and Hill, 2007; Cordeaux *et al.*, 2007; Middleton *et al.*, 2007; Kilpatrick *et al.*, 2017). Working best at lower concentrations is particularly useful for GPCR investigation, where obtaining sufficient quantity of purified

protein for biophysical analysis remains a technical hurdle (Rawlings, 2018).

This chapter aimed to explore the first application of FCS to quantify ligand binding to SMALP solubilised adenosine 2A receptor ($A_{2A}R$). The $A_{2A}R$ is one of four receptor subtypes belonging to family A GPCRs (A_1, A_{2A}, A_{2B}, and A_3, collectively ARs). All are activated by endogenous ligand, adenosine, and have roles in angiogenesis, sleep regulation and immune system regulation (Sheth *et al.*, 2014). ARs are expressed in the central nervous system, as well as peripherally in cardiovascular, respiratory and renal tissue. Ligand affinity and G-protein selectivity is what largely separates this family of receptors, with $A_{2A}R$ being $G\alpha_s$-coupled. There are 57 solved $A_{2A}R$ structures (correct as of February 2021), and it is one of the most characterised, and inherently more stable GPCRs. Because of this, a number of sub-type selective and non-selective ligands have been developed, including fluorescent probes. Furthermore, the $A_{2A}R$ was the first documented GPCR to be successfully extracted using SMA, without any detriment to ligand binding, as determined by radioligand assay. It is for these reasons that the $A_{2A}R$ was chosen as an archetypical GPCR, to explore if quantification of binding was possible with $A_{2A}R$-SMALPs using FCS.

The successful application of FCS would validate a novel means by which SMALP-solubilised GPCRs can be investigated. Furthermore, the clarity of signal achieved using purified GPCR-SMALPs in solution, as opposed to live-cells, can provide a useful and rapid method for characterising novel fluorescent ligands, especially with the ability to perform high-throughput solution-based FCS (Koltermann *et al.*, 1998; Wachsmuth *et al.*, 2015; Fu *et al.*, 2020). Furthermore, solution-based FCS studies may be useful in characterising novel antibodies generated against GPCR-targets.

3.2 Results

3.2.1 Generation of A_{2A}R-SMALPs

Human A_{2A}R was expressed in *P. pastoris*, the construct used is described in (Fraser, 2006; Jamshad *et al.*, 2015a) (sequence in appendix E; receptor 'snake plot' in appendix F). Membrane preparations were generated as described in section 2.2.11. A_{2A}R-SMALPs were generated using SMA (2.5 % w/v) to extract receptors, followed by Ni^{2+}-NTA purification as described in section 2.2.15. Prior to solubilisation, ZM241385 binding affinity of membrane-bound receptors was assessed with radioligand binding assay using [^{3}H]ZM241385 as tracer, and confirmed $pK_i = 8.8 \pm 0.2$ ($n = 4$) (figure 3.1a). Post-purification, the ability to bind ZM241385 was confirmed again, however full competition binding curves were not generated due to limited sample volume (figure 3.1b). Previous work had already established no loss in affinity post-SMALP solubilisation and immobilised metal affinity chromatography (IMAC) purification (Jamshad *et al.*, 2015a). SDS-PAGE revealed the presence of a discrete protein band at a molecular mass consistent with the predicted size of A_{2A}R, 45 kDa (figure 3.2).

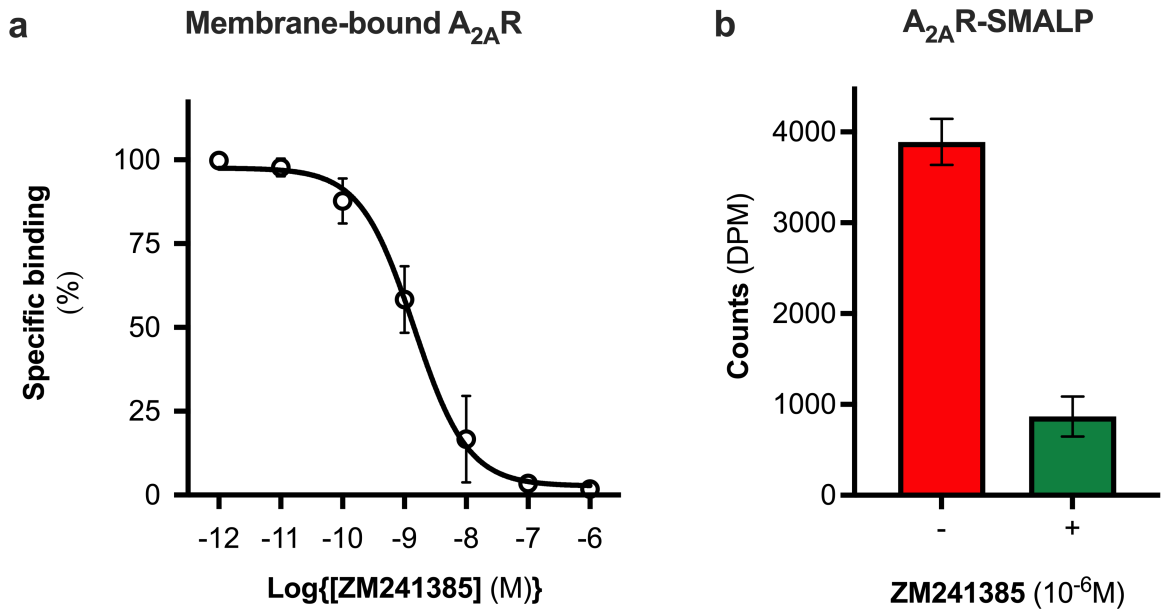

Figure 3.1: **Binding of ZM241385 to A_{2A}R using [^{3}H]ZM241385 as tracer. (a)** Competition binding curve for membrane-bound A_{2A}R. **(b)** A_{2A}R-SMALPs were incubated with radioactive tracer, in the absence (-) or presence (+) of unlabelled ZM241385 (10^{-6} M). Data represent mean ± s.e.m for four independent experiments.

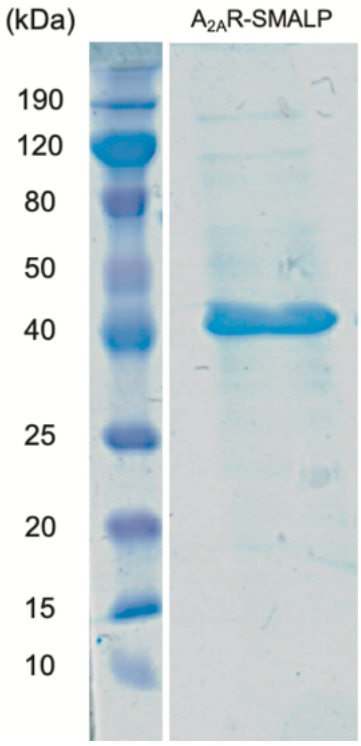

Figure 3.2: **Purification of $A_{2A}R$ by immobilised metal affinity chromatography, following SMALP solubilisation.** The eluted fraction was concentrated by centrifugation and resolved on 12 % SDS-PAGE.

3.2.2 FCS experiments

The fluorescent ligand chosen in this study was CA200645, which comprises the AR antagonist xanthine amine congener (XAC) linked to a red BODIPY 630/650 fluorophore via a β-alanine linker (Stoddart *et al.*, 2012). CA200645 has been utilised previously in FCS studies exploring dimerisation and allostery of A_3R in live-cells (Stoddart *et al.*, 2012). Pharmacological characterisation has demonstrated that CA200645 binds to $A_{2A}R$ with high affinity (Vernall *et al.*, 2013).

It was initially important to determine optimal concentration of CA200645 for solution-based FCS, to ensure that specific binding to the $A_{2A}R$ was high, relative to non-specific binding. CA200645 concentration was varied between 5–300 nM, and non-specific binding was determined via the addition of a saturating concentration of unlabelled ligand, ZM241385 (1 μM). Specific binding varied between 20 ± 11 % and 70 ± 12 % (figure 3.3), with 25 nM subsequently being used in all future experiments. During these experiments,

a scanning time of 10 s was deemed to provide ample fluorescent fluctuation data for analysis and so was routinely employed.

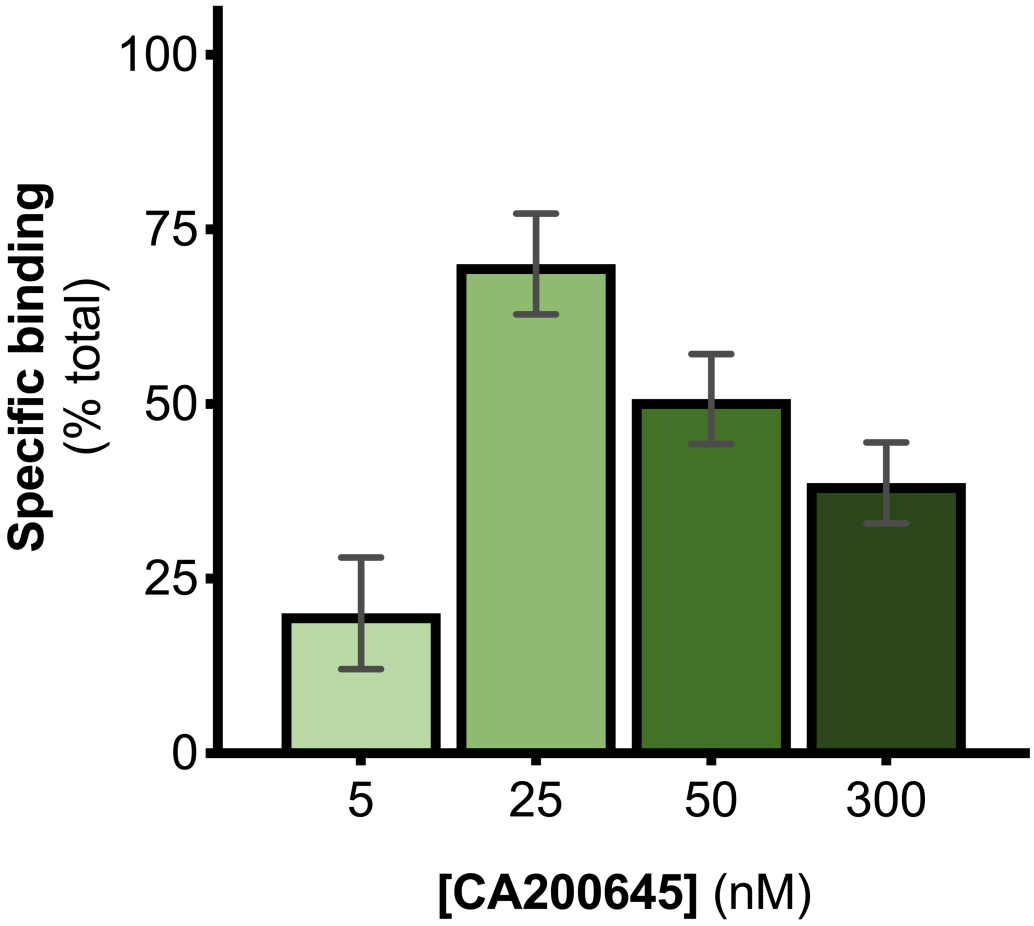

Figure 3.3: **Optimisation of tracer ligand concentration for solution-based FCS with A_{2A}R-SMALPs.** Total binding of CA200645 was determined at the stated concentrations. Non-specific binding was determined by addition of a saturating concentration of non-fluorescent, competing ligand ZM241385 (1 μM). Data are mean ± s.e.m of three independent experiments.

Initial FCS experiments observed CA200645 (25 nM) alone in assay buffer, in order to determine characteristics of free ligand. Fluctuations in fluorescent intensity for free ligand are shown in figure 3.4a. Autocorrelation analysis revealed a monophasic autocorrelation curve, with an average dwell time (τ_D) of the fluorescent moiety within the detection volume of 68 ± 2 μs, representing a diffusion coefficient (D) of 287 ± 15 μm^2 s^{-1} (figure 3.4b). Residual plot confirmed there was no systematic deviation to the fitted curve (figure 3.4c). FCS experiments were then repeated, with the additional presence of A_{2A}R-SMALP, and fluctuations in fluorescent intensity are shown in figure 3.4d. Autocorrelation analysis revealed an altered autocorrelation curve, showing a biphasic curve, exhibiting fast- and slow- diffusing components (τ_{D1} and τ_{D2}, respectively) (figure 3.4e). The fast-diffusing component demonstrated a dwell time (τ_{D1}) consistent with free ligand. The slow-diffusing component demonstrated a dwell time (τ_{D2}) of 625 ± 23 μs, resulting in D = 30 ± 4 μm^2 s^{-1} (figure 3.4e). Residual plot confirmed no systematic deviation to the fit (figure 3.4f). A_{2A}R-SMALPs were also observed in assay buffer (alone, with no ligand) to check for autofluorescence, of which no significant autofluorescence was observed (figure 3.4g and 3.4h).

The diffusion coefficient of the CA200645:A_{2A}R-SMALP complex (D = 30 ± 4 μm^2 s^{-1}) was used to estimate the hydrodynamic radius of the A_{2A}R-SMALP, calculated with the Stokes-Einstein equation (equation 2.5), with the caveat that SMALPs are disc-shaped, as opposed to spherical. Calculated values obtained ranged between ∼7–8 nm, consistent with the established diameter of a SMALP (Lee *et al.*, 2016).

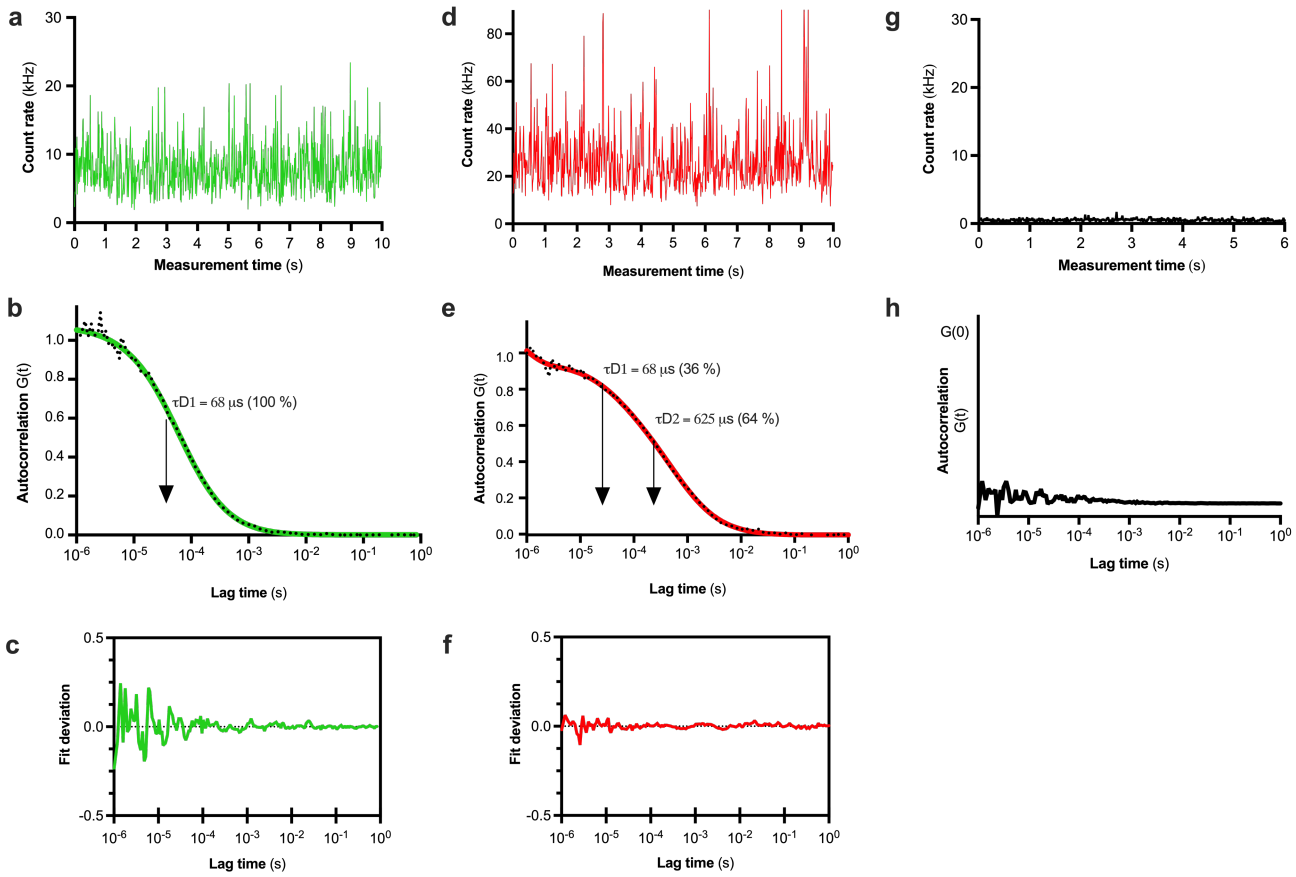

Figure 3.4: **FCS analysis of CA200645 binding to purified A_{2A}R-SMALP.** **(a)** Fluctuations in fluorescent intensity for CA200645 alone in assay buffer. **(b)** Autocorrelation curve of free ligand fitted to a one-component three-dimensional diffusion model. **(c)** Residual plot for autocorrelation fit model of CA200645 in assay buffer. **(d)** Fluctuations in fluorescent intensity for CA200645 + A_{2A}R-SMALP. **(e)** Autocorrelation curve whereby a two-component three-dimensional diffusion model was used to fit the data. **(f)** Residual plot for autocorrelation fit model of CA200645 + A_{2A}R-SMALP. **(g)** Fluorescent fluctuations for A_{2A}R-SMALPs alone in assay buffer. **(h)** Autocorrelation curve for A_{2A}R-SMALPs in assay buffer.

3.2.3 Characterisation of the slow-diffusing component (τ_{D2})

The logical explanation for the emergence of the slower diffusing component (τ_{D2}) upon addition of A_{2A}R-SMALP to the system is the binding of CA200645 to A_{2A}R, and that both free and bound ligand were being detected by FCS simultaneously (figure 3.4e). In order to establish whether the binding observed is specific to A_{2A}R, or simply non-specific interaction, the pharmacological properties of A_{2A}R were exploited. Competition binding experiments were performed with CA200645 as fluorescent tracer, and a saturating concentration of ZM241385 (1μM) (unlabelled competitive ligand). In the presence of saturating ZM241385 the τ_{D2} component particle number (N) decreased by an average of 62 % (figure 3.5). In contrast, control experiments demonstrated there was no effect of ZM241385 (1 μM) when using a different SMALP-solubilised membrane protein, ZipA (derived from *E. coli*). Furthermore, ZipA-SMALP showed lower τ_{D2} particle number than A_{2A}R-SMALP, this was expected because ZipA does not bind CA200645 (figure 3.5).

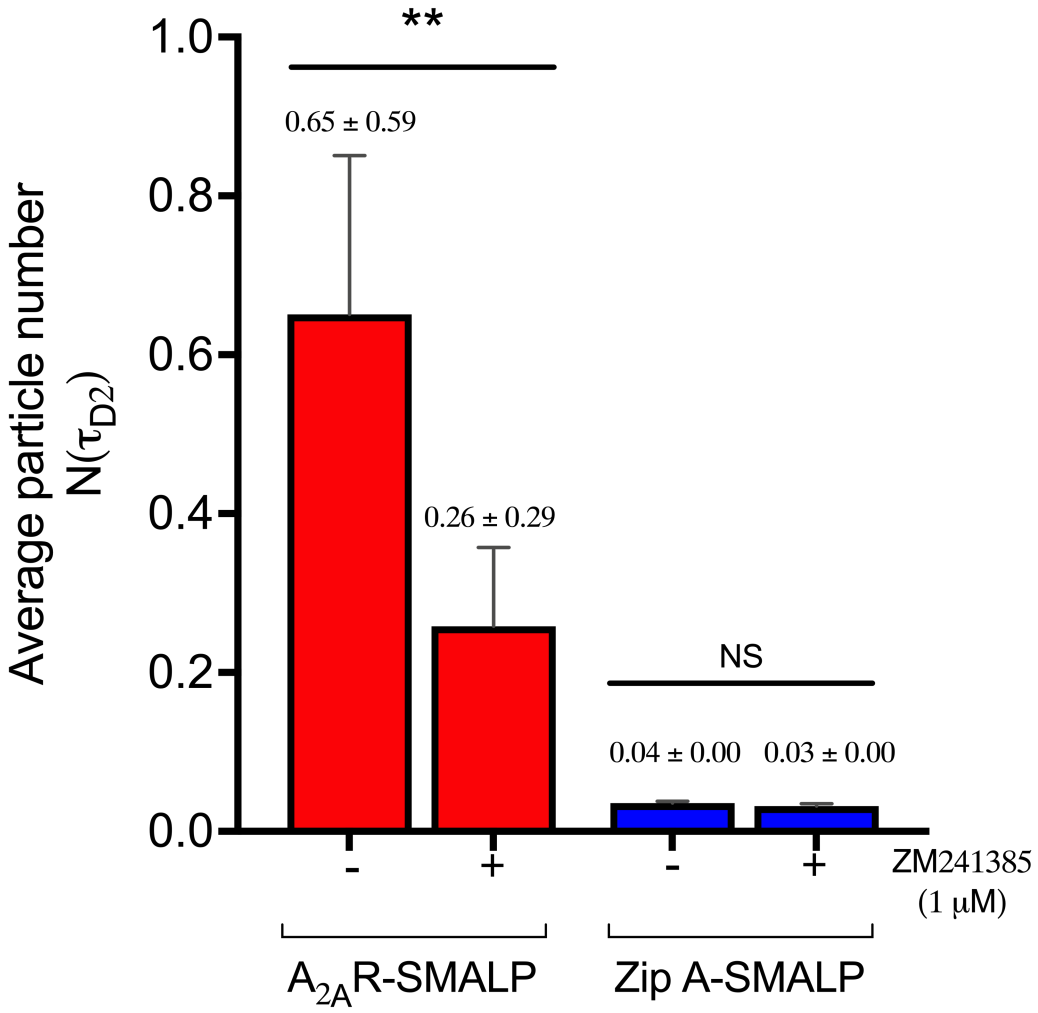

Figure 3.5: **Specific binding of CA200645 to A_{2A}R-SMALP.** Particle number (average number of fluorescent particles in the detection volume at point of measurement) of the slower diffusing component (τ_{D2}) from the autocorrelation curves is shown for CA200645 (25 nM), in the absence (-) or presence (+) of ZM241385 (1 μM). Significance determined by paired t-test, ** p <0.01, NS = not significant. Data are mean ± s.e.m of three independent experiments.

Following demonstration that FCS detectable binding at A_{2A}R-SMALP is displaceable with unlabelled competitive antagonist, a competition binding curve was constructed using ZM241385 concentrations from 10^{-6}–10^{-12} M (figure 3.6). From these data affinity (pK_i) of ZM241385 for the A_{2A}R-SMALP was calculated at 8.2 ± 0.5 (n=3).

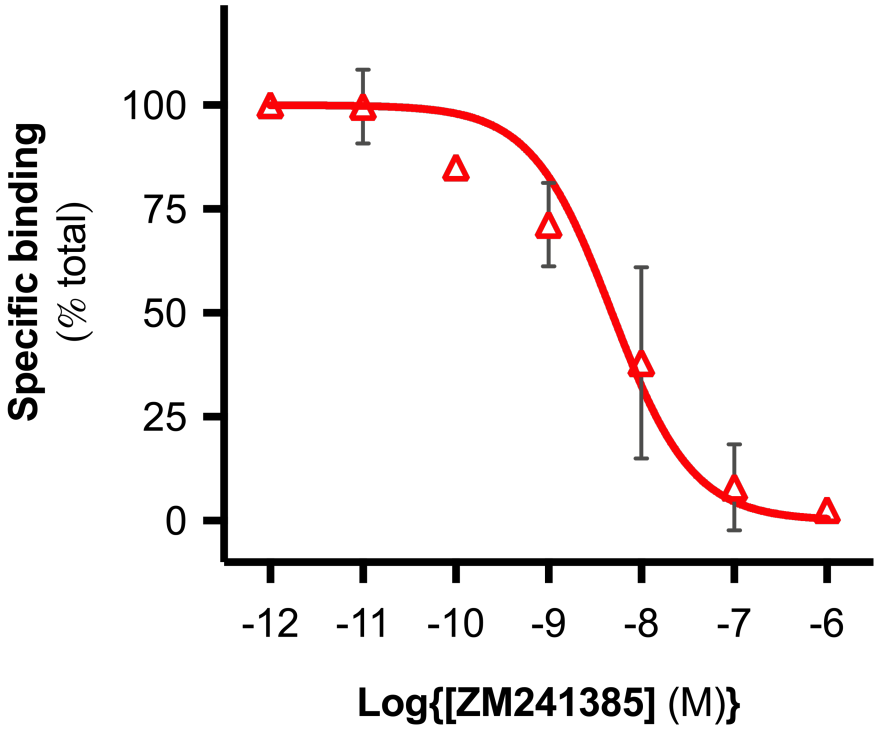

Figure 3.6: **Competition binding curve derived from FCS with A_{2A}R-SMALP utilising CA200645 as fluorescent tracer.** ZM241385 was used at concentrations indicated. Data are mean ± s.e.m of three independent experiments.

3.3 Discussion

3.3.1 Overview

Established here was the first reported use of solution-based FCS to characterise binding to a purified GPCR, solubilised in the absence of detergent, using styrene malic acid derived nanodiscs. FCS binding studies require a soluble, fluorescently labelled ligand, with high photostability. The CA200645 ligand consists of the non-selective adenosine receptor antagonist, XAC, linked to the red BODIPY 630/650 fluorophore via a β-alanine linker. CA200645 has been extensively pharmacologically characterised (Stoddart *et al.*, 2012; Vernall *et al.*, 2013), and used previously in FCS experiments with live cells, demonstrating an affinity to $A_{2A}R$ of 42 nM ($pK_i = 7.4 \pm 0.2$) (Corriden *et al.*, 2014). Therefore, rationalising the decision to utilise CA200645 as the choice of ligand to ascertain if GPCR-SMALPs were amenable to FCS-based investigations.

3.3.2 Preparation of $A_{2A}R$-SMALP

It was necessary to establish affinity of $A_{2A}R$ for ZM241385 prior to solubilisation and FCS studies in order to confirm receptor integrity. Competition radioligand binding studies on membrane-bound receptors derived a pK_i of 8.8 ± 0.2 for ZM241385 (figure 3.1a). This aligned with previous data that established $pK_i = 8.8$–9.1 (Ongini *et al.*, 1999; Charlton, 2015). Following SMALP-solubilisation and Ni^{2+}-NTA purification, the ability of $A_{2A}R$ to bind ZM241385, in a competitive manner, was confirmed once again via radioligand binding assay. Exact affinity was not established in order to retain sample for FCS studies. $A_{2A}R$-SMALPs retained ability to bind ZM241385 in a displaceable manner (figure 3.1b). It is established that purified $A_{2A}R$-SMALP retains WT-like affinity (Charlton, 2015; Jamshad *et al.*, 2015a), therefore, it was concluded that the generated $A_{2A}R$-SMALPs would be suitable for examining with FCS.

3.3.3 FCS to detect specific binding at $A_{2A}R$

Initial FCS experiments optimised the concentration of fluorescent ligand (found to be 25 nM) and focused on characterising the diffusion of free ligand in assay buffer (figure 3.4a–c), as well as confirming that $A_{2A}R$-SMALPs do not demonstrate autofluorescence (figure 3.4g–h). These controls were necessary to calculate free ligand diffusion time, as well as ensure optimal signal to background levels. It was then investigated whether FCS could be used to observe and quantify binding to $A_{2A}R$-SMALP. Autocorrelation analysis of CA200645 + $A_{2A}R$-SMALP was best fit using a two-component three-dimensional diffusion model, which indicated the presence of fast and slow diffusing components (figure 3.4d–f). Logical deduction reasoned that FCS was detecting both free and bound ligand simultaneously. Indeed, the simultaneous determination of free ligand concentration precisely where the binding event is occurring is a particular advantage of FCS for characterising ligand:receptor complexes. It was necessary to confirm whether the binding being observed was specific binding to $A_{2A}R$. Non-specific interaction may have arisen from partitioning of ligand into the lipid bilayer of the SMALP, or via interaction of the ligand to the surrounding polymer. To explore this, a competition binding experiment was performed with CA200645 as fluorescent tracer and ZM241385 as competing unlabelled ligand. Saturating ZM241385 would occupy all specific binding sites, displacing CA200645. This was observed for $A_{2A}R$, where a 62 % reduction in particle number was observed in the slow-diffusing component upon saturation with ZM241385 (figure 3.5). The same experiment was performed with a non-receptor, SMALP-solubilised control. Purified ZipA-SMALP (kindly gifted by Dr. Zoe Stroud, University of Birmingham, UK) demonstrated overall very low binding of CA200645 and subsequently no competition with addition of ZM241385 was detected. This is indicative that the binding observed at $A_{2A}R$-SMALP is specific to the $A_{2A}R$, and not the SMALP, as it was expected that CA200645 would not bind to ZipA. Finally, a competition binding curve derived a pK_i of 8.2 ± 0.5, which is consistent with ZM241385 affinity measured at original membranes, 8.8 $\pm$ 0.2 (figure 3.1a). These data conclusively established that FCS can be used to quantify

specific binding to a SMALP-encapsulated GPCR.

3.3.4 Summary and future work

There are many applications of FCS with GPCR-SMALPs that could be envisaged. Allosteric modulation, whereby a modulator binds to a site distinct from the endogenous ligand binding site (orthosteric site), is of great pharmaceutical interest and can be investigated with FCS. One property of FCS is that the dwell time (τ_D) is proportional to the cube-root of its molecular mass, so a doubling of mass increases τ_D by 1.3-fold. Two fluorescent species can only be resolved if the mass difference is great enough to yield a 1.6-fold change in τ_D (Ruttinger *et al.*, 2010). The size-differential that FCS permits between fluorescent species means allosteric modulators can be investigated. A wide range of allosteric modulators could be examined, from small molecules to therapeutic antibodies.

FCS can be applied to other nano-encapsulation strategies. Apolipoprotein-stabilised nanodiscs have been used to quantify binding in membrane proteins previously (Ly *et al.*, 2014). It stands to reason that other SMA-like polymers would also be compatible with FCS. The applications of SMALPs to study membrane proteins has been expanding rapidly. Recently, SMALPs have been used to obtain high-resolution structures from both crystallographic, and cryo-EM studies. Notably, the proton pump bacteriorhodopsin was transferred from SMALPs into lipidic-cubic phase in meso-crystallisation (Broecker *et al.*, 2017), and the cryo-EM structure of alternative complex III in a super-complex with cytochrome oxidase encapsulated in a SMALP has been resolved (Sun *et al.*, 2018). A combination of fluorescence imaging and SMALP-solubilisation is becoming increasingly versatile. Site-specific substitution by unnatural amino acids has been utilised to fluorescently label SMA-solubilised proteins, and FCS has directly been applied to confirm the presence of dimers in multidrug transporter ABCG2 (Horsey *et al.*, 2020; Swiecicki *et al.*, 2020). Demonstration of the expanding down-stream compatibility of SMALPs has been a driver in the development of novel amphipathic co-polymers that retain the ability of SMA to directly excise proteins from a membrane bilayer, but exhibit different physicochemical properties to SMA. Second generation polymers generate lipid nanoparticles in

the absence of detergents, preserving native lipids in close association with membrane proteins. This is particularly important for GPCRs which have been shown to be regulated by the juxtaposition of specific membrane lipids. Cholesterols have been demonstrated to modulate receptor conformation (Muth *et al.*, 2011) and function (Gimpl *et al.*, 1997; Pang *et al.*, 1999). Phosphatidylethanolamine and phosphatidylglycerol have both shown to favour inactive and active states of β2-adrenoreceptors (Dawaliby *et al.*, 2016). Furthermore, a specific cholesterol binding site which incorporates a 'cholesterol consensus motif' has been proposed for many GPCRs, following the identification of cholesterols in crystal structures (Hanson *et al.*, 2008). Moreover, the selectivity of β1-adrenoreceptors for Gα_s signalling in preference to other G-proteins is enhanced by membrane lipid PIP2, but not by structural homologues (Yen *et al.*, 2018). There are of course differences in plasma membrane composition of *P. pastoris* from that of mammalian cell membranes, notably the substitution of cholesterol by ergosterol, however the major classes of phospholipids are similar, and $A_{2A}R$ is shown to be fully pharmacologically active, both here and previously (Jamshad *et al.*, 2015a; Routledge *et al.*, 2020).

Overall this work establishes a platform for investigating ligand:GPCR-SMALP interactions, demonstrating the first published application of solution-based FCS to quantify ligand binding to a GPCR-SMALP. The versatility of FCS, combined with detergent-free nano-encapsulation strategies should provide a versatile technique capable of characterising ligands, investigating effects of allosteric modulators, such as therapeutic antibodies and nanobodies, as well as being capable of investigating oligomeric states of encapsulated membrane proteins.

Chapter 4: Conformational dynamics exhibited by rhodopsin in lipid nano-particles

4.1 Introduction

The preparation of homogenous and functional samples for membrane protein investigation remains a technical hurdle. The use of detergents to solubilise and extract membrane proteins from the bilayer is still widely adopted. This approach, which generates proteinaceous samples surrounded by detergent-micelles, strips away native lipids, which perturbs protein conformation. For particularly dynamic membrane proteins, such as GPCRs, this is problematic due to resultant protein instability in the detergent-micelle. The biological significance of GPCRs and other membrane proteins has resulted in the development of membrane-mimetics (discussed in detail; chapter 1). One such approach stabilises a protein-lipid core with a surrounding amphipathic protein belt, forming nanodiscs known as nano-lipoprotein particles (Bayburt and Sligar, 2010; Hernandez-Rocamora *et al.*, 2014). An alternative approach, and the focus of this thesis, utilises amphipathic polymers which form a stabilising ring around the membrane protein and retains native lipids, the best characterised being SMA (Jamshad *et al.*, 2015a). The utility of SMALPs is wide-ranging. They have supported biophysical studies (Grime *et al.*, 2020; Bassard and Laursen, 2019), structural studies (Reading, 2019; Su *et al.*, 2019; Yokogawa *et al.*, 2019) and are being utilised as a platform for drug discovery (Dalela *et al.*, 2015; Deak *et al.*, 2019). Beyond SMA is an emerging toolbox of amphipathic polymers, each with their own distinct chemical structure, resulting in polymers with ranging chemical and biophysical properties (reviewed in full; (Stroud *et al.*, 2018)). These include derivatised versions of SMA, such as the addition of sulphydryl functional groups (SMA-SH), which permits application of numerous bioconjugation chemistries (Lindhoud *et al.*, 2016). Further to this, the acid-compatible poly(**s**tyrene-*co*-**m**ale**i**mide) (SMI) has been shown to form similar

nanoparticles to SMA, with comparable efficiency (Hall *et al.*, 2018). SMI and its resultant nanodiscs; **SMI**-**l**ipid **p**articles (SMILPs), are not only soluble in acidic conditions, but are more tolerant of higher concentrations of divalent cations than their counterpart, SMA. While SMI results from an alteration of the hydrophilic monomer unit, alteration of the hydrophobic monomer unit also yields polymers with similar nano-encapsulation properties. Poly(**di**-**i**so**b**utylene-*alt*-**m**aleic-**a**cid) (DIBMA) is capable of extracting membrane proteins, and the absence of a styrene ring permits UV-spectroscopic studies of the nano-encapsulated membrane proteins (Oluwole *et al.*, 2017a). Calorimetry and Raman spectroscopy experiments have demonstrated that intercalation of the diisobutylene chains into the lipid bilayer leads to less perturbation of phospholipid bilayer dynamics than compared with the phenyl rings from SMA (Oluwole *et al.*, 2017b). This intercalation of the phenyl-ring component of SMA and SMI has been shown to occur in a similar manner to cholesterol (Jamshad *et al.*, 2015b). It is hypothesised that this interaction will reduce dynamic motion of nearby lipids, and has potential to disrupt overall structure or function of the encapsulated membrane protein. Site-directed spin labelling, time-resolved optical spectroscopy and EPR spectroscopy have been used to characterise bacterial photoreceptors, and demonstrated that, in a SMALP, conformational freedom is restricted (Mosslehy *et al.*, 2019). However, beyond this, there is little characterisation of the conformational transition capabilities of nano-encapsulated membrane proteins, especially in mammalian systems. This chapter aimed to address such a question and characterised conformational dynamics of the archetypical GPCR, rhodopsin, solubilised with SMA, SMI and DIBMA.

Rhodopsin is perhaps the most widely characterised GPCR. It is the visual pigment found in rod photoreceptor cells in the retina, and controls scotopic vision (Zhou *et al.*, 2012). Rhodopsin (bovine) comprises a 39.1 kDa apoprotein (opsin) containing 348 amino acid residues in a single polypeptide chain, and a covalently bound ligand chromophore, 11-*cis*-retinal (a derivative of vitamin A) (receptor 'snake plot'; appendix F). Rhodopsin undergoes a series of post-translational modifications including palmitoylation at the C-terminus; acetylation at its N-terminal methionine; phosphorylation at three C-terminal

sites; N-linked glycosylation at its extracellular N-terminus; and ubiquitinylation at a number of cytoplasmic lysine residues (Murray *et al.*, 2009). The binding site for 11-*cis*-retinal is located within the helical bundle, where it forms a protonated Schiff base (PSB) at Lys^{296} (figure 4.1). The PSB linkage creates a positive charge within the interior TMD of the receptor, for which the negatively-charged carboxylate group of Glu^{113} ($E^{3.28}$) provides a counter-ion (Meng and Bourne, 2001). This resultant salt-bridge between TM3 and TM7 partly contributes to receptor stability. Upon activation by a photon, the retinal undergoes isomerisation from 11-*cis* to all-*trans* (Meyer *et al.*, 2000). The photon-induced *cis–trans* transition of the retinal leads to a sterically strained excited-state rhodopsin that thermally decays through a series of photo-intermediates, each with its own distinctive maximal spectrophotometric absorbance peak (γ_{max}). Inactive (dark-state) rhodopsin presents with a distinct γ_{max} 500 nm. Upon photo-bleaching rhodopsin transitions rapidly through the following conformational intermediates, each with their own distinctive γ_{max}; photorhodopsin (570 nm), bathorhodopsin (543 nm), blue-shifted intermediate (470 nm), lumirhodopsin (497 nm), metarhodopsin I (meta I/MI) (478 nm), and finally, the active-state metarhodopsin II (meta II/MII) (382 nm) (figure 4.2). MI formation is characterised by the formation of all-*trans* retinal, with the Schiff base remaining protonated. In MII, the Schiff base linkage between the all-*trans*-retinal and Lys^{296} is still intact but deprotonated, this represents active rhodopsin (Zhou *et al.*, 2012). During this thermal relaxation, conformational changes lead to the opening of the cytoplasmic side of the 7TM bundle, permitting $G_{(t)}$ coupling (figure 4.1).

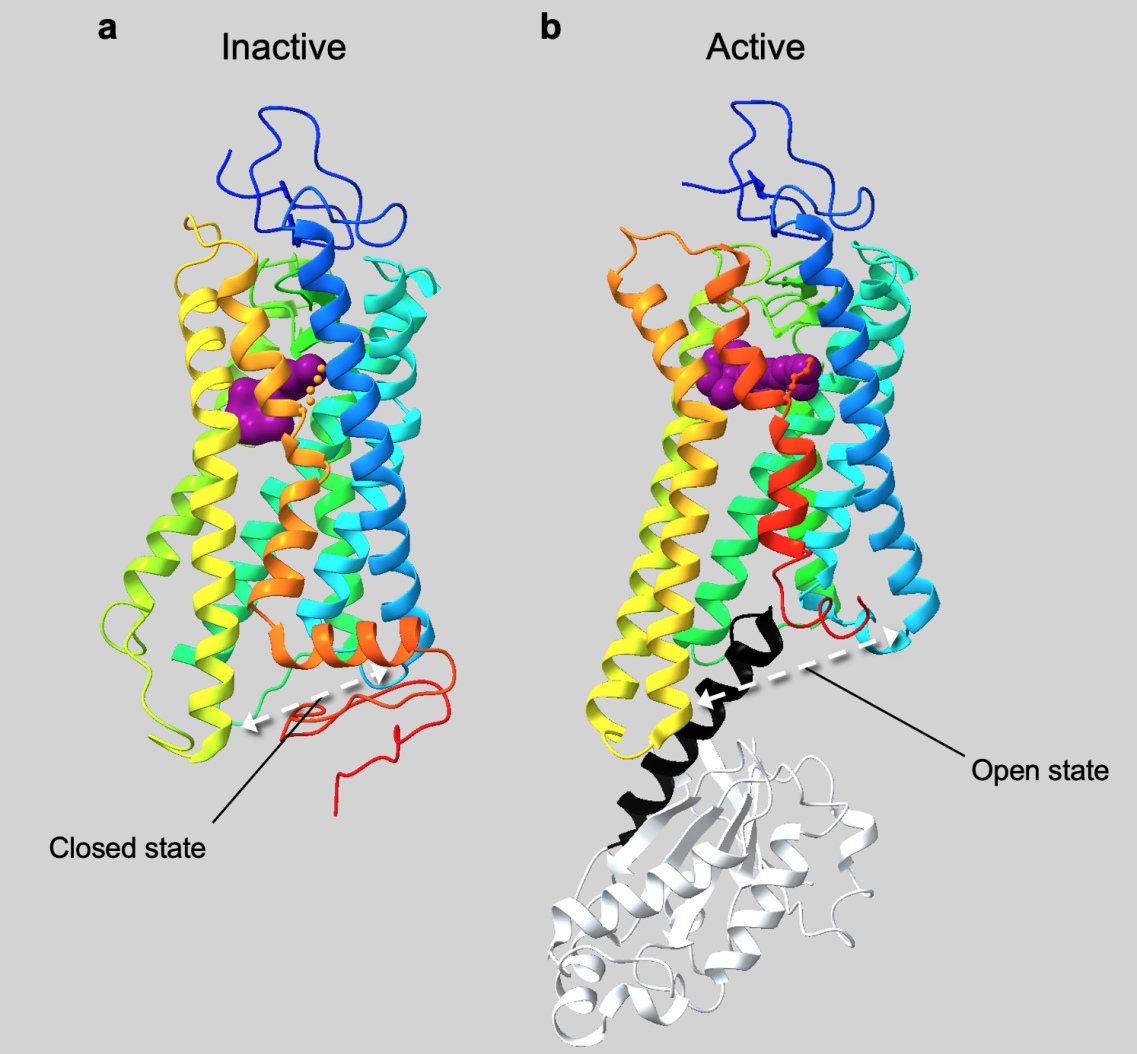

Figure 4.1: **Inactive and active structures of bovine rhodopsin.** Structures of bovine rhodopsin (rainbow) solved via X-Ray crystallography. Retinal is shown (purple) and Lys^{296} is highlighted by ball and stick model. **(a)** Inactive rhodopsin (PDB 3OAX) (Makino *et al.*, 2010) and **(b)** active rhodopsin bound to mini-G_o (white) where the $\alpha 5$ helix of mini-G_o is highlighted (black) (PDB 6FUF) (Tsai *et al.*, 2018). Upon activation, conformational changes occur whereby the cytoplasmic side of rhodopsin opens up to permit G-protein coupling (indicated by the white dashed arrows).

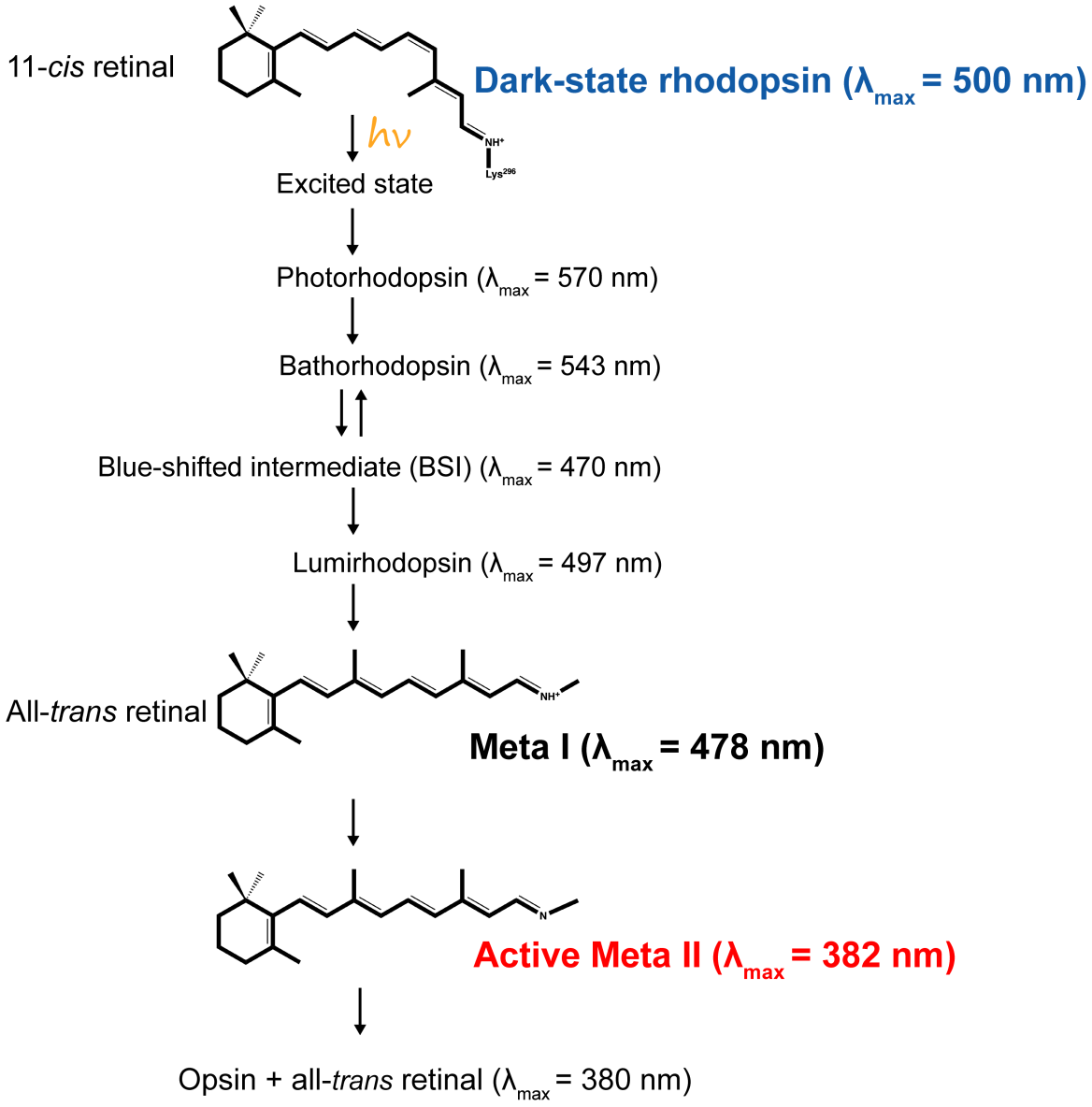

Figure 4.2: **Light-induced activation states of rhodopsin.** The chromophore (11-*cis*-retinal) undergoes *cis* to *trans* isomerisation upon photo-activation. Each rhodopsin state has its own distinctive maximal spectrophotometric absorbance (γ_{max}). Metarhodopsin II (Meta II) represents activated rhodopsin.

4.2 Results

4.2.1 Solubilisation of rhodopsin from rod outer segments (ROS)

It was initially important to establish if the polymers (SMA, SMI and DIBMA) were capable of solubilising rhodopsin to comparable levels of those achieved with detergents, such as N-dodecyl-β-D-maltoside (DDM). Spectrophotometric analysis (absorbance at 500 nm) of the solubilised fractions permitted quantification of solubilisation efficiency. It was demonstrated that SMA (2.5 %), SMI (2.5 %) and DIBMA (5 %) were able to consistently solubilise to levels >90 % that of DDM (1 %) (figure 4.3; table 4.1). DIBMA concentration was optimised systematically after initial attempts at 2.5 % yielded less consistent solubilisation efficacies than did 5 % (table 4.2).

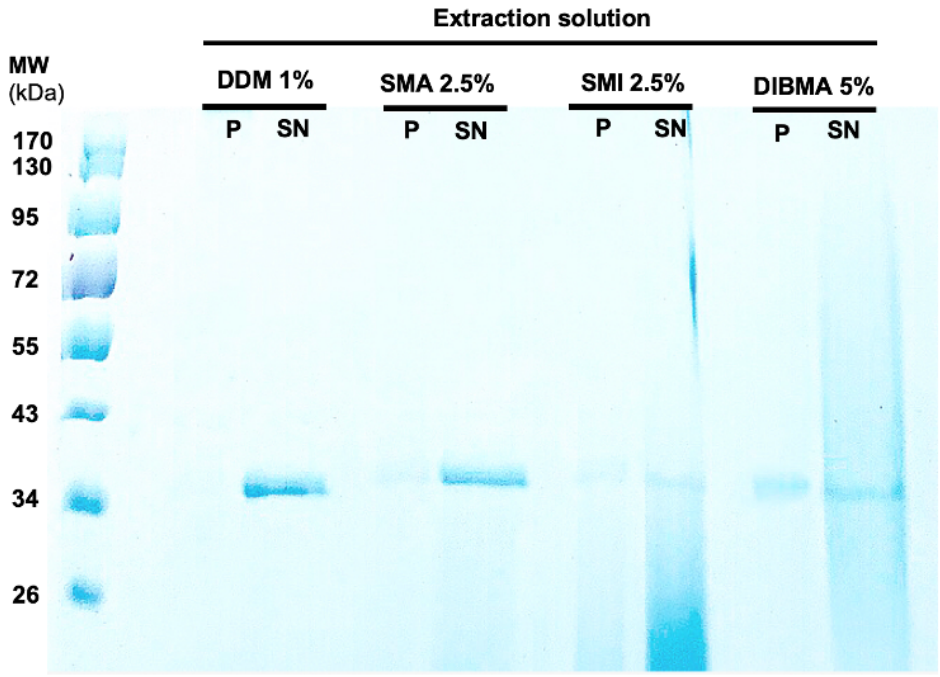

Figure 4.3: **Solubilisation of rhodopsin from rod outer segments (ROS) with conventional detergent (DDM 1 %), or polymers (SMA 2.5 %, SMI 2.5 %, or DIBMA 5 %).** SDS-PAGE (12 %) image showing the ROS extracts after solubilisation. The insoluble pellet (P) fraction, and the soluble supernatant (SN) fraction is shown. Bovine rhodopsin has a predicted molecular mass of ∼43 kDa.

Table 4.1: **Solubilisation efficiencies of rhodopsin from rod outer segments (ROS) with different solubilisation agents.** Efficiency was determined by UV-visible absorption spectroscopy. Absorbance at 500 nm was determined for each solubilised sample, and normalised relative to extraction achieved with DDM 1 %.

	Extraction efficiency (% DDM)				
Solubilisation condition	1	2	3	**Mean** (%)	SD
DDM (1 %)	100	100	100	**100**	0
SMA (2.5 %)	94	105	99	**99**	5.5
SMI (2.5 %)	95	100	96	**97**	2.6
DIBMA (5 %)	87	94	91	**91**	3.5

Table 4.2: **Optimisation of DIBMA solubilisation.** Stated concentrations of DIBMA were used to solubilise rod outer segments. Solubilised material was analysed by UV-vis spectroscopy (absorbance at 500 nm) to determine rhodopsin solubilisation efficiency against that of DDM 1 %.

	Extraction efficiency (% DDM)				
Solubilisation condition	1	2	3	**Mean** (%)	SD
DDM	100	100	100	**100**	0.0
DIBMA (1 %)	80	18	49	**49**	31.0
DIBMA (2.5 %)	104	32	86	**74**	37.5
DIBMA (5 %)	108	93	94	**98**	8.4
DIBMA (10 %)	119	104	98	**107**	10.8

4.2.2 Photoactivation of rhodopsin in SMA, SMI and DIBMA

Having determined that bovine rhodopsin could be successfully solubilised, to high efficiency with SMA, SMI and DIBMA, it was next important to characterise their conformational profiles upon light-activation. All samples demonstrated a dark-state absorbance peak at 500 nm, consistent with successful extraction of inactive rhodopsin (figure 4.4). In the DDM-extraction, rhodopsin demonstrated full conversion to MII immediately after photoactivation (30 s photobleach), as determined by characteristic loss of the peak at 500 nm and appearance of an absorbance peak at 382 nm, consistent with published data for WT rhodopsin (figure 4.4a) (Resek *et al.*, 1993). In both SMA- and SMI- solubilised rhodopsin, photoconversion did not appear to go beyond MI, even after an extended photobleaching period (150 s), as demonstrated by the absorbance peak shown at 478 nm. SMA and SMI both contain a styrene moiety, which accounted for the interference seen in the UV-region ($\sim$ <300 nm) of the UV-visible absorption spectra (figure 4.4b and 4.4c). In contrast to this, rhodopsin-DIBMALPs achieved photoconversion to MII upon photo-activation (figure 4.4d). The upward slope ($\sim$430–550 nm) on the photobleached UV-visible absorption spectra for rhodopsin-DIBMALP may indicate the presence of photo-intermediates, or represent scatter resultant from the polymer itself (figure 4.4d).

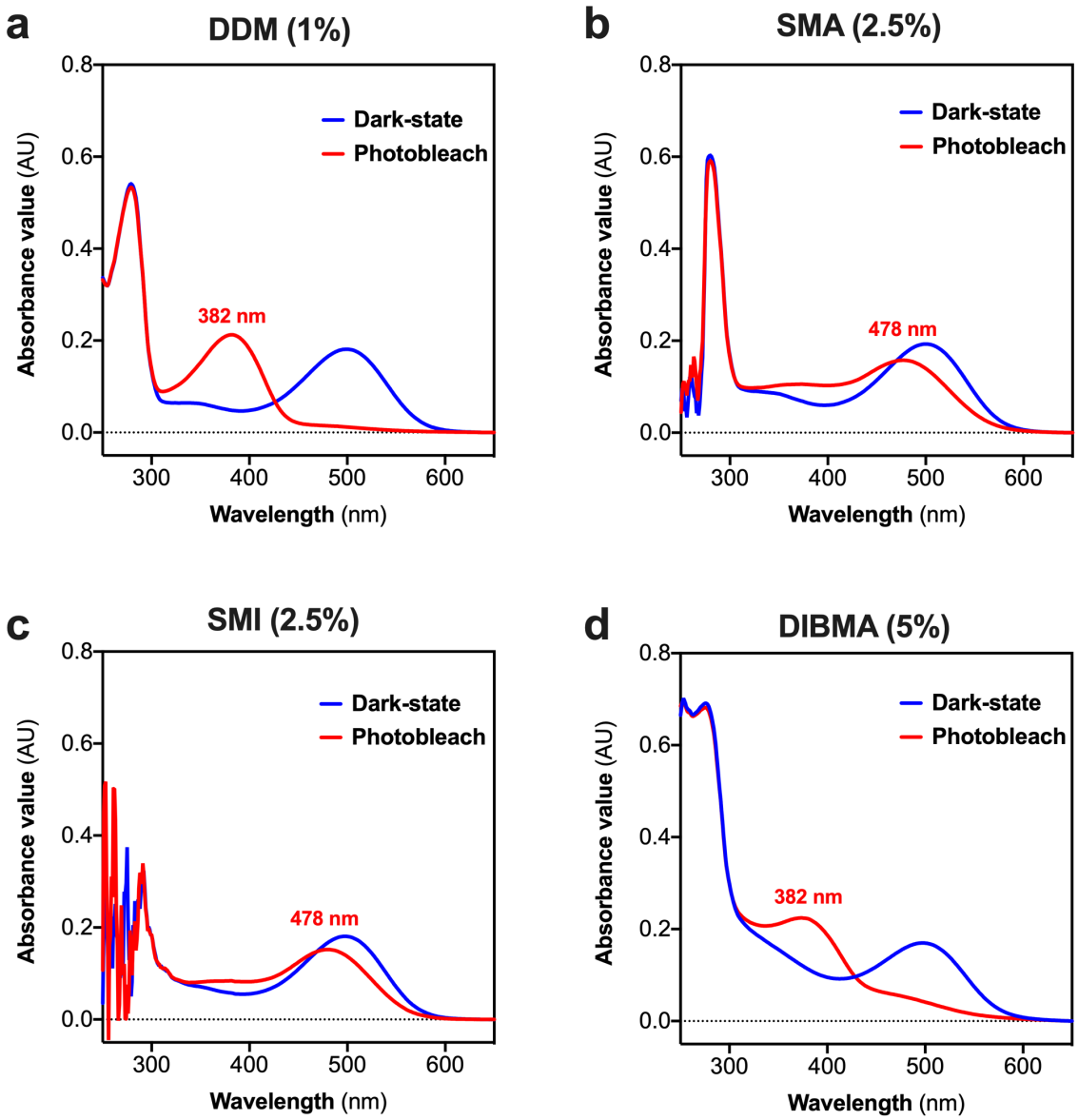

Figure 4.4: **UV-visible absorption spectroscopy of solubilised ROS samples in either (a) DDM (1 %), (b) SMA (2.5 %), (c) SMI (2.5 %) or (d) DIBMA (5 %).** Blue line indicates absorbance spectra in dark-state, and red line shows absorbance spectra after photobleaching period (150 s). Data are representative spectra obtained from at least three independent experiments.

4.2.3 The effect of $G_{(t)}$-peptide or mini-G_o protein on photoactivation of rhodopsin

Following the discovery that SMA-, and SMI-, solubilised rhodopsin are unable to transition from MI to fully active MII, approaches were taken in an attempt to stabilise the active receptor conformation, and establish whether MII could form. These approaches were also attempted on rhodopsin-DIBMALP to investigate if there was any shift in the spectrum, possibly related to the presence of photo-intermediates. Excess polymer was removed from the samples by gel-filtration, which resulted in subsequent negative absorbance seen on the UV-vis spectra ($\sim$ <350 nm) (figure 4.5). Following the removal of free-polymer, no change was seen in relative A_{500} levels, or light-induced conformational changes (figure 4.5). Rhodopsin -SMALPs, -SMILPs, and -DIBMALPs (herein collectively referred to as rhodopsin-LPs), were then incubated with either a transducin $G_{(t)}$-peptide (VLEDLKSCGLF), or an engineered mini-G_o protein (Nehme *et al.*, 2017). Both the $G_{(t)}$-peptide and mini-G_o have been shown to be fully capable of stabilising active receptor state, driving formation of MII conformation. They are capable of recapitulating the increase in agonist affinity observed upon coupling of a native heterotrimeric G-protein in GPCRs with diffusible ligands (Kisselev *et al.*, 1999; Carpenter and Tate, 2016; Nehme *et al.*, 2017; Tsai *et al.*, 2018). For the mini-G_o assay, rhodopsin-LPs were incubated with varying molar ratios of rhodopsin-LP to mini-G_o (1:1.2, 1:5 and 1:50). For the $G_{(t)}$-peptide assay, 500 μM final concentration of peptide was used. Following incubation with either the mini-G_o or $G_{(t)}$-peptide, no change in either dark-state, or light-activated conformational changes were seen (figure 4.6). Together, these data suggest that the restricted MI to MII transition observed in light-activated rhodopsin -SMALPs and -SMILPs is due to major conformational restriction placed on either lipids or protein. Restrictions may arise due to interaction from polymer itself, possibly interactions arising from the styrene-ring that both SMA and SMI share.

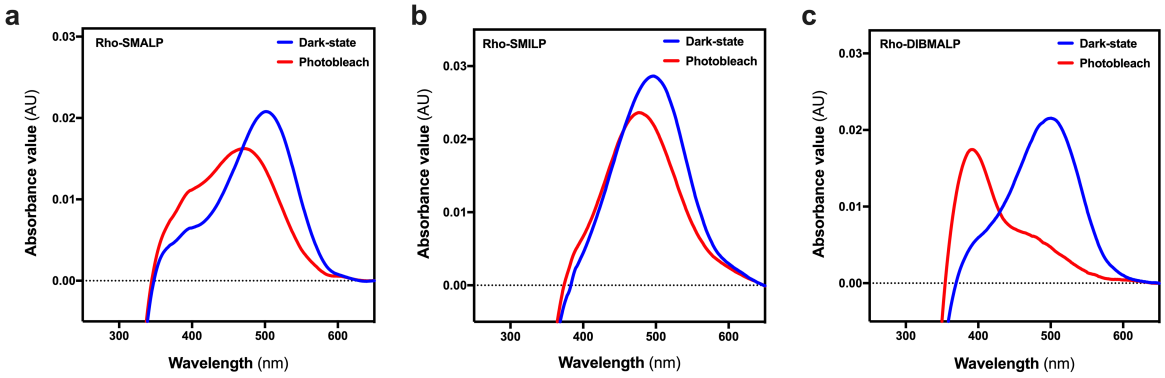

Figure 4.5: **UV-visible absorption spectroscopy of gel-filtered, solubilised ROS.** Solubilised fractions were passed through Sephadex® G-25 columns to remove excess free-polymer. **(a)** Rhodopsin-SMALPs; **(b)** Rhodopsin-SMILPs; **(c)** Rhodopsin-DIBMALPs. Dark-state spectra (blue line) and photobleached (150 s) spectra (red line) are shown. Data are representative spectra obtained from at least 3 independent experiments.

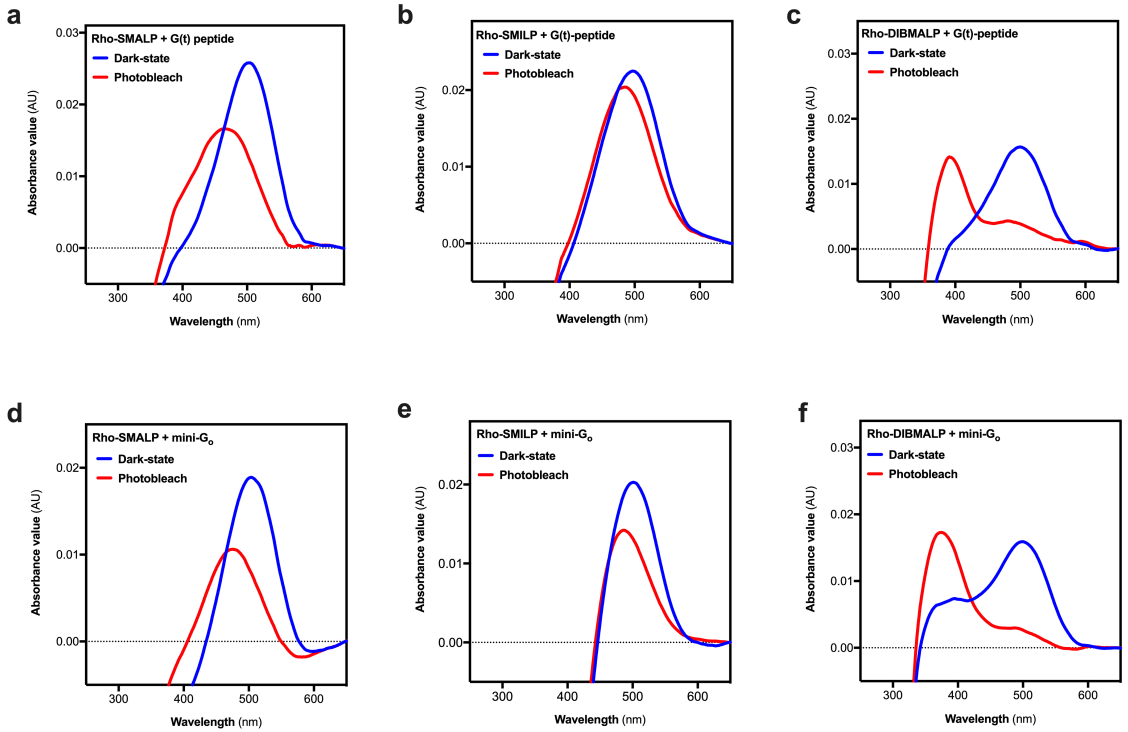

Figure 4.6: **UV-vis spectra of rhodopsin-LPs when incubated with either $G_{(t)}$-peptide or mini-G_o protein.** Representative spectra obtained ($n = 3$) from incubating solubilised rhodopsin-LP samples with $G_{(t)}$-peptide (panels **a**, **b** and **c**). Representative spectra obtained ($n = 3$) from incubating solubilised rhodopsin-LP samples with mini-G_o protein (panels **d**, **e** and **f**). **(a, d)** Rhodopsin-SMALPs; **(b, e)** Rhodopsin-SMILPs; **(c, f)** Rhodopsin-DIBMALPs.

4.2.4 Particle size analysis by dynamic light scattering (DLS)

Particle sizes of the rhodopsin-LPs were analysed using DLS. This is important to determine in order to ascertain the degree of conformational change possible within a given nanoparticle, based on available diameter. Thermal stability of the particles was examined by DLS combined with discrete temperature ramping, with a 30 min incubation at stated temperature, before taking DLS reads. Particle sizes observed were consistent with literature values (Stroud *et al.*, 2018), where -SMALPs and -SMILPs formed nanoparticles of ∼10 nm in diameter (9.9 ± 0.2 nm, and 8.7 ± 0.3 nm, respectively) (mean ± s.e.m, $n = 3$). Rhodopsin-DIBMALPs formed nanoparticles of ∼20 nm in diameter (18.9 ± 2.9 nm) (mean ± s.e.m, $n = 3$) (figure 4.7; table 4.3). In terms of thermal stability, rhodopsin-SMALPs appeared to degrade beyond 40 °C, where particle size could no longer be determined due to loss of autocorrelation (figure 4.8). This is suggestive of full disc-breakdown. In contrast to this, rhodopsin-SMILPs and rhodopsin-DIBMALPs displayed marked stability up to 60 °C. In particular, rhodopsin-SMILPs maintained stability up to 50 °C with an average diameter of 8.7 ± 0.3 nm, above this a slight increase in diameter is observed to 15.0 ± 0.9 nm (mean ± s.e.m, $n = 3$) (figure 4.8).

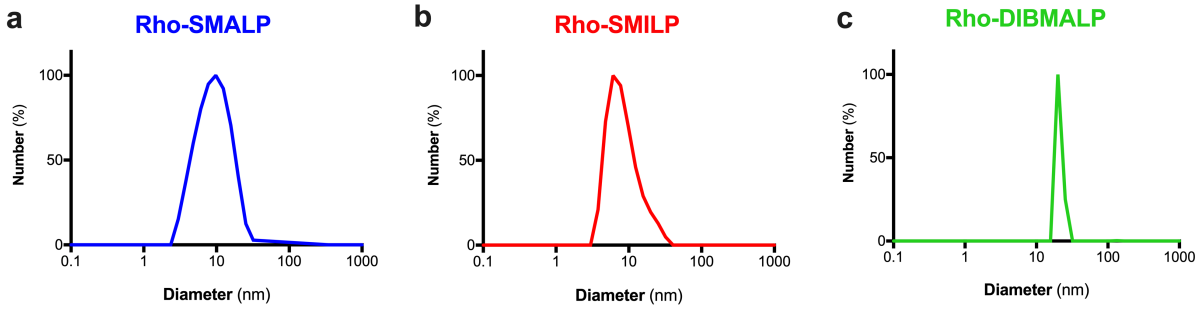

Figure 4.7: **Diameter (nm) of rhodopsin-LP nanodiscs as determined by DLS (a)** SMALPs (blue); **(b)** SMILPs (red); **(c)** DIBMALPs (green). Data displayed are representative traces obtained from a single DLS experiment ($n = 3$).

Table 4.3: **Mean particle diameter observed for the solubilisation of ROS with SMA, SMI and DIBMA.** Data are mean ± s.e.m, $n = 3$.

Rhodopsin-LP	**Mean diameter** (nm)	s.e.m
SMALP	**9.9**	0.2
SMILP	**8.7**	0.3
DIBMALP	**18.9**	2.9

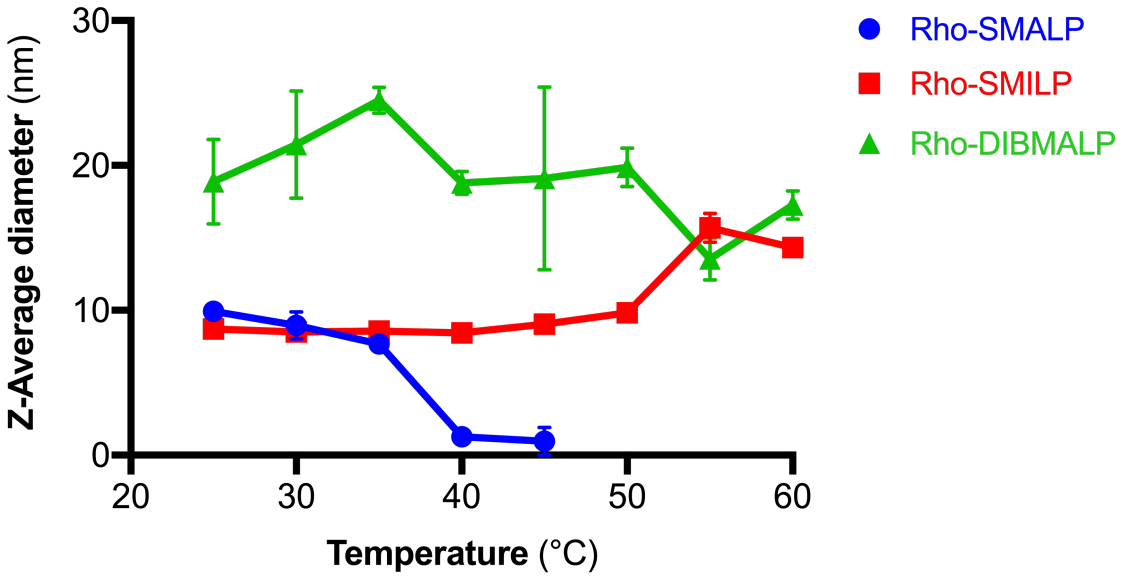

Figure 4.8: **Particle thermal stability as determined by DLS.** Shown are rhodopsin-SMALPs (blue circles), rhodopsin-SMILPs (red squares), rhodopsin-DIBMALPs (green triangles). The temperature of the DLS sample-holder was discretely ramped to stated temperature, and allowed to equilibrate for 30 min before DLS readings were taken and particle diameter recorded. Data are mean ± s.e.m, $n = 3$.

4.2.5 Thermal stability of rhodopsin-LPs

Stability of rhodopsin-LPs at 37 °C

Rhodopsin-LP samples were incubated (dark-state) in a spectrophotometer pre-heated to 37 °C. A_{500} was then monitored over a period of 16 h. A $t_{1/2}$ value was calculated which represents the time at which 50 % of rhodopsin had decayed, as determined by A_{500}. Rhodopsin-SMALPs displayed markedly reduced stability ($t_{1/2}$ = 183 ± 5 min) (mean ± s.e.m, $n = 3$) compared to rhodopsin-SMILPs, or rhodopsin-DIBMALPs, which did not decay over the assayed time (figure 4.9).

a

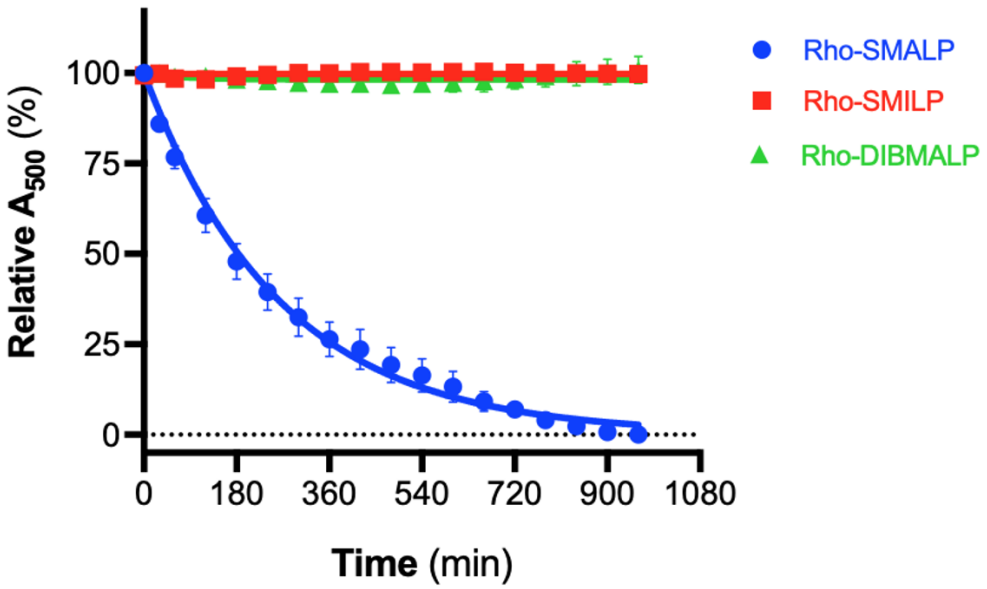

b

Rhodopsin-LP	$t_{1/2}$ (min)
SMALP	185 ± 5
SMILP	> 960
DIBMALP	> 960

Figure 4.9: **Thermal stability of rhodopsin at 37 °C. (a) Graph;** Thermal stability curves for rhodopsin-SMALPs (blue circles), which was fitted to non-linear one-phase decay model. Rhodopsin-SMILPs (red squares) and rhodopsin-DIBMALPs (green triangles) were fitted with simple linear regression. **(b) Data table;** Calculated half-life ($t_{1/2}$). Data are mean ± s.e.m, $n = 3$.

Overall thermal stability of rhodopsin-LPs

Thermal stability of the rhodopsin-LPs was determined over a range of fixed temperatures. The integrity of rhodopsin was assessed by monitoring absorbance at 500 nm, from which a T_{50} value was calculated; the temperature at which 50 % of rhodopsin had decayed, as assessed by A_{500}. Rhodopsin-SMALPs displayed the lowest decay temperature (T_{50} = 45.7 ± 0.5 °C) compared to rhodopsin-DIBMALPs (T_{50} = 51.4 ± 0.8 °C), and rhodopsin-SMILPs (mean ± s.e.m, $n = 3$). T_{50} was not determined for rhodopsin-SMILPs as when heated above 55 °C, the sample appeared to phase-shift and spectra could not be analysed. This change in observation of SMI above 55 °C, may account for the apparent increase in diameter seen in the DLS experiments (figure 4.10). Overall, the thermal decay data shown here align with that of the DLS thermal stability data (figure 4.8), which is indicative that the lessened thermal stability exhibited by rhodopsin-SMALPs is due to denaturing of the polymer, rather than unfolding of the protein.

As a final test of rigour, the rhodopsin-LPs and rhodopsin-DDM were subject to lyophilisation and subsequent resuspension in buffer. It was shown that rhodopsin-SMALPs retained 54 ± 3 % folded rhodopsin, rhodopsin-SMILPs retained 106 ± 2 %, rhodopsin-DIBMALPs retained 48 ± 7 %, and rhodopsin-DDM retained 55 ± 19 % as determined by monitoring A_{500} pre- and post- lyophilisation (mean ± s.e.m, $n = 3$) (figure 4.11).

a

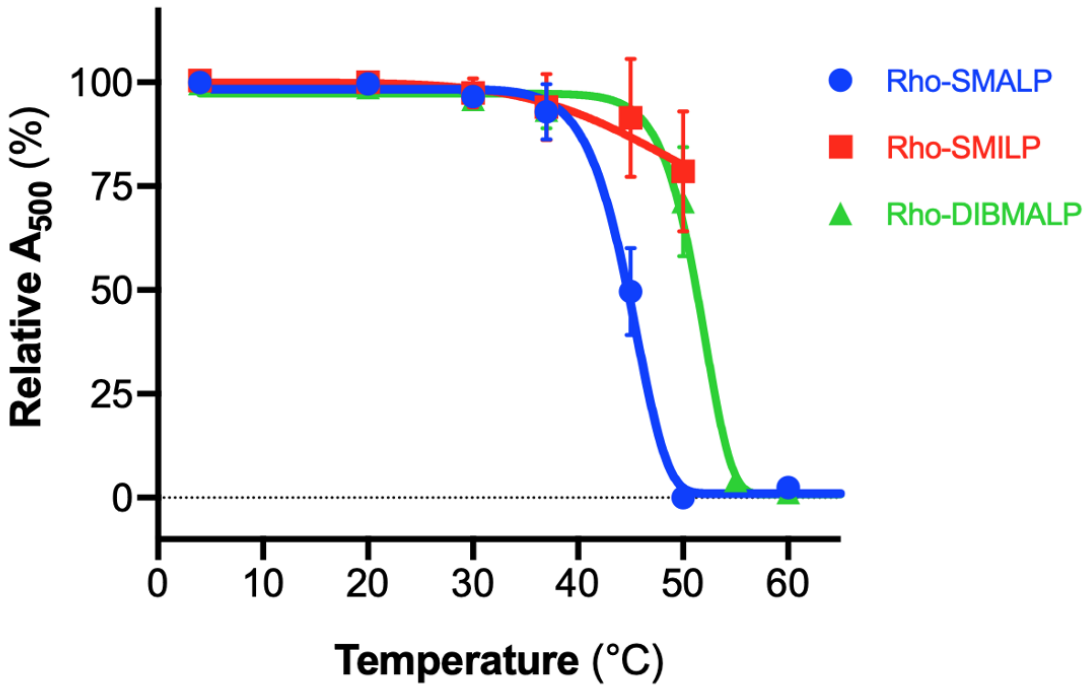

b

Rhodopsin-LP	T_{50} (ºC)
SMALP	45.7 ± 0.5
SMILP	> 50
DIBMALP	51.4 ± 0.8

Figure 4.10: **Thermal stability of rhodopsin-LPs.** Samples were incubated at stated temperature for 30 min before recording absorbance at 500 nm. **(a) Graph;** Rhodopsin-SMALPs (blue circles), rhodopsin-SMILPs (red squares) and rhodopsin-DIBMALPs (green triangles) were fitted to a five-parameter logistic equation to calculate the point at which 50 % folded rhodopsin had decayed (T_{50}), determined by monitoring A_{500}. **(b) Data table;** Calculated T_{50} values (°C). Data are mean ± s.e.m, $n = 3$.

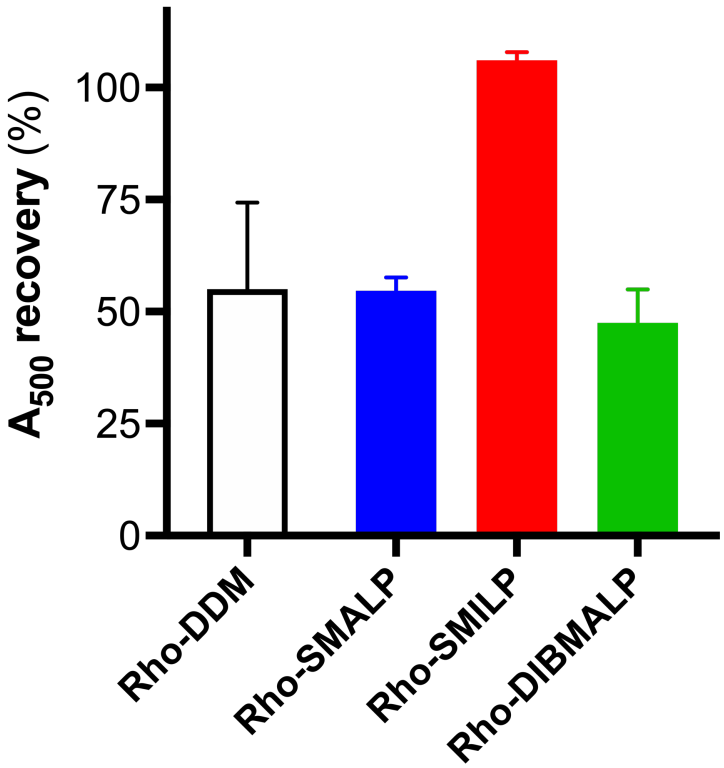

Figure 4.11: **Recovery of rhodopsin after lyophilisation.** Samples were frozen at -80 °C for 24 h, lyophilised (48 h), then placed in -80 °C for 24 h, before resuspension in original volume of buffer. A_{500} was recorded before and after the lyophilisation process. Data are mean ± s.e.m, $n = 3$.

4.2.6 Analytical ultracentrifugation (AUC) of rhodopsin-LPs

AUC of the rhodopsin-LPs was performed to gain insight into the oligomeric state of the solubilised material. SEDNTERP was utilised to calculate the partial specific volume of rhodopsin (υ) and yielded a value of 0.75. Analysis with SEDFIT utilised the in-built continuous distribution ($C_{(S)}$) model. Subsequent RMSD values for all the presented rhodopsin-LP samples were less than 0.01, indicating appropriate fit to the $C_{(S)}$ model. The distribution of residuals were observed to be normal, which indicated appropriate fitting limits of the sample meniscus and bottom. Following model fitting, the distributions of the resultant sedimentation peaks were integrated and molecular weight analyses provided the calculated molecular weights (figure 4.12 and figure 4.13). Two distinct peaks were identified on the sedimentation traces for each polymer (figure 4.12). The first peak (S = 1.34, 1.65 and 2.95 for rhodopsin -SMALP, -SMILP and -DIBMALP, respectively) likely corresponds to the presence of residual free-polymer and ill-defined aggregates, or buffer mismatch between the sample and reference solution. The second peak (S = 4.6, 4.1 and 5.2 for rhodopsin -SMALP, -SMILP and -DIBMALP, respectively) likely corresponds to encapsulated rhodopsin, with additional mass contribution from surrounding polymer and lipids (figure 4.12). Predicted molar masses were 89 kDa, 87 kDa and 117 kDa for rhodopsin -SMALP, -SMILP and -DIBMALP, respectively.

In order to aid resolution of the presence of either monomers or dimers, AUC was performed with 'empty' nanodiscs, comprising 1,2-dimyristoyl-sn-glycero-3-phosphocholine (DMPC). DMPC-SMILP generated a sedimentation coefficient of S = 2.5 and predicted molecular mass of 56 kDa. DMPC-DIBMALP generated a peak at S = 3.35, with a predicted molecular mass of 65 kDa (figure 4.13), overall consistent with DIBMA forming nanodiscs capable of encapsulating greater lipid mass than the smaller SMILP nanodiscs (table 4.3).

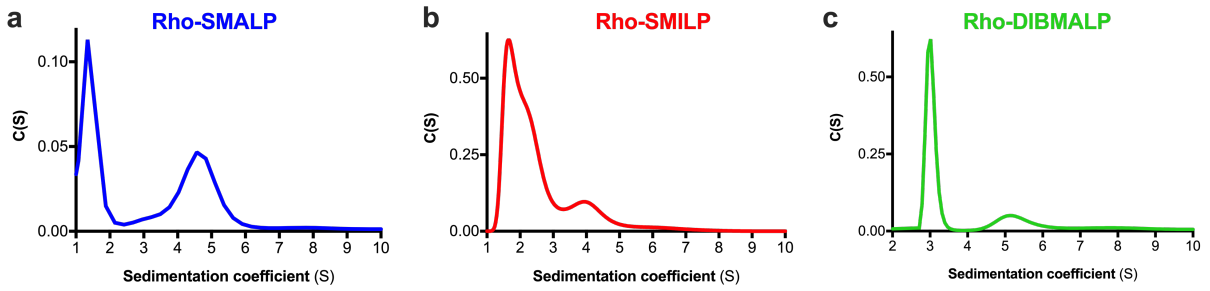

Figure 4.12: **Sedimentation velocity AUC profiles of rhodopsin-LPs.** For each profile, two distinct peaks were identified. The first peak likely represents free-polymer/aggregates/impurities. The second peak indicates monomeric rhodopsin, with additional mass contributed by polymer and lipids. **(a)** Rhodopsin-SMALPs (blue), peak S = 4.6 predicted molecular mass of 89 kDa. **(b)** Rhodopsin-SMILPs (red), peak S = 4.1 predicted molecular mass of 87 kDa. **(c)** Rhodopsin-DIBMALPs (green), peak S = 5.2 predicted molecular mass of 117 kDa.

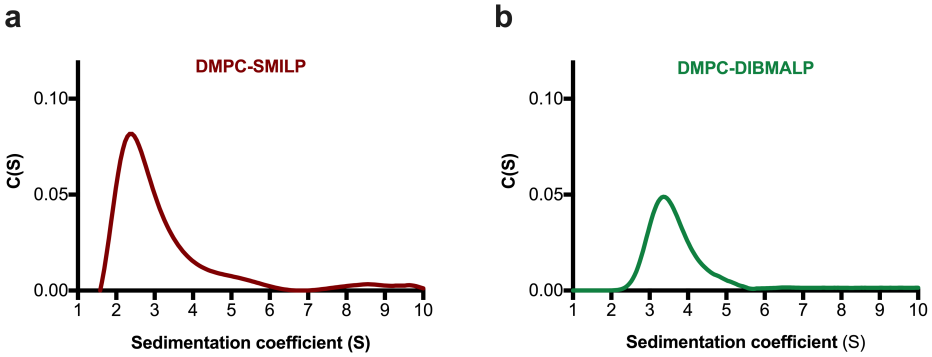

Figure 4.13: **Sedimentation velocity AUC profiles 'empty'-discs.** **(a)** DMPC-SMILPs, S = 2.5 with predicted molecular mass of 56 kDa and **(b)** DMPC-DIBMALPs, S = 3.35 with predicted molecular mass of 65 kDa.

In order to resolve the oligomeric state of the rhodopsin-LPs, the predicted rhodopsin-LP mass was subtracted from the predicted mass of the 'empty' nanodisc. For rhodopsin -SMILP and -DIBMALP, this generated a polymer and lipid contribution of 31 kDa and 52 kDa, respectively. These values are consistent with the previously determined polymer and lipid contribution of SMALPs, 35 kDa (Lee *et al.*, 2016). The calculated polymer and lipid contribution mass was then subtracted from the original predicted mass of the rhodopsin-LP, to determine the mass attributed to rhodopsin protein. It was concluded that for all rhodopsin-LPs, only monomeric rhodopsin was encapsulated (table 4.4).

Table 4.4: **Determination of the oligomeric state of rhodopsin-LPs.** AUC was used to estimate the molecular mass of the stated rhodopsin-LP and 'empty'-LP (DMPC-nanodisc). The estimated mass contribution by polymer and lipid was calculated via the difference between rho-LP and 'empty'-LP. For SMALP, literature value was used; [a]Lee *et al.* (2016). 'Remainder' represents the remaining mass after polymer/lipid contribution and rhodopsin mass (43 kDa) was subtracted from the original rho-LP mass.

	Molecular mass (kDa)			
	AUC-predicted		Calculated	
	Rho-LP	**'Empty'-LP**	**Polymer/lipid contribution**	**Remainder**
Rho-SMALP	89	–	35[a]	11
Rho-SMILP	87	56	31	13
Rho-DIBMALP	117	65	52	22

4.3 Discussion

4.3.1 Overview

Nanodisc technology is becoming a widely adopted strategy for membrane protein solubilisation, due to benefits provided by polymer-based technologies over their detergent counterparts. Proteins are solubilised directly with preservation of the lipid annulus, maintaining a native environment for the membrane protein. The majority of polymer-based solubilisation strategy has, thus far, focused largely on SMA. There is sparse literature available about the behaviour of membrane proteins in emergent, second-generation polymers such as SMI or DIBMA. This chapter aimed to address such question, characterising the solubility, stability and conformational changes of rhodopsin in three commercially-available polymers, SMA, SMI and DIBMA. It was demonstrated that all three polymers were capable of solubilising ROS to high efficiencies (>91 % recovery compared to DDM, table 4.1). The ability to quantify the solubilisation efficiency of properly folded rhodopsin (demonstrated the by absorbance at 500 nm) represents one advantage presented by this light-activated protein compared with other GPCR counterparts. Densitometric analysis of an SDS-PAGE against samples of known protein concentration presents an alternative method for calculating solubilisation efficiency, however does not provide insight into the folded-state of the protein. Results presented in table 4.1 highlight that despite the changes in functional groups, the polymers do not lose their ability to generate membrane protein lipid-discs containing correctly folded rhodopsin. However, conformational changes of the protein can vary depending on extraction method.

4.3.2 Conformational restriction of rho-SMALP and rho-SMILP

Rhodopsin is an extremely well characterised GPCR and several spectroscopic and EPR studies have elucidated light-induced conformational changes of rhodopsin (Kusnetzow *et al.*, 2006), bacteriorhodopsin (Steinhoff *et al.*, 1994; Klare *et al.*, 2004) and other early-photoreceptors (Wegener *et al.*, 2000, 2001) in a variety of contexts including detergent micelles and artificial bilayers. Upon photo-activation, rhodopsin's covalently-bound ligand,

11-*cis*-retinal, undergoes isomerisation to all-*trans*. Several short-lived photo-intermediate states occur, notably, the penultimate state prior to full activation is MI formation. MI is characterised by γ_{max} 478 nm. In MI, retinal has undergone full isomerisation, however the protonated Schiff base remains present. The final stage of rhodopsin activation is formation of MII, characterised by γ_{max} 382 nm and de-protonation of the Schiff base (accompanied by a large outward movement of TM6). Here, these conformational transitions have been followed using UV-visible absorption spectroscopy to study the potential influence of nano-encapsulation within SMALPs, SMILPs and DIBMALPs. It is readily apparent that light-induced conformational changes of rhodopsin are restricted in SMALPs and SMILPs. Both rhodopsin -SMALPs and -SMILPs are able to transition from dark-state to MI, however, are unable to transition from MI to MII (figure 4.4). This indicates both SMALPs and SMILPs provide less flexibility, reducing the dynamic conformational range adopted by the protein. This finding is consistent with a recent study that identified significant side-chain immobility in the SMALP-solubilised bacterial photoreceptor sensory rhodopsin II of *Natronomonas pharaonis* (NpSRII) (Mosslehy *et al.*, 2019). In marked contrast to this, DIBMALPs were able to reach full MII (figure 4.4). SMA and SMI have commonality of a styrene moiety, with differing secondary moieties (maleic acid in SMA, and maleic imide in SMI). The hydrophobic styrene group has been shown to intercalate perpendicularly to the lipid acyl chains (Jamshad *et al.*, 2015b). This intercalation may reduce dynamism of either local lipid or protein groups, which may account for the reduced activation capability seen in this study. In particular, GPCR activation requires a large outward movement of TM6 to enable accommodation of G-proteins (Deupi and Standfuss, 2011). If the polymer is resulting in a freezing effect, then such helical movements would be unable to occur. This, in part, led to the rationale for the stabilising experiments performed with either $G_{(t)}$-peptide, or the mini-G_o. The $G_{(t)}$-peptide is a high-affinity peptide, derived from transducin α-5 helix, which docks into the receptor core and shifts MI/MII equilibrium toward MII in a dose-dependent manner (Kisselev *et al.*, 1999). The mini-G_o is a modified subunit of Gα and recapitulates G-protein specificity.

Mini-G_o comprises the guanosine triphosphatase (GTPase) domain of the α subunit of heterotrimeric G-proteins. Mini-G_o has previously been shown to couple effectively to rhodopsin solubilised in detergent, creating a stabilised active receptor complex (Tsai *et al.*, 2018). Addition of either of these components did not alter the rhodopsin activation spectrum in SMALP, SMILP, or DIBMALP (figure 4.6). Given the high-affinity nature of the $G_{(t)}$-peptide and mini-G_o, and the excess concentrations used in this study, it is unlikely the lack of receptor MII formation is due to depletion or non-specific binding to the polymer. It is possible the polymers cause an accessibility issue, masking all, or some, of the Gα docking site. Another possibility is the inability of the TM helices to rearrange such that they can accommodate the $G_{(t)}$-peptide or mini-G_o. Given that the rhodopsin -SMALPs and -SMILPs result in MI formation, and -DIBMALPs result in MII formation, it is logical to pinpoint conformational restriction to the presence of the styrene ring. DIBMA consists of aliphatic diisobutylene and maleic acid units. Data have shown that DIBMA causes less perturbation to lipid bilayers than SMALPs, which may have significant implications on local fluidity (Cuevas Arenas *et al.*, 2017). DIBMA has also been shown to form larger nanodiscs than SMA or SMI (Oluwole *et al.*, 2017a), consistent with the sizes reported here by DLS experiments (table 4.3). It is possible that a larger nanodisc would allow for greater conformational range, allowing receptor activation to occur, however given the distance of the helical movement required for agonist-induced receptor activation (∼10–18 $\mathring{A}$) and the diameter of an SMA/SMI nanodisc (∼100 $\mathring{A}$), size is unlikely to be a limiting factor.

4.3.3 Oligomeric state of rhodopsin-LPs

The oligomeric state of a GPCR can affect receptor activation, and remains a point of contention that is technically difficult to assess, especially in native environments (Carroll *et al.*, 2012). The quaternary structures isolated from solubilised rhodopsin appear to vary greatly depending on type and concentration of detergent used (Jastrzebska *et al.*, 2006). There is evidence that indicates rhodopsin in ROS forms rows of organised dimers, as visualised directly by transmission electron microscopy (Suda *et al.*, 2004). However,

monomeric rhodopsin is able to fully activate $G_{(t)}$ and reach MII conformation (Bayburt *et al.*, 2011). There is evidence that activation of rhodopsin occurs faster in dimeric and higher-order oligomeric states, as opposed to monomerically isolated rhodopsin (Jastrzebska *et al.*, 2006). Of course, previous studies have utilised detergents which perturb native lipids, which unsurprisingly, appears to perturb receptor organisation. Given how polymer-based solubilisation strategies excise segments of the membrane in a less disruptive way, useful insight may be gained from oligomeric-state analysis in these kinds of nanodisc. Here, AUC was used to assess the sedimentation velocity of rhodopsin in SMALPs, SMILPs and DIBMALPs. The amino acid sequence of rhodopsin was input into SEDNTERP to calculate the partial specific volume of rhodopsin, and yielded a value of 0.75. Determination of an accurate partial specific volume is important for the determination of sedimentation rate and subsequently particle size. Given that the rhodopsin-LPs contain a mixture of polymer, lipid and protein the partial specific volume generate a level of inaccuracy. The use of differential sedimentation (whereby samples are sedimented in either water or deuterium) can improve the accuracy of the calculation of partial specific volume, and has been demonstrated once previously with bacterial divisome proteins ZipA and FtsBL (Stroud, 2019). Differential sedimentation of ZipA-SMALP and FtsBL-SMALP generated a υ of 0.73 and 0.74, respectively (Stroud, 2019). Future work should employ differential sedimentation to rhodopsin-LPs, which was beyond the scope of this thesis. Given the lack of available data for SMA-, SMI- or DIBMA- solubilised proteins AUC data was analysed using the SEDNTERP-calculated partial specific volume.

All three sample types showed similar looking traces, giving sedimentation coefficients (S) between 4.1–5.2 (figure 4.12). The exact interpretation however, remains challenging due to the added mass from polymer and lipid. The predicted molecular masses (Mw) for the rhodopsin -SMALPs, -SMILPs and -DIBMALPs were 89, 87 and 117 kDa, respectively (figure 4.12). Given the predicted Mw of rhodopsin is 43 kDa, this would indicate either the presence of monomers, or dimers, depending on how much mass is attributed to polymer and lipid. Previous work with SMALP-solubilised membrane proteins has

demonstrated that ∼35 kDa is contributed by polymer and lipid (Lee *et al.*, 2016). In-depth work has been performed using differential sedimentation of a well-characterised protein (BSA), DMPC-SMALPs and a SMALP-solubilised *E.coli* protein, Zip-A. Samples were sedimented in either water or deuterium, and the resultant change in sedimentation coefficient was used to calculate an accurate partial specific volume of the particle (υ). Ultimately, it was found that the SMA and lipids contributed between 35.5–62 kDa in mass (Stroud, 2019). AUC performed in this study on 'empty'-SMILPs and -DIBMALPs resulted in polymer and lipid mass contributions of 31 kDa and 52 kDa being estimated for SMILP and DIBMALP, respectively (figure 4.13). Upon subtraction of the estimated polymer and lipid contribution and the mass of rhodopsin from the AUC calculated masses of the rhodopsin-LPs, it was concluded that monomeric rhodopsin was encapsulated in all three polymers (table 4.4). Of course, further work could fully characterise the sedimentation behaviour of SMILPs and DIBMALPs, ideally with differential sedimentation approaches, similar to those performed previously with SMALPs (Stroud, 2019).

4.3.4 Thermal stability of rhodopsin-LPs

This study highlights how important the development of novel nanodisc-based polymer agents will be. Any solubilisation agent is not without limitations, and it is likely strategies in the future will involve 'polymer screens', in a very similar manner as used with detergents currently. Besides from the difference in conformational dynamics seen between polymer, further differences became apparent when thermal stability was investigated. Rhodopsin-SMALPs were the least thermo-stable of the three polymers, demonstrating a T_{50} of 45.7 ± 0.5 °C. This T_{50} is still well above physiological temperature, indicating suitable levels of stability for *in vitro* study. The SMALP thermal stability data shown here also corroborate with previous experimental work performed on another family A GPCR, $A_{2A}R$. With $A_{2A}R$-SMALPs, a $t_{1/2}$ at 37 °C was found to be 148 ± 13 min, compared with 183 ± 5 min for rhodopsin-SMALP in this study (figure 4.9) (Jamshad *et al.*, 2015a). Combined with the DLS data obtained here which showed the SMALP-sized nanoparticles being undetectable at ≥40 °C, this is suggestive that the thermal stability

is less protein-specific and more of a generic property of SMA.

4.3.5 Summary and future work

This work highlights, for the first time, in-depth characterisation of a GPCR solubilised with three, commercially-available polymers, SMA, SMI and DIBMA. Marked differences in receptor activation are demonstrated, with SMA and SMI constraining rhodopsin in the intermediate MI state. Full activation (MII formation) was observed with the use of DIBMA. The ability to isolate usually short-lived intermediate activation states may provide a useful tool for drug discovery. There is growing interest in the development of anti-GPCR antibodies, not just as research tools, but also as therapeutics. The development of conformational specific antibodies can help map activation domains, and has the potential to be used in native tissues and on endogenous receptors. Furthermore, conformation-specific antibodies can be used in drug screens, particularly identifying compounds that act as allosteric modulators, which is of therapeutic interest. Resolving an intermediately-active structure could also provide valuable insights into the mechanisms of receptor activation, that is potentially applicable to all family A GPCRs. Intermediate structures would have great value in structure-based drug design. Overall, this work highlights the ability of SMA and SMA-like polymers to be used as useful research tools. The differing conformational capabilities and biochemical properties seen in this study, demonstrate the importance of continuing with the development of a 'polymer tool kit' to facilitate in the continued study of membrane proteins.

Chapter 5: Generation, pharmacological characterisation and SMALP-solubilisation of inducible cell lines for oxytocin receptor and parathyroid hormone 1 receptor.

5.1 Introduction

The previous chapters explored how polymer-solubilised GPCRs can be pharmacologically and biophysically characterised, using two prototypical receptors as experimental models (rhodopsin and $A_{2A}R$). This chapter explores how two inherently less-stable, and less well-characterised GPCRs behave within a SMALP context, beginning with the design of novel receptor constructs and generation of inducible cell lines to enable their study. Increasingly, existing methods are being validated for use with SMALPs and SMALP-like polymers. It is important to be able to expand this beyond prototypical membrane proteins and into a wider range of drug targets. The oxytocin receptor (OTR) is a family A GPCR which has a stringent, functional requirement for cholesterol for high-affinity agonist binding (Gimpl and Farenholz, 2000). Peripherally, OTR regulates parturition and lactation. Oxytocin (OT), the endogenous ligand, and OT-derived analogues are used clinically to induce labour (Hidalgo-Lopezosa *et al.*, 2016). OTRs are also present in the central nervous system where they modulate behaviours such as social-bonding, aggression, stress and anxiety responses, social memory and recognition (Hawtin *et al.*, 2001a). The parathyroid hormone 1 receptor (PTH1R) is a family B GPCR that regulates calcium homeostasis, and is of high pharmaceutical interest (Zhao *et al.*, 2019). Currently, two PTH1R-targeting therapeutics exist for the treatment of osteoporosis (teriparatide and abaloparatide), which are analogues of the endogenous ligands parathyroid hormone (PTH) and parathyroid hormone-related protein (PTHrP). While effective, the treatment is costly, and requires daily injections. At present, there are no orally efficacious drugs for the treatment of osteoporosis, despite significant research efforts. Like many other

GPCRs, this difficulty in drug design is, in part, due to lack of structural and functional understanding of the receptor, which is partly due to technical difficulties in the production of suitable quantity and quality of membrane proteins in general (Kesidis *et al.*, 2020). Although the recent structures of OTR (Waltenspuhl *et al.*, 2020) and PTH1R (Ehrenmann *et al.*, 2018; Zhao *et al.*, 2019) do provide structural insights, further mechanistic insights, using biophysical techniques still requires the generation of a suitable quantity and quality of human membrane proteins. Retention of the native lipid environment is technically challenging when extracting membrane proteins. Therefore, commonly employed expression methods such as *Sf*9 (insect), or *E. coli* (bacteria) may be sub-optimal (Kesidis *et al.*, 2020). The demand for mammalian over-expression systems is increasing, due to near-native translocation machinery, post-translation modifications and lipid environment (Chaudhary *et al.*, 2012). Particularly, OTR has N-linked glycosylation sites, which may be inappropriately processed in non-mammalian systems. Stably-transfected, inducible mammalian cell lines are of increasing use. Tetracycline-induced mammalian cell systems are becoming increasingly utilised due to their consistent ability to express the desired protein uniformly, compared with transiently transfected cells. Inducible systems allow for relatively large quantities of protein to be generated, as high-density cultures can be obtained pre-induction. Theoretically, upon induction, every cell would be producing protein, which provides consistency against varying transient transfection efficiencies. Furthermore, inducible-expression systems can circumvent challenges associated with cytotoxicity (Waltenspuhl *et al.*, 2020). With regards to tetracycline-induced systems, a tetracycline-operator sequence (tetO) is incorporated into a plasmid, containing the gene of interest. The tetO sequence is subsequently recognised by a tetracycline-repressor (tetR) gene, which is incorporated into mammalian cells of choice. In the absence of tetracycline, the tetR protein binds to the tetO sequence that is generally incorporated into the promoter region of the plasmid, rendering expression inactive. The addition of tetracycline results in the tetR protein competitively binding the tetracycline, enabling transcription to be activated. Commonly, induction medium is supplemented with low-millimolar levels

of sodium butyrate, which acts as a histone-deacetylase inhibitor, increasing expression. Recombinant technology has undoubtedly aided in fundamental understanding of receptor pharmacology, however, it is still just one part of a larger process. Experimental tools such as fluorescent ligands permit the monitoring and quantification of binding events. This chapter aimed to establish the tools required for the study of pharmacologically-relevant receptors OTR and PTH1R (receptor 'snake plots'; appendix F). Beginning with receptor construct design, to establishment of stable cell lines, purification and the design and characterisation of a novel PTH1R fluorescent ligand.

5.2 Results

5.2.1 Design of receptor constructs

To enable the study of OTR and PTH1R, new receptor constructs were designed with affinity tags to permit downstream purification, detection and immobilisation of the receptors. A deca-His tag and an HA-tag were incorporated onto the N-terminus of the OTR and PTH1R. At the C-terminus, an Avidity Avitag™ (GLNDIFEAQKIEWHE) was incorporated (figure 5.1). Denotation of the OTR, or PTH1R containing the Avitag sequence will be herein referred to as OTR_{Avi} and $PTH1R_{Avi}$, respectively (construct sequences; appendix E). Receptor constructs were manufactured into a custom-made plasmid (pACMV_tetO) designed and kindly donated by Dr. Philip J. Reeves (University of Essex, UK) (figure 5.1). The pACMV_tetO plasmid was engineered for tetracycline-regulated gene expression, and has been successfully utilised previously to express milligram quantities of inherently cytotoxic rhodopsin mutants (Waltenspuhl *et al.*, 2020). HEK 293S cells incorporating a tetR gene (denoted HEK 239S_tetR cells) were stably-transfected with either OTR_{Avi} or $PTH1R_{Avi}$ constructs exactly as described in 2.2.7. OTR_{Avi} and $PTH1R_{Avi}$ were also cloned into pcDNA3.1(+) for transient expression in HEK 293T or COS-7 cells, to permit comparable pharmacological characterisation with existing lab constructs.

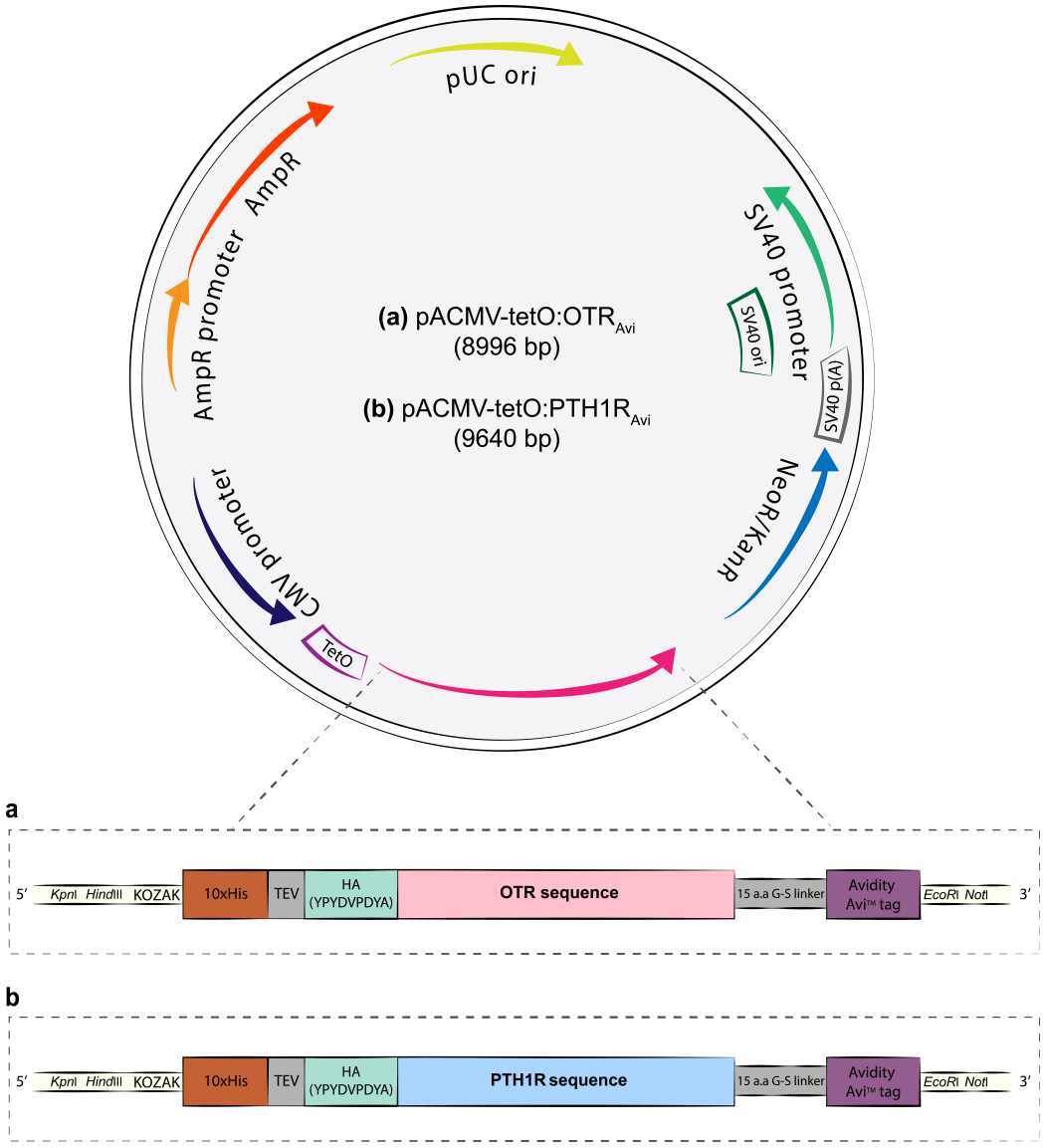

Figure 5.1: **Schematic of how OTR$_{Avi}$ and PTH1R$_{Avi}$ constructs were cloned into the pACMV_tetO plasmid.** **(a)** OTR$_{Avi}$, **(b)** PTH1R$_{Avi}$ sequence is cloned just down-stream of a CMV promotor and tetracycline-operator sequence (tetO). KOZAK sequence (GCCACC), and TEV-cleavage site (GAGAATCTTTACTTTCAATCT) was incorporated. The plasmid contains resistance genes for ampicillin (AmpR) and G418 (NeoR/KanR).

5.2.2 Pharmacological characterisation of OTR_{Avi}

Cell-surface expression and internalisation within vector pcDNA3.1(+), in transiently transfected HEK 293T cells

Cell-surface expression and OT-induced internalisation in HEK 293T cells of OTR_{Avi} was determined by ELISA, exploiting the HA-tag, and compared with the WT OTR. Both constructs were in vector pcDNA3.1(+). This enabled direct comparison of the Avi-tagged receptor construct, to the WT, to establish if the affinity tags altered receptor phenotype. The results demonstrated that the OTR_{Avi} construct is able to express at 80 ± 9 % of the WT receptor ($p = 0.04$). Internalisation of OTR_{Avi} is also similar to WT. OTR_{Avi} internalised by 43 ± 12 % ($p = 0.02$), compared to unstimulated. WT OTR internalised by 38 ± 4 % after OT-stimulation ($p = 0.002$), data are mean ± s.e.m, $n = 4$ (figure 5.2).

a

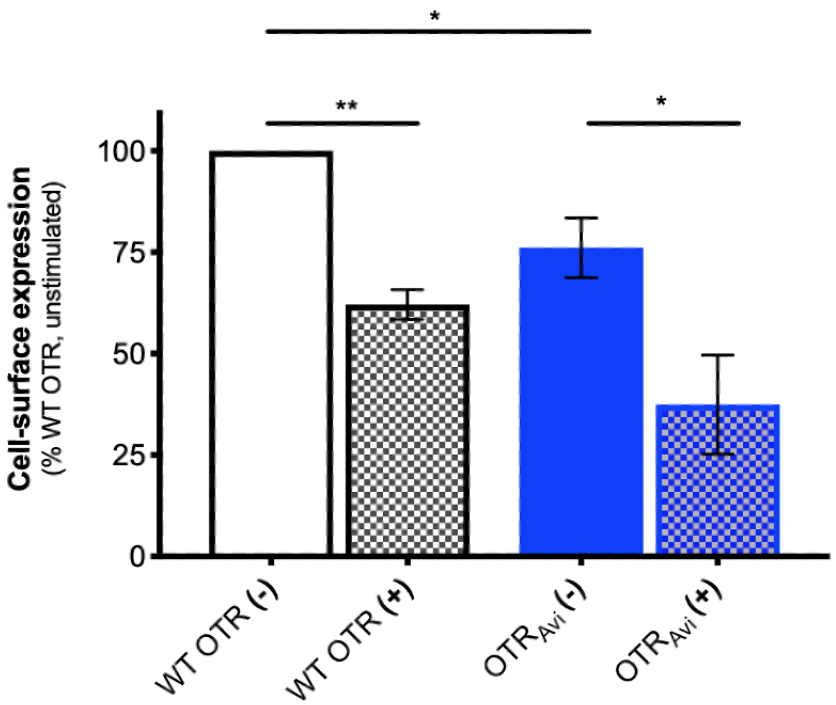

b

Receptor construct	Cell-surface expression (% WT)	OT stimulated internalisation (%)
WT OTR	100	38 ± 4
OTR_{Avi}	80 ± 9	43 ± 12

Figure 5.2: **Cell-surface expression and internalisation of WT OTR and OTR_{Avi}.** **(a)** Graph; **(b)** table showing cell-surface expression of WT OTR and OTR_{Avi} in pcDNA3.1(+), in transiently transfected HEK 293T cells. Expression is shown in the absence (-) or presence (+) of 10^{-6} M OT, stimulated for 30 min, detected via ELISA, exploiting an HA-tag on the receptor. Data are mean ± s.e.m from 4 separate experiments, each performed in triplicate. Significance determined by paired t-tests (*, $p < 0.05$; **, $p = 0.002$).

Inducible cell-surface expression and internalisation of OTR_{Avi} within vector pACMV_tetO, in stably-transfected HEK 293S_tetR cells

Inducible expression was investigated for stably-transfected cells that successfully grew in selection media (stable cell generation described; section 2.2.7). The colonies that demonstrated the highest level of inducible expression were expanded into viable cell lines. High levels of inducible expression were observed for stably-transfected OTR_{Avi} cells, with an average 4.1-fold increase in cell-surface expression upon induction, compared with non-induced cells (figure 5.3). Upon agonist challenge, OTR_{Avi} demonstrated 31 $\pm$ 8 % internalisation ($p = 0.03$; mean $\pm$ s.e.m, $n = 3$). To determine the optimal receptor-expression levels, cells were plated out and induced at different time points, including a non-induced control (figure 5.4). Cell viability was qualitatively assessed at each time point, with notable cell-death after 70 h. Membranes were harvested via osmotic shock, resolved on SDS-PAGE and subsequent Western-blot performed. Optimal cell-expression was deemed to be approximately 44 h. The predicted molecular mass of OTR_{Avi} is 49 kDa. A band is visible on the Western blot at approximately 50 kDa (figure 5.4).

a

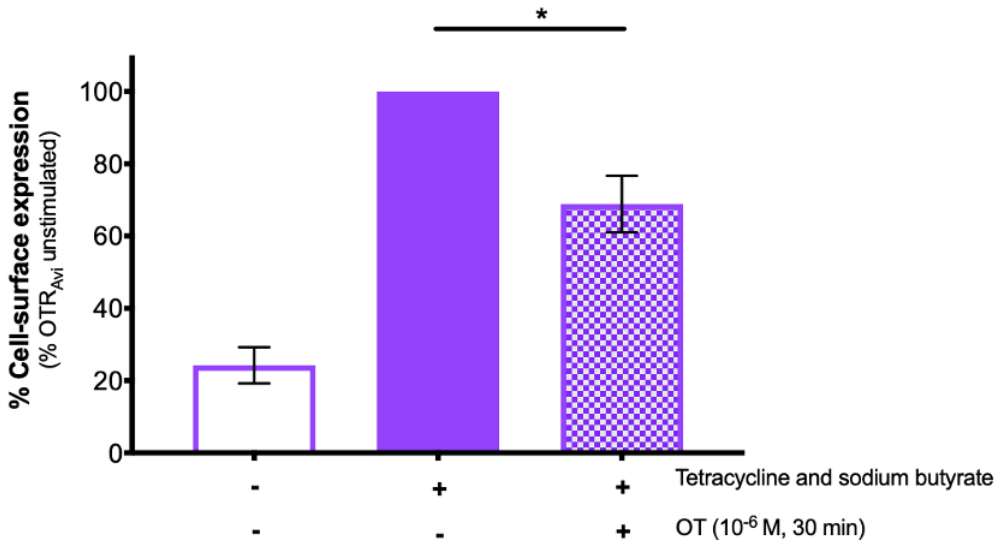

b

	Cell-surface expression (% OTR_{Avi} unstimulated)		
Receptor construct	**Non-induced**	**Induced**	**Internalisation**
OTR_{Avi}	24 ± 5	100	31 ± 8

Figure 5.3: **(a)** Graph; **(b)** table showing cell-surface expression of OTR_{Avi}, expression is shown normalised to induced-self, determined by ELISA. Induction is indicated by the presence (+) of tetracycline (2 μg/ml) and sodium butyrate (5 mM). Internalisation was assessed in the presence (+) of oxytocin (OT, 10^{-6} M). Absence of either compounds is denoted by minus symbol (-). Data are mean ± s.e.m from 3 separate experiments, each performed in triplicate. Significance determined by paired t-test (*, $p = 0.03$).

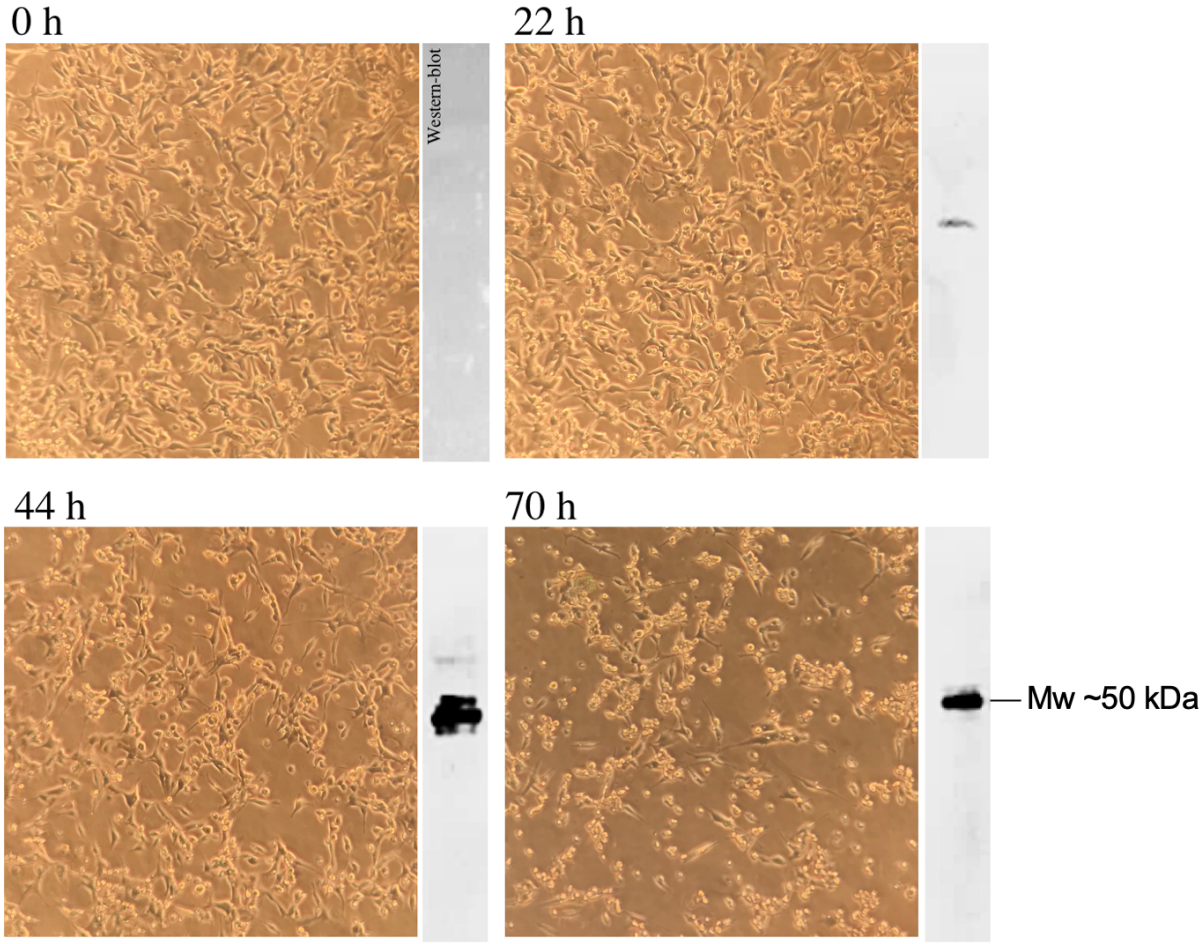

Figure 5.4: **Expression time-course of OTR$_{Avi}$ HEK 293S_tetR cells.** Stably-transfected OTR$_{Avi}$ HEK 293S_tetR cells were induced at different time points with tetracycline (2 µg/ml) and sodium butyrate (5 mM). At each time point, cells were photographed (phase-contrast, 10X objective) immediately before membrane harvest, resolved by SDS-PAGE and subsequent Western-blot performed using anti-HA antibody.

Radioligand binding of OTR_{Avi}

Self-competition binding assay demonstrated no significant difference in OT affinity between WT OTR and OTR_{Avi} constructs in either pcDNA3.1(+) (OTR_{Avi} HEK 293T; $p = 0.93$) or pACMV_tetO (OTR_{Avi} HEK 293S_tetR; $p = 0.54$). In HEK 293T cells, WT OTR and OTR_{Avi} derived a pIC_{50} of 9.4 ± 0.2 (figure 5.5). In HEK 293S_tetR cells, OTR_{Avi} derived a pIC_{50} of 9.0 ± 0.2 (figure 5.5).

a

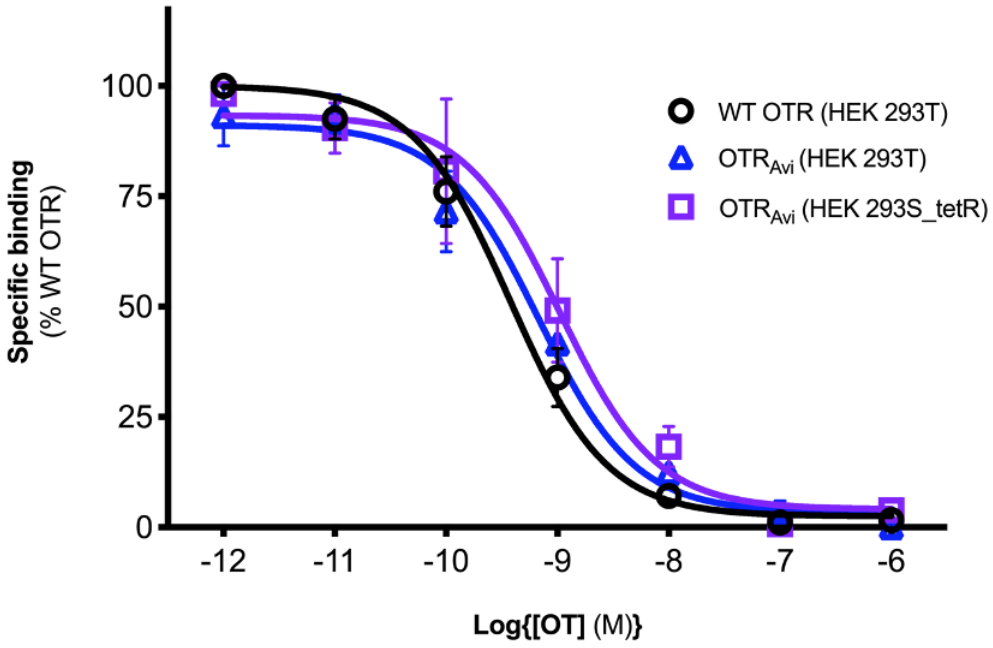

b

Receptor (cellular context)	OT binding (pIC_{50})
WT OTR (HEK 293T)	9.4 ± 0.2
OTR_{Avi} (HEK 293T)	9.4 ± 0.2
OTR_{Avi} (HEK 293S_tetR)	9.0 ± 0.2

Figure 5.5: **Competition radioligand binding.** **(a)** Binding curves; **(b)** data table showing competition radioligand binding with oxytocin (OT). Membranes were harvested from HEK 293T cells transiently-transfected with either WT OTR or OTR_{Avi}, or induced HEK 293S_tetR cells stably-transfected with OTR_{Avi}. Data are mean ± s.e.m from at least 3 separate experiments, each performed in triplicate. Paired ANOVA determined no significant differences compared to WT OTR (OTR_{Avi} HEK 293T, $p = 0.93$; OTR_{Avi} HEK 293S_tetR, $p = 0.54$).

Agonist-induced inositol phosphates accumulation

Inositol phosphates accumulation assay on the OTR constructs showed that OTR_{Avi} retained WT-like potency and E_{max} capability in both HEK 293T and HEK 293S_tetR contexts. WT OTR demonstrated a pEC_{50} of 8.6 ± 0.1. OTR_{Avi} in HEK 293T derived a pEC_{50} of 8.5 ± 0.1, and an E_{max} of 99 ± 0.01 % ($p = 0.53$, compared to WT OTR). OTR_{Avi} in HEK 293S_tetR derived a pEC_{50} of 8.4 ± 0.3, and an E_{max} of 99 ± 1 % ($p = 0.66$, compared to WT OTR).

a

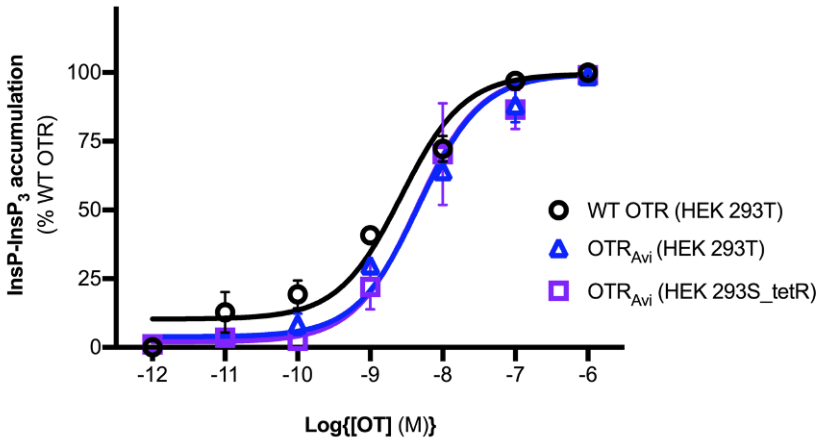

b

	Inositol phosphates accumulation	
Receptor (cellular context)	**pEC_{50}**	**E_{max} (%)**
WT OTR (HEK 293T)	8.6 ± 0.1	100
OTR_{Avi} (HEK 293T)	8.5 ± 0.1	99 ± 0
OTR_{Avi} (HEK 293S_tetR)	8.4 ± 0.3	99 ± 1

Figure 5.6: **InsP-InsP$_3$ accumulation for OTR_{Avi}.** **(a)** Curve; **(b)** data table showing inositol phosphates accumulation assay with OT for transiently transfected HEK 293T cells for either WT OTR or OTR_{Avi}, or, induced stably-transfected OTR_{Avi} HEK 293S_tetR cells. Data are mean ± s.e.m from 3 separate experiments each performed in triplicate. Paired ANOVA determined no significant differences compared to WT OTR (OTR_{Avi} HEK 293T, $p = 0.53$; OTR_{Avi} HEK 293S_tetR, $p = 0.66$).

OTR_{Avi} in a SMALP

To assess whether OTR_{Avi} SMALP-solubilised in a binding competent state, radioligand binding experiments were performed. Previous work demonstrated high-levels of non-specific binding of [^{3}H]OT tracer to an 'empty' SMALP, which meant a competition-style binding assay performed post-SMALP solubilisation was unsuitable (Charlton, 2015). To overcome this, cells were pre-labelled with [^{3}H]OT tracer ligand, prior to SMALP-solubilisation. Dishes of whole HEK 293S_tetR cells expressing OTR_{Avi} were pre-labelled with 1 nm [^{3}H]OT (tracer) in the presence or absence of 1 μM OT (unlabelled competitor). Unbound ligand was removed by aspiration, before samples were SMALP solubilised (as outlined; section 2.2.20). Post-centrifugation (150,000 g, 1 h), aliquots were taken for liquid scintillation counting, to determine specific binding for each sample. Where, total binding was determined by counts derived from dishes incubated with [^{3}H]OT only. Non-specific binding was determined by counts derived from dishes incubated with both [^{3}H]OT and 1 μM OT. High levels of specific binding (93 %) were observed, indicating that SMALP-solubilisation was not detrimental to ligand binding capability (figure 5.7). As a control, HEK 293S cells expressing $PTH1R_{Avi}$ were utilised and the exact process as described above was carried out alongside (mock). [^{3}H]OT tracer did not bind, therefore no specific binding was determined.

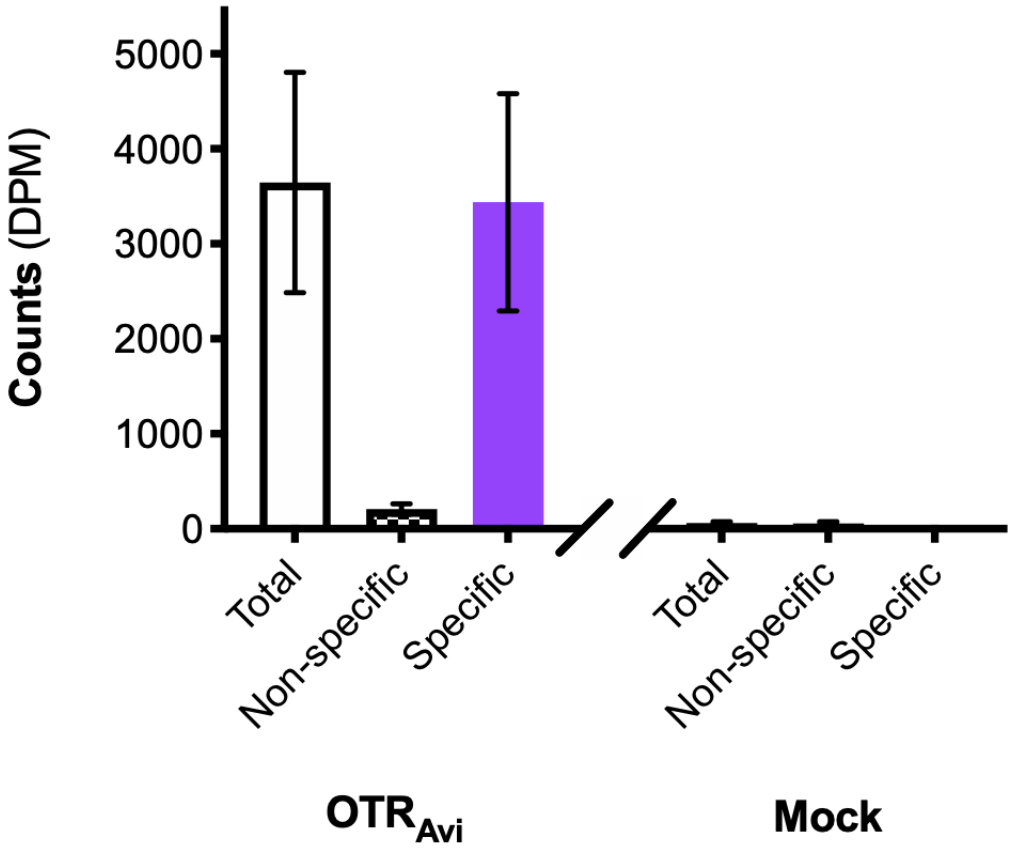

Figure 5.7: **Pre-labelled radioligand binding observed in OTR-SMALPs.** Specific binding was determined for OTR_{Avi} expressed in HEK 293S_tetR cells utilising 1 nM radioligand ([^{3}H]OT), in the presence or absence of 1 μM OT. Mock represents the same experiment repeated with $PTH1R_{Avi}$ expressing HEK 293S_tetR cells. Data are mean ± s.d from 3 separate experiments, each performed in triplicate.

Purification of OTR$_{Avi}$-SMALP

OTR$_{Avi}$ from HEK 293S_tetR cells was SMALP solubilised and purified exactly as described in 2.2.13. Elution from the Ni^{2+}-NTA column was achieved with 300 mM imidazole. The eluted fractions were pooled, concentrated and buffer-exchanged via size-exclusion before resolving all obtained fractions on an SDS-PAGE for Western blot analysis utilising anti-HA primary antibody. Discrete bands are visible in the elution fraction (figure 5.8).

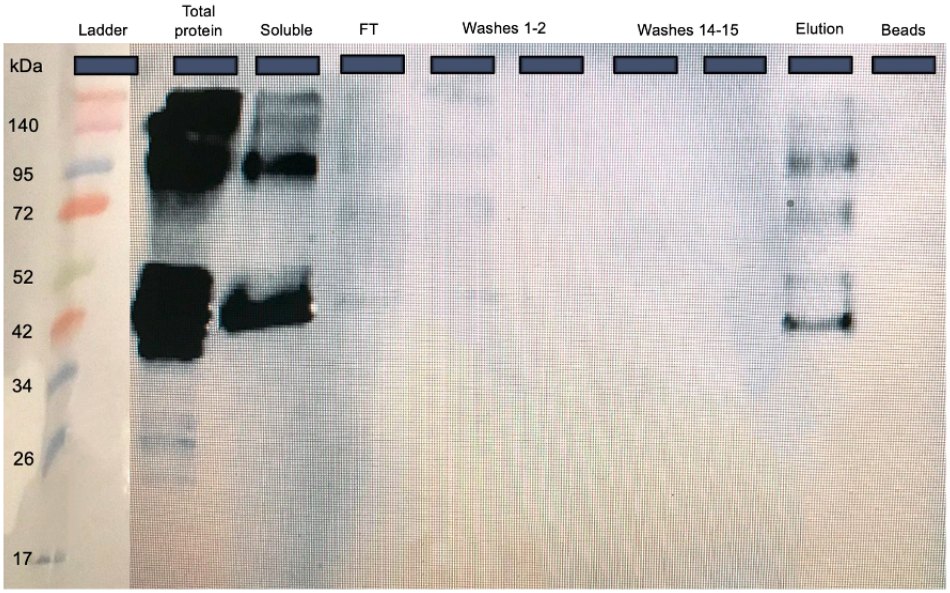

Figure 5.8: **Western-blot analysis of OTR$_{Avi}$ Ni^{2+}-NTA purification.** HEK 293S_tetR cells expressing OTR$_{Avi}$ (total protein) were SMALP-solubilised and supernatant containing OTR$_{Avi}$-SMALPs (soluble) were incubated with Ni^{2+}-NTA resin. Unbound material was collected in the flow through (FT). Column was washed with 15 column volumes of low imidazole (20 mM) buffer (washes). Elution was achieved with 300 mM imidazole and the fraction was concentrated and buffer-exchanged. A sample of Ni^{2+}-NTA resin was taken for analysis on SDS-PAGE post-imidazole elution (beads).

5.2.3 Pharmacological characterisation of PTH1R$_{Avi}$

Cell-surface expression and internalisation of PTH1R$_{Avi}$ within vector pcDNA3.1(+), in transiently transfected COS-7 cells

It was important to initially establish when maximum internalisation of PTH1R$_{Avi}$ occurred after agonist challenge at a saturating concentration of PTH$_{1-34}$ (10^{-6} M; carried out at 37 °C). This established maximum internalisation at 30 min (figure 5.9). Cell-surface expression levels and internalisation response were determined by ELISA, exploiting the HA-tag on the receptor. The results demonstrated that PTH1R$_{Avi}$ is able to express at the cell surface of COS-7 cells and internalise by 48 ± 9 % after 30 min of agonist stimulation ($p = 0.021$; mean ± s.e.m, $n = 4$) (figure 5.10).

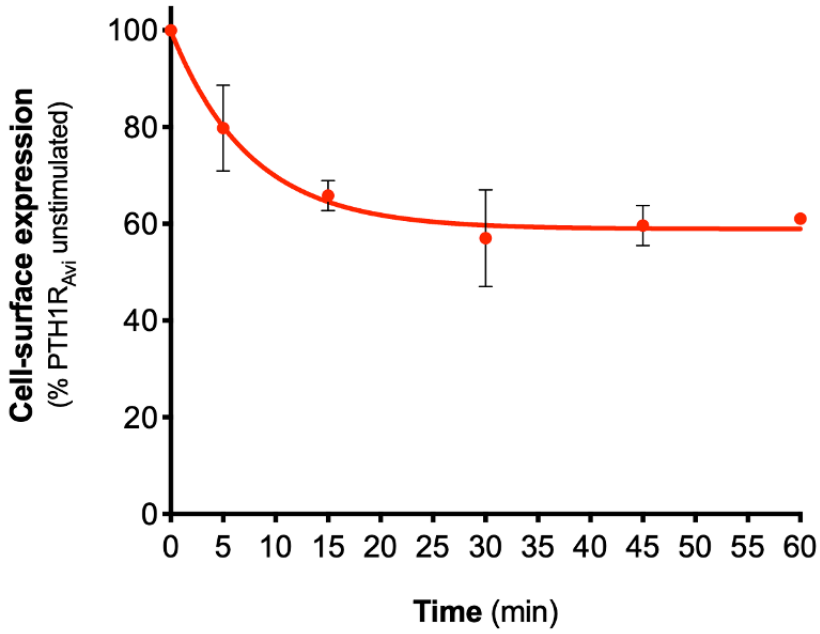

Figure 5.9: **Time-course of PTH$_{1-34}$ stimulated PTH1R$_{Avi}$ internalisation.** PTH1R$_{Avi}$ was stimulated with 10^{-6} M PTH$_{1-34}$ and cell-surface expression determined by ELISA, using the anti-HA antibody. Data are mean ± s.e.m from 3 separate experiments each performed in triplicate.

a

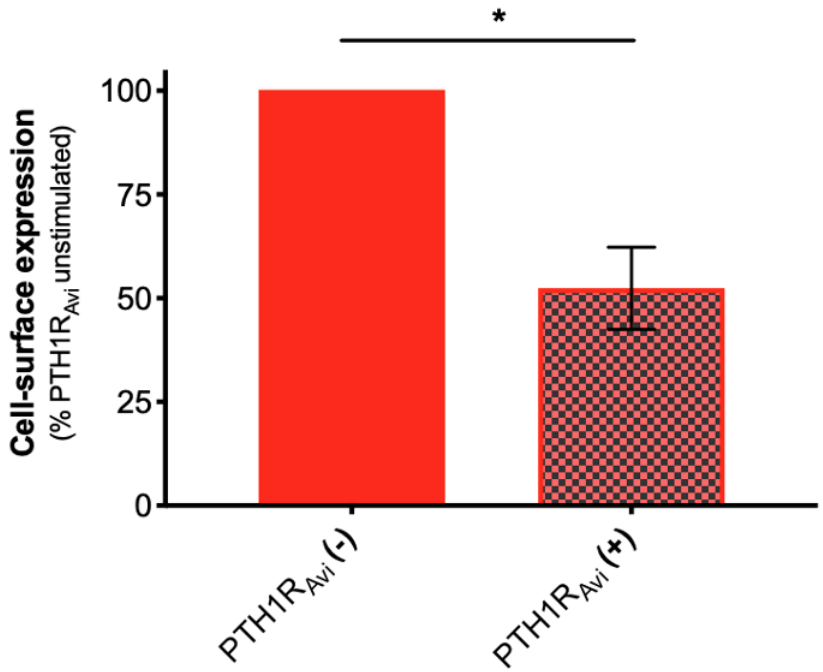

b

Receptor (cellular context)	Cell-surface expression (% WT)	$PTH_{1\text{-}34}$ stimulated internalisation (%)
$PTH1R_{Avi}$ (COS-7)	100	48 ± 9

Figure 5.10: **Cell-surface expression and internalisation of $PTH1R_{Avi}$ in transiently transfected COS-7 cells. (a)** Graph **(b)** table showing cell-surface expression of $PTH1R_{Avi}$ in pcDNA3.1(+) in transiently transfected COS-7 cells. Expression is shown in the absence (-) and presence (+) of 10^{-6} M PTH_{1-34}, stimulated for 30 min, determined by ELISA, exploiting the HA-tag. Data are mean ± s.e.m from 4 separate experiments, each performed in triplicate. Paired t-test determined significance (*, $p = 0.021$).

Due to the known interactions between family B GPCRs and receptor activity modifying proteins (RAMPs), cell-surface expression was assessed following co-transfection with either RAMP 1, 2 or 3. To ensure functionality of the co-transfection with one of the three RAMPs, CLR was used as a positive control. RAMP 1, 2 and 3 all assisted in trafficking of CLR to the plasma membrane, consistent with known receptor pharmacology (Hay *et al.*, 2019). At the CLR, co-transfection with RAMP 1, 2 or 3 resulted in a 265 %, 207 % and 324 % increase in cell-surface expression, respectively (figure 5.11). In contrast, change in receptor cell-surface trafficking was not observed when $PTH1R_{Avi}$ was co-transfected with either RAMP 1, 2 or 3. Cell-surface expression of the $PTH1R_{Avi}$ construct was sufficient enough for continued pharmacological characterisation without requiring co-transfection (figure 5.11).

a

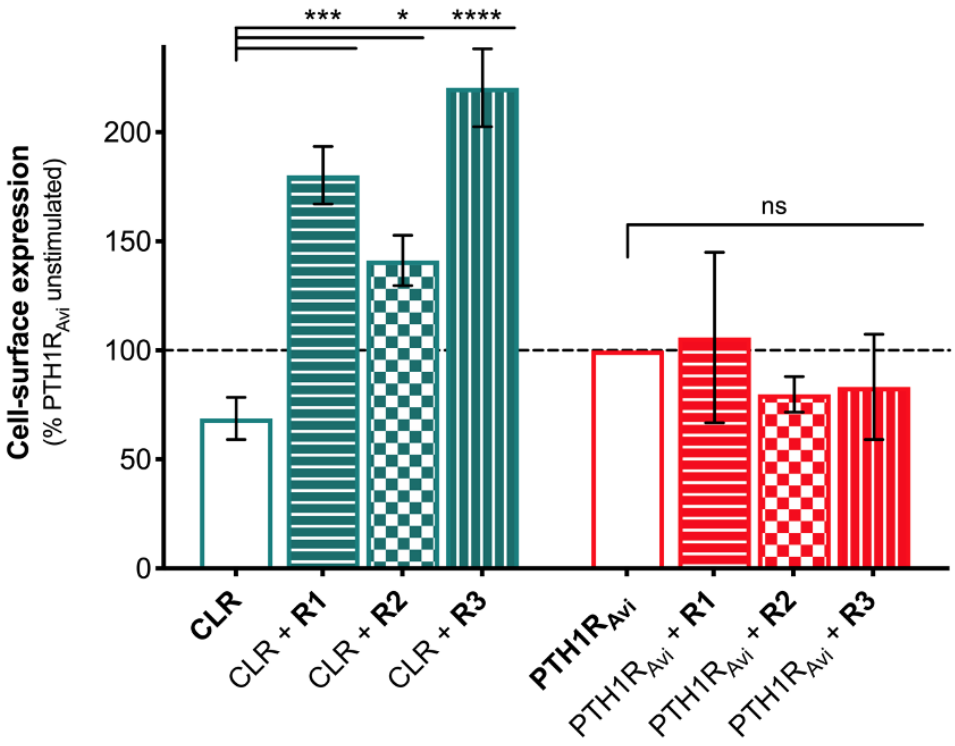

b

	Cell-surface expression (% PTH1R$_{Avi}$)			
Receptor construct	**Receptor only**	**Co-transfection**		
		RAMP1	**RAMP2**	**RAMP3**
CLR	69 ± 10	180 ± 13	141 ± 11	220 ± 18
PTH1R$_{Avi}$	**100**	106 ± 39	80 ± 8	83 ± 24

Figure 5.11: **Cell-surface expression of CLR and PTH1R$_{Avi}$ in pcDNA3.1(+) in transiently transfected COS-7 cells.** **(a)** Graph **(b)** table showing cell-surface expression of CLR and PTH1R$_{Avi}$ when transfected either alone, or co-transfected (1:1) with either RAMP 1, 2 or 3. Expression is normalised to PTH1R$_{Avi}$ only. Data are mean ± s.e.m from 3 separate experiments, each performed in triplicate. Significance determined by paired ANOVA with Sidak multiple comparisons (ns, not significant; *, $p = 0.01$; ***, $p = 0.0001$; ****, $p < 0.0001$).

Inducible cell-surface expression and internalisation of PTH1R$_{Avi}$ within vector pACMV_tetO, in stably-transfected HEK 293S_tetR cells

Stable cell lines were generated described in section 2.2.7. Inducible expression was investigated for cells that successfully grew in selection media. Colonies that demonstrated the highest level of inducible expression were expanded into viable cell lines. High levels of inducible expression were observed for stably-transfected PTH1R$_{Avi}$ (figure 5.12). To determine the optimal receptor-expression levels, PTH1R$_{Avi}$ cells were plated out and induced at different time points, including a non-induced control (figure 5.13). Cell viability was qualitatively assessed at each time point, with notable cell-death apparent after 70 h. Membranes were harvested via osmotic shock, resolved on SDS-PAGE and subsequent Western-blot performed. The predicted molecular mass of PTH1R$_{Avi}$ is 72 kDa, with a band visible at this approximate size on the Western blot (figure 5.13). Optimal cell-expression was deemed to be approximately 44 h.

a

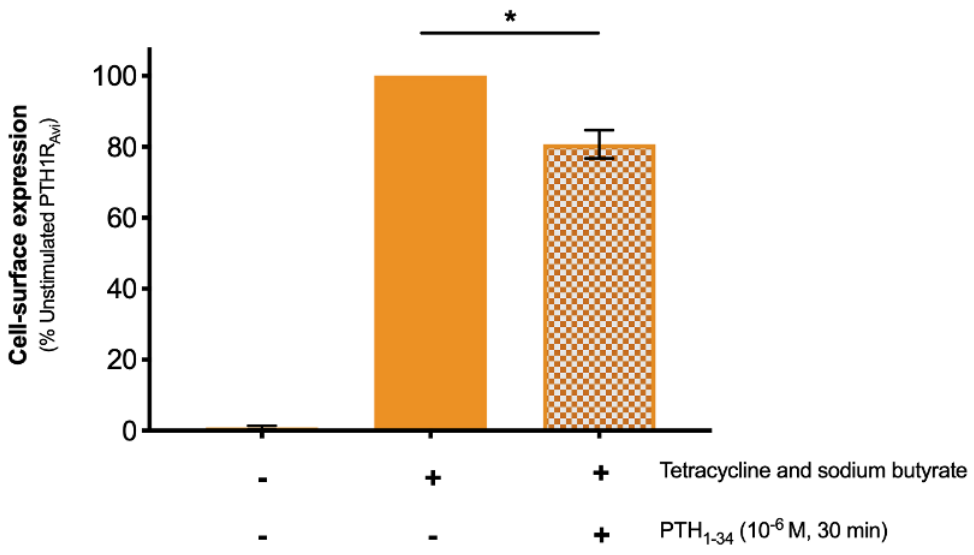

b

Receptor construct	Cell-surface expression (% PTH1R$_{Avi}$ unstimulated)		
	Non-induced	Induced	Internalisation
PTH1R$_{Avi}$	0.8 ± 0.5	100	19.4 ± 3.9

Figure 5.12: **Inducible expression of PTH1R$_{Avi}$ in stably-transfected HEK 293S_tetR cells.** **(a)** Graph **(b)** table showing cell-surface expression of PTH1R$_{Avi}$, as determined by ELISA exploiting the HA-tag on the receptor. Data are mean ± s.e.m from 3 separate experiments, each performed in triplicate. Significance determined by paired t-test ($p = 0.04$).

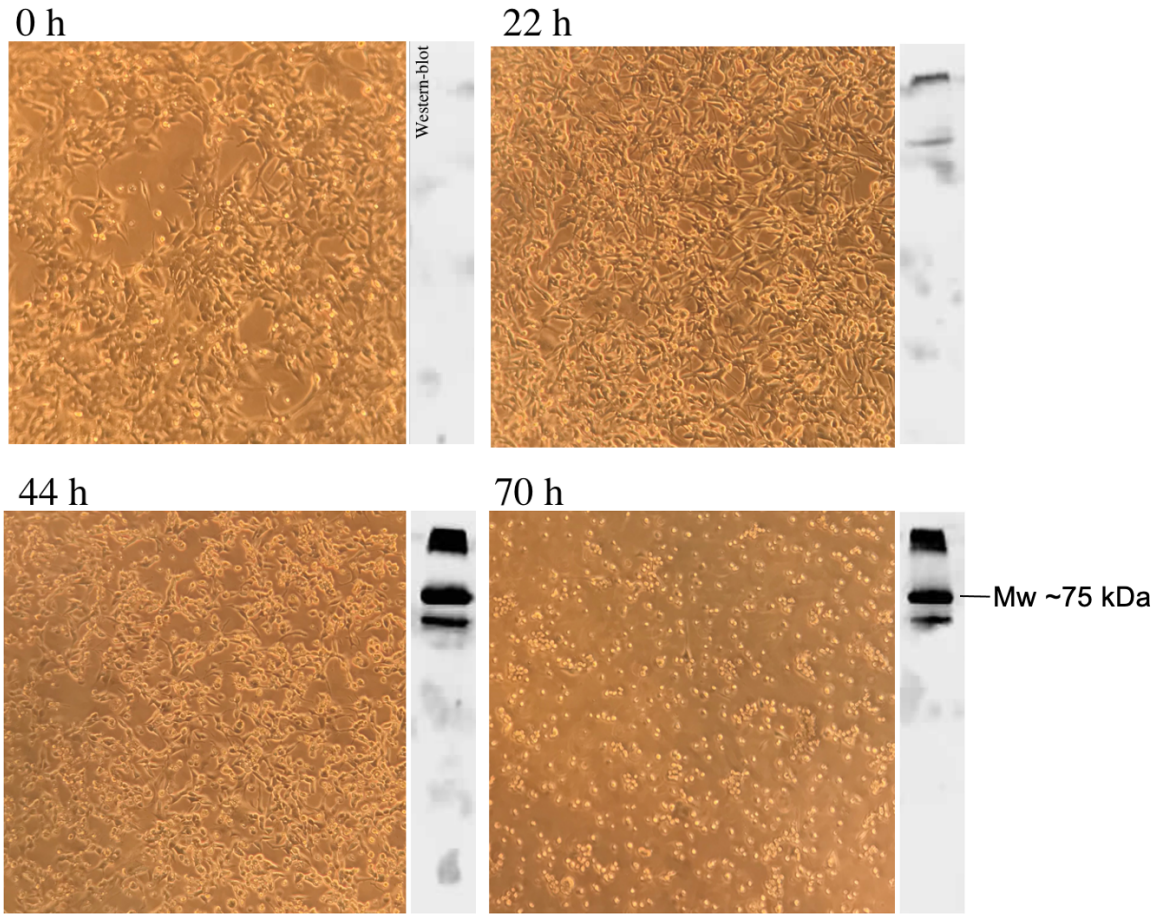

Figure 5.13: **Expression time-course of PTH1R$_{Avi}$ HEK 293S_tetR cells.** Stably-transfected PTH1R$_{Avi}$ HEK 293S_tetR cells were induced at different time points with tetracycline (2 µg/ml) and sodium butyrate (5 mM). Cells were photographed (phase-contrast, 10X objective) immediately before membrane harvest, resolved on SDS-PAGE and subsequent Western-blot performed using anti-HA primary antibody.

Agonist-induced cAMP accumulation of PTH1R$_{Avi}$

The signalling capability of PTH1R$_{Avi}$ upon PTH$_{1-34}$ (10^{-6} to 10^{-12} M) stimulation was assessed via cAMP assay for PTH1R$_{Avi}$ within vector pcDNA3.1(+) (COS-7 cells) and vector pACMV_tetO (HEK 293S_tetR cells). PTH$_{1-34}$ stimulated cAMP production pEC$_{50}$ value for transiently transfected COS-7 cells was 9.6 ± 0.1 (figure 5.14). This was not significantly different from the pEC$_{50}$ derived with induced HEK 293S_tetR cells of 9.3 ± 0.2 ($p = 0.5$). E$_{max}$ of PTH1R$_{Avi}$ was 95 ± 3 % and 93 ± 5 % for COS-7 and HEK 293S_tetR cells, respectively (data given are mean ± s.e.m, $n = 5$).

a

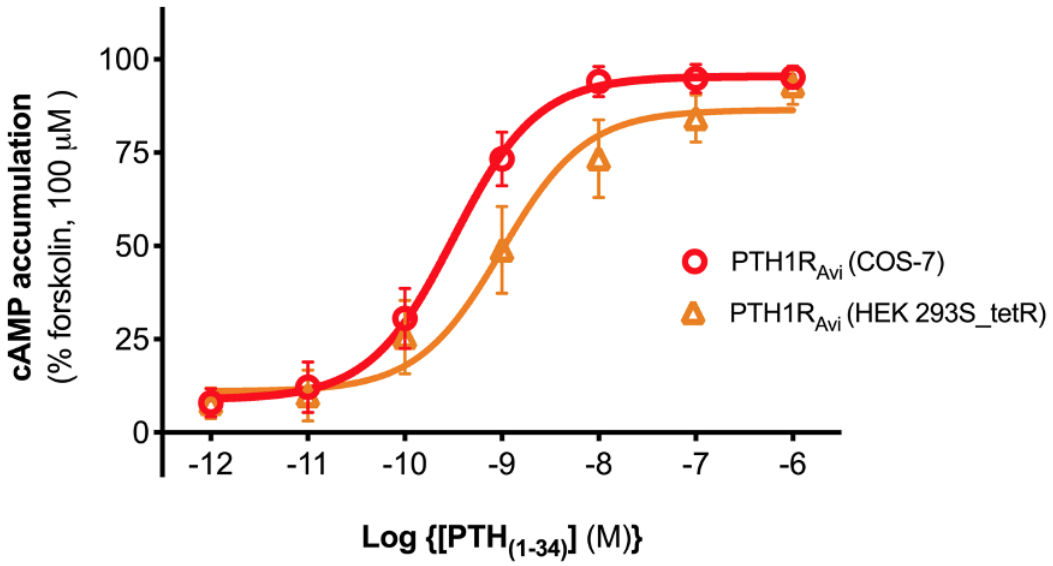

b

	cAMP accumulation	
Receptor context	**pEC_{50}**	**E_{max} (% forskolin, 100 µM)**
$PTH1R_{Avi}$ (COS-7)	9.6 ± 0.1	95 ± 3
$PTH1R_{Avi}$ (HEK 293S_tetR)	9.3 ± 0.2	93 ± 5

Figure 5.14: **cAMP dose-response curve for $PTH1R_{Avi}$ in COS-7 and HEK 293S_tetR cells. (a)** Graph **(b)** table. Agonist-induced cAMP accumulation was determined in a dose-response manner after stimulation with PTH_{1-34}, at stated concentrations. Data are mean ± s.e.m from 5 separate experiments, each performed in triplicate. Paired t-test determined no significant difference between derived pEC_{50} values ($p = 0.5$).

Purification of PTH1R$_{Avi}$ in pACMV_tetO

PTH1R$_{Avi}$ was SMALP-solubilised exactly as described in 2.2.13. HEK 293S-tetR cells stably expressing PTH1R$_{Avi}$ were induced and crude-membranes harvested 44–48 h later, via osmotic shock. Crude preparations were then SMALP-solubilised, and non-solubilised material was sedimented via ultracentrifugation (150,000 g, 1 h). Supernatant containing the SMALP-solubilised PTH1R$_{Avi}$ was collected, and incubated with Ni^{2+}-NTA resin, overnight at 4 °C. The resin-protein mix was placed into a gravity-flow column and washed with 20 mM imidazole. PTH1R$_{Avi}$ was eluted with 250 mM imidazole. Eluted fractions were pooled, concentrated and buffer-exchanged to get rid of imidazole, before silver stain and Western-blot performed. A clear, distinct band can be seen between 50–80 kDa on the silver stain gel in the eluted fraction (figure 5.15a). A discrete band can also be seen on the Western-blot, detected with anti-HA antibody between 50–80 kDa (figure 5.15b). The predicted molecular mass of PTH1R$_{Avi}$ is 72 kDa.

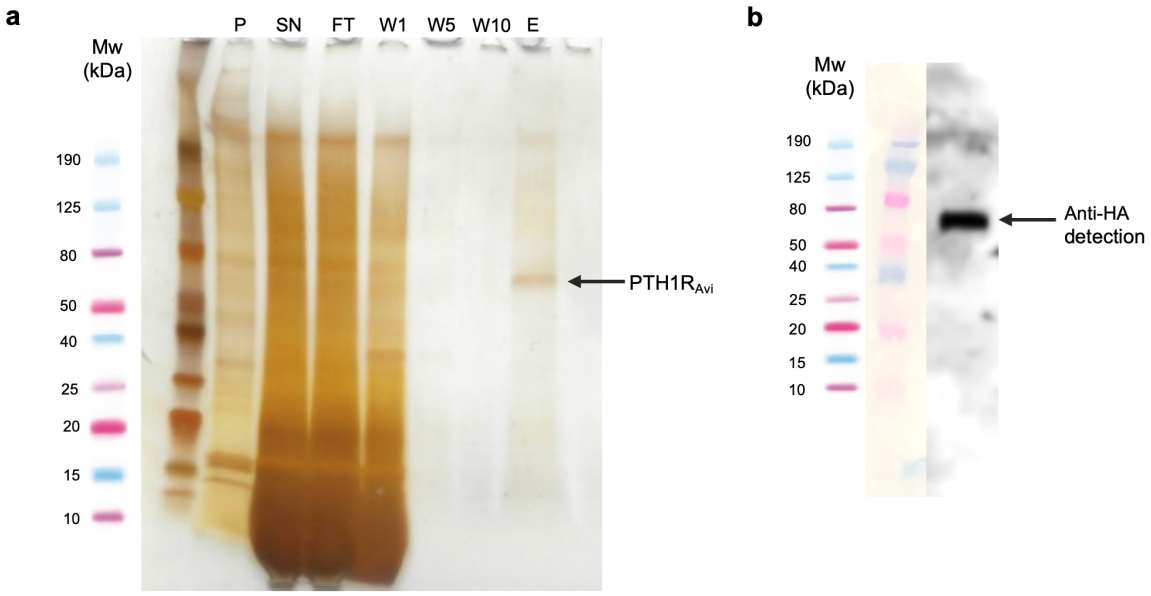

Figure 5.15: **Silver stain and Western-blot, demonstrating SMALP solubilisation and Ni^{2+}-NTA purification of PTH1R$_{Avi}$ from stably-transfected, induced HEK 293S_tetR cells. (a)** Molecular mass marker is shown in the first lane and with marker key on the left-hand side showing masses (kDa). Key: **P:** Insoluble pellet from SMALP solubilisation. **SN:** Supernatant fraction containing PTH1R$_{Avi}$-SMALPs. **FT:** Flow-through collected after overnight, batch bind onto Ni^{2+}-NTA resin. **W1–10:** Column washes (20 mM imidazole). **E:** Pooled and concentrated elution. Eluted fractions (250 mM imidazole) were collected and pooled and concentrated to ∼0.5 ml using a Vivaspin concentrator (MWCO 10 kDa) and buffer-exchanged to get rid of imidazole. **(b)** Pooled and concentrated elution fractions, detected via Western-blot, with anti-HA. Representative gels from three experiments.

5.2.4 Design and characterisation of novel PTH_{1-34}:BODIPY ligand

A novel PTH1R fluorescent ligand was designed and pharmacologically characterised with regards to cAMP accumulation. At present, no radiolabelled, or fluorescently labelled PTH1R ligand is commercially-available. Chapter 3 demonstrated the successful application of FCS to quantify ligand binding to a GPCR-SMALP, utilising a BODIPY 630/650 labelled ligand (Grime *et al.*, 2020). BODIPY 630/650 has also been successfully used in GPCR-based bioluminescence resonance energy transfer (BRET) and Förster resonance energy transfer (FRET) experiments (Stoddart *et al.*, 2015b). Consequently, it was deemed the label of choice for PTH1R fluorescent ligand design. In previous studies, Lys^{13} has been used successfully to conjugate a fluorescent moiety (Guo *et al.*, 2012). Furthermore, analysis of the PTH1R crystal structure (Ehrenmann *et al.*, 2018) revealed Lys^{13} of the bound PTH ligand projected into space and did not form any local interactions with peptide or receptor. Therefore, PTH_{1-34} was designed with a BODIPY 630/650 fluorophore conjugated to Lys^{13}, herein referred to as PTH_{1-34}:BODIPY, which was custom synthesised by Cambridge Research Biochemicals, UK (figure 5.16).

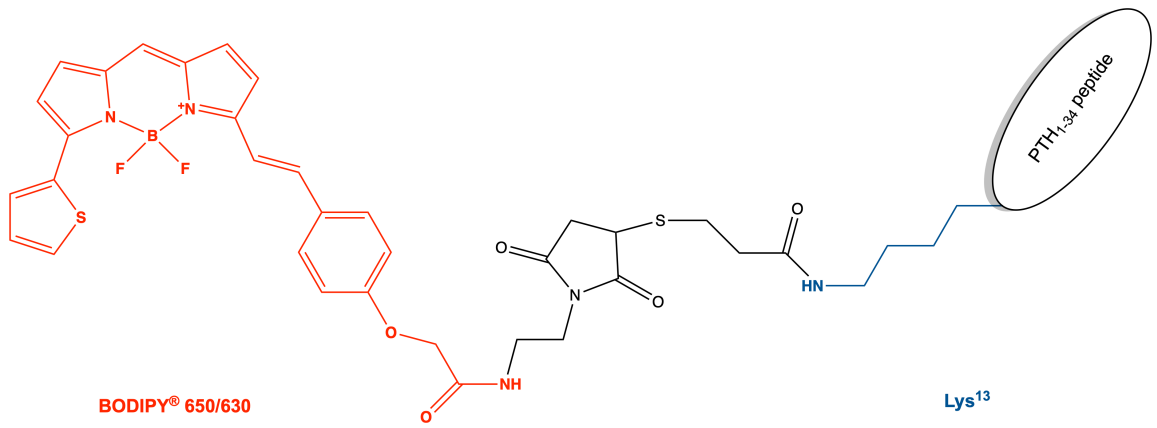

Figure 5.16: **Schematic of the PTH_{1-34}:BODIPY peptide.** PTH_{1-34} was conjugated to a BODIPY 630/650 moiety (red) on Lys^{13} (blue).

It was important to determine if the custom-synthesised PTH_{1-34}:BODIPY retained agonism. PTH_{1-34}:BODIPY was pharmacologically characterised via cAMP accumulation assay on live COS-7 cells expressing $PTH1R_{Avi}$. Stimulation with unlabelled PTH_{1-34} was carried out alongside to enable direct comparison of derived EC_{50} and E_{max} values. PTH_{1-34}:BODIPY retained WT-like signalling capability, demonstrating a pEC_{50} of 10.1 $\pm$ 0.4, compared with 10.1 $\pm$ 0.2 observed with PTH_{1-34} ($p = 0.8$; mean $\pm$ s.e.m, $n = 3$). E_{max} was unaffected by addition of the fluorescent moiety, with E_{max} values of 92 $\pm$ 4 % and 96 $\pm$ 3 % being achieved for PTH_{1-34} and PTH_{1-34}:BODIPY respectively, compared to forskolin response (100 μM) (figure 5.17).

a

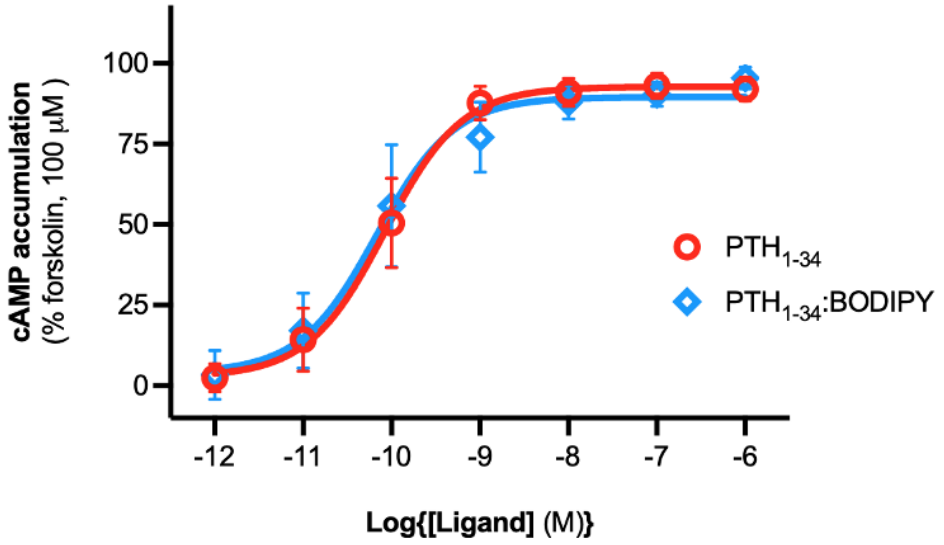

b

	cAMP accumulation	
Ligand	**pEC_{50}**	**E_{max} (% forskolin, 100 µM)**
PTH_{1-34}	10.1 ± 0.2	92 ± 4
PTH_{1-34}:BODIPY	10.1 ± 0.4	96 ± 3

Figure 5.17: **cAMP dose-response curve of PTH1R$_{Avi}$ in response to PTH$_{1-34}$ or PTH$_{1-34}$:BODIPY.** **(a)** Graph **(b)** table. cAMP accumulation was determined with stated ligand at indicated concentrations (10^{-12} to 10^{-6} M). Data are mean ± s.e.m from 3 separate experiments, each performed in triplicate.

5.3 Discussion

5.3.1 Cell line characterisation

Presented in this chapter is the generation and pharmacological characterisation of two novel receptor constructs and inducible cell lines for expressing OTR_{Avi} or $PTH1R_{Avi}$, plus subsequent SMALP-solubilisation and Ni^{2+}-NTA purification. Generation of stably-transfected, inducible cell lines was required, as one of the major technical hurdles to GPCR study is obtaining sufficient quantity of receptor for downstream analysis. Being integral membrane proteins, interaction with membrane lipids is an important factor for receptor functionality (Sengupta *et al.*, 2018). Specifically, membrane cholesterol is required for high-affinity ligand binding at the OTR. Depletion of cholesterol with a quenching agent (methyl-β-cyclodextrin) resulted in almost 100-fold loss of OT affinity in mammalian myometrial membranes which was reversible upon replenishment (Klein *et al.*, 1995). The cholesterol-dependence of the physiological function and thermal stability of OTR is well documented (Gimpl and Farenholz, 2000; Gimpl and Fahrenholz, 2002). More recently, the inaugural structure of the oxytocin receptor elucidated a distinct cholesterol binding site at an extrahelical groove amongst helices TM4 and TM5 (Waltenspuhl *et al.*, 2020). Cholesterol is known to modulate many GPCRs, therefore a mammalian cell membrane represents the ideal receptor environment (Pucadyil and Chattopadhyay, 2006). Successful extraction of a receptor, whilst maintaining the native lipid annulus would provide a valuable foundation for drug discovery platforms. Receptor constructs were designed with affinity tags to facilitate detection, immobilisation and purification. A deca-His tag and an HA-tag were incorporated onto the N-terminus of the OTR and PTH1R (figure 5.1). At the C-terminus, an Avidity Avitag^{TM} (GLNDIFEAQKIEWHE) was incorporated. The Avitag^{TM} allows an enzymatic conjugation of a single biotin on a unique 15-residue peptide tag which can be biotinylated by the *E. coli* enzyme, biotin ligase (BirA) (Beckett *et al.*, 1999). Whilst not exploited in this study, the Avitag^{TM} may assist in receptor immobilisation for future studies, particularly in anti-GPCR antibody

generation. It was important to establish that the addition of these tags did not impair native receptor folding, trafficking or function (Lichty *et al.*, 2011). For instance, fusion of a hexa-His tag to the human μ-opioid receptor N-terminus diminished cell-surface expression 10-fold, while it had no influence when fused to the C-terminus of the receptor (Massotte, 2003). Both OTR_{Avi} and $PTH1R_{Avi}$ were pharmacologically characterised in both a stable-cell context (HEK 293S_tetR), and in transiently transfected, HEK 293T cells. In particular, this allowed for direct comparison between OTR_{Avi} and a WT-OTR that was engineered previously (Hawtin *et al.*, 2001b). OTR_{Avi} expressed at 80 % of WT OTR (figure 5.2) which, while a small decrease, was acceptable. The lower OTR expression observed could be due to the addition of the deca-His and Avitag^{TM}, resulting in less efficient receptor trafficking. Alternatively, it may be possible that the close proximity of the deca-His and HA sequences resulted in reduced anti-HA antibody detection. With regards to $PTH1R_{Avi}$, interaction with receptor activity modifying proteins (RAMPs) was investigated. RAMPs are single-pass transmembrane proteins that form complexes with some family B GPCRs, and are known to alter receptor phenotype and trafficking. Three RAMPs have been identified (Hay *et al.*, 2006). PTH1R has been shown to be regulated by RAMP2 (Kadmiel *et al.*, 2017), however beyond this, the interaction is poorly understood. The interactions between CLR (a family B GPCR) and RAMPs are well characterised, with CLR alone expressing poorly at the cell surface (Poyner *et al.*, 2002). CLR was used as a positive control alongside $PTH1R_{Avi}$ in cell-surface expression ELISA in order to determine if RAMPs altered $PTH1R_{Avi}$ expression. It was shown that co-transfection with RAMPs 1–3 significantly increased CLR trafficking (figure 5.11). No significant changes in $PTH1R_{Avi}$ expression were observed with co-transfection with any of the RAMPs, therefore co-transfection was not continued. Overall, both OTR_{Avi} and $PTH1R_{Avi}$ demonstrated acceptable cell-surface expression. Both receptors internalised upon agonist challenge to levels consistent with WT, and those determined previously (Syme *et al.*, 2005). Previous work in the Wheatley laboratory established maximum OTR internalisation at 30 min (Bailey, 2017). Altogether these data establish the engineered

receptor constructs are pharmacologically WT-like with regards to receptor trafficking and internalisation. Ligand binding assays for OTR_{Avi} and inositol phosphates accumulation assay further supported the conclusion that OTR_{Avi} behaves like a WT-receptor (figure 5.5; figure 5.6). The same was observed for $PTH1R_{Avi}$ where derived EC_{50} values were consistent with literature (figure 5.14) (Bisello *et al.*, 2019).

Characterisation of the novel PTH_{1-34}:BODIPY ligand demonstrated that addition of the BODIPY 630/650 fluorophore to the peptide did not alter receptor signalling efficacy, achieving exactly WT-like responses when measured via cAMP accumulation assay (figure 5.17). This is a significant finding as the availability of a high-affinity fluorescent ligand provides a valuable tool to understanding receptor pharmacology. This novel labelled agonist could have many downstream applications, such as FRET/BRET, FCS, super-resolution microscopy, labelling of endogenous tissues and internalisation studies, all of which could be used to enhance knowledge of receptor pharmacology, or aid characterisation of drug-like molecule or antibodies which may allosterically modulate the receptor (Stoddart *et al.*, 2015a).

5.3.2 GPCR extraction and purification

This chapter also demonstrated the first-documented detergent-free solubilisation and purification of PTH1R and OTR, providing a foundation for future down-stream applications. At present, there are two solved PTH1R structures, both utilised insect cells for receptor expression and detergents for solubilisation (Ehrenmann *et al.*, 2018; Zhao *et al.*, 2019). Specifically, (Zhao *et al.*, 2019) reported on a discernable lipid belt in the detergent micelle, and hypothesised how structural lipids may have contributed to the stability of the complex in its active conformation. It would be of interest to examine the lipid-PTH1R interactions in a more native state, and probe how native mammalian lipids affect conformational stability, or G-protein coupling. Future work should aim to assess the functional state of the receptor in a SMALP. This could be achieved utilising the PTH_{1-34}:BODIPY ligand combined with FCS, as examined in chapter 3. Confirming the retention of high-affinity ligand binding post-solubilisation is a crucial step. The

application of drug discovery platforms, such as the use of phage-display to generate nanobodies, or immobilisation of a GPCR-SMALP on an SPR chip, requires correctly folded receptor. With regards to the OTR, pre-labelling studies demonstrated that the OTR SMALP-solubilised in a binding-competent state which is suggestive that SMALP-solubilised OTR retains native folding (figure 5.7). Future studies should aim to derive an affinity value for OT binding to the OTR post-solubilisation, however due to the peptide nature of the ligand, overcoming high-levels of non-specific binding to the SMALP remains a technical issue. The recent crystal structure of the human oxytocin receptor utilised small-molecule antagonist retosiban as ligand of choice to stabilise inactive receptor conformation, and affinities were derived using fluorescently labelled OT (HiLyte Fluor 488-Orn8 OT) (Waltenspuhl *et al.*, 2020). The use of fluorescent techniques may provide alternative avenues from radioligand experiments and should be explored with SMA and SMA-like polymers. It is worth noting that high-affinity agonist binding sites are not always preserved due to the absence of G-protein, which stabilises active receptor state. Whether GPCR-lipid particles extract with a G-protein bound remains to be clarified. Western-blot analysis of SMALP-solubilised, purified of OTR_{Avi} revealed discrete bands at multiple molecular masses at and above that of the predicted molecular mass of OTR_{Avi}, 49 kDa. Future work could define these bands, mass spectrometry could provide insight into whether these are oligomers of OTR, or if G-protein is present in the nanodisc. Despite the potential benefits of SMA and SMA-like polymers in protein biochemistry, there remain limitations. SMA may mask orthosteric and allosteric binding sites making purified receptors technically challenging to pharmacologically characterise. Analysis of the cryo-EM structure of the alternative complex III supercomplex revealed SMA contributed to a very thin layer of density, which followed the contours of the entire protein, with slightly more SMA-density present in a disc-like shape around the transmembrane regions (Sun *et al.*, 2018). The SMA-solubilised cryo-EM structure of the *A. baumannii* AdeB multidrug efflux pump revealed SMA only contributing to a belt surrounding the transmembrane region. Polymer-protein interactions are likely to have a degree of

protein-specificity to them. The location of orthosteric and allosteric binding sites may determine how a polymer-encapsulated GPCR can be pharmacologically assessed. In the OTR crystal structure, an allosteric divalent cation binding site was proposed at the top of TM1 and TM2 and was experimentally validated (Waltenspuhl *et al.*, 2020). Divalent cations have been shown to positively modulate OTRs, permitting high-affinity binding (Antoni and Chadio, 1989). The use of polymer-screens should be encouraged, whereby multiple amphipathic SMA-like polymers are characterised to determine the most appropriate extraction agent for the desired application. Future work should examine SMI- and DIBMA- solubilisation of PTH1R and OTR, in a systematic and similar manner to work presented in chapter 4.

5.3.3 Summary and future work

The generation of sufficient quantity and quality of GPCRs remains a technical hurdle for biophysical and structural analysis. The successful design, generation, pharmacological characterisation and proof-of-concept purification of OTR and PTH1R presented here provides essential tools required for future pharmacological study. It is feasible these cell lines generated could be used alongside techniques such as FCS to investigate the effects of allosteric modulators, such as therapeutic antibodies and nanobodies. Furthermore, they may provide a useful platform for structural studies which would aid drug discovery efforts.

Chapter 6: Ligand-specific interactions identified at the first extracellular loop of calcitonin receptor-like receptor

The work presented within this chapter was awarded a 'Flash Poster Prize' after presentation at The British Pharmacological Society's flagship annual meeting; Pharmacology 2019, Edinburgh, UK (appendix C)

6.1 Introduction

The previous chapters within this thesis focused on validating the use of, and exploring down-stream applications for polymer-based nano-encapsulation strategies. SMALPs and emerging second-generation polymers are useful tools for the study of membrane-bound proteins, and ultimately drug discovery. GPCRs demonstrate incredibly complex pharmacology, and thus require multiple approaches to study them. This final chapter explores a phenomenon observed within family B GPCRs; their interaction with receptor activity modifying proteins (RAMPs). Specifically, the functional importance of loop length of ECL1 of calcitonin receptor-like receptor (CLR) is investigated with respect to RAMP association and signalling efficacy via site-directed mutagenesis. Family B GPCRs respond to peptide hormones and regulate vital physiological responses. They are tractable drug-targets, with a range of therapeutic peptides and peptide-mimetics being used to treat diseases such as osteoporosis, diabetes mellitus, migraine and obesity (Karageorgos *et al.*, 2018). Understanding their structure and function is therefore essential for the development of novel therapeutics. Family B GPCR pharmacology is made more complex by their association with one of three RAMPs. RAMPs are single-pass transmembrane proteins that form functional heterodimers with GPCRs, capable of significantly altering receptor phenotype. More recently, evidence of RAMPs interacting with a broader subset of GPCRs has emerged however, they are best characterised for their interaction

with calcitonin receptor (CTR) and CLR (Conner *et al.*, 2004). CLR interacts with the different RAMPs to yield distinct receptor phenotypes. When associating with RAMP1 it acts as the calcitonin gene-related peptide (CGRP) receptor (CGRPR). CGRP is a neuropeptide that has roles in metabolism, blood-pressure regulation, inflammation and auditory-nerve development (Wimalawansa, 1996). CGRPR is implicated in migraine and several clinically-approved antibody-based therapeutics exist to treat the pathology (Stoker and Baker, 2018; Hussar and Moyer, 2019; Friedman and Cohen, 2020). When CLR associates with RAMP 2 or 3, it forms the adrenomedullin receptor 1 (AM_1R) and 2 (AM_2R), respectively (Poyner *et al.*, 2002). Adrenomedullin (AM) is a potent vasodilatory hormone, essential for angiogenesis, as well as vascular and lymphatic development. More recently, AM and its receptors have been implicated in fertility. Inter-uterine delivery of AM prior to blastocyst transfer resulted in improved embryo implantation rate in AM deficient mice models (Kadmiel *et al.*, 2017). A recent human study uncovered a recessive in-frame deletion of Val^{205} of CLR resulting in nonimmune hydrops fetalis (NIHF), where homozygosity results in foetal loss due to NIHF, and heterozygosity results in subfertility (Mackie *et al.*, 2018). Val^{205} resides within ECL1 of CLR. It remains unclear if the phenotype observed is specifically due to the loss of Val^{205} or from the shortening of ECL1. ECLs are known to contribute to receptor structure and function. Indeed, loss or mutation of residues within the ECLs is associated with altered ligand selectivity, varied binding and signalling profiles, and is implicated in disease. The extracellular loop regions of the parathyroid hormone (PTH) 2 receptor (family B) determine signalling selectivity for PTH and PTH-related peptide (Bergwitz *et al.*, 1997). Furthermore, $A^{204}E$ mutation (ECL2) of the ghrelin receptor (family A) results in loss of constitutive activity causing growth failure in humans (Pantel *et al.*, 2006). In the vasopressin receptor (family A), Arg^{116} and Arg^{125} (ECL1) are required for agonist binding, where loss of a positive charge at either residue results in ablated agonist binding and subsequent loss of signalling activity (Hawtin *et al.*, 2006). ECL1 of family B GPCRs is the most varied in length, compared with other family B ECLs (figure 6.1). ECL1 is particularly elongated in the parathyroid

receptors (∼26 residues in humans). In human CLR, ECL1 is ∼10 residues in length, making it one of the shortest within family B GPCRs, alongside corticotropin-releasing factor receptors (CLR receptor 'snake plot'; appendix F). ECL1 demonstrates almost no homology within family B receptors making it difficult to draw transferable insights from one receptor to another. Despite lack of homology, there is marked conservation within ECL1 of CLR across species (figure 6.2). Asn^{200}, Asn^{201}, Gln^{202}, Leu^{204} and Val^{205} all demonstrate >99 % conservation.

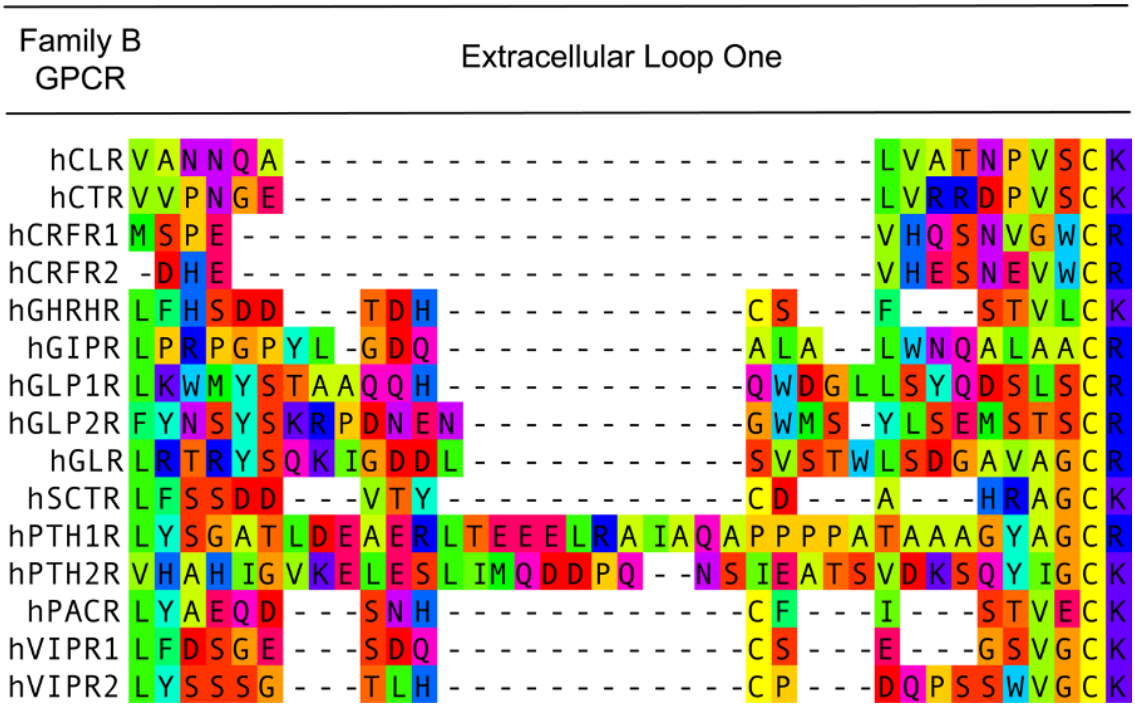

Figure 6.1: **Alignment of ECL1 within family B GPCRs.** Human sequences of the receptors were aligned with ClustalO version 1.2.2 (http://www.clustal.org/omega/). Residues are colour coded using the 'Taylor' system (Taylor, 1997).

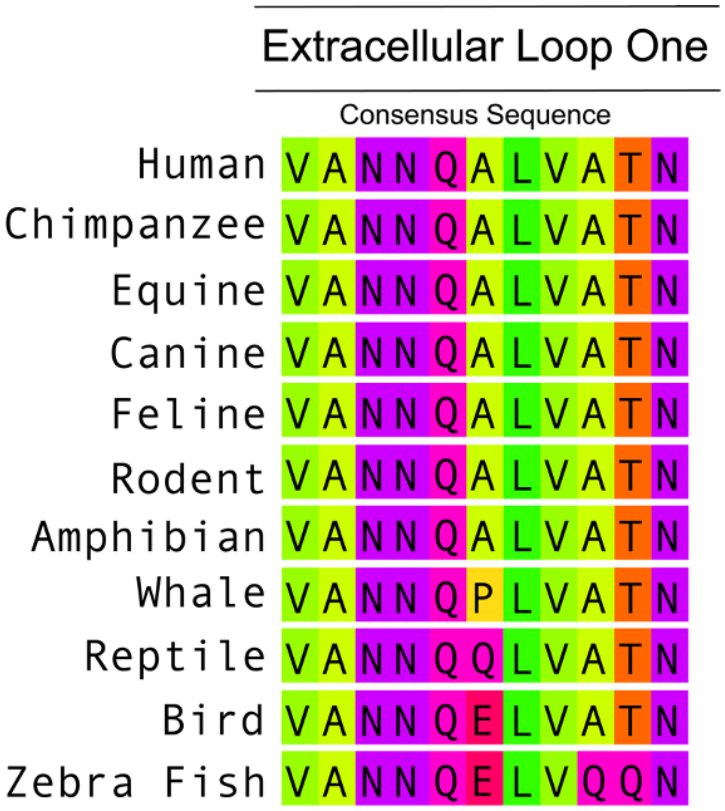

Figure 6.2: **Consensus alignment of ECL1 in calcitonin receptor-like receptors (CLRs) across species.** A total of 247 species were analysed and consensus sequences generated. Aligned with ClustalO version 1.2.2 (http://www.clustal.org/omega/). Residues are colour coded using the 'Taylor' system (Taylor, 1997).

Of the 90 unique GPCR structures that have been solved, 11 of these are full-length, high-resolution structures of family B GPCRs, which has provided valuable mechanistic insight into this therapeutically important class of receptors (correct as of February 2021). The 3.3 Å cryo-EM structure of the calcitonin receptor (CTR) elucidated how the peptide agonist engaged the receptor by binding to an extended hydrophobic pocket, facilitated by a large outward movement of the extracellular ends of transmembrane TM6 and TM7 (Liang *et al.*, 2017). Alongside this, mutagenesis identified that the stalk of TM1 and ECL1 are involved in bias between cAMP versus pERK signalling (Dal Maso *et al.*, 2019). The 3.3 Å cryo-EM structure of an active, Gα_s-coupled, CGRPR confirmed that RAMP1 stabilises ECL2 (Liang *et al.*, 2018). Finally, in March 2020, full-length structures of AM_1R and AM_2R were solved, providing yet more insight into GPCR-RAMP interaction (Liang *et al.*, 2020). The orientations of the ECD (relative to the receptor core) between CGRPR, AM_1R and AM_2R were identified to be receptor-specific, highlighting further, the importance of ECDs. Molecular dynamic simulations also suggested that ECD dynamics could influence G-protein interactions. These cryo-EM structures provide great understanding into the allosteric modulation of GPCRs by RAMPs. With the clinical significance of residues such as Val^{205} emerging, elucidating the roles of other residues within ECL1 may provide novel insights into receptor structure and function. This study particularly aimed to identify if deletion of other residues within ECL1 resulted in perturbation of receptor function, or whether this is a feature unique to Val^{205}. At CGRPR (CLR + RAMP1), previous alanine scanning showed relatively few effects on receptor pharmacology, with Ala^{203}Leu and Ala^{206}Leu found to influence the ability of CGRP to stimulate cAMP, with a minor increase in the pEC_{50} (Barwell *et al.*, 2011). Investigated in this chapter was the effect of deletion mutations along ECL1. Subsequent, single-, double- and triple- residue deletions were carried out and mutants were characterised with respect to receptor-RAMP trafficking and agonist activity via cAMP signalling.

6.2 Results

6.2.1 Design of mutant receptor constructs

A WT CLR construct which contained an N-terminal HA-tag was used in this study (construct sequence; appendix E). Each residue within ECL1 of CLR was sequentially deleted from Asn^{200} to Asn^{208} to probe the role of individual amino acids (figure 6.3). A double deletion of both Asn^{200} and Asn^{201} was included, as well as an insertion of Asn between residues 200 and 201, to probe the consequence of loop shortening and lengthening, respectively (table 6.1). Furthermore, two triple-deletion constructs where engineered to generate a CLR construct with an ECL1 shorter than any found within family B GPCRs (table 6.1). Mutagenic primers were designed for use with QuikChange™ site-directed mutagenesis; sequences were confirmed by Sanger Sequencing Services in sense, and antisense direction (appendix D) (methods described in 2.2.1).

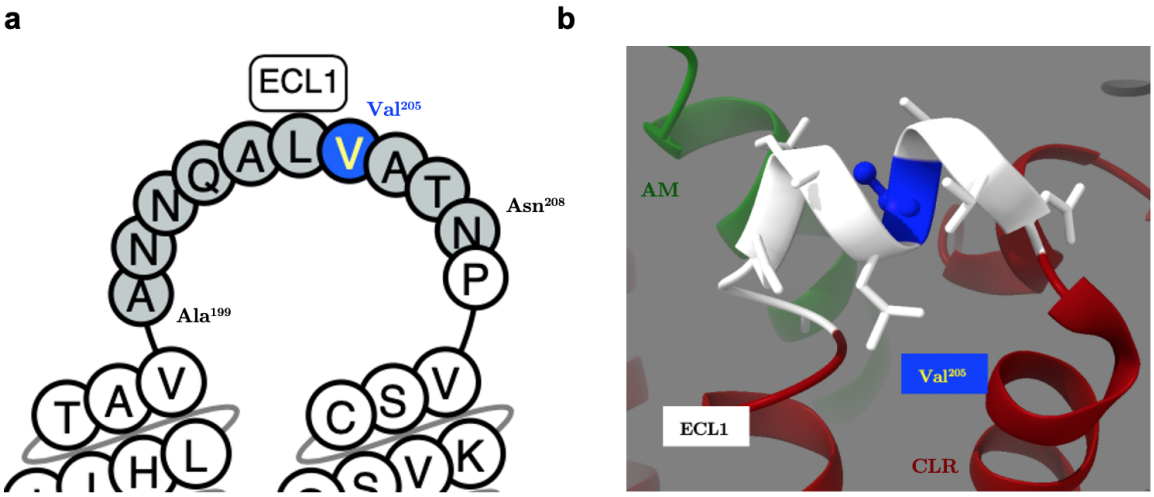

Figure 6.3: **Extracellular loop one (ECL1) of calcitonin receptor-like receptor (CLR). (a)** Schematic of ECL1 highlighting individual residues mutated in this study (grey), as well as clinically identified Val^{205} (blue). **(b)** Extracellular loop one (white) of adrenomedullin 1 receptor (dark-red) bound to adrenomedullin (green), with Val^{205} shown in blue. Image generated in UCSF ChimeraX v0.091 (Goddard *et al.*, 2018). Adapted from PDB file 6UUN (Liang *et al.*, 2020).

Table 6.1: **Oligonucleotide sequences utilised to generate mutant calcitonin receptor-like receptor (CLR) constructs.** Bases shown in dark red denote the region either side of deleted codon(s). Bases shown underlined in blue denote codon insertion. *(s)* sense; *(as)* antisense.

Receptor mutation		Primer sequence
[$N^{201}\Delta$]CLR	*(s)*	5'– CT-GCA-GTG-GCC-AAC-CAG-GCC-TTA-GTA-GC –3'
	(as)	5'– GT-GGC-TAC-TAA-GGC-CTG-GTT-GGC-CAC-TG –3'
[$Q^{202}\Delta$]CLR	*(s)*	5'– GCA-GTG-GCC-AAC-AAC-GCC-TTA-GTA-GCC-ACA –3'
	(as)	5'– TGT-GGC-TAC-TAA-GGC-GTT-GTT-GGC-CAC-TGC –3'
[$A^{203}\Delta$]CLR	*(s)*	5'– CA-GTG-GCC-AAC-AAC-CAG-TTA-GTA-GCC-ACA-AAT-CC –3'
	(as)	5'– C-AGG-ATT-TGT-GGC-TAC-TAA-CTG-GTT-GTT-GGC-CAC –3'
[$L^{204}\Delta$]CLR	*(s)*	5'– GCC-AAC-AAC-CAG-GCC-GTA-GCC-ACA-AAT-CCT –3'
	(as)	5'– AGG-ATT-TGT-GGC-TAC-GGC-CTG-GTT-GTT-GGC –3'
[$V^{205}\Delta$]CLR	*(s)*	5'– G-GCC-AAC-AAC-CAG-GCC-TTA-GCC-ACA-AAT-CC –3'
	(as)	5'– GG-ATT-TGT-GGC-TAA-GGC-CTG-GTT-GTT-GGC-C –3'
[$A^{206}\Delta$]CLR	*(s)*	5'– GCC-AAC-AAC-CAG-GCC-TTA-GTA-ACA-AAT-CCT-GTT-AGT-T –3'
	(as)	5'– A-ACT-AAC-AGG-ATT-TGT-TAC-TAA-GGC-CTG-GTT-GTT-GGC –3'
[$T^{207}\Delta$]CLR	*(s)*	5'– AC-CAG-GCC-TTA-GTA-GCC-AAT-CCT-GTT-AGT-TGC-AA –3'
	(as)	5'– TT-GCA-ACT-AAC-AGG-ATT-GGC-TAC-TAA-GGC-CTG-GT –3'

Receptor mutation		Primer sequence
[$N^{208}\Delta$]CLR	*(s)*	5'– C-CAG-GCC-TTA-GTA-GCC-ACA-CCT-GTT-AGT-TGC-A –3'
	(as)	5'– T-GCA-ACT-AAC-AGG-TGT-GGC-TAC-TAA-GGC-CTG-G –3'
[$N^{200,201}\Delta$]CLR	*(s)*	5'– TC-ACT-GCA-GTG-GCC-CAG-GCC-TTA-GTA-GC –3'
	(as)	5'– GC-TAC-TAA-GGC-CTG-GGC-CAC-TGC-AGT-GA –3'
[$A^{199}\Delta$,$N^{200,201}\Delta$]CLR	*(s)*	5'– CC-TTA-GTA-GCC-ACA-CCT-GTT-AG –3'
	(as)	5'- CT-AAC-AGG-TGT-GGC-TAC-TAA-GG -3'
[$N^{200,201,208}\Delta$]CLR	*(s)*	5'- CTC-ACT-GCA-GTG-CAG-GCC-TTA-GTA-G -3'
	(as)	5'- C-TAC-TAA-GGC-CTG-CAC-TGC-AGT-GAG -3'
[N^{200}NN]CLR	*(s)*	5'– C-ACT-GCA-GTG-GCC-AAC-AAT-AAC-CAG-GCC-TTA-GTA-G –3'
	(as)	5'- C-TAC-TAA-GGC-CTG-GTT-ATT-GTT-GGC-CAC-TGC-AGT-G –3'

6.2.2 AM_1R cell-surface expression

Cell-surface expression levels for WT AM_1R (CLR + RAMP2) and each of the constructs was determined via ELISA, exploiting the HA-tag on the N-terminus of the receptor (the RAMP2 construct had no affinity tags). WT CLR alone (without RAMP2) demonstrated poor cell-surface expression, achieving 34 ± 3 % relative to WT AM_1R (p = 0.0005; mean ± s.e.m, n = 3), consistent with published values (Hay *et al.*, 2006). All mutant constructs were assayed following co-transfection with RAMP2, to form AM_1R. Results showed that all constructs expressed at WT-like levels, varying between 83–129 % relative to WT AM_1R (figure 6.4; table 6.2). The clinically identified [$V^{205}\Delta$]AM_1R demonstrated cell-surface expression at 103 ± 9 % that of WT (mean ± s.e.m, n = 3) (figure 6.4; table 6.2).

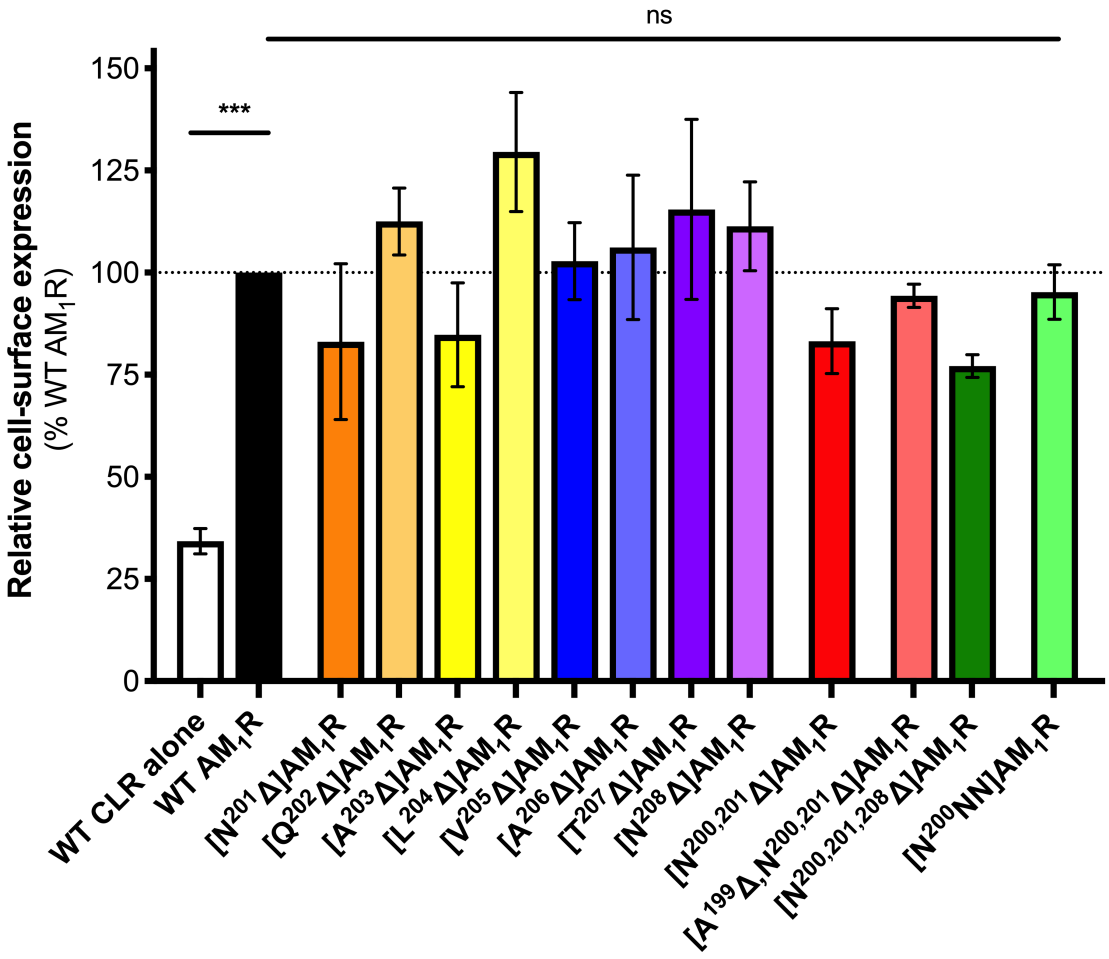

Figure 6.4: **Cell-surface expression of CLR + RAMP2 (AM_1R) ECL1 deletion scan mutants.** Cell-surface expression was assayed utilising anti-HA primary antibody. HA-tagged receptors were co-transfected (1:1) with untagged-RAMP2 in COS-7 cells. Data are mean ± s.e.m from three independent experiments, performed in triplicate, values relative to WT AM_1R. Significance determined by paired ANOVA with Dunnett's multiple comparisons (ns, not significant; ***, $p = 0.0005$).

Table 6.2: **Cell-surface expression of CLR + RAMP2 (AM_1R) ECL1 deletion scan.** WT sequence and region of deleted or inserted codons is shown for clarity. Cell-surface expression is relative to WT AM_1R. Data are mean ± s.e.m from three independent experiments, performed in triplicate.

Receptor construct	**Sequence** (5'–3')	**Relative expression** (% ± s.e.m)
WT CLR		34 ± 3
WT AM_1R	GCC-AAC-AAC-CAG-GCC-TTA-GTA-GCC-ACA-AAT-CCT	**100 ± 0**
[$N^{201}\Delta$]AM_1R	------ΔΔΔ----------	83 ± 19
[$Q^{202}\Delta$]AM_1R	---------ΔΔΔ----------	112 ± 8
[$A^{203}\Delta$]AM_1R	----------ΔΔΔ----------	85 ± 12
[$L^{204}\Delta$]AM_1R	----------ΔΔΔ----------	129 ± 14
[$V^{205}\Delta$]AM_1R	----------ΔΔΔ----------	103 ± 9
[$A^{206}\Delta$]AM_1R	----------ΔΔΔ---------	106 ± 17
[$T^{207}\Delta$]AM_1R	----------ΔΔΔ------	115 ± 21
[$N^{208}\Delta$]AM_1R	----------ΔΔΔ---	111 ± 11
[$N^{200,201}\Delta$]AM_1R	---ΔΔΔΔΔ----------	83 ± 8
[$A^{199}\Delta$,$N^{200,201}\Delta$]AM_1R	ΔΔΔΔΔΔΔΔΔ----------	94 ± 3
[$N^{200,201,208}\Delta$]AM_1R	---ΔΔΔΔΔ----------ΔΔΔ---	77 ± 3
[N^{200}NN]AM_1R	---AAT----------	95 ± 7

6.2.3 RAMP2 cell-surface trafficking at WT AM_1R and $[V^{205}\Delta]AM_1R$

Following the deletion scan, cell-surface expression of the clinically identified $V^{205}\Delta$-RAMP2 heterodimer was probed in more detail. Both receptor and RAMP2 trafficking were assessed independently via ELISA in COS-7 and HEK 293T cell lines. Receptor trafficking was assessed exploiting the HA-tag on the N-terminus of the receptor. RAMP2 trafficking was assessed exploiting a FLAG-tag at the RAMP2 N-terminus (RAMP sequence; appendix E).

In both cell lines, $[V^{205}\Delta]AM_1R$ expression was enhanced by co-transfection with RAMP2, to a WT-like level (figure 6.5). In COS-7 cells, $[V^{205}\Delta]AM_1R$ expression went from (relative to WT) 57 ± 10 % to 135 ± 25 % after RAMP2 co-transfection (figure 6.5a). In HEK 293T cells, $[V^{205}\Delta]AM_1R$ expression went from a relative 36 ± 5 % to 147 ± 28 % after RAMP2 co-transfection (figure 6.5c) (data are mean ± s.e.m, $n = 3$).

RAMP2 trafficking appeared unaffected by deletion of Val^{205}, retaining WT properties in both COS-7 and HEK 293T cell lines (figure 6.5). In COS-7 cells, RAMP2 expressed at 107 ± 4 % when co-transfected with $[V^{205}\Delta]CLR$, relative to RAMP2 expression with WT CLR (figure 6.5b). In HEK 293T cells, RAMP2 expressed at 97 ± 14 % when co-transfected with $[V^{205}\Delta]CLR$, relative to RAMP2 expression with WT CLR (figure 6.5d) (data are mean ± s.e.m, $n = 3$).

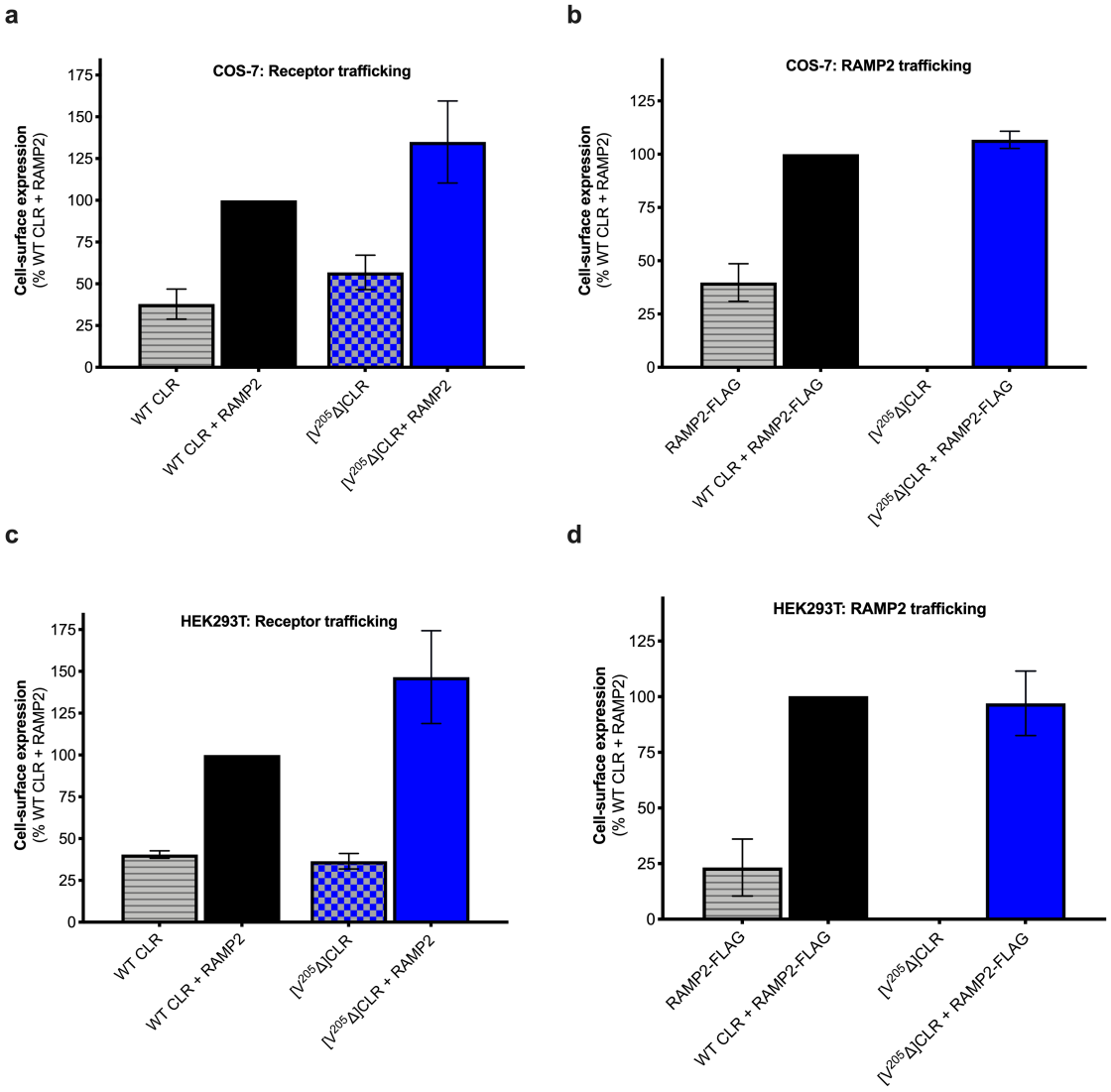

Figure 6.5: **Probing the trafficking of the clinically apparent $[V^{205}\Delta]AM_1R$.** Receptor cell-surface expression was monitored in **(a)** COS-7 cells and **(c)** HEK 293T cells. HA-tagged receptors were co-transfected (1:1) with untagged-RAMP2. RAMP2 cell-surface expression was monitored in **(b)** COS-7 cells and **(d)** HEK 293T cells. FLAG-tagged RAMP2 was co-transfected (1:1) with receptor constructs. Data are mean ± s.e.m from three separate experiments, performed in triplicate.

6.2.4 Agonist-induced cAMP production

Having established that all receptor constructs retain WT-like cell-surface expression (when co-transfected with RAMP2), agonist-induced cAMP production was assessed for WT and mutant constructs for AM_1R (CLR + RAMP2), AM_2R (CLR + RAMP3) and CGRPR (CLR + RAMP1).

The effect of $V^{205}\Delta$ on agonist-induced cAMP production

COS-7 cells were transfected with either WT CLR or [$V^{205}\Delta$]CLR, along with the appropriate RAMP to generate either CGRPR, AM_1R or AM_2R. Cells were then challenged with either CGRP (for CGRPR), or AM_{13-52} (for CGRPR, AM_1R and AM_2R) and cAMP response was measured. AM_{13-52} is a high-affinity agonist at adrenomedullin receptors and routinely employed for the study of CLR (Garelja *et al.*, 2020).

At [$V^{205}\Delta$]CGRPR, a significant 200-fold loss of CGRP potency was observed from 9.9 ± 0.3 (WT) to 7.9 ± 0.4 ($p = 0.002$) (figure 6.6a; table 6.3). A 3-fold loss of AM_{13-52} potency was seen at [$V^{205}\Delta$]CGRPR, from 8.1 ± 0.2 (WT) to 7.7 ± 0.2 ($p = 0.04$) (figure 6.6b; table 6.3). At the clinically identified [$V^{205}\Delta$]AM_1R, a 13-fold loss of AM_{13-52} potency was observed, from 9.6 ± 0.3 (WT) to 8.4 ± 0.4 (not significant, $p = 0.06$) (figure 6.6c; table 6.3). At [$V^{205}\Delta$]AM_2R, a 5-fold reduction in potency seen which did not reach significance (9.7 ± 0.4 at [$V^{205}\Delta$]AM_2R, compared with 10.4 ± 0.1 at WT, $p = 0.4$) (figure 6.6d; table 6.3) (data are mean $\pm$ s.e.m, $n = 3$). At all receptors, E_{max} responses appeared unaffected by deletion of V^{205} (table 6.3).

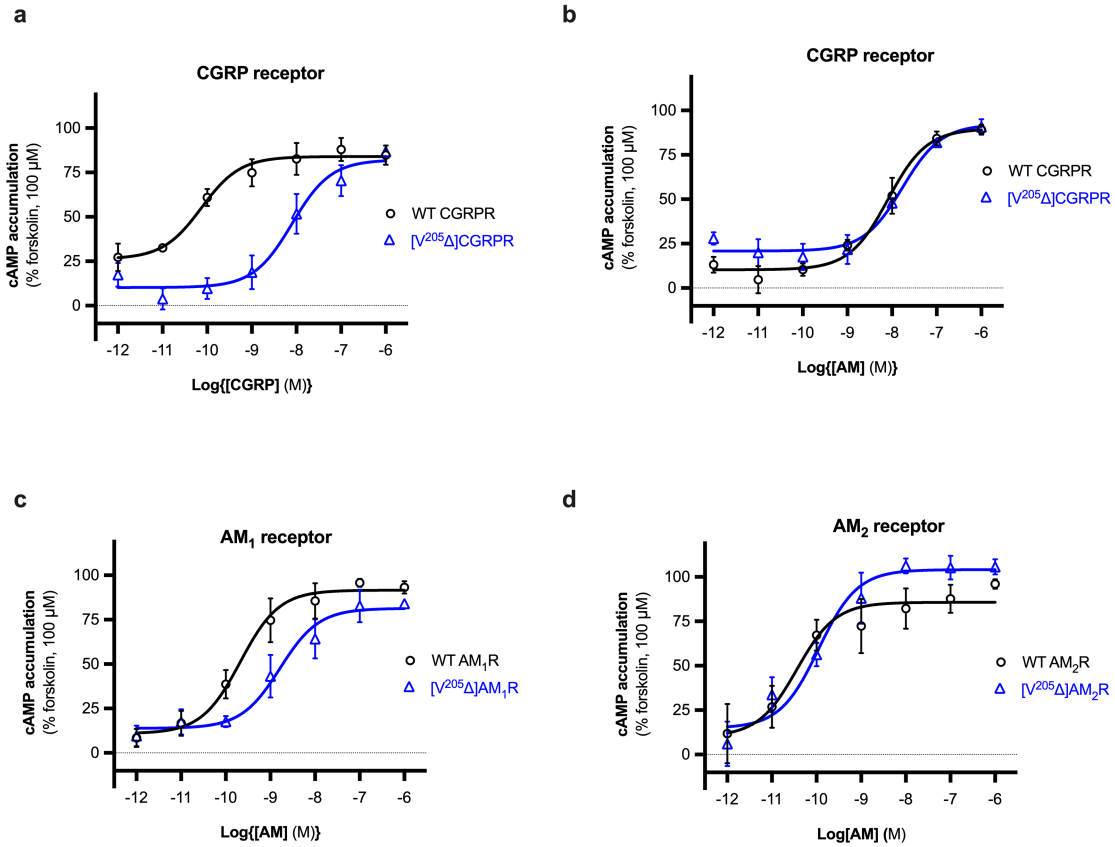

Figure 6.6: **Effect of deletion of CLR residue V^{205} on agonist-induced cAMP production.** Agonist-induced dose-response curves at **(a)**, **(b)** CGRPR; **(c)** AM_1R; or **(d)** AM_2R. Data are mean ± s.e.m from three separate experiments, each performed in triplicate.

Table 6.3: **Effect of deletion of CLR residue Val^{205} on agonist-induced cAMP production.** Agonist-induced cAMP accumulation at stated ligand/receptor constructs. Values are mean ± s.e.m for three independent experiments, performed in triplicate. Significance determined by paired t-test (*, $p = 0.04$; **, $p = 0.002$).

		cAMP accumulation	
Receptor	**Ligand**	**pEC$_{50}$**	**E$_{max}$** (% forskolin, 100 μM)
WT CGRPR	CGRP	9.9 ± 0.3	85 ± 5
[V^{205}Δ]CGRPR	CGRP	7.9 ± 0.4 **	87 ± 2
WT CGRPR	AM$_{13-52}$	8.1 ± 0.2	89 ± 3
[V^{205}Δ]CGRPR	AM$_{13-52}$	7.7 ± 0.2 *	91 ± 4
WT AM$_1$R	AM$_{13-52}$	9.6 ± 0.3	92 ± 2
[V^{205}Δ]AM$_1$R	AM$_{13-52}$	8.4 ± 0.5	88 ± 4
WT AM$_2$R	AM$_{13-52}$	10.4 ± 0.1	96 ± 3
[V^{205}Δ]AM$_2$R	AM$_{13-52}$	9.7 ± 0.4	106 ± 4

Effect of deletion mutations at AM_1R

Following on from investigating the cAMP-response in the clinically apparent V^{205} deletion, the other mutant constructs were assessed via cAMP assay. COS-7 cells were co-transfected with the appropriate CLR construct and RAMP2, to form the AM_1R. Cells were then stimulated with AM_{13-52} and cAMP response measured in a dose-dependent manner.

In response to AM_{13-52}, WT AM_1R generated a pEC_{50} of 9.6 ± 0.3, consistent with literature (Hay *et al.*, 2019). The following mutations; $N^{201}\Delta$, $Q^{202}\Delta$, $A^{203}\Delta$, $L^{204}\Delta$, $A^{206}\Delta$ and $T^{207}\Delta$ all showed significantly reduced potencies for AM_{13-52} ($p = <0.033$; mean ± s.e.m, $n \geq 3$) (figure 6.7; table 6.4). Both $L^{204}\Delta$ and $A^{206}\Delta$ also demonstrated a significant reduction in maximum response (68 ± 10 % and 65 ± 12 %, respectively), as well as a ∼20-fold loss in potency. All other constructs demonstrated WT-like potency and maximum response (table 6.4).

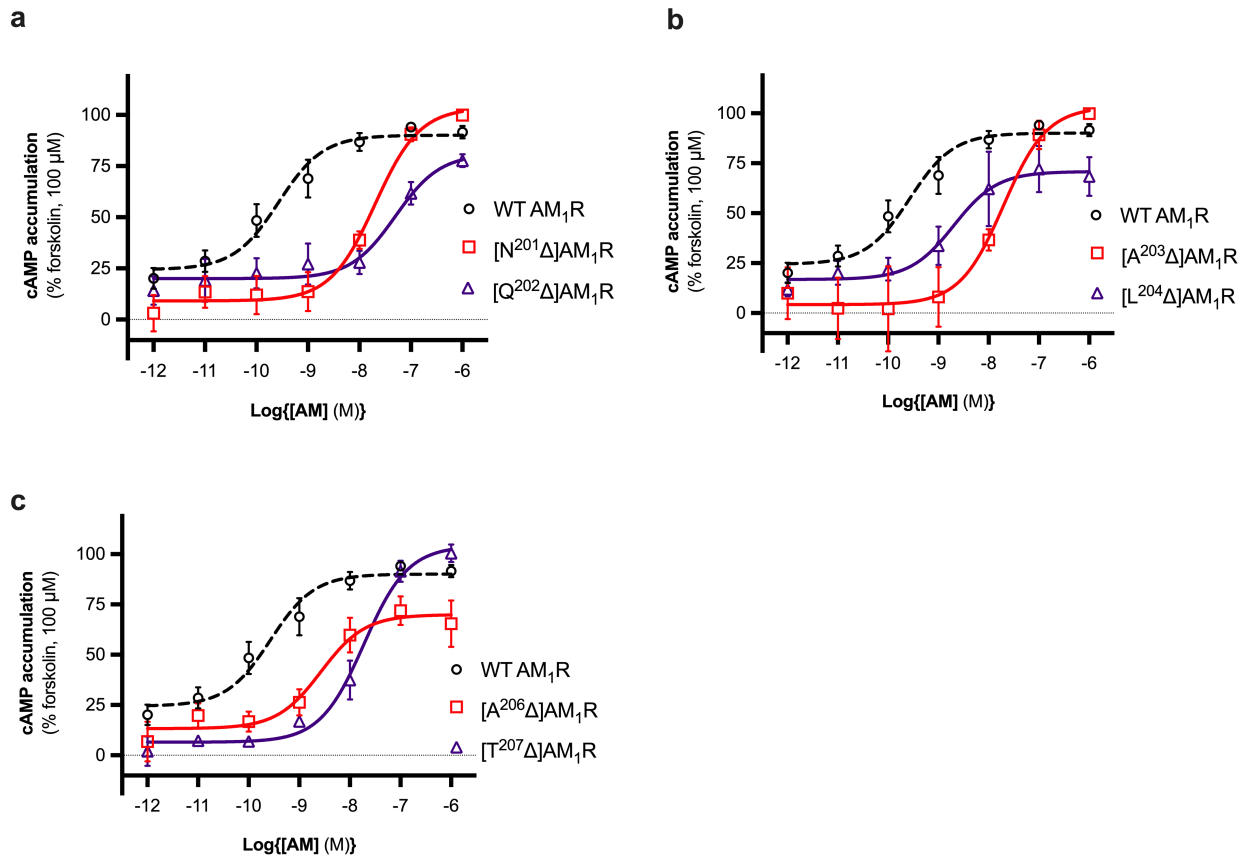

Figure 6.7: **Adrenomedullin$_{13-52}$ stimulated dose-response curves for AM$_1$R transfected COS-7 cells.** Constructs which demonstrated significant losses in potency are shown. **(a)** [N$^{201}\Delta$]AM$_1$R and [Q$^{202}\Delta$]AM$_1$R; **(b)** [A$^{203}\Delta$]AM$_1$R and [L$^{204}\Delta$]AM$_1$R; **(c)** [A$^{206}\Delta$]AM$_1$R and [T$^{207}\Delta$]AM$_1$R. WT receptor; open circles. Mutant receptors; open squares or open triangles. Data are mean ± s.e.m for at least three independent experiments.

Table 6.4: Ability of mutant AM_1Rs to stimulate cAMP production. Values are mean ± s.e.m for given number of experiments. Significance determined by ANOVA with Dunnett's multiple comparisons to WT AM_1R (*, p <0.033; **, p <0.002; ***, p <0.0002).

Receptor	Ligand	*n*	pEC_{50}	E_{max}
WT AM_1R	AM_{13-52}	9	9.6 ± 0.3	92 ± 3
[$N^{201}\Delta$]AM_1R	AM_{13-52}	3	7.7 ± 0.04 **	100 ± 2
[$Q^{202}\Delta$]AM_1R	AM_{13-52}	3	7.3 ± 0.1 ***	78 ± 3
[$A^{203}\Delta$]AM_1R	AM_{13-52}	3	7.7 ± 0.1 **	100 ± 1
[$L^{204}\Delta$]AM_1R	AM_{13-52}	4	8.3 ± 0.4 *	68 ± 10 *
[$V^{205}\Delta$]AM_1R	AM_{13-52}	3	8.4 ± 0.5	88 ± 4
[$A^{206}\Delta$]AM_1R	AM_{13-52}	5	8.2 ± 0.1 *	65 ± 12 *
[$T^{207}\Delta$]AM_1R	AM_{13-52}	3	7.7 ± 0.1 **	100 ± 4
[$N^{208}\Delta$]AM_1R	AM_{13-52}	4	8.8 ± 0.3	98 ± 2
[$N^{200,201}\Delta$]AM_1R	AM_{13-52}	3	9.5 ± 0.05	96 ± 3
[$A^{199}\Delta$,$N^{200,201}\Delta$]AM_1R	AM_{13-52}	3	9.0 ± 0.02	88 ± 6
[$N^{200,201,208}\Delta$]AM_1R	AM_{13-52}	3	9.3 ± 0.4	80 ± 8
[N^{200}NN]AM_1R	AM_{13-52}	3	9.6 ± 0.5	98 ± 7

Effect of mutations at CGRPR

Constructs were further assessed via cAMP assay with co-transfection with RAMP1 to form the CGRPR, and stimulated with either AM_{13-52} or CGRP.

Of all constructs, only [$Q^{202}\Delta$]CGRPR demonstrated a statistically significant loss of AM_{13-52} potency and accurate pEC_{50} was not determinable at concentrations of AM_{13-52} tested ($\sim$100 nM). [$Q^{202}\Delta$]CGRPR E_{max} recorded at 10^{-6} M AM_{13-52} was 27 $\pm$ 11 % that of WT ($p = <0.0001$) (figure 6.8; table 6.5). All other constructs retained WT-like efficacy and E_{max}, or demonstrated minor losses in potency following AM_{13-52} stimulation (table 6.5).

In response to CGRP, WT CGRPR generated pEC_{50} of 10.2 $\pm$ 0.1, consistent with the literature (Hay *et al.*, 2019). Mutations $N^{201}\Delta$, $Q^{202}\Delta$, $L^{204}\Delta$, $A^{206}\Delta$, $T^{207}\Delta$, $N^{208}\Delta$, $N^{200,201}\Delta$, $A^{199}\Delta$, $N^{200,201}\Delta$, $N^{200,201,208}\Delta$ and N^{200}NN, all showed significantly reduced potencies for CGRP ($p = <0.033$; mean $\pm$ s.e.m, $n \geq 3$) (figure 6.9; table 6.6).

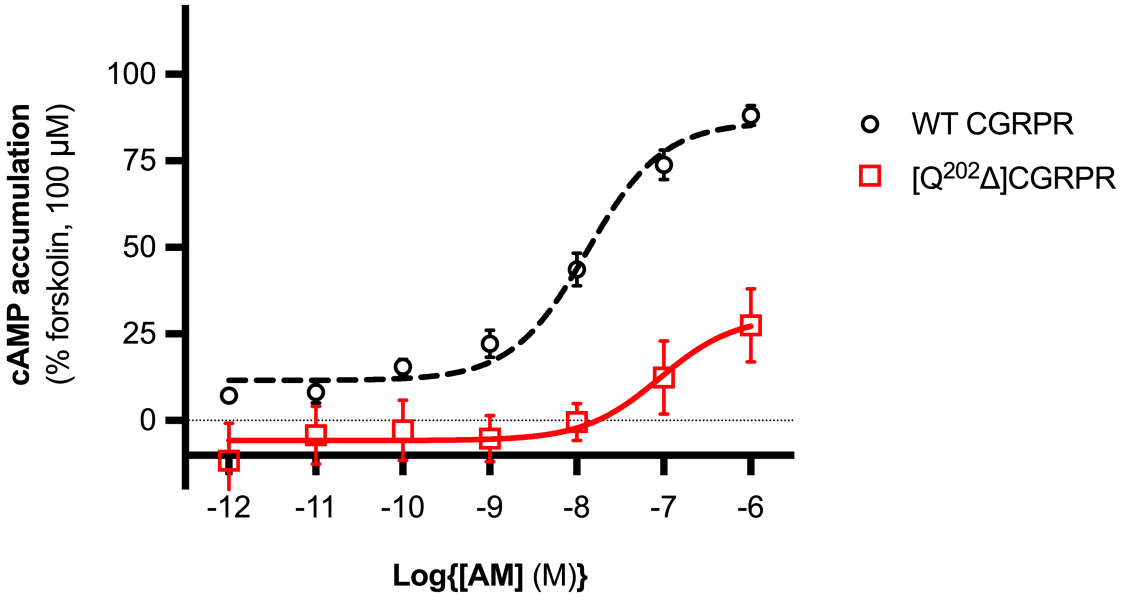

Figure 6.8: **Effect of deletion of CLR residue Q^{202} on agonist-induced cAMP production.** cAMP dose-response curve of $[Q^{202}\Delta]$CGRPR in response to AM_{13-52}. Data are mean ± s.e.m for at least three independent experiments.

Table 6.5: **Ability of mutant CGRPRs to stimulate cAMP production after AM_{13-52} stimulation.** Values are mean ± s.e.m for stated number of independent experiments. Significance determined by paired ANOVA with Dunnett's multiple comparisons to the WT CGRPR (****, p = <0.0001; ŧ = response too small for an accurate determination).

Receptor	Ligand	*n*	pEC_{50}	E_{max}
WT CGRPR	AM_{13-52}	14	7.9 ± 0.2	89 ± 2
[$N^{201}\Delta$]CGRPR	AM_{13-52}	3	7.3 ± 0.2	83 ± 10
[$Q^{202}\Delta$]CGRPR	AM_{13-52}	3	~7.0 ŧ	27 ± 11 ****
[$A^{203}\Delta$]CGRPR	AM_{13-52}	3	7.3 ± 0.3	79 ± 6
[$L^{204}\Delta$]CGRPR	AM_{13-52}	3	7.7 ± 0.2	77 ± 7
[$V^{205}\Delta$]CGRPR	AM_{13-52}	3	7.7 ± 0.2 *	91 ± 4 ****
[$A^{206}\Delta$]CGRPR	AM_{13-52}	3	7.2 ± 0.6	87 ± 5
[$T^{207}\Delta$]CGRPR	AM_{13-52}	3	7.3 ± 0.4	74 ± 17
[$N^{208}\Delta$]CGRPR	AM_{13-52}	3	7.9 ± 0.1	98 ± 1
[$N^{200,201}\Delta$]CGRPR	AM_{13-52}	3	7.0 ± 0.3	91 ± 6
[$A^{199}\Delta$,$N^{200,201}\Delta$]CGRPR	AM_{13-52}	2	5.2 ± 1.8	76 ± 12
[$N^{200,201,208}\Delta$]CGRPR	AM_{13-52}	4	6.9 ± 0.9	82 ± 7
[N^{200}NN]CGRPR	AM_{13-52}	3	7.4 ± 0.7	99 ± 6

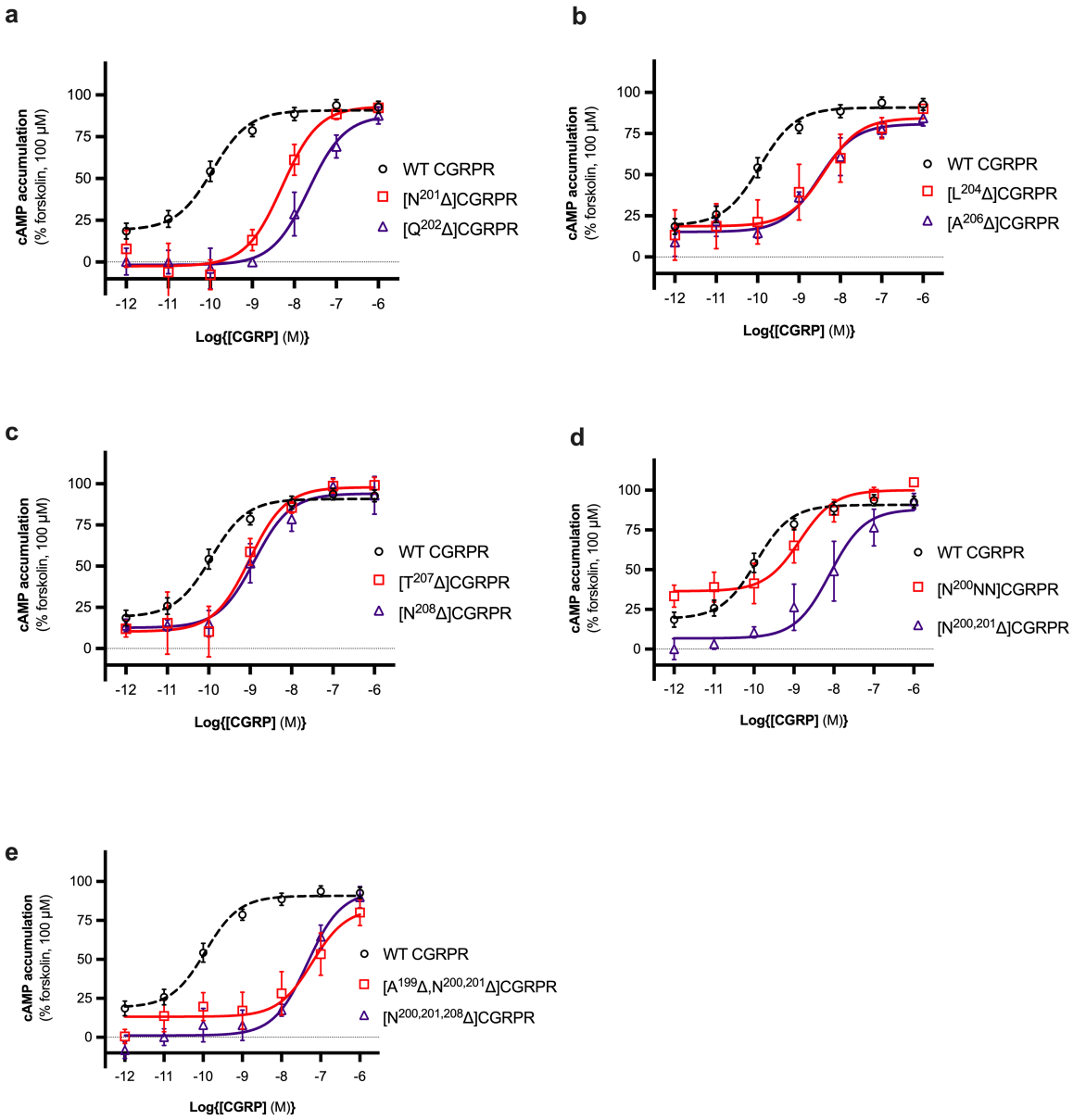

Figure 6.9: **CGRP stimulated dose-response curves for CGRPR (CLR + RAMP1) mutants.** Activity curves demonstrating significant loss of CGRP potency. **(a)** $N^{201}\Delta$, $Q^{202}\Delta$; **(b)** $L^{204}\Delta$ and $A^{206}\Delta$; **(c)** $T^{207}\Delta$ and $N^{208}\Delta$; **(d)** $N^{200}NN$ and $N^{200,201}\Delta$; **(e)** $A^{199}\Delta$,$N^{200,201}\Delta$ and $N^{200,201,208}\Delta$. WT receptors; open circles. Mutant receptors; open squares or open triangles. Data are mean ± s.e.m for at least three independent experiments.

Table 6.6: **Ability of mutant CGRPRs to stimulate cAMP production after CGRP stimulation.** Values are mean ± s.e.m for stated number of independent experiments. Significance determined by paired ANOVA with Dunnett's multiple comparisons to the WT CGRPR (*, p <0.033; **, p <0.002).

Receptor	Ligand	*n*	pEC_{50}	E_{max}
WT CGRPR	CGRP	12	10.2 ± 0.1	92 ± 4
[N^{201}Δ]CGRPR	CGRP	3	8.3 ± 0.2 *	92 ± 3
[Q^{202}Δ]CGRPR	CGRP	3	7.6 ± 0.2 *	88 ± 5
[A^{203}Δ]CGRPR	CGRP	3	8.7 ± 0.7	97 ± 3
[L^{204}Δ]CGRPR	CGRP	3	8.6 ± 0.5 *	90 ± 4
[V^{205}Δ]CGRPR	CGRP	3	7.9 ± 0.4 **	87 ± 2
[A^{206}Δ]CGRPR	CGRP	3	8.4 ± 0.4 **	84 ± 5
[T^{207}Δ]CGRPR	CGRP	3	8.8 ± 0.2 *	99 ± 5
[N^{208}Δ]CGRPR	CGRP	3	8.8 ± 0.2 *	93 ± 11
[$N^{200,201}$Δ]CGRPR	CGRP	4	8.1 ± 0.5 **	93 ± 5
[A^{199}Δ,$N^{200,201}$Δ]CGRPR	CGRP	3	7.3 ± 0.3 *	80 ± 8
[$N^{200,201,208}$Δ]CGRPR	CGRP	3	7.4 ± 0.04 **	90 ± 7
[N^{200}NN]CGRPR	CGRP	3	8.9 ± 0.4 *	105 ± 2

6.2.5 Summary of agonist-induced cAMP data

In order to simplify comparison between ligand-efficacy changes as a consequence of residue mutation within ECL1, fold-loss compared with WT was calculated (table 6.7). CGRP-mediated signalling at CGRPR appeared most sensitive to changes in the ECL1 loop-length, displaying potency losses with all constructs. However, AM_{13-52}-mediated CGRPR signalling appeared much more tolerant of single residue deletion or insertion, with the majority of constructs signalling at WT-like levels. AM_{13-52}-mediated-AM_1R signalling was moderately affected by deletion mutations, with seven of the twelve constructs displaying at least a 13-fold loss in AM_{13-52} potency. Residue [$Q^{202}\Delta$]CLR was the only construct which resulted in significant losses in agonist potency in all contexts.

To further compare effects of mutations, the difference in relative selectivity (RS) was plotted in two ways. The first, relative CGRPR selectivity was assessed to give a global overview of the relative losses observed between CGRP and AM_{13-52} potency at CGRPR mutants (same RAMP; different ligand). The second, AM_{13-52} ligand selectivity was assessed to give a global overview of the relative losses in potency at either CGRPR or AM_1R (same ligand; different RAMP). Log(RS) was calculated following normalisation of mutant pEC_{50} values to their respective WT. Δlog(RS) calculated as log[aEC_{50}/bEC_{50}], where 'a' and 'b' represent the compared variables.

Table 6.7: **Fold-losses in EC_{50} for CLR mutants.** Fold-loss in ligand potency with stated receptor/ligand combination was calculated relative to WT. Potency loss ≥500-fold is coloured red; Potency loss ≥50-fold is coloured orange; Potency loss ≥10-fold is coloured yellow; 'Em'-dash (—) indicates uncollected data.

	Fold-loss in ligand potency from WT			
	Receptor/ligand			
Construct	AM_1R/AM_{13-52}	CGRPR/CGRP	$CGRPR/AM_{13-52}$	AM_2R/AM_{13-52}
WT CLR	1	1	1	1
[$N^{201}\Delta$]CLR	79	79	4	—
[$Q^{202}\Delta$]CLR	200	398	>1000	—
[$A^{203}\Delta$]CLR	79	32	4	—
[$L^{204}\Delta$]CLR	20	40	2	—
[$V^{205}\Delta$]CLR	13	100	3	5
[$A^{206}\Delta$]CLR	25	63	5	—
[$T^{207}\Delta$]CLR	79	25	4	—
[$N^{208}\Delta$]CLR	6	25	1	—
[$N^{200,201}\Delta$]CLR	1	126	8	—
[$A^{199}\Delta$,$N^{200,201}\Delta$]CLR	4	794	501	—
[$N^{200,201,208}\Delta$]CLR	2	631	10	—
[N200NN]CLR	1	20	3	—

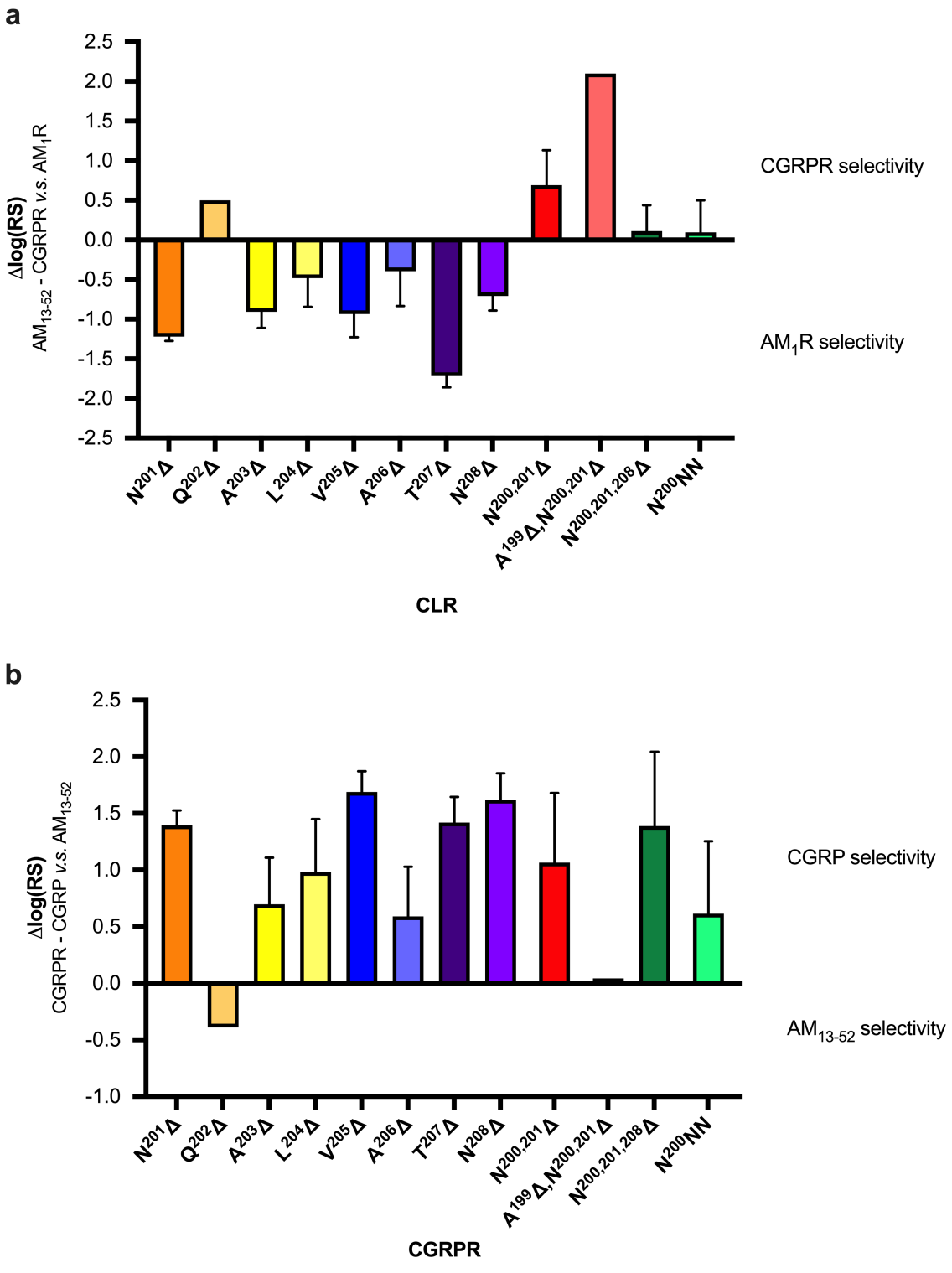

Figure 6.10: **Selectivity profiles for ECL1 mutations.** Relative selectivity (RS) was calculated as $\Delta\log(\mathrm{RS})$. **(a)** AM_{13-52} potency was assessed at CGRPR and $\mathrm{AM}_1\mathrm{R}$ (same ligand; different RAMP). **(b)** Ligand selectivity at CGRPR was assessed with CGRP and AM_{13-52} (same RAMP; different ligand).

6.3 Discussion

6.3.1 Rationale and importance of extracellular loops

Carried out here was a deletion scan of the first extracellular loop of CLR. The rationale of the work was to not only probe the role of ECL1 and loop length in general, but to also examine the clinically apparent [$V^{205}\Delta$]CLR mutation which results in sub-fertility and miscarriage. [$V^{205}\Delta$]CLR is not unique in being important functionally for the receptor. In fact, several ECL1 residues effected function upon deletion. Furthermore, the effect of deletion of a residue within ECL1 is dictated by the RAMP subtype present in the dimer, as well as the ligand. ECL1 of CLR is one of the shortest in all family B members. Loop length was interrogated via generation of single-, double- and triple- deletion mutants, plus a single residue insertion. The double-deletion construct, [$N^{200,201}\Delta$]CLR, placed ECL1 at joint-shortest within family B, alongside corticotropin releasing hormone receptor 1. The two triple-deletion constructs resulted in a loop length shorter than that found in any family B GPCR. An insertion of Asn between Asn^{200} and Asn^{201} was generated to probe the consequence of loop-lengthening. Despite the vast range of roles GPCRs play in physiology, as well as their diversity in protein sequence, they display remarkably similar topology. Seven transmembrane helices are linked by intracellular and extracellular loops. In family A GPCRs the binding pocket for small molecules, or small amines is located deep within the TM bundle (Rosenbaum *et al.*, 2009). G-proteins, beta-arrestins and other scaffold proteins interact with the intracellular face of the receptor. Extracellular domains and ECLs demonstrate remarkable diversity in sequence and length, even within sub-families. As a result, historically, ECLs were thought to serve as simply linkers between the TMs, and play few roles in receptor trafficking and signalling, however this is not the case (Wheatley *et al.*, 2012). For example, rhodopsin ECL2 comprises two β-sheets which forms a twisted β-hairpin (β3, β4). This hairpin interacts with another β-hairpin (β1, β2) within the N-terminus of rhodopsin, and forms a 'lid' over the receptor. This contributes significantly to rhodopsin stability. Further to this, point mutations within

all three ECLs have been identified in thyroid-stimulating hormone receptor, and result in receptor constitutive activity (Kleinau *et al.*, 2013). Indeed, there are many examples demonstrating the important role of ECLs (reviewed in (Wheatley *et al.*, 2012); discussed in section 6.1). Results from this study provide new insight into the specific ligand-receptor and RAMP-CLR interactions that occur at ECL1 for CGRPR and AM receptors.

6.3.2 Cell-surface trafficking

In this study, deletion mutation at any single residue within ECL1 of CLR, including double- and triple- residue deletion, did not significantly alter receptor cell-surface expression of the AM_1R (CLR + RAMP2) (table 6.2). Further to this, it was shown that RAMP2 trafficking was unaffected by deletion at Val^{205} (figure 6.5). These results suggest that ECL1 plays little involvement in trafficking of the receptor to the cell-surface. This contrasts to results that reported deletion at Val^{205} resulted in reduced cell-surface expression by approximately 40 % (Mackie *et al.*, 2018). However, plasmid and cellular context may present influencing factors, for example, different cell lines have varying endogenous levels of RAMPs. It is of note that in all three CLR cryo-EM structures, RAMPs are primarily located in the ECD, upper half of TM5 and base of TM3 and TM4, away from ECL1 (Liang *et al.*, 2018). It is well established that RAMPs are required for CLR trafficking to the cell-surface (McLatchie *et al.*, 1998), the data in this study support a conclusion that no individual residue within ECL1 is required for AM_1R cell-surface expression. Future work could investigate the effects of deletion mutants on cell-surface trafficking of CLR and RAMP1/3.

6.3.3 Effect of Val^{205} deletion on agonist-induced cAMP accumulation

Despite cell-surface expression of all receptors being WT-like, marked differences in ability to stimulate cAMP production upon agonist challenge were observed. Firstly, the deletion at $[V^{205}\Delta]AM_1R$ (which in humans has been shown to cause NIHF), demonstrated a 13-fold loss in AM_{13-52} potency. This is consistent with previous work that derived an 11-fold loss in potency at $[V^{205}\Delta]AM_1R$ (Mackie *et al.*, 2018). When examining the other

[$V^{205}\Delta$]CLR-RAMP heterodimers, the most notable change was an 100-fold loss in CGRP potency at [$V^{205}\Delta$]CGRPR (figure 6.6). In the cryo-EM structure of active CGRPR, serine^{17} of CGRP is angled towards ECL1, and is in proximity with Val^{205}, which itself, is angled towards the ligand (∼5–6 Å between Ser^{17} and Val^{205}). In contrast to this, the cryo-EM structure of active AM_1R, shows that while AM is in the proximity of ECL1, there is a greater distance between the peptide and ECL (∼9–10 Å), and that no peptide residues project directly toward Val^{205}. This provides a feasible mechanism for data found here, highlighting ligand-specific interactions of CGRPR and Val^{205} at CGRPR.

AM_{13-52} stimulation at [$V^{205}\Delta$]CGRPR and [$V^{205}\Delta$]AM_2R resulted in just 3- and 5-fold losses in AM_{13-52} potency, respectively (figure 6.6). Upon examination of the cryo-EM structure of AM_2R in complex with AM (Liang *et al.*, 2020), Val^{205} points slightly down towards the receptor core with the ligand angled away from Val^{205}. This may explain the relatively mild impact of residue deletion.

The severity of phenotype observed in individuals with homozygous in-frame deletion of Val^{205} in the CLR, combined with the remarkable sequence conservation across evolutionary species, highlights how ECL1 is a functionally critical structure (Mackie *et al.*, 2018) (figure 6.2). Data presented here address the contribution of Val^{205}, highlighting functionally significant ligand-specific interactions.

6.3.4 Effect of ECL1 deletions on agonist-induced cAMP accumulation

Effect of loop length of CGRPR

It is clear from table 6.7, that ECL1 plays a functionally important role, and that ligand-receptor-RAMP interactions are highly specific. A previous alanine scan of CGRPR ECL1 found that [A^{203}L]CGRPR and [A^{206}L]CGRPR slightly increased CGRP potency (Barwell *et al.*, 2011), however deletion of any single residue within ECL1 resulted in ∼25–400 -fold losses in CGRP potency. This is suggestive that loop length itself is an integral factor of CGRP-CGRPR signalling. Lengthening ECL1 by a single residue ([N^{200}NN]CLR) resulted in a 20-fold loss of CGRP potency at CGRPR, however was WT-like for AM_{13-52}-

stimulated receptors. This sensitivity of CGRP-CGRPR to changes in loop length was further highlighted by the double and triple deletions. Double deletion resulted in a 126-fold loss of CGRP potency, while triple deletion constructs resulted in ∼600–700 -fold losses (figure 6.9). These results suggest CGRP-mediated CGRPR signalling relies on specific organisation of ECL1 and perturbation leads of loss of receptor functionality.

Despite the sensitivity of CGRPR ECL1 loop length on CGRP signalling, AM_{13-52}-mediated CGRPR signalling was remarkably robust to changes in loop length. [$Q^{202}\Delta$]CGRPR resulted in almost ablated cAMP accumulation (>1000-fold loss of AM_{13-52} potency), however, beyond this only the triple deletion constructs resulted in >10-fold losses in ligand potency. [$A^{199}\Delta$,$N^{200,201}\Delta$]CGRPR demonstrated a 500-fold loss in AM_{13-52}, which is contrasting to the 10-fold loss observed at the other triple-deletion construct [$N^{200,201,208}\Delta$]CGRPR. The loss of three consecutive residues at the start of the loop is expected to perturb conformation to a greater extent than loosing residues at either end of the loop. This may provide insight into areas of ligand-specific interaction. The contrasting differences of CGRPR to tolerate changes in ECL1 loop length for CGRP or AM_{13-52} activity provides useful insight into how the two ligands might bind the receptor differently.

Effect of loop length of AM_1R

Significant losses in AM_{13-52} potency were observed for 6 out of 10 AM_1R constructs (figure 6.7). The most notable was [$Gln^{202}\Delta$]AM_1R, which resulted in a 200-fold potency loss. Indeed [$Gln^{202}\Delta$]CLR demonstrated severe perturbation of signalling for all ligand-receptor combinations examined (table 6.7). Examination of the available CLR structures revealed that at CGRPR, Gln^{202} forms H-bonds with Ser^{17} of CGRP. At AM_1R, Gln^{202} is angled directly toward AM, and is within proximity (3–5 Å) of Tyr^{31} of AM. Evidently, Gln^{202} forms important interactions for either ligand binding, or receptor activation. Mutation of this residue to Ala did not result in a statistically significant loss CGRP potency, again indicating that loop length is a determining factor, and loss of the amino acid backbone results in structural shifts that drastically alter receptor phenotype.

Both Leu^{204} and Ala^{206} are within a short helix within ECL1. This small, structural component could provide a stabilising network, which could explain the loss in potency and E_{max} observed at AM_1R (table 6.4), and loss of potency observed at CGRPR.

Indeed, it appears that deletion at Val^{205} actually represents one of the least-disrupted phenotypes, compared with other residue deletions within ECL1. The clinical presentation of $[V^{205}\Delta]AM_1R$ shows that homozygosity results in fetal loss due to NIHF, and heterozygosity results in sub-fertility and miscarriage (Mackie *et al.*, 2018). Deletion of other residues may not be clinically identified due to the catastrophic nature of the phenotype (not compatible with life).

6.3.5 Summary and future work

Work performed here revealed key residues within ECL1 that are important for CLR receptor activation. Due to the diversity of ECLs in family B GPCRs, they could serve as useful drug targets, so understanding their function is of great importance. Loop length is an important factor for receptor function, as previous alanine scanning yielded little alterations to agonist-induced cAMP production (Barwell *et al.*, 2011). Overall, this study is consistent with the latest cryo-EM structures of CGRPR, AM_1R and AM_2R, which place the peptide ligands in proximity to ECL1. Important insight into the ligand-specific nature of the ligand-receptor interactions is gained here, observed by the contrasting functional changes seen at CGRPR agonist-induced cAMP responses. Given the sensitivity of the CGRP-CGRPR complex to loop length, follow-up (radioligand) binding assay may provide further discernment into the nature of these ligand-specific interactions. Furthermore, binding experiments at all mutants that demonstrated large losses in potency would provide useful insights. Given the availability of high-resolution CLR structures, molecular modelling of specific mutants and molecular dynamics simulations may prove useful in elucidating key ligand-specific interactions of this pharmacologically relevant receptor.

Chapter 7: Summary and future work

"One of the symptoms of an approaching nervous breakdown is the belief that ones work is terribly important." - Bertrand Russell, The Conquest of Happiness

GPCRs are of great interest to the pharmaceutical industry. Understanding of receptor pharmacology has been hindered due to their inherent hydrophobicity, flexibility, dynamic nature and instability when extracted from the membrane. This thesis explored the use of novel nano-encapsulation strategies to solubilise GPCRs and validate, or apply, downstream techniques in order to gain insight into receptor pharmacology and mechanisms. Alongside this, traditional mutagenic approaches were used to address the contribution of individual amino acids within ECL1 of CLR and gain insight into the complex nature of family-B receptor pharmacology.

Presented in chapter 3 was the first documented application of FCS to characterise binding at a GPCR-SMALP. There are increasing barriers to the use of radioligands for characterising ligand binding. The development of fluorescent ligands has made tremendous progress over the last few years, meaning existing technologies, such as FCS, can have their potential realised. It was demonstrated that FCS could be successfully used with purified A_{2A}R-SMALP to observe binding events and derive accurate affinity values. One advantage of FCS is that the free ligand concentration and bound ligand can be determined in the same place at the same time. The use of FCS combined with nano-encapsulated GPCRs presents many potential avenues for further study. In particular, investigations relating to allosteric modulation and the effect of nanobodies on receptor binding would be of great pharmaceutical interest. Modulator proteins, such as RAMP interaction, could be probed using FCS, which would be highly useful as many receptor-RAMP interactions are poorly characterised. Given the increasing availability of fluorescent ligands (includ-

ing the design of PTH_{1-34}:BODIPY presented in chapter 5), the validation of FCS with GPCR-SMALPs will have positive applications in the future.

Chapter 4 explored the development of a polymer tool kit, aiming to gain insight into how different solubilisation polymers behave within the same context. SMA, SMI and DIBMA were used to solubilise rhodopsin, which was characterised with regards to light-induced receptor activation, thermal stability, oligomeric state and particle size. This was the first documented use of DIBMA and SMI to extract rhodopsin from bovine retina. The conformational range adopted by rhodopsin was different with each polymer. SMA and SMI prevented transition to fully-active receptor states (transitioning to meta I, but not to meta II), whereas DIBMA permitted transition to fully-active meta II. In a similar manner that detergent-screens are currently performed, one can envisage polymer-screens being used in order to ascertain the most appropriate polymer for receptor extraction. The differing capabilities of the polymers to support conformational changes could prove extremely useful from a structural perspective. The resolution of intermediate-state structures could provide useful insight into the dynamics of receptor activation. This, as well as the application of biophysical techniques, hinges on the successful purification of nano-encapsulated GPCR and future work should aim to explore and optimise purification of rhodopsin. In particular, the ability to purify recombinant rhodopsin from HEK 293 cells would permit valuable insight into pathologically relevant mutants that cause diseases such as retinitis pigmentosa and may open new opportunities to study cone-opsins. Structural knowledge of the cone-opsins which provide colour vision (red, green and blue) lags far behind that of rhodopsin currently, with no high resolution structures. Purification of conformation-specific GPCRs could also aid the development of conformation-specific nanobodies, which may allosterically modulate receptor function in a pharmacologically useful way.

Chapter 5 presented the development and validation of novel GPCR receptor constructs, inducible cell lines and the validation of a novel fluorescent PTH1R agonist. This chapter established the tools required to widen the application of nano-encapsulation

strategies to pharmacologically-important GPCR targets, OTR and PTH1R. Further work should investigate the functional state of the receptors within a SMALP. At the OTR, overcoming high levels of non-specific OT-binding to the polymer remains an issue. Future work could examine the extraction and purification of the receptors using alternative polymers, such as work carried out in chapter 4. The fluorescent agonist, PTH_{1-34}:BODIPY, could be used alongside FCS studies to ascertain PTH1R-SMALP binding capability. The ligand may also have wider application, providing a useful tool in the characterisation of anti-PTH1R antibodies or nanobodies.

In chapter 6, a directed mutagenic approach identified the functional importance of specific individual residues in ECL1 and loop length on agonist-induced cAMP signalling at the CLR. Specifically, this was dependent upon which RAMP was in association with CLR, and which ligand was examined. CGRPR-CGRP mediated cAMP signalling was particularly sensitive to alterations in loop length, with CGRP affinity losses observed at all deletion constructs (both single residue deletion and multiple residue deletion). Furthermore, CGRPR-CGRP signalling was perturbed by lengthening the loop by a single residue. However, at the same receptor, with a different ligand (AM_{13-52}), few changes in potency were observed, with only the triple residue deletion and [$Q^{202}\Delta$]CLR displaying losses. Varied losses (>10 to 200-fold) in AM_{13-52} potency were observed at seven of the single residue deletions at the AM_1R. These findings provide insight into how the ligands engage with each receptor in subtly different ways and highlight how RAMPs alter receptor pharmacology. A previous alanine scan of CGRPR ECL1 yielded little changes in CGRP potency (Barwell *et al.*, 2011), reinforcing the conclusion that loop length (loss of the amino acid backbone) is a detrimental factor. Given the recent availability of high-resolution cryo-EM structures of CLR, molecular modelling and molecular dynamics simulations may provide insight into the dynamics of receptor activation for WT and mutant constructs. This pharmacological insight is relevant as deletion at Val^{205} within ECL1 of CLR has been identified clinically. Dissecting the contribution of individual amino acids on receptor function is important for aiding rational drug design. Further characterisations

such as cell-surface expression and ligand binding assays should be performed on deletion mutants that resulted in lost or ablated signalling, notably [$Q^{202}\Delta$]CLR and the clinically-relevant [$V^{205}\Delta$]CLR. An ECL1 alanine scan of AM_1R may also provide further insight into the contribution of individual amino acids. Characterisation of constructs at different signalling pathways, such as MAPK/ERK1/2 pathway and by extension, characterisation with respect to their ability to interact with beta-arrestin, may also provide further insight into the apparent biased nature of these mutants ability to influence receptor signalling.

Overall, this thesis contributes towards the understanding of GPCR pharmacology, and provides answers for key questions regarding the utility of SMA and SMA-like polymers, whilst opening up further avenues of research which will benefit from polymer-based nano-encapsulation.

References

Alexander, S.P., Christopoulos, A., Davenport, A.P., Kelly, E., Marrion, N.V., Peters, J.A., Faccenda, E., Harding, S.D., Pawson, A.J., Sharman, J.L., Southan, C. and Davies, J.A. (2017); 'The Concise Guide to Pharmacology 2017/18: G-protein-coupled receptors', *British Journal of Pharmacology*, **174**, pp 17–129.

Antoni, F.A. and Chadio, S.E. (1989); 'Essential role of magnesium in oxytocin-receptor affinity and ligand specificity', *Biochemical Journal*, **257**(2), pp 611–614.

Audet, M. and Bouvier, M. (2012); 'Restructuring G-protein- coupled receptor activation', *Cell*, **151**(1), pp 14–23.

Ayoub, M.A., Crepieux, P., Koglin, M., Parmentier, M., Pin, J.P., Poupon, A., Reiter, E., Smit, M., Steyaert, J., Watier, H. and Wilkinson, T. (2017); 'Antibodies targeting G protein-coupled receptors: Recent advances and therapeutic challenges', *mAbs*, **9**(5), pp 735–741.

Babcock, G.J., Mirzabekov, T., Wojtowicz, W. and Sodroski, J. (2001); 'Ligand binding characteristics of CXCR4 incorporated into paramagnetic proteoliposomes', *Journal of Biological Chemistry*, **276**(42), pp 38433–38440.

Bailey, S. (2017); *The structure and function of the human vasopressin receptors*, Thesis, School of Biosciences, University of Birmingham.

Ballesteros, J.A. and Weinstein, H. (1995); 'Integrated methods for the construction of three-dimensional models and computational probing of structure-function relations in G protein-coupled receptors', *Methods in Neurosciences*, **25**, pp 366–428.

Baltoumas, F.A., Theodoropoulou, M.C. and Hamodrakas, S.J. (2013); 'Interactions of the alpha-subunits of heterotrimeric G-proteins with GPCRs, effectors and RGS proteins: a critical review and analysis of interacting surfaces, conformational shifts, structural diversity and electrostatic potentials', *Journal of Structural Biology*, **182**(3), pp 209–218.

Barwell, J., Conner, A. and Poyner, D.R. (2011); 'Extracellular loops 1 and 3 and their associated transmembrane regions of the calcitonin receptor-like receptor are needed for CGRP receptor function', *Biochimica et Biophysica Acta*, **1813**(10), pp 1906–1916.

Barwell, J., Gingell, J.J., Watkins, H.A., Archbold, J.K., Poyner, D.R. and Hay, D.L. (2012); 'Calcitonin and calcitonin receptor-like receptors: common themes with family B GPCRs?', *British Journal of Pharmacology*, **166**(1), pp 51–65.

Bassard, J.E. and Laursen, T. (2019); 'Molecular snapshots of dynamic membrane-bound metabolons', *Methods in Enzymology*, **617**, pp 1–27.

Bayburt, T.H. and Sligar, S.G. (2010); 'Membrane protein assembly into Nanodiscs', *FEBS Letters*, **584**(9), pp 1721–1727.

Bayburt, T.H., Vishnivetskiy, S.A., McLean, M.A., Morizumi, T., Huang, C.C., Tesmer, J.J., Ernst, O.P., Sligar, S.G. and Gurevich, V.V. (2011); 'Monomeric rhodopsin is sufficient for normal rhodopsin kinase (GRK1) phosphorylation and arrestin-1 binding', *Journal of Biological Chemistry*, **286**(2), pp 1420–1428.

Beckett, D., Kovaleva, E. and Schatz, P.J. (1999); 'A minimal peptide substrate in biotin holoenzyme synthetase-catalyzed biotinylation', *Protein Science*, **8**(4), pp 921–929.

Bergwitz, C., Jusseaume, S.A., Luck, M.D., Juppner, H. and Gardella, T.J. (1997); 'Residues in the membrane-spanning and extracellular loop regions of the parathyroid hormone (PTH)-2 receptor determine signaling selectivity for PTH and PTH-related peptide', *Journal of Biological Chemistry*, **272**(46), pp 28861–28868.

Bisello, A., Chorev, M., Friedman, P.A., Gardella, T., Hills, R., Jueppner, H., Martin, T.J., Nissenson, R.A., Potts, Jr., J.T., Silve, C., Usdin, T.B. and Vilardaga, J.P. (2019); 'Parathyroid hormone receptors (version 2019.4) in the IUPHAR/BPS Guide to Pharmacology Database', *IUPHAR/BPS Guide to Pharmacology*, **2019**(4).

Briddon, S.J. and Hill, S.J. (2007); 'Pharmacology under the microscope: the use of fluorescence correlation spectroscopy to determine the properties of ligand-receptor complexes', *Trends in Pharmacological Sciences*, **28**(12), pp 637–645.

Briddon, S.J., Kellam, B. and Hill, S.J. (2011); 'Design and use of fluorescent ligands to study ligand-receptor interactions in single living cells', *Methods in Molecular Biology*, **746**, pp 211–236.

Broecker, J., Eger, B.T. and Ernst, O.P. (2017); 'Crystallogenesis of Membrane Proteins Mediated by Polymer-Bounded Lipid Nanodiscs', *Structure*, **25**(2), pp 384–392.

Butz, J.A., Niebauer, R.T. and Robinson, A.S. (2003); 'Co-expression of molecular chaperones does not improve the heterologous expression of mammalian G-protein coupled receptor expression in yeast', *Biotechnology and Bioengineering*, **84**(3), pp 292–304.

Bymaster, F.P., Calligaro, D.O., Falcone, J.F., Marsh, R.D., Moore, N.A., Tye, N.C., Seeman, P. and Wong, D.T. (1996); 'Radioreceptor binding profile of the atypical antipsychotic olanzapine', *Neuropsychopharmacology*, **14**(2), pp 87–96.

Carpenter, B. and Tate, C.G. (2016); 'Engineering a minimal G protein to facilitate crystallisation of G protein-coupled receptors in their active conformation', *Protein Engineering Design and Selection*, **29**(12), pp 583–594.

Carroll, C.E., Marada, S., Stewart, D.P., Ouyang, J.X. and Ogden, S.K. (2012); 'The extracellular loops of Smoothened play a regulatory role in control of Hedgehog pathway activation', *Development*, **139**(3), pp 612–621.

Chapple, J.P. and Cheetham, M.E. (2003); 'The chaperone environment at the cytoplasmic face of the endoplasmic reticulum can modulate rhodopsin processing and inclusion formation', *Journal of Biological Chemistry*, **278**(21), pp 19087–19094.

Charlton, J. (2015); *Solubilisation and Characterisation of G Protein-Coupled Receptors Using Styrene Maleic Acid Polymer*, Thesis, School of Biosciences, University of Birmingham.

Chaudhary, S., Pak, J.E., Gruswitz, F., Sharma, V. and Stroud, R.M. (2012); 'Overexpressing human membrane proteins in stably transfected and clonal human embryonic kidney 293S cells', *Nature Protocols*, **7**(3), pp 453–466.

Cheng, Y. and Prusoff, W.H. (1973); 'Relationship between the inhibition constant (K1) and the concentration of inhibitor which causes 50 per cent inhibition (I50) of an

enzymatic reaction', *Biochemical Pharmacology*, **22**(23), pp 3099–30108.

Cherezov, V., Rosenbaum, D.M., Hanson, M.A., Rasmussen, S.G., Thian, F.S., Kobilka, T.S., Choi, H.J., Kuhn, P., Weis, W.I., Kobilka, B.K. and Stevens, R.C. (2007); 'High-resolution crystal structure of an engineered human beta2-adrenergic G protein-coupled receptor', *Science*, **318**(5854), pp 1258–1265.

Chun, L., Zhang, W.H. and Liu, J.F. (2012); 'Structure and ligand recognition of class C GPCRs', *Acta Pharmacologica Sinica*, **33**(3), pp 312–323.

Ciruela, F., Jacobson, K.A. and Fernandez-Duenas, V. (2014); 'Portraying G protein-coupled receptors with fluorescent ligands', *ACS Chemical Biology*, **9**(9), pp 1918–1928.

Coleman, D.E., Berghuis, A.M., Lee, E., Linder, M.E., Gilman, A.G. and Sprang, S.R. (1994); 'Structures of active conformations of Gi alpha 1 and the mechanism of GTP hydrolysis', *Science*, **265**(5177), pp 1405–1412.

Congreve, M., Andrews, S.P., Dore, A.S., Hollenstein, K., Hurrell, E., Langmead, C.J., Mason, J.S., Ng, I.W., Tehan, B., Zhukov, A., Weir, M. and Marshall, F.H. (2012); 'Discovery of 1,2,4-triazine derivatives as adenosine A(2A) antagonists using structure based drug design', *Journal of Medicinal Chemistry*, **55**(5), pp 1898–1903.

Congreve, M. and Marshall, F. (2010); 'The impact of GPCR structures on pharmacology and structure-based drug design', *British Journal of Pharmacology*, **159**(5), pp 986–996.

Conibear, A.E., Asghar, J., Hill, R., Henderson, G., Borbely, E., Tekus, V., Helyes, Z., Palandri, J., Bailey, C., Starke, I., von Mentzer, B., Kendall, D. and Kelly, E. (2020); 'A Novel G Protein-Biased Agonist at the delta Opioid Receptor with Analgesic Efficacy in Models of Chronic Pain', *Journal of Pharmacology and Experimental Therapeutics*, **372**(2), pp 224–236.

Conner, A.C., Simms, J., Hay, D.L., Mahmoud, K., Howitt, S.G., Wheatley, M. and Poyner, D.R. (2004); 'Heterodimers and family-B GPCRs: RAMPs, CGRP and adrenomedullin', *Biochemical Society Transactions*, **32**(Pt 5), pp 843–846.

Cordeaux, Y., Briddon, S.J., Alexander, S.P.H., Kellam, B. and Hill, S.J. (2007); 'Agonist-occupied A3 adenosine receptors exist within heterogeneous complexes in membrane microdomains of individual living cells', *The FASEB Journal*, **22**(3), pp 850–860.

Corriden, R., Kilpatrick, L.E., Kellam, B., Briddon, S.J. and Hill, S.J. (2014); 'Kinetic analysis of antagonist-occupied adenosine-A3 receptors within membrane microdomains of individual cells provides evidence of receptor dimerization and allosterism', *The FASEB Journal*, **28**(10), pp 4211–4222.

Cuevas Arenas, R., Danielczak, B., Martel, A., Porcar, L., Breyton, C., Ebel, C. and Keller, S. (2017); 'Fast Collisional Lipid Transfer Among Polymer-Bounded Nanodiscs', *Scientific Reports*, **7**, page 45875.

Dal Maso, E., Glukhova, A., Zhu, Y., Garcia-Nafria, J., Tate, C.G., Atanasio, S., Reynolds, C.A., Ramirez-Aportela, E., Carazo, J.M., Hick, C.A., Furness, S.G.B., Hay, D.L., Liang, Y.L., Miller, L.J., Christopoulos, A., Wang, M.W., Wootten, D. and Sexton, P.M. (2019); 'The Molecular Control of Calcitonin Receptor Signaling', *ACS Pharmacology and Translational Science*, **2**(1), pp 31–51.

Dalela, M., Shrivastav, T.G., Kharbanda, S. and Singh, H. (2015); 'pH-Sensitive Biocompatible Nanoparticles of Paclitaxel-Conjugated Poly(styrene-co-maleic acid) for Anticancer Drug Delivery in Solid Tumors of Syngeneic Mice', *ACS Applied Materials and Interfaces*, **7**(48), pp 26530–26548.

Dawaliby, R., Trubbia, C., Delporte, C., Masureel, M., Van Antwerpen, P., Kobilka, B.K. and Govaerts, C. (2016); 'Allosteric regulation of G protein-coupled receptor activity by phospholipids', *Nature Chemical Biology*, **12**(1), pp 35–39.

Deak, A., Sebk, D., Csap, E., Brczi, A., Dkny, I., Zimnyi, L. and Janovk, L. (2019); 'Evaluation of pH- responsive poly(styrene-co-maleic acid) copolymer nanoparticles for the encapsulation and pH- dependent release of ketoprofen and tocopherol model drugs', *European Polymer Journal*, **114**, pp 361 – 368.

Deupi, X. and Standfuss, J. (2011); 'Structural insights into agonist-induced activation of G-protein-coupled receptors', *Current Opinion in Structural Biology*, **21**(4), pp

541–551.

DeWire, S.M., Yamashita, D.S., Rominger, D.H., Liu, G., Cowan, C.L., Graczyk, T.M., Chen, X.T., Pitis, P.M., Gotchev, D., Yuan, C., Koblish, M., Lark, M.W. and Violin, J.D. (2013); 'A G protein-biased ligand at the mu-opioid receptor is potently analgesic with reduced gastrointestinal and respiratory dysfunction compared with morphine', *Journal of Pharmacology and Experimental Therapeutics*, **344**(3), pp 708–717.

Dijkman, P.M. and Watts, A. (2015); 'Lipid modulation of early G protein-coupled receptor signalling events', *Biochimica et Biophysica Acta*, **1848**(11 Pt A), pp 2889–2897.

Dominguez-Pardo, J.J., Dorr, J.M., Iyer, A., Cox, R.C., Scheidelaar, S., Koorengevel, M.C., Subramaniam, V. and Killian, J.A. (2017); 'Solubilization of lipids and lipid phases by the styrene-maleic acid copolymer', *European Biophysics Journal*, **46**(1), pp 91–101.

Dorsam, R.T. and Gutkind, J.S. (2007); 'G-protein-coupled receptors and cancer', *Nature Reviews Cancer*, **7**(2), pp 79–94.

Ehrenmann, J., Schoppe, J., Klenk, C., Rappas, M., Kummer, L., Dore, A.S. and Plückthun, A. (2018); 'High-resolution crystal structure of parathyroid hormone 1 receptor in complex with a peptide agonist', *Nature Structural and Molecular Biology*, **25**(12), pp 1086–1092.

Elson, E.L. (2013); '40 years of FCS: how it all began', *Methods in Enzymology*, **518**, pp 1–10.

FDA (2018); *Drugs at FDA: Drug products approved since 1939*, Food and Drug Administration, viewed 03 April 2019, https://www.fda.gov/drugs/drug-approvals-and-databases/about-drugsfda.

Ferguson, S.S., Barak, L.S., Zhang, J. and Caron, M.G. (1996); 'G-protein-coupled receptor regulation: role of G-protein-coupled receptor kinases and arrestins', *Canadian Journal of Physiology and Pharmacology*, **74**(10), pp 1095–1110.

Fiori, M.C., Jiang, Y., Altenberg, G.A. and Liang, H. (2017); 'Polymer-encased nanodiscs

with improved buffer compatibility', *Scientific Reports*, **7**(1), page 7432.

Flanagan, C.A. (2016); 'GPCR-radioligand binding assays', *Methods in Cellular Biology*, **132**, pp 191–215.

Flordellis, C.S. (2012); 'The plasticity of the 7TMR signaling machinery and the search for pharmacological selectivity', *Current Pharmaceutical Design*, **18**(2), pp 145–160.

Fraser, N.J. (2006); 'Expression and functional purification of a glycosylation deficient version of the human adenosine 2a receptor for structural studies', *Protein Expression and Purification*, **49**(1), pp 129–37.

Fredriksson, R., Lagerstrom, M.C., Lundin, L.G. and Schioth, H.B. (2003); 'The G-protein-coupled receptors in the human genome form five main families. Phylogenetic analysis, paralogon groups, and fingerprints', *Molecular Pharmacology*, **63**(6), pp 1256–1272.

Friedman, D.I. and Cohen, J.M. (2020); 'Fremanezumab: a disease-specific option for the preventive treatment of migraine, including difficult-to-treat migraine', *Emerging Topics in Life Sciences*, pp 179–190.

Fu, X., Song, Y., Masud, A., Nuti, K., DeRouchey, J.E. and Richards, C.I. (2020); 'High-throughput fluorescence correlation spectroscopy enables analysis of surface components of cell-derived vesicles', *Analytical and Bioanalytical Chemistry*, **412**(11), pp 2589–2597.

Gainetdinov, R.R., Premont, R.T., Bohn, L.M., Lefkowitz, R.J. and Caron, M.G. (2004); 'Desensitization of G protein-coupled receptors and neuronal functions', *Annual Review of Neuroscience*, **27**, pp 107–144.

Garelja, M.L., Au, M., Brimble, M.A., Gingell, J.J., Hendrikse, E.R., Lovell, A., Prodan, N., Sexton, P.M., Siow, A., Walker, C.S., Watkins, H.A., Williams, G.M., Wootten, D., Yang, S.H., Harris, P.W.R. and Hay, D.L. (2020); 'Molecular Mechanisms of Class B GPCR Activation: Insights from Adrenomedullin Receptors', *ACS Pharmacology & Translational Science*, **3**(2), pp 246–262.

Gether, U. (2000); 'Uncovering molecular mechanisms involved in activation of G protein-

coupled receptors', *Endocrine Reviews*, **21**(1), pp 90–113.

Gimpl, G., Burger, K. and Fahrenholz, F. (1997); 'Cholesterol as Modulator of Receptor Function', *Biochemistry*, **36**(36), pp 10959–10974.

Gimpl, G. and Fahrenholz, F. (2002); 'Cholesterol as stabilizer of the oxytocin receptor', *Biochimica et Biophysica Acta*, **1564**(2), pp 384–392.

Gimpl, G. and Farenholz, F. (2000); 'Human oxytocin receptors in cholesterol-rich vs. cholesterol-poor microdomains of the plasma membrane', *European Journal of Biochemistry*, **267**(9), pp 2483–2497.

Glukhova, A., Draper-Joyce, C.J., Sunahara, R.K., Christopoulos, A., Wootten, D. and Sexton, P.M. (2018); 'Rules of Engagement: GPCRs and G Proteins', *ACS Pharmacology and Translational Science*, **1**(2), pp 73–83.

Goddard, T.D., Huang, C.C., Meng, E.C., Pettersen, E.F., Couch, G.S., Morris, J.H. and Ferrin, T.E. (2018); 'UCSF ChimeraX: Meeting modern challenges in visualization and analysis', *Protein Science*, **27**(1), pp 14–25.

Goodman, O. B., J., Krupnick, J.G., Santini, F., Gurevich, V.V., Penn, R.B., Gagnon, A.W., Keen, J.H. and Benovic, J.L. (1996); 'Beta-arrestin acts as a clathrin adaptor in endocytosis of the beta2-adrenergic receptor', *Nature*, **383**(6599), pp 447–450.

Govaerts, C., Lefort, A., Costagliola, S., Wodak, S.J., Ballesteros, J.A., Van Sande, J., Pardo, L. and Vassart, G. (2001); 'A conserved Asn in transmembrane helix 7 is an on/off switch in the activation of the thyrotropin receptor', *Journal of Biological Chemistry*, **276**(25), pp 22991–22999.

Grim, T.W., Schmid, C.L., Stahl, E.L., Pantouli, F., Ho, J.H., Acevedo-Canabal, A., Kennedy, N.M., Cameron, M.D., Bannister, T.D. and Bohn, L.M. (2020); 'A G protein signaling-biased agonist at the mu-opioid receptor reverses morphine tolerance while preventing morphine withdrawal', *Neuropsychopharmacology*, **45**(2), pp 416–425.

Grime, R.L., Goulding, J., Uddin, R., Stoddart, L.A., Hill, S.J., Poyner, D.R., Briddon, S.J. and Wheatley, M. (2020); 'Single molecule binding of a ligand to a G-protein-

coupled receptor in real time using fluorescence correlation spectroscopy, rendered possible by nano-encapsulation in styrene maleic acid lipid particles', *Nanoscale*, **12**(21), pp 11518–11525.

Guo, J., Song, L., Liu, M. and Mahon, M.J. (2012); 'Fluorescent ligand-directed co-localization of the parathyroid hormone 1 receptor with the brush-border scaffold complex of the proximal tubule reveals hormone-dependent changes in ezrin immunoreactivity consistent with inactivation', *Biochimica et Biophysica Acta*, **1823**(12), pp 2243–2253.

Hall, S.C.L., Tognoloni, C., Charlton, J., Bragginton, E.C., Rothnie, A.J., Sridhar, P., Wheatley, M., Knowles, T.J., Arnold, T., Edler, K.J. and Dafforn, T.R. (2018); 'An acid-compatible co-polymer for the solubilization of membranes and proteins into lipid bilayer-containing nanoparticles', *Nanoscale*, **10**(22), pp 10609–10619.

Hanlon, C.D. and Andrew, D.J. (2015); 'Outside-in signaling–a brief review of GPCR signaling with a focus on the Drosophila GPCR family', *Journal of Cell Science*, **128**(19), pp 3533–3542.

Hanson, M.A., Cherezov, V., Griffith, M.T., Roth, C.B., Jaakola, V.P., Chien, E.Y., Velasquez, J., Kuhn, P. and Stevens, R.C. (2008); 'A specific cholesterol binding site is established by the 2.8 A structure of the human beta2-adrenergic receptor', *Structure*, **16**(6), pp 897–905.

Harvey, S.R. and Wysocki, V.H. (2015); 'Mass spectrometry: Bound in flight', *Nature Chemistry*, **7**(3), pp 189–190.

Hausch, F. (2017); 'Cryo-EM Structures of Class B GPCR Reveal the Activation Mechanism', *Angewandte Chemie: international edition*, **56**(41), pp 12412–12414.

Hawtin, S.R., Howard, H.C. and Wheatley, M. (2001a); 'Identification of an extracellular segment of the oxytocin receptor providing agonist-specific binding epitopes', *Biochemical Journal*, **354**(Pt 2), pp 465–472.

Hawtin, S.R., Simms, J., Conner, M., Lawson, Z., Parslow, R.A., Trim, J., Sheppard, A. and Wheatley, M. (2006); 'Charged extracellular residues, conserved throughout a G-

protein-coupled receptor family, are required for ligand binding, receptor activation, and cell-surface expression', *Journal of Biological Chemistry*, **281**(50), pp 38478–38488.

Hawtin, S.R., Tobin, A.B., Patel, S. and Wheatley, M. (2001b); 'Palmitoylation of the vasopressin V1a receptor reveals different conformational requirements for signaling, agonist-induced receptor phosphorylation, and sequestration', *Journal of Biological Chemistry*, **276**(41), pp 38139–38146.

Hay, D., Poyner, D.R. and Walker, C.S. (2019); 'Calcitonin receptors (version 2019.4) in the IUPHAR/BPS Guide to Pharmacology Database', *IUPHAR/BPS Guide to Pharmacology*, **2019**(4).

Hay, D.L., Poyner, D.R. and Sexton, P.M. (2006); 'GPCR modulation by RAMPs', *Pharmacology and Therapeutics*, **109**(1-2), pp 173–197.

He, Y., Wang, K. and Yan, N. (2014); 'The recombinant expression systems for structure determination of eukaryotic membrane proteins', *Protein and Cell*, **5**(9), pp 658–672.

Hernandez-Rocamora, V.M., Garcia-Montanes, C. and Rivas, G. (2014); 'Phospholipid bilayer nanodiscs: a powerful tool to study the structural organization and biochemical reactivity of proteins in membrane-like environments', *Current Topics in Medicinal Chemistry*, **14**(23), pp 2637–2646.

Hidalgo-Lopezosa, P., Hidalgo-Maestre, M. and Rodriguez-Borrego, M.A. (2016); 'Labor stimulation with oxytocin: effects on obstetrical and neonatal outcomes', *Latin American Journal of Nursing*, **24**, page e2744.

Hill, S.J. (2006); 'G-protein-coupled receptors: past, present and future', *British Journal of Pharmacology*, **147**, pp 27–37.

Hollenstein, K., de Graaf, C., Bortolato, A., Wang, M.W., Marshall, F.H. and Stevens, R.C. (2014); 'Insights into the structure of class B GPCRs', *Trends in Pharmacological Sciences*, **35**(1), pp 12–22.

Horsey, A.J., Briggs, D.A., Holliday, N.D., Briddon, S.J. and Kerr, I.D. (2020); 'Application of fluorescence correlation spectroscopy to study substrate binding in styrene

maleic acid lipid copolymer encapsulated ABCG2', *Biochimica et Biophysica Acta - Biomembranes*, **1862**(6), page 183218.

Hussar, D.A. and Moyer, M.R. (2019); 'Baloxavir marboxil, Fremanezumab-vfrm, Galcanezumab-gnlm, and Lofexidine hydrochloride', *Journal of the American Pharmacists Association*, **59**(1), pp 141–144.

Irannejad, R., Tomshine, J.C., Tomshine, J.R., Chevalier, M., Mahoney, J.P., Steyaert, J., Rasmussen, S.G., Sunahara, R.K., El-Samad, H., Huang, B. and von Zastrow, M. (2013); 'Conformational biosensors reveal GPCR signalling from endosomes', *Nature*, **495**(7442), pp 534–538.

Jaakola, V.P., Griffith, M.T., Hanson, M.A., Cherezov, V., Chien, E.Y., Lane, J.R., Ijzerman, A.P. and Stevens, R.C. (2008); 'The 2.6 angstrom crystal structure of a human A2A adenosine receptor bound to an antagonist', *Science*, **322**(5905), pp 1211–1217.

Jacobson, K.A. (2015); 'New paradigms in GPCR drug discovery', *Biochemical Pharmacology*, **98**(4), pp 541–555.

Jamshad, M., Charlton, J., Lin, Y.P., Routledge, S.J., Bawa, Z., Knowles, T.J., Overduin, M., Dekker, N., Dafforn, T.R., Bill, R.M., Poyner, D.R. and Wheatley, M. (2015a); 'G-protein coupled receptor solubilization and purification for biophysical analysis and functional studies, in the total absence of detergent', *Bioscience Reports*, **35**(2).

Jamshad, M., Grimard, V., Idini, I., Knowles, T.J., Dowle, M.R., Schofield, N., Sridhar, P., Lin, Y.P., Finka, R., Wheatley, M., Thomas, O.R., Palmer, R.E., Overduin, M., Govaerts, C., Ruysschaert, J.M., Edler, K.J. and Dafforn, T.R. (2015b); 'Structural analysis of a nanoparticle containing a lipid bilayer used for detergent-free extraction of membrane proteins', *Nano Research*, **8**(3), pp 774–789.

Jarvis, D.L. and Finn, E.E. (1995); 'Biochemical analysis of the N-glycosylation pathway in baculovirus-infected lepidopteran insect cells', *Virology*, **212**(2), pp 500–511.

Jastrzebska, B., Fotiadis, D., Jang, G.F., Stenkamp, R.E., Engel, A. and Palczewski, K. (2006); 'Functional and structural characterization of rhodopsin oligomers', *Journal of Biological Chemistry*, **281**(17), pp 11917–11922.

Jovcevska, I. and Muyldermans, S. (2020); 'The Therapeutic Potential of Nanobodies', *BioDrugs*, **34**(1), pp 11–26.

Kadmiel, M., Matson, B.C., Espenschied, S.T., Lenhart, P.M. and Caron, K.M. (2017); 'Loss of receptor activity-modifying protein 2 in mice causes placental dysfunction and alters PTH1R regulation', *PLoS One*, **12**(7), page e0181597.

Karageorgos, V., Venihaki, M., Sakellaris, S., Pardalos, M., Kontakis, G., Matsoukas, M.T., Gravanis, A., Margioris, A. and Liapakis, G. (2018); 'Current understanding of the structure and function of family B GPCRs to design novel drugs', *Hormones (Athens)*, **17**(1), pp 45–59.

Katritch, V., Cherezov, V. and Stevens, R.C. (2013); 'Structure-function of the G protein-coupled receptor superfamily', *Annual Review of Pharmacology and Toxicology*, **53**, pp 531–556.

Kesidis, A., Depping, P., Lode, A., Vaitsopoulou, A., Bill, R.M., Goddard, A.D. and Rothnie, A.J. (2020); 'Expression of eukaryotic membrane proteins in eukaryotic and prokaryotic hosts', *Methods*, **180**, pp 3–18.

Kilpatrick, L.E., Friedman-Ohana, R., Alcobia, D.C., Riching, K., Peach, C.J., Wheal, A.J., Briddon, S.J., Robers, M.B., Zimmerman, K., Machleidt, T., Wood, K.V., Woolard, J. and Hill, S.J. (2017); 'Real-time analysis of the binding of fluorescent VEGF165a to VEGFR2 in living cells: Effect of receptor tyrosine kinase inhibitors and fate of internalized agonist-receptor complexes', *Biochemical Pharmacology*, **136**, pp 62–75.

Kisselev, O.G., Meyer, C.K., Heck, M., Ernst, O.P. and Hofmann, K.P. (1999); 'Signal transfer from rhodopsin to the G-protein: evidence for a two-site sequential fit mechanism', *Proceedings of the National Academy of Sciences USA*, **96**(9), pp 4898–4903.

Klare, J.P., Bordignon, E., Engelhard, M. and Steinhoff, H.J. (2004); 'Sensory rhodopsin II and bacteriorhodopsin: light activated helix F movement', *Photochemical and Photobiological Sciences*, **3**(6), pp 543–547.

Klein, U., Gimpl, G. and Fahrenholz, F. (1995); 'Alteration of the myometrial plasma

membrane cholesterol content with beta-cyclodextrin modulates the binding affinity of the oxytocin receptor', *Biochemistry*, **34**(42), pp 13784–13793.

Kleinau, G., Neumann, S., Gruters, A., Krude, H. and Biebermann, H. (2013); 'Novel insights on thyroid-stimulating hormone receptor signal transduction', *Endocrine Reviews*, **34**(5), pp 691–724.

Knowles, T.J., Finka, R., Smith, C., Lin, Y.P., Dafforn, T. and Overduin, M. (2009); 'Membrane proteins solubilized intact in lipid containing nanoparticles bounded by styrene maleic acid copolymer', *Journal of the American Chemical Society*, **131**(22), pp 7484–7485.

Kolakowski, L. F., J. (1994); 'GCRDb: a G-protein-coupled receptor database', *Receptors and Channels*, **2**(1), pp 1–7.

Koltermann, A., Kettling, U., Bieschke, J., Winkler, T. and Eigen, M. (1998); 'Rapid assay processing by integration of dual-color fluorescence cross-correlation spectroscopy: high throughput screening for enzyme activity', *Proceedings of the National Academy of Sciences USA*, **95**(4), pp 1421–1426.

Komatsu, H. (2015); 'Novel Therapeutic GPCRs for Psychiatric Disorders', *International Journal of Molecular Sciences*, **16**(6), pp 14109–14121.

Krautwurst, D., Yau, K.W. and Reed, R.R. (1998); 'Identification of ligands for olfactory receptors by functional expression of a receptor library', *Cell*, **95**(7), pp 917–926.

Kuhlbrandt, W. (2014); 'Biochemistry. The resolution revolution', *Science*, **343**(6178), pp 1443–1444.

Kumar, K., Shalev-Benami, M., Robertson, M.J., Hu, H., Banister, S.D., Hollingsworth, S.A., Latorraca, N.R., Kato, H.E., Hilger, D., Maeda, S., Weis, W.I., Farrens, D.L., Dror, R.O., Malhotra, S.V., Kobilka, B.K. and Skiniotis, G. (2019); 'Structure of a Signaling Cannabinoid Receptor 1-G Protein Complex', *Cell*, **176**(3), pp 448–458.

Kusnetzow, A.K., Altenbach, C. and Hubbell, W.L. (2006); 'Conformational states and dynamics of rhodopsin in micelles and bilayers', *Biochemistry*, **45**(17), pp 5538–5550.

Lambright, D.G., Sondek, J., Bohm, A., Skiba, N.P., Hamm, H.E. and Sigler, P.B. (1996);

'The 2.0 A crystal structure of a heterotrimeric G protein', *Nature*, **379**(6563), pp 311–319.

Laue, T., Shah, B., T.M., R. and S.L., P. (1992); *Analytical Ultracentrifugation in Biochemistry and Polymer Science*, Royal Society of Chemistry, Royal Society of Chemistry (Edited by S. Harding and A. Rowe).

Laukens, B., De Wachter, C. and Callewaert, N. (2015); 'Engineering the Pichia pastoris N-Glycosylation Pathway Using the GlycoSwitch Technology', *Methods in Molecular Biology*, **1321**, pp 103–122.

Lee, S.C., Knowles, T.J., Postis, V.L., Jamshad, M., Parslow, R.A., Lin, Y.P., Goldman, A., Sridhar, P., Overduin, M., Muench, S.P. and Dafforn, T.R. (2016); 'A method for detergent-free isolation of membrane proteins in their local lipid environment', *Nature Protocols*, **11**(7), pp 1149–1162.

Lee, S.C. and Pollock, N.L. (2016); 'Membrane proteins: is the future disc shaped?', *Biochemical Society Transactions*, **44**(4), pp 1011–1018.

Leeson, P.D. and Springthorpe, B. (2007); 'The influence of drug-like concepts on decision-making in medicinal chemistry', *Nature Reviews Drug Discovery*, **6**(11), pp 881–890.

Lefkowitz, R.J. (2013); 'A brief history of G-protein coupled receptors (Nobel Lecture)', *Angewandte Chemie: international edition*, **52**(25), pp 6366–6378.

Leitz, A.J., Bayburt, T.H., Barnakov, A.N., Springer, B.A. and Sligar, S.G. (2006); 'Functional reconstitution of Beta2-adrenergic receptors utilizing self-assembling Nanodisc technology', *Biotechniques*, **40**(5), pp 601–606.

Liang, Y.L., Belousoff, M.J., Fletcher, M.M., Zhang, X., Khoshouei, M., Deganutti, G., Koole, C., Furness, S.G.B., Miller, L.J., Hay, D.L., Christopoulos, A., Reynolds, C.A., Danev, R., Wootten, D. and Sexton, P.M. (2020); 'Structure and Dynamics of Adrenomedullin Receptors AM1 and AM2 Reveal Key Mechanisms in the Control of Receptor Phenotype by Receptor Activity-Modifying Proteins', *ACS Pharmacology and Translational Science*, **3**(2), pp 263–284.

Liang, Y.L., Khoshouei, M., Deganutti, G., Glukhova, A., Koole, C., Peat, T.S., Rad-

jainia, M., Plitzko, J.M., Baumeister, W., Miller, L.J., Hay, D.L., Christopoulos, A., Reynolds, C.A., Wootten, D. and Sexton, P.M. (2018); 'Cryo-EM structure of the active, Gs-protein complexed, human CGRP receptor', *Nature*, **561**(7724), pp 492–497.

Liang, Y.L., Khoshouei, M., Radjainia, M., Zhang, Y., Glukhova, A., Tarrasch, J., Thal, D.M., Furness, S.G.B., Christopoulos, G., Coudrat, T., Danev, R., Baumeister, W., Miller, L.J., Christopoulos, A., Kobilka, B.K., Wootten, D., Skiniotis, G. and Sexton, P.M. (2017); 'Phase-plate cryo-EM structure of a class B GPCR-G-protein complex', *Nature*, **546**(7656), pp 118–123.

Lichty, J.J., Malecki, J.L., Agnew, H.D., Michelson-Horowitz, D.J. and Tan, S. (2011); 'Reprint of: Comparison of affinity tags for protein purification', *Protein Expression and Purification*.

Lindhoud, S., Carvalho, V., Pronk, J.W. and Aubin-Tam, M.E. (2016); 'SMA-SH: Modified Styrene-Maleic Acid Copolymer for Functionalization of Lipid Nanodiscs', *Biomacromolecules*, **17**(4), pp 1516–1522.

Litosch, I. (2016); 'Decoding Galphaq signaling', *Life Sciences*, **152**, pp 99–106.

Liu, W., Chun, E., Thompson, A.A., Chubukov, P., Xu, F., Katritch, V., Han, G.W., Roth, C.B., Heitman, L.H., AP, I.J., Cherezov, V. and Stevens, R.C. (2012); 'Structural basis for allosteric regulation of GPCRs by sodium ions', *Science*, **337**(6091), pp 232–236.

Liu, X., Masoudi, A., Kahsai, A.W., Huang, L.Y., Pani, B., Staus, D.P., Shim, P.J., Hirata, K., Simhal, R.K., Schwalb, A.M., Rambarat, P.K., Ahn, S., Lefkowitz, R.J. and Kobilka, B. (2019); 'Mechanism of beta2AR regulation by an intracellular positive allosteric modulator', *Science*, **364**(6447), pp 1283–1287.

Lohiya, N.K., Alam, I., Hussain, M., Khan, S.R. and Ansari, A.S. (2014); 'RISUG: an intravasal injectable male contraceptive', *Indian Journal of Medical Research*, **140**, pp 63–72.

Ly, S., Bourguet, F., Fischer, N.O., Lau, E.Y., Coleman, M.A. and Laurence, T.A. (2014);

'Quantifying interactions of a membrane protein embedded in a lipid nanodisc using fluorescence correlation spectroscopy', *Biophysical Journal*, **106**(2), pp L05–8.

Mackie, D.I., Al Mutairi, F., Davis, R.B., Kechele, D.O., Nielsen, N.R., Snyder, J.C., Caron, M.G., Kliman, H.J., Berg, J.S., Simms, J., Poyner, D.R. and Caron, K.M. (2018); 'hCALCRL mutation causes autosomal recessive nonimmune hydrops fetalis with lymphatic dysplasia', *Journal of Experimental Medicine*, **215**(9), pp 2339–2353.

Maeda, S. and Schertler, G.F. (2013); 'Production of GPCR and GPCR complexes for structure determination', *Current Opinion in Structural Biology*, **23**(3), pp 381–392.

Magalhaes, A.C., Dunn, H. and Ferguson, S.S. (2012); 'Regulation of GPCR activity, trafficking and localization by GPCR-interacting proteins', *British Journal of Pharmacology*, **165**(6), pp 1717–1736.

Magde, D., Elson, E.L. and Webb, W.W. (1974); 'Fluorescence correlation spectroscopy. II. An experimental realization', *Biopolymers*, **13**(1), pp 29–61.

Makino, C., Riley, C., Looney, J., Crouch, R. and Okada, T. (2010); 'Binding of More Than One Retinoid to Visual Opsins', *Biophysical Journal*, **99**, pp 2366–2373.

Marsh, D. (2007); 'Lateral pressure profile, spontaneous curvature frustration, and the incorporation and conformation of proteins in membranes', *Biophysical Journal*, **93**(11), pp 3884–3899.

Mary, S., Damian, M., Rahmeh, R., Mouillac, B., Marie, J., Granier, S. and Baneres, J.L. (2014); 'Amphipols in G protein-coupled receptor pharmacology: what are they good for?', *Journal of Membrane Biology*, **247**(9-10), pp 853–860.

Massotte, D. (2003); 'G protein-coupled receptor overexpression with the baculovirus-insect cell system: a tool for structural and functional studies', *Biochimica et Biophysica Acta*, **1610**(1), pp 77–89.

Matthews, J.M. and Sunde, M. (2012); 'Dimers, oligomers, everywhere', *Advances in Experimental Medicine and Biology*, **747**, pp 1–18.

McLatchie, L.M., Fraser, N.J., Main, M.J., Wise, A., Brown, J., Thompson, N., Solari, R., Lee, M.G. and Foord, S.M. (1998); 'RAMPs regulate the transport and ligand

specificity of the calcitonin-receptor-like receptor', *Nature*, **393**(6683), pp 333–339.

Meissner, O. and Haberlein, H. (2003); 'Lateral mobility and specific binding to GABA(A) receptors on hippocampal neurons monitored by fluorescence correlation spectroscopy', *Biochemistry*, **42**(6), pp 1667–1672.

Meng, E.C. and Bourne, H.R. (2001); 'Receptor activation: what does the rhodopsin structure tell us?', *Trends in Pharmacological Sciences*, **22**(11), pp 587–593.

Meyer, C.K., Bohme, M., Ockenfels, A., Gartner, W., Hofmann, K.P. and Ernst, O.P. (2000); 'Signaling states of rhodopsin. Retinal provides a scaffold for activating proton transfer switches', *Journal of Biological Chemistry*, **275**(26), pp 19713–19718.

Michel, M.C., Wieland, T. and Tsujimoto, G. (2009); 'How reliable are G-protein-coupled receptor antibodies?', *Naunyn-Schmiedeberg's Archives of Pharmacology*, **379**(4), pp 385–388.

Middleton, R.J., Briddon, S.J., Cordeaux, Y., Yates, A.S., Dale, C.L., George, M.W., Baker, J.G., Hill, S.J. and Kellam, B. (2007); 'New fluorescent adenosine A1-receptor agonists that allow quantification of ligand-receptor interactions in microdomains of single living cells', *Journal of Medicinal Chemistry*, **50**(4), pp 782–793.

Milligan, G., Shimpukade, B., Ulven, T. and Hudson, B.D. (2017); 'Complex Pharmacology of Free Fatty Acid Receptors', *Chemical Reviews*, **117**(1), pp 67–110.

Mitra, N., Liu, Y., Liu, J., Serebryany, E., Mooney, V., DeVree, B.T., Sunahara, R.K. and Yan, E.C. (2013); 'Calcium-dependent ligand binding and G-protein signaling of family B GPCR parathyroid hormone 1 receptor purified in nanodiscs', *ACS Chemical Biology*, **8**(3), pp 617–625.

Moore, C.A., Milano, S.K. and Benovic, J.L. (2007); 'Regulation of receptor trafficking by GRKs and arrestins', *Annual Review of Physiology*, **69**, pp 451–482.

Morrison, K.A., Akram, A., Mathews, A., Khan, Z.A., Patel, J.H., Zhou, C., Hardy, D.J., Moore-Kelly, C., Patel, R., Odiba, V., Knowles, T.J., Javed, M.U., Chmel, N.P., Dafforn, T.R. and Rothnie, A.J. (2016); 'Membrane protein extraction and purification using styrene-maleic acid (SMA) copolymer: effect of variations in polymer

structure', *Biochemical Journal*, **473**(23), pp 4349–4360.

Mosslehy, W., Voskoboynikova, N., Colbasevici, A., Ricke, A., Klose, D., Klare, J.P., Mulkidjanian, A.Y. and Steinhoff, H.J. (2019); 'Conformational Dynamics of Sensory Rhodopsin II in Nanolipoprotein and Styrene-Maleic Acid Lipid Particles', *Photochemistry and Photobiology*, **95**(5), pp 1195–1204.

Muller, J.C. (2013); *Small molecules or biologics? That is the question*, MedNous, viewed 05 February 2021, http://btobioinnovation.com/small-molecules-or-biologics/.

Murray, A.R., Fliesler, S.J. and Al-Ubaidi, M.R. (2009); 'Rhodopsin: the functional significance of asn-linked glycosylation and other post-translational modifications', *Ophthalmic Genetics*, **30**(3), pp 109–120.

Muth, S., Fries, A. and Gimpl, G. (2011); 'Cholesterol-induced conformational changes in the oxytocin receptor', *Biochemical Journal*, **437**(3), pp 541–553.

Nath, A., Atkins, W.M. and Sligar, S.G. (2007); 'Applications of phospholipid bilayer nanodiscs in the study of membranes and membrane proteins', *Biochemistry*, **46**(8), pp 2059–2069.

Nehme, R., Carpenter, B., Singhal, A., Strege, A., Edwards, P.C., White, C.F., Du, H., Grisshammer, R. and Tate, C.G. (2017); 'Mini-G proteins: Novel tools for studying GPCRs in their active conformation', *PLoS One*, **12**(4), page e0175642.

Nehme, R., Joubert, O., Bidet, M., Lacombe, B., Polidori, A., Pucci, B. and Mus-Veteau, I. (2010); 'Stability study of the human G-protein coupled receptor, Smoothened', *Biochimica et Biophysica Acta*, **1798**(6), pp 1100–1110.

NHS (2019); *NHS England commissioned new medicines, mogamulizumab*, Specialist Pharmacy Service, viewed 03 November 2020, https://www.sps.nhs.uk/medicines/mogamulizumab/.

NHS (2020); *NHS England commissioned new medicines, caplacizumab*, Specialist Pharmacy Service, viewed 03 November 2020, https://www.sps.nhs.uk/medicines/caplacizumab/.

Oddi, S., Dainese, E., Sandiford, S., Fezza, F., Lanuti, M., Chiurchiu, V., Totaro, A.,

Catanzaro, G., Barcaroli, D., De Laurenzi, V., Centonze, D., Mukhopadhyay, S., Selent, J., Howlett, A.C. and Maccarrone, M. (2012); 'Effects of palmitoylation of Cys(415) in helix 8 of the CB(1) cannabinoid receptor on membrane localization and signalling', *British Journal of Pharmacology*, **165**(8), pp 2635–2651.

Oldham, W.M. and Hamm, H.E. (2008); 'Heterotrimeric G protein activation by G-protein-coupled receptors', *Nature Reviews Molecular Cell Biology*, **9**(1), pp 60–71.

Oluwole, A.O., Danielczak, B., Meister, A., Babalola, J.O., Vargas, C. and Keller, S. (2017a); 'Solubilization of Membrane Proteins into Functional Lipid-Bilayer Nanodiscs Using a Diisobutylene/Maleic Acid Copolymer', *Angewandte Chemie: international edition*, **56**(7), pp 1919–1924.

Oluwole, A.O., Klingler, J., Danielczak, B., Babalola, J.O., Vargas, C., Pabst, G. and Keller, S. (2017b); 'Formation of Lipid-Bilayer Nanodiscs by Diisobutylene/Maleic Acid (DIBMA) Copolymer', *Langmuir*.

Ongini, E., Dionisotti, S., Gessi, S., Irenius, E. and Fredholm, B.B. (1999); 'Comparison of CGS 15943, ZM 241385 and SCH 58261 as antagonists at human adenosine receptors', *Naunyn-Schmiedeberg's Archives of Pharmacology*, **359**(1), pp 7–10.

Palczewski, K., Kumasaka, T., Hori, T., Behnke, C.A., Motoshima, H., Fox, B.A., Le Trong, I., Teller, D.C., Okada, T., Stenkamp, R.E., Yamamoto, M. and Miyano, M. (2000); 'Crystal structure of rhodopsin: A G protein-coupled receptor', *Science*, **289**(5480), pp 739–745.

Pandy-Szekeres, G., Munk, C., Tsonkov, T.M., Mordalski, S., Harpsoe, K., Hauser, A.S., Bojarski, A.J. and Gloriam, D.E. (2018); 'GPCRdb in 2018: adding GPCR structure models and ligands', *Nucleic Acids Research*, **46**(D1), pp D440–D446.

Pang, L., Graziano, M. and Wang, S. (1999); 'Membrane cholesterol modulates galanin-GalR2 interaction', *Biochemistry*, **38**(37), pp 12003–12011.

Pantel, J., Legendre, M., Cabrol, S., Hilal, L., Hajaji, Y., Morisset, S., Nivot, S., Vie-Luton, M.P., Grouselle, D., de Kerdanet, M., Kadiri, A., Epelbaum, J., Le Bouc, Y. and Amselem, S. (2006); 'Loss of constitutive activity of the growth hormone

secretagogue receptor in familial short stature', *Journal of Clinical Investigation*, **116**(3), pp 760–768.

Papermaster, D.S. (1982); 'Preparation of retinal rod outer segments', *Methods in Enzymology*, **81**, pp 48–52.

Parayath, N.N., Nehoff, H., Muller, P., Taurin, S. and Greish, K. (2015); 'Styrene maleic acid micelles as a nanocarrier system for oral anticancer drug delivery - dual uptake through enterocytes and M-cells', *International Journal of Nanomedicine*, **10**, pp 4653–4667.

Parmar, M., Rawson, S., Scarff, C.A., Goldman, A., Dafforn, T.R., Muench, S.P. and Postis, V.L.G. (2017); 'Using a SMALP platform to determine a sub-nm single particle cryo-EM membrane protein structure', *Biochimica et Biophysica Acta*.

Pavlos, N.J. and Friedman, P.A. (2017); 'GPCR Signaling and Trafficking: The Long and Short of It', *Trends in endocrinology and metabolism*, **28**(3), pp 213–226.

Pierce, K.L. and Lefkowitz, R.J. (2001); 'Classical and new roles of beta-arrestins in the regulation of G-protein-coupled receptors', *Nature Reviews Neuroscience*, **2**(10), pp 727–733.

Pierce, K.L., Premont, R.T. and Lefkowitz, R.J. (2002); 'Seven-transmembrane receptors', *Nature Reviews Molecular Cell Biology*, **3**(9), pp 639–650.

Popot, J.L. (2010); 'Amphipols, nanodiscs, and fluorinated surfactants: three nonconventional approaches to studying membrane proteins in aqueous solutions', *Annual Review of Biochemistry*, **79**, pp 737–775.

Poyner, D.R., Sexton, P.M., Marshall, I., Smith, D.M., Quirion, R., Born, W., Muff, R., Fischer, J.A. and Foord, S.M. (2002); 'International Union of Pharmacology. XXXII. The mammalian calcitonin gene-related peptides, adrenomedullin, amylin, and calcitonin receptors', *Pharmacological Reviews*, **54**(2), pp 233–246.

Prive, G.G. (2007); 'Detergents for the stabilization and crystallization of membrane proteins', *Methods*, **41**(4), pp 388–397.

Probst, W.C., Snyder, L.A., Schuster, D.I., Brosius, J. and Sealfon, S.C. (1992); 'Sequence

alignment of the G-protein coupled receptor superfamily', *DNA and Cell Biology*, **11**(1), pp 1–20.

Pucadyil, T.J. and Chattopadhyay, A. (2006); 'Role of cholesterol in the function and organization of G-protein coupled receptors', *Progress in Lipid Research*, **45**(4), pp 295–333.

Raehal, K.M., Walker, J.K. and Bohn, L.M. (2005); 'Morphine side effects in beta-arrestin 2 knockout mice', *Journal of Pharmacology and Experimental Therapeutics*, **314**(3), pp 1195–1201.

Ravula, T., Hardin, N.Z., Ramadugu, S.K. and Ramamoorthy, A. (2017); 'pH Tunable and Divalent Metal Ion Tolerant Polymer Lipid Nanodiscs', *Langmuir*, **33**(40), pp 10655–10662.

Rawlings, A.E. (2018); 'Membrane protein engineering to the rescue', *Biochemical Society Transactions*, **46**(6), pp 1541–1549.

Reading, E. (2019); 'Assessing Membrane Protein Structural Dynamics within Lipid Nanodiscs', *Trends in Biochemical Sciences*, **44**(11), pp 989–990.

Reeves, P.J., Kim, J.M. and Khorana, H.G. (2002); 'Structure and function in rhodopsin: a tetracycline-inducible system in stable mammalian cell lines for high-level expression of opsin mutants', *Proceedings of the National Academy of Sciences of the USA*, **99**(21), pp 13413–13418.

Resek, J.F., Farahbakhsh, Z.T., Hubbell, W.L. and Khorana, H.G. (1993); 'Formation of the meta II photointermediate is accompanied by conformational changes in the cytoplasmic surface of rhodopsin', *Biochemistry*, **32**(45), pp 12025–12032.

Rosenbaum, D.M., Rasmussen, S.G. and Kobilka, B.K. (2009); 'The structure and function of G-protein-coupled receptors', *Nature*, **459**(7245), pp 356–363.

Routledge, S.J., Jamshad, M., Little, H.A., Lin, Y.P., Simms, J., Thakker, A., Spickett, C.M., Bill, R.M., Dafforn, T.R., Poyner, D.R. and Wheatley, M. (2020); 'Ligand-induced conformational changes in a SMALP-encapsulated GPCR', *Biochimica et Biophysica Acta - Biomembranes*, **1862**(6), page 183235.

Rovati, G.E., Capra, V. and Neubig, R.R. (2007); 'The highly conserved DRY motif of class A G protein-coupled receptors: beyond the ground state', *Molecular Pharmacology*, **71**(4), pp 959–964.

Ruttinger, S., Kapusta, P., Patting, M., Wahl, M. and Macdonald, R. (2010); 'On the resolution capabilities and limits of fluorescence lifetime correlation spectroscopy (FLCS) measurements', *Journal of Fluorescence*, **20**(1), pp 105–114.

Santos, R., Ursu, O., Gaulton, A., Bento, A.P., Donadi, R.S., Bologa, C.G., Karlsson, A., Al-Lazikani, B., Hersey, A., Oprea, T.I. and Overington, J.P. (2017); 'A comprehensive map of molecular drug targets', *Nature Reviews Drug Discovery*, **16**(1), pp 19–34.

Sarkar, K., Joedicke, L., Westwood, M., Burnley, R., Wright, M., McMillan, D. and Byrne, B. (2019); 'Modulation of PTH1R signaling by an ECD binding antibody results in inhibition of beta-arrestin 2 coupling', *Scientific Reports*, **9**(1), page 14432.

Schertler, G.F., Villa, C. and Henderson, R. (1993); 'Projection structure of rhodopsin', *Nature*, **362**(6422), pp 770–772.

Schioth, H.B. and Fredriksson, R. (2005); 'The GRAFS classification system of G-protein coupled receptors in comparative perspective', *General and Comparative Endocrinology*, **142**(1-2), pp 94–101.

Schmid, C.L., Kennedy, N.M., Ross, N.C., Lovell, K.M., Yue, Z., Morgenweck, J., Cameron, M.D., Bannister, T.D. and Bohn, L.M. (2017); 'Bias Factor and Therapeutic Window Correlate to Predict Safer Opioid Analgesics', *Cell*, **171**(5), pp 1165–1175 e13.

Schuck, P., Gillis, R.B., Besong, T.M., Almutairi, F., Adams, G.G., Rowe, A.J. and Harding, S.E. (2014); 'SEDFIT-MSTAR: molecular weight and molecular weight distribution analysis of polymers by sedimentation equilibrium in the ultracentrifuge', *Analyst*, **139**(1), pp 79–92.

Seddon, A.M., Curnow, P. and Booth, P.J. (2004); 'Membrane proteins, lipids and detergents: not just a soap opera', *Biochimica et Biophysica Acta*, **1666**(1-2), pp 105–117.

Sengupta, D., Prasanna, X., Mohole, M. and Chattopadhyay, A. (2018); 'Exploring GPCR-Lipid Interactions by Molecular Dynamics Simulations: Excitements, Challenges, and the Way Forward', *Journal of Physical Chemistry B*, **122**(22), pp 5727–5737.

Serrano-Vega, M.J., Magnani, F., Shibata, Y. and Tate, C.G. (2008); 'Conformational thermostabilization of the beta1-adrenergic receptor in a detergent-resistant form', *Proceedings of the National Academy of Sciences USA*, **105**(3), pp 877–882.

Sheth, S., Brito, R., Mukherjea, D., Rybak, L.P. and Ramkumar, V. (2014); 'Adenosine receptors: expression, function and regulation', *International Journal of Molecular Sciences*, **15**(2), pp 2024–2052.

Shiroishi, M., Kobayashi, T., Ogasawara, S., Tsujimoto, H., Ikeda-Suno, C., Iwata, S. and Shimamura, T. (2011); 'Production of the stable human histamine H(1) receptor in Pichia pastoris for structural determination', *Methods*, **55**(4), pp 281–286.

Shukla, A.K., Xiao, K. and Lefkowitz, R.J. (2011); 'Emerging paradigms of beta-arrestin-dependent seven transmembrane receptor signaling', *Trends in Biochemical Sciences*, **36**(9), pp 457–469.

Simms, J., Hay, D.L., Bailey, R.J., Konycheva, G., Bailey, G., Wheatley, M. and Poyner, D.R. (2009); 'Structure-function analysis of RAMP1 by alanine mutagenesis', *Biochemistry*, **48**(1), pp 198–205.

Singh, S., Gras, A., Fiez-Vandal, C., Ruprecht, J., Rana, R., Martinez, M., Strange, P.G., Wagner, R. and Byrne, B. (2008); 'Large-scale functional expression of WT and truncated human adenosine A2A receptor in Pichia pastoris bioreactor cultures', *Microbial Cell Factories*, **7**, page 28.

Siu, F.Y., He, M., de Graaf, C., Han, G.W., Yang, D., Zhang, Z., Zhou, C., Xu, Q., Wacker, D., Joseph, J.S., Liu, W., Lau, J., Cherezov, V., Katritch, V., Wang, M.W. and Stevens, R.C. (2013); 'Structure of the human glucagon class B G-protein-coupled receptor', *Nature*, **499**(7459), pp 444–449.

SMC (2019); *Scottish Medicines Consortium advice on new medicines, erenumab*,

Scottish Medicines Consortium (SMC), viewed 08 February 2021, https://www.scottishmedicines.org.uk/media/4317/erenumab-aimovig-final-march-2019-amended-030419-for-website.pdf.

Sprang, S.R. (1997); 'G proteins, effectors and GAPs: structure and mechanism', *Current Opinion in Structural Biology*, **7**(6), pp 849–856.

Sriram, K. and Insel, P.A. (2018); 'G Protein-Coupled Receptors as Targets for Approved Drugs: How Many Targets and How Many Drugs?', *Molecular Pharmacology*, **93**(4), pp 251–258.

Stadel, J.M., Nambi, P., Shorr, R.G., Sawyer, D.F., Caron, M.G. and Lefkowitz, R.J. (1983); 'Catecholamine-induced desensitization of turkey erythrocyte adenylate cyclase is associated with phosphorylation of the beta-adrenergic receptor', *Proceedings of the National Academy of Sciences USA*, **80**(11), pp 3173–3177.

Steinhoff, H.J., Mollaaghababa, R., Altenbach, C., Hideg, K., Krebs, M., Khorana, H.G. and Hubbell, W.L. (1994); 'Time-resolved detection of structural changes during the photocycle of spin-labeled bacteriorhodopsin', *Science*, **266**(5182), pp 105–107.

Stoddart, L.A., Kilpatrick, L.E., Briddon, S.J. and Hill, S.J. (2015a); 'Probing the pharmacology of G protein-coupled receptors with fluorescent ligands', *Neuropharmacology*, **98**, pp 48–57.

Stoddart, L.A., Vernall, A.J., Briddon, S.J., Kellam, B. and Hill, S.J. (2015b); 'Direct visualisation of internalization of the adenosine A3 receptor and localization with arrestin3 using a fluorescent agonist', *Neuropharmacology*, **98**, pp 68–77.

Stoddart, L.A., Vernall, A.J., Denman, J.L., Briddon, S.J., Kellam, B. and Hill, S.J. (2012); 'Fragment screening at adenosine-A(3) receptors in living cells using a fluorescence-based binding assay', *Chemistry and Biology*, **19**(9), pp 1105–1115.

Stoddart, L.A., White, C.W., Nguyen, K., Hill, S.J. and Pfleger, K.D. (2016); 'Fluorescence- and bioluminescence-based approaches to study GPCR ligand binding', *British Journal of Pharmacology*, **173**(20), pp 3028–3037.

Stoker, K. and Baker, D.E. (2018); 'Erenumab-aooe', *Hospital Pharmacy*, **53**(6), pp 363–

368.

Stroud, Z. (2019); *Understanding bacterial cell division proteins using novel nanoencapsulation methods*, Thesis, School of Biosciences, University of Birmingham.

Stroud, Z., Hall, S.C.L. and Dafforn, T.R. (2018); 'Purification of membrane proteins free from conventional detergents: SMA, new polymers, new opportunities and new insights', *Methods*, **147**, pp 106–117.

Su, C.C., Morgan, C.E., Kambakam, S., Rajavel, M., Scott, H., Huang, W., Emerson, C.C., Taylor, D.J., Stewart, P.L., Bonomo, R.A. and Yu, E.W. (2019); 'Cryo-Electron Microscopy Structure of an Acinetobacter baumannii Multidrug Efflux Pump', *MBio*, **10**(4).

Suda, K., Filipek, S., Palczewski, K., Engel, A. and Fotiadis, D. (2004); 'The supramolecular structure of the GPCR rhodopsin in solution and native disc membranes', *Molecular Membrane Biology*, **21**(6), pp 435–446.

Sun, C., Benlekbir, S., Venkatakrishnan, P., Wang, Y., Hong, S., Hosler, J., Tajkhorshid, E., Rubinstein, J.L. and Gennis, R.B. (2018); 'Structure of the alternative complex III in a supercomplex with cytochrome oxidase', *Nature*, **557**(7703), pp 123–126.

Suzuki, N., Hajicek, N. and Kozasa, T. (2009); 'Regulation and physiological functions of G12/13-mediated signaling pathways', *Neurosignals*, **17**(1), pp 55–70.

Swainsbury, D.J.K., Scheidelaar, S., Foster, N., van Grondelle, R., Killian, J.A. and Jones, M.R. (2017); 'The effectiveness of styrene-maleic acid (SMA) copolymers for solubilisation of integral membrane proteins from SMA-accessible and SMA-resistant membranes', *Biochimica et Biophysica Acta*, **1859**(10), pp 2133–2143.

Swiecicki, J.M., Santana, J.T. and Imperiali, B. (2020); 'A Strategic Approach for Fluorescence Imaging of Membrane Proteins in a Native-like Environment', *Cell Chemical Biology*, **27**(2), pp 245–251.

Syme, C.A., Friedman, P.A. and Bisello, A. (2005); 'Parathyroid hormone receptor trafficking contributes to the activation of extracellular signal-regulated kinases but is not required for regulation of cAMP signaling', *Journal of Biological Chemistry*,

280(12), pp 11281–11288.

Taylor, W.R. (1997); 'Residual colours: a proposal for aminochromography', *Protein Engineering*, **10**(7), pp 743–746.

Tonge, S.R. and Tighe, B.J. (2001); 'Responsive hydrophobically associating polymers: a review of structure and properties', *Advanced Drug Delivery Review*, **53**(1), pp 109–122.

Trahey, M., Li, M.J., Kwon, H., Woodahl, E.L., McClary, W.D. and Atkins, W.M. (2015); 'Applications of Lipid Nanodiscs for the Study of Membrane Proteins by Surface Plasmon Resonance', *Current Protocols in Protein Science*, **81**, pp 29131–291316.

Tsai, C.J., Pamula, F., Nehme, R., Muhle, J., Weinert, T., Flock, T., Nogly, P., Edwards, P.C., Carpenter, B., Gruhl, T., Ma, P., Deupi, X., Standfuss, J., Tate, C.G. and Schertler, G.F.X. (2018); 'Crystal structure of rhodopsin in complex with a mini-Go sheds light on the principles of G protein selectivity', *Science Advances*, **4**(9), page eaat7052.

Valtcheva, N., Primorac, A., Jurisic, G., Hollmen, M. and Detmar, M. (2013); 'The orphan adhesion G protein-coupled receptor GPR97 regulates migration of lymphatic endothelial cells via the small GTPases RhoA and Cdc42', *Journal of Biological Chemistry*, **288**(50), pp 35736–35748.

Vernall, A.J., Hill, S.J. and Kellam, B. (2014); 'The evolving small-molecule fluorescent-conjugate toolbox for Class A GPCRs', *British Journal of Pharmacology*, **171**(5), pp 1073–1084.

Vernall, A.J., Stoddart, L.A., Briddon, S.J., Ng, H.W., Laughton, C.A., Doughty, S.W., Hill, S.J. and Kellam, B. (2013); 'Conversion of a non-selective adenosine receptor antagonist into A3-selective high affinity fluorescent probes using peptide-based linkers', *Organic and Biomolecular Chemistry*, **11**(34), pp 5673–5682.

Vohra, S., Taddese, B., Conner, A.C., Poyner, D.R., Hay, D.L., Barwell, J., Reeves, P.J., Upton, G.J. and Reynolds, C.A. (2013); 'Similarity between class A and class B G-protein-coupled receptors exemplified through calcitonin gene-related peptide

receptor modelling and mutagenesis studies', *Journal of the Royal Society Interface*, **10**(79), page 20120846.

Vold, R.R., Prosser, R.S. and Deese, A.J. (1997); 'Isotropic solutions of phospholipid bicelles: a new membrane mimetic for high-resolution NMR studies of polypeptides', *Journal of Biomolecular NMR*, **9**(3), pp 329–335.

Wachsmuth, M., Conrad, C., Bulkescher, J., Koch, B., Mahen, R., Isokane, M., Pepperkok, R. and Ellenberg, J. (2015); 'High-throughput fluorescence correlation spectroscopy enables analysis of proteome dynamics in living cells', *Nature Biotechnology*, **33**(4), pp 384–389.

Wald, G. and Brown, P.K. (1953); 'The molar extinction of rhodopsin', *Journal of General Physiology*, **37**(2), pp 189–200.

Waltenspuhl, Y., Schppe, J., Ehrenmann, J., Kummer, L. and Pluckthun, A. (2020); 'Crystal structure of the human oxytocin receptor', *Science Advances, Structural Biology*, **6**(29), page eabb5419.

Wang, L., Yao, D., Deepak, R., Liu, H., Xiao, Q., Fan, H., Gong, W., Wei, Z. and Zhang, C. (2018); 'Structures of the Human PGD2 Receptor CRTH2 Reveal Novel Mechanisms for Ligand Recognition', *Molecular Cell*, **72**(1), pp 48–59.

Wedekind, A., O'Malley, M.A., Niebauer, R.T. and Robinson, A.S. (2006); 'Optimization of the human adenosine A2a receptor yields in Saccharomyces cerevisiae', *Biotechnology Progress*, **22**(5), pp 1249–1255.

Wegener, A.A., Chizhov, I., Engelhard, M. and Steinhoff, H.J. (2000); 'Time-resolved detection of transient movement of helix F in spin-labelled pharaonis sensory rhodopsin II', *Journal of Molecular Biology*, **301**(4), pp 881–891.

Wegener, A.A., Klare, J.P., Engelhard, M. and Steinhoff, H.J. (2001); 'Structural insights into the early steps of receptor-transducer signal transfer in archaeal phototaxis', *EMBO J*, **20**(19), pp 5312–5319.

Weis, W.I. and Kobilka, B.K. (2018); 'The Molecular Basis of G Protein-Coupled Receptor Activation', *Annual Review of Biochemistry*, **87**, pp 897–919.

Wess, J., Nanavati, S., Vogel, Z. and Maggio, R. (1993); 'Functional role of proline and tryptophan residues highly conserved among G protein-coupled receptors studied by mutational analysis of the m3 muscarinic receptor', *EMBO Journal*, **12**(1), pp 331–338.

Wheatley, M., Charlton, J., Jamshad, M., Routledge, S.J., Bailey, S., La-Borde, P.J., Azam, M.T., Logan, R.T., Bill, R.M., Dafforn, T.R. and Poyner, D.R. (2016); 'GPCR-styrene maleic acid lipid particles (GPCR-s): their nature and potential', *Biochemical Society Transactions*, **44**(2), pp 619–623.

Wheatley, M., Howl, J., Yarwood, N.J., Davies, A.R. and Parslow, R.A. (1997); 'Preparation of a membrane fraction for receptor studies and solubilization of receptor proteins with retention of biological activity', *Methods in Molecular Biology*, **73**, pp 305–322.

Wheatley, M., Wootten, D., Conner, M.T., Simms, J., Kendrick, R., Logan, R.T., Poyner, D.R. and Barwell, J. (2012); 'Lifting the lid on GPCRs: the role of extracellular loops', *British Journal of Pharmacology*, **165**(6), pp 1688–1703.

Wimalawansa, S.J. (1996); 'Calcitonin gene-related peptide and its receptors: molecular genetics, physiology, pathophysiology, and therapeutic potentials', *Endocrine Reviews*, **17**(5), pp 533–585.

Wootten, D., Simms, J., Miller, L.J., Christopoulos, A. and Sexton, P.M. (2013); 'Polar transmembrane interactions drive formation of ligand-specific and signal pathway-biased family B G protein-coupled receptor conformations', *Proceedings of the National Academy of Sciences USA*, **110**(13), pp 5211–5216.

Wu, D., Sedgwick, A.C., Gunnlaugsson, T., Akkaya, E.U., Yoon, J. and James, T.D. (2017); 'Fluorescent chemosensors: the past, present and future', *Chemical Society Reviews*, **46**(23), pp 7105–7123.

Yen, H.Y., Hoi, K.K., Liko, I., Hedger, G., Horrell, M.R., Song, W., Wu, D., Heine, P., Warne, T., Lee, Y., Carpenter, B., Pluckthun, A., Tate, C.G., Sansom, M.S.P. and Robinson, C.V. (2018); 'PtdIns(4,5)P2 stabilizes active states of GPCRs and

enhances selectivity of G-protein coupling', *Nature*, **559**(7714), pp 423–427.

Yokogawa, M., Fukuda, M. and Osawa, M. (2019); 'Nanodiscs for Structural Biology in a Membranous Environment', *Chemical and Pharmaceutical Bulletin*, **67**(4), pp 321–326.

Yurugi-Kobayashi, T., Asada, H., Shiroishi, M., Shimamura, T., Funamoto, S., Katsuta, N., Ito, K., Sugawara, T., Tokuda, N., Tsujimoto, H., Murata, T., Nomura, N., Haga, K., Haga, T., Iwata, S. and Kobayashi, T. (2009); 'Comparison of functional non-glycosylated GPCRs expression in Pichia pastoris', *Biochemical and Biophysical Research Communications*, **380**(2), pp 271–276.

Zhang, H., Unal, H., Desnoyer, R., Han, G.W., Patel, N., Katritch, V., Karnik, S.S., Cherezov, V. and Stevens, R.C. (2015); 'Structural Basis for Ligand Recognition and Functional Selectivity at Angiotensin Receptor', *Journal of Biological Chemistry*, **290**(49), pp 29127–29139.

Zhang, Y., Sun, B., Feng, D., Hu, H., Chu, M., Qu, Q., Tarrasch, J.T., Li, S., Sun Kobilka, T., Kobilka, B.K. and Skiniotis, G. (2017); 'Cryo-EM structure of the activated GLP-1 receptor in complex with a G protein', *Nature*, **546**(7657), pp 248–253.

Zhao, L.H., Ma, S., Sutkeviciute, I., Shen, D.D., Zhou, X.E., de Waal, P.W., Li, C.Y., Kang, Y., Clark, L.J., Jean-Alphonse, F.G., White, A.D., Yang, D., Dai, A., Cai, X., Chen, J., Li, C., Jiang, Y., Watanabe, T., Gardella, T.J., Melcher, K., Wang, M.W., Vilardaga, J.P., Xu, H.E. and Zhang, Y. (2019); 'Structure and dynamics of the active human parathyroid hormone receptor-1', *Science*, **364**(6436), pp 148–153.

Zhou, X.E., Melcher, K. and Xu, H.E. (2012); 'Structure and activation of rhodopsin', *Acta Pharmacologica Sinica*, **33**(3), pp 291–299.

Appendices

Appendix A: Manuscript

Find attached a printed manuscript copy of the below publication (obtained February 2021):

Grime, R.L., Goulding, J., Uddin, R., Stoddart, L.A., Hill, S.J., Poyner, D.R., Briddon, S.J., Wheatley, M. (2020) 'Single molecule binding of a ligand to a G-protein-coupled receptor in real time using fluorescence correlation spectroscopy, rendered possible by nano-encapsulation in styrene maleic acid lipid particles.' *Nanoscale*, **12**, pp 11518-11525, DOI: https://doi.org/10.1039/D0NR01060J

Nanoscale

PAPER

View Article Online
View Journal | View Issue

Cite this: *Nanoscale*, 2020, **12**, 11518

Single molecule binding of a ligand to a G-protein-coupled receptor in real time using fluorescence correlation spectroscopy, rendered possible by nano-encapsulation in styrene maleic acid lipid particles†

Rachael L. Grime, [a,b] Joelle Goulding, [b,c] Romez Uddin, [d] Leigh A. Stoddart, [b,c] Stephen J. Hill, [b,c] David R. Poyner, [d] Stephen J. Briddon [b,c] and Mark Wheatley *[b,e]

The fundamental importance of membrane proteins in cellular processes has driven a marked increase in the use of membrane mimetic approaches for studying and exploiting these proteins. Nano-encapsulation strategies which preserve the native lipid bilayer environment are particularly attractive. Consequently, the use of poly(styrene *co*-maleic acid) (SMA) has been widely adopted to solubilise proteins directly from cell membranes by spontaneously forming "SMA Lipid Particles" (SMALPs). G-protein-coupled receptors (GPCRs) are ubiquitous "chemical switches", are central to cell signalling throughout the evolutionary tree, form the largest family of membrane proteins in humans and are a major drug discovery target. GPCR-SMALPs that retain binding capability would be a versatile platform for a wide range of downstream applications. Here, using the adenosine A_{2A} receptor ($A_{2A}R$) as an archetypical GPCR, we show for the first time the utility of fluorescence correlation spectroscopy (FCS) to characterise the binding capability of GPCRs following nano-encapsulation. Unbound fluorescent ligand CA200645 exhibited a monophasic autocorrelation curve (dwell time, τ_D = 68 ± 2 μs; diffusion coefficient, D = 287 ± 15 μm^2 s^{-1}). In the presence of $A_{2A}R$-SMALP, bound ligand was also evident (τ_D = 625 ± 23 μs; D = 30 ± 4 μm^2 s^{-1}). Using a non-receptor control (ZipA-SMALP) plus competition binding confirmed that this slower component represented binding to the encapsulated $A_{2A}R$. Consequently, the combination of GPCR-SMALP and FCS is an effective platform for the quantitative real-time characterisation of nano-encapsulated receptors, with single molecule sensitivity, that will have widespread utility for future exploitation of GPCR-SMALPs in general.

Received 6th February 2020,
Accepted 26th March 2020

DOI: 10.1039/d0nr01060j

rsc.li/nanoscale

Introduction

Membrane proteins have evolved to function within the unique environment of the hydrated membrane bilayer, which locates proteins in close association with lipids and provides lateral pressure. Extracting membrane proteins from this bilayer for purification and characterisation has, until recently, universally required detergents. This detergent solubilisation strips away closely-associated lipids, removes lateral pressure and perturbs the protein conformation, resulting in protein instability in the detergent micelle.[1,2] This is particularly problematic for highly dynamic membrane proteins such as G-protein-coupled receptors (GPCRs).[3] GPCRs all share a common protein architecture of a bundle of seven transmembrane helices and adopt a wide spectrum of conformational states in executing their cell signalling role.[4] They are found in organisms throughout the phylogenetic tree including humans, fish, insects, plants, slime-moulds and viruses (but not bacteria) and form the largest class of 'chemical switches' in biology. They transduce signals from chemical messengers acting on a cell, such as hormones and neurotransmitters,

[a]*School of Biosciences, University of Birmingham, Birmingham, B15 2TT, UK*
[b]*Centre of Membrane Proteins and Receptors (COMPARE), University of Birmingham and University of Nottingham, Midlands, UK*
[c]*Division of Physiology, Pharmacology and Neuroscience, School of Life Sciences, University of Nottingham, Nottingham, NG7 2UH, UK*
[d]*Life and Health Sciences, Aston University, Birmingham B4 7ET, UK*
[e]*Centre for Sport, Exercise and Life Sciences, Faculty of Health and Life Sciences, Alison Gingell Building, Coventry University, CoventryCV1 2DS, UK.*
E-mail: mark.wheatley@coventry.ac.uk

†Electronic supplementary information (ESI) available: Supplementary figures (Fig. S1–S3). See DOI: 10.1039/d0nr01060j

into biochemical changes within the cell *via* activation of intracellular signalling cascades.[5] As a result, they regulate almost every physiological process. Consequently, GPCRs are the largest class of membrane proteins in the human genome (with >800 receptors). Furthermore, they are very important to the pharmaceutical industry as they are the therapeutic target of 30–40% of clinically-prescribed drugs.[6,7]

In recent years, a detergent-free method has been developed for solubilising membrane proteins using poly(styrene *co*-maleic acid) (SMA). SMA spontaneously incorporates into membranes to generate nanoscale sections of the lipid bilayer as discs (~10 nm in diameter) containing encapsulated membrane protein, referred to as styrene maleic acid lipid particles (SMALPs).[8–12] Nanoscale encapsulation of GPCRs in SMALPs (GPCR-SMALPs) has potential utility for facilitating a wide range of downstream approaches such as; supporting biophysical[10,11] and structural studies,[13,14] a platform for discovery of GPCR-targeted therapeutic antibodies using phage display libraries, and for high-throughput screening in drug discovery following immobilisation of GPCR-SMALPs on surface plasmon resonance (SPR) chips.[3] In addition, there is potential for harnessing the exquisite ligand-recognition capability of GPCR-SMALPs into bespoke molecular detection devices using synthetic biology. A pre-requisite to all of these applications is establishing that the ligand-binding capability of the encapsulated GPCR is preserved in the GPCR-SMALP.

It is noteworthy that in recent years there has been a rapid increase in the design of fluorescent ligands for quantitative characterisation of binding to GPCRs.[15–17] This development has enabled fluorescence correlation spectroscopy (FCS) to be applied to studying GPCRs in cells.[18] FCS is a quantitative technique with single molecule sensitivity which uses confocal optics and a high numerical aperture objective lens to generate a small, defined illumination volume (~0.25 fL). As a fluorescent species moves through the detection volume, fluctuations in fluorescent intensity are recorded in real time. Statistical analysis of the time-dependency of these fluctuations using autocorrelation analysis allows the average dwell time of the fluorescent moiety within the detection volume to be determined.[18] Additionally, the amplitude of the autocorrelation curve is inversely proportional to the average concentration of fluorescent particles in the detection volume. This makes FCS particularly sensitive for investigating low concentrations of particles, a definite advantage for studying low-abundance targets such as GPCRs. A property of FCS is that the dwell time (τ_D) is proportional to the cube root of the molecular mass, so a doubling of mass only increases τ_D by 1.3-fold. When two fluorescent species are present in the detection volume simultaneously, they can only be resolved by FCS if the difference in their masses is large enough to yield a difference in τ_D values of at least 1.6-fold.[19] Consequently, this combination of fluorescent probes and FCS has proven to be highly effective for studying GPCRs embedded in the surface of live cells.[20–24] In this study we establish that nano-encapsulation of a GPCR within a SMALP provides the required size differential to make this a versatile strategy for quantitative analysis of ligand : GPCR complex formation by FCS. In addition, it is likely that the utility of FCS is not restricted to SMALPs but could apply more widely to GPCRs embedded in nanoscale discs of membrane irrespective of the method of encapsulation.

The adenosine A_{2A} receptor ($A_{2A}R$) is a typical GPCR with a well-defined pharmacology. It belongs to a family of four GPCRs (A_1R, $A_{2A}R$, $A_{2B}R$, A_3R) that mediate the actions of adenosine and are attractive drug targets.[25] The $A_{2A}R$ regulates the release of the neurotransmitters dopamine and glutamate in the brain, regulates blood flow to cardiac muscle and is the target for the most widely used psychoactive drug – caffeine, which blocks this receptor.[26] In this study, utilising the human $A_{2A}R$ as the GPCR, we demonstrate for the first time, the application of FCS to provide quantitative data on the binding characteristics of a GPCR that has been purified embedded within the nanoscale bilayer of the SMALP. This SMALP strategy ensures that the native lipid in close-association with the receptor protein has never been disrupted by detergent at any stage. Our study not only establishes the utility of employing FCS for characterising GPCR-SMALPs, but opens up the possibility of exploiting high-throughput solution-based FCS,[27] and highlights the potential for identifying novel fluorescent ligands targeted to specific GPCRs. In recent years, SMA has been widely used to solubilise structurally-diverse membrane proteins from a wide range of species (including bacteria, yeast, plants, insect cells and mammalian cells). The application of SMA for studying GPCRs and other membrane proteins is increasing rapidly as the utility of SMALPs becomes ever more apparent. Furthermore, 'second-generation' SMA-like polymers have already been reported that possess different properties to SMA, so the field is still expanding.[28–30] The application of FCS as a quantitative, real-time technique, with single molecule sensitivity will have widespread utility for the development of down-stream applications of SMALPs as an investigation platform in this growing field.

Experimental

Materials

CA200645 was supplied by HelloBio (Bristol, UK). SMA2000 anhydride was from Cray Valley (UK). ZM241385 {4-(2-[7-amino-2-(2-furyl)[1,2,4]triazolo[2,3-*a*][1,3,5]triazin-5yl amino] ethyl)phenol} was purchased from Tocris.

Human $A_{2A}R$ expression

Human $A_{2A}R$ was expressed in *Pichia pastoris* as described previously.[11] Prior to SMA-extraction, cells were disrupted following suspension in breaking buffer (50 mM sodium-phosphate buffer, 100 mM NaCl, 5% glycerol, EDTA-free protease inhibitor, pH 7.5, 4 °C) by 3–5 passes using an Avestin-C3 cell-disrupter. Unbroken cells and debris were removed by centrifugation (5000*g*, 10 min, 4 °C). The $A_{2A}R$-expressing membrane fraction was then sedimented (100 000*g*, 60 min, 4 °C) and re-suspended to 80 mg mL^{-1} (wet weight) in extraction buffer

(300 mM NaCl, 20 mM HEPES, pH 7.5). Membranes were stored at −80 °C until needed.

Generation of A_{2A}R-SMALPs

SMA was prepared from SMA anhydride and used to solubilise A_{2A}R from membranes as described previously.[11,12] Briefly, A_{2A}R-expressing membrane preparations were thawed on ice, and an equal volume of 2× SMA buffer (5% w/v SMA, 300 mM NaCl, 20 mM HEPES, EDTA-free protease inhibitor, pH 7.5) added to yield a final concentration of 40 mg mL^{-1} (wet weight) in 2.5% (w/v) SMA. Following gentle agitation for 1 h at room temperature, non-solubilised material was removed by centrifugation (100 000*g*, 60 min, 4 °C) to yield a supernatant containing A_{2A}R-SMALPs.

Purification of A_{2A}R-SMALPs

All purification steps were carried out at 4 °C. The A_{2A}R-SMALP supernatant was incubated with ~1 mL Ni^{2+}-NTA resin, overnight on an end-over-end rotator. The column was washed with 20 column volumes (cv) of wash buffer (300 mM NaCl, 20 mM HEPES, 25 mM imidazole, EDTA-free protease inhibitor pH 7.5). Elution of A_{2A}R-SMALP was achieved with 10 cv of elution buffer (300 mM NaCl, 20 mM HEPES, 250 mM imidazole, EDTA-free protease inhibitor pH 7.5). Elution fractions were pooled, buffer-exchanged into assay buffer (300 mM NaCl, 20 mM HEPES, pH 7.5) and concentrated using spin-concentrators (10 kDa cut-off). Concentrations of purified A_{2A}R-SMALP were determined using SDS-PAGE and densiometric analysis against protein standards in ImageJ.[31] Final concentrations ranged between 0.2–1 mg mL^{-1}.

FCS protocols

Solution-based FCS was performed essentially as described previously.[15] FCS measurements were carried out on Nunc Lab-Tek 8-well chambered #1.0 cover-glasses (Thermo Scientific, UK), using a ZEISS LSM510 Confocor3 using 633 nm excitation (0.5–1 kW cm^{-2}), with emission collected through an LP650 filter. The confocal volume was placed 200 μm above the surface of the coverslip. Cy5 NHS ester (Amersham Pharmacia Bioscience) was prepared in high performance liquid chromatography grade water (Chromasolv, Sigma-Aldrich, UK). As Cy5 has a known diffusion coefficient (D = 3.16 × 10^{-10} m^2 s^{-1}), it was employed as the standard fluorescent dye (10 nM and 500 nM) to calculate the confocal volume dimensions using eqn (1), where V = volume (mL), $\mathscr{W}_1$ is the radius of the confocal volume, determined from $\mathscr{W}_1$ = $(4{\cdot}D{\cdot}\tau_{D1})$½, where D and τ_{D1} are the diffusion coefficient and dwell time of Cy5, respectively. $\mathscr{W}_2$ represents half the height of the confocal volume and is calculated by multiplying $\mathscr{W}_1$ by the structural parameter (S). Calibration readings were taken on each day's experiments. FCS measurements were performed in a final assay volume of 200 μL. A_{2A}R-SMALPs were incubated with CA200645 (25 nM), in the presence or absence of varying concentrations of ZM241385 as stated. Equilibrium was established at 30 min and four read-times, each of 10 s, were employed to record time-dependent fluctuations in fluorescent intensity.

Data analysis

Autocorrelation analysis was performed using Zeiss AIM 4.2 software. Cy5 calibration data were used to calibrate the detection volume as previously described.[15] Experimental data were fitted to eqn (2), where N = particle number, f_i is fraction of i^{th} component, τ_{Di} is dwell time of i^{th} component, S = structure parameter (ratio of diameter to height of volume). A 1-component or 2-component 3-D diffusion model was used incorporating a triplet state component fitted using a pre-exponential. Fit quality was assessed on residuals to the fit. For 2-component fits, the first component (τ_{D1}), representing free ligand, was fixed during the fitting process to the value determined for CA200645 alone, and the second component (τ_{D2}) represented bound ligand. The concentrations of free and bound components were then calculated directly from their relative contributions to the amplitude of the autocorrelation function. Specific binding was determined using eqn (3). Total binding was defined as $N(\tau_{D2})$ (nM) as calculated from the autocorrelation analysis curve for A_{2A}R-SMALPs in the absence of competing ligand. Non-specific binding was defined as $N(\tau_{D2})$ (nM) calculated from the autocorrelation analysis curve for A_{2A}R-SMALPs in the presence of saturating competing ligand. The affinity (pK_i) of ZM241385 binding to the A_{2A}R-SMALP was determined from the IC_{50} value of the ZM241385 competition binding curve following correction for occupancy by the tracer ligand CA200645.[32] The Stokes–Einstein equation (eqn (4)) was utilised to probe the relationship between the diffusion time of the SMALP nanoparticle and its' hydrodynamic radius; where D = diffusion coefficient, k_B is Boltzmann's constant, T = temperature (K), η = dynamic viscosity and r = radius of the particle. Pooled data are presented as the mean ± s.e.m. for 3, or 4, independent preparations of A_{2A}R-SMALP. Significance ($p < 0.05$) was determined by Student's paired t-test.

$$V = \pi^{\frac{3}{2}} \cdot (_1)^2 \cdot _2 \quad (1)$$

$$G(\tau) = 1 + \frac{1}{N} \cdot \sum_{i=1}^{m} f_i \cdot \left(1 + \frac{\tau}{\tau_{Di}}\right)^{-1} \cdot \left(1 + \frac{\tau}{S^2 \cdot \tau_{Di}}\right)^{-\frac{1}{2}} \quad (2)$$

$$\text{Specific binding} = \text{Total binding} - \text{Nonspecific binding} \quad (3)$$

$$D = \frac{k_B T}{6\pi\eta r} \quad (4)$$

Results and discussion

A_{2A}R-SMALPs provides a platform for FCS

The A_{2A}R-SMALPs were generated using SMA (2.5% w/v) to extract the receptors from A_{2A}R-expressing membranes into SMALPs, followed by purification of the A_{2A}R-SMALPs as previously described (Fig. S1†).[11] The current studies utilized the

fluorescent ligand CA200645, which comprises the adenosine receptor antagonist xanthine amine congener (XAC) linked to a red BODIPY630/650 fluorophore *via* a β-alanine linker.[33] CA200645 is a high affinity ligand for both the A_1R and A_3R subtypes[33–35] and was used previously as the tracer ligand to investigate dimerization and allostery of A_3R in whole live cells using FCS.[20] Given that CA200645 is derived from the non-selective adenosine receptor antagonist XAC, it was hypothesized that CA200645 would not be A_1R/A_3R-selective and would also bind to the $A_{2A}R$. Subsequent pharmacological characterization established that CA200645 bound to the $A_{2A}R$ with high affinity (42 nM; $pA_2 = 7.37 \pm 0.17$, $n = 3$; Fig. S2†).

The initial stage of the investigation was to optimize the concentration of CA200645 for solution-based FCS, to ensure that specific binding to the $A_{2A}R$ encapsulated in the SMALP was high compared to non-specific binding. The CA200645 concentration was varied between 5–300 nM and non-specific binding determined in each case by adding a saturating concentration of a non-fluorescent competing $A_{2A}R$ ligand (ZM241385,[36] 1 μM). Specific binding varied between 20 ± 11% and 70 ± 12% of total binding (Fig. 1), with 25 nM CA200645 being used in all subsequent experiments. A data-collection time of 10 s was routinely employed which provided ample fluorescent fluctuation data for autocorrelation analysis.

The initial FCS experiments were performed with CA200645 alone in assay buffer to determine the characteristics of the free ligand. Fluctuations in fluorescence intensity for CA200645 over time are shown in Fig. 2a. Autocorrelation analysis of these fluctuations revealed a monophasic autocorrelation curve (Fig. 2b) with an average dwell time (τ_D) of the fluorescent moiety within the detection volume of 68 ± 2 μs and a diffusion coefficient $D = 287 \pm 15$ μm^2 s^{-1}, (mean ± s.e.m., n = 4) with residuals (Fig. 2c) confirming that there was no systematic deviation in the fitted curve. The experiments were then repeated using CA200645 in the presence of $A_{2A}R$-SMALP. The fluorescence intensity fluctuations for CA200645 + $A_{2A}R$-SMALP are shown in Fig. 2d. Analysis of these fluctuations revealed that the autocorrelation curve for CA200645 was significantly altered by the addition of $A_{2A}R$-SMALP. In contrast to the monophasic curve observed for ligand alone (Fig. 2b), the autocorrelation curve for CA200645 + $A_{2A}R$-SMALP was clearly biphasic (Fig. 2e) exhibiting fast and slow diffusing components (τ_{D1} and τ_{D2}, respectively) with the residuals (Fig. 2f) confirming that there was no systematic deviation in the fitted curve. The faster diffusing component exhibited a dwell-time (τ_{D1}) consistent with the free ligand (Fig. 2b). The slower component had an average dwell-time (τ_{D2}) for CA200645 of 625 ± 23 μs and a diffusion coefficient $D = 30 \pm 4$ μm^2 s^{-1} (mean ± s.e.m., n = 4). As a control, $A_{2A}R$-SMALPs alone were shown to have no detectable autofluorescence (Fig. S3†).

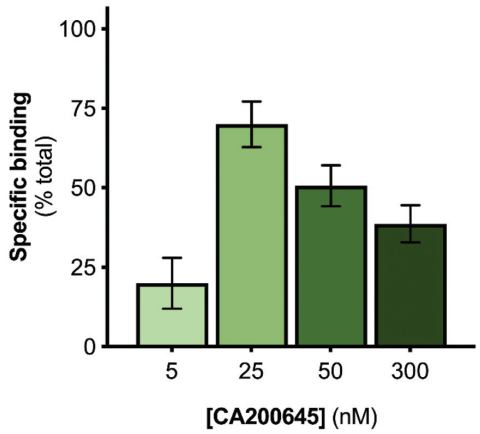

Fig. 1 Optimisation of tracer ligand concentration for solution-based FCS with $A_{2A}R$-SMALPs. The specific binding of CA200645 to $A_{2A}R$ encapsulated in a SMALP was determined at the stated concentrations. Non-specific binding was defined by a saturating concentration of ZM241385 (1 μM). Data are mean ± s.e.m. (n = 3).

Characterization of the slower diffusing component (τ_{D2})

The logical explanation for the emergence of the slower diffusing component in the presence of $A_{2A}R$-SMALP is that the ligand was binding to the receptor in the $A_{2A}R$-SMALP and that both free and bound CA200645 were being detected by FCS simultaneously as τ_{D1} and τ_{D2} respectively (Fig. 2e). Indeed, the simultaneous determination of the free ligand concentration precisely where the binding event is occurring is a particular benefit of FCS for characterising ligand : GPCR complexes. The binding of CA200645 to the $A_{2A}R$-SMALP could have been specific binding to the encapsulated GPCR or could possibly have been non-specific binding caused by partitioning of CA200645 into the lipid bilayer of the SMALP or interaction of the ligand with the SMA polymer surrounding the SMALP. The pharmacological properties of the receptor were exploited to establish the nature of the binding. A competing $A_{2A}R$-selective ligand ZM241385 was used at a saturating concentration. This would fully occupy the available $A_{2A}R$ binding sites and prevent binding of CA200645 but would not prevent any non-specific binding. The τ_{D2} component of the autocorrelation curve for CA200645 + $A_{2A}R$-SMALP in the absence, and presence, of ZM241385 (1 μM) is shown in Fig. 3. In the presence of ZM241385, the τ_{D2} component particle number (N) decreased by 62%, as the ZM241385 competed for the ligand binding site of the receptor and prevented CA200645 binding. In contrast, there was no effect of ZM241385 (1 μM) in control experiments performed using a different membrane protein encapsulated in a SMALP (ZipA, derived from *Escherichia coli*). ZipA-SMALP showed a lower particle number than $A_{2A}R$-SMALP consistent with low CA200645 binding expected in the absence of receptor (Fig. 3).

A range of ZM241385 concentrations between 10^{-12} M–10^{-6} M was used to construct a competition curve for ZM241385 binding to the nano-encapsulated $A_{2A}R$ using FCS with CA200645 as tracer ligand (Fig. 4). From these data, the affinity (pK_i) of ZM241385 for the $A_{2A}R$-SMALP was calculated as 8.2 ± 0.5 (mean ± s.e.m., n = 3). This is not significantly different to

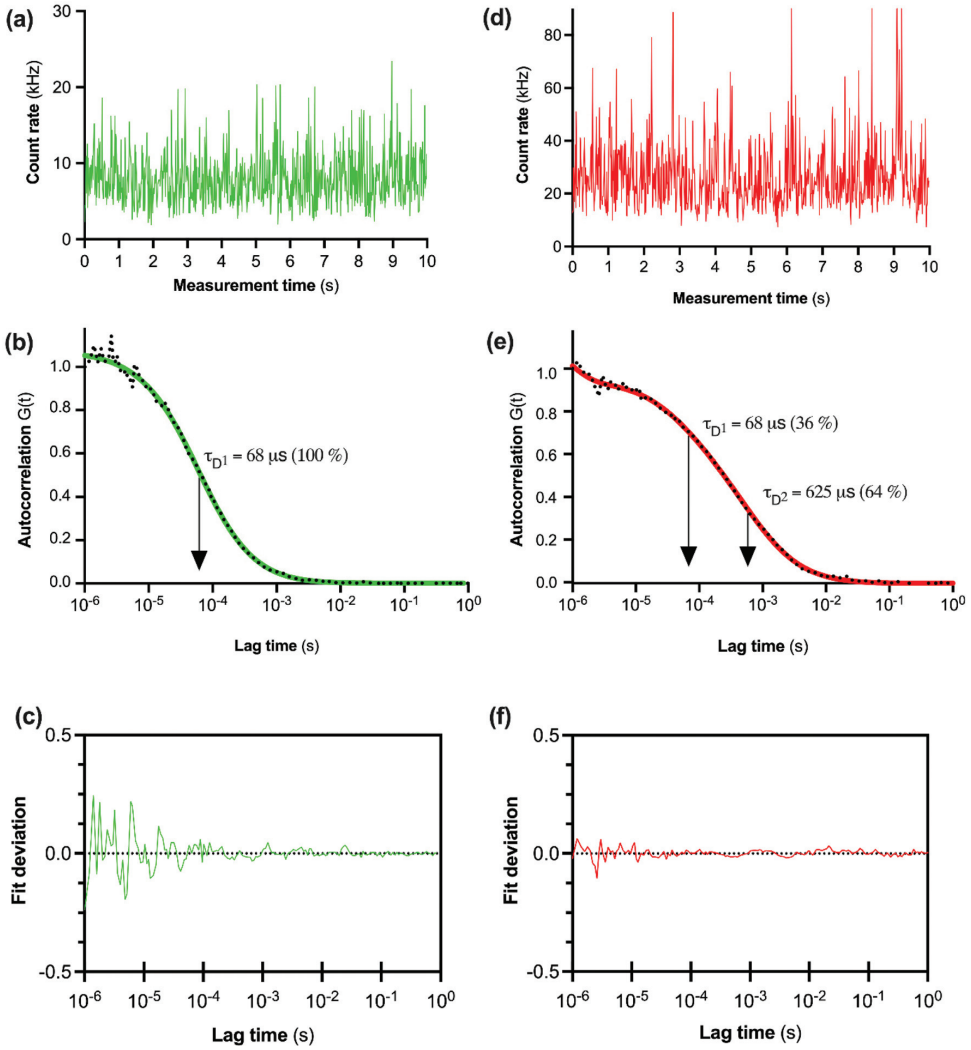

Fig. 2 FCS analysis of CA200645 binding to purified A_{2A}R-SMALP. (a) Fluctuations in fluorescent intensity with CA200645 alone. (b) Autocorrelation curve for CA200645 alone, fitted to a single-component diffusion model. (c) Deviation of data for CA200645 alone from the fitted curve. (d) Fluctuations in fluorescent intensity with CA200645 + A_{2A}R-SMALP. (e) Autocorrelation curve for CA200645 + A_{2A}R-SMALP fitted to a two-component diffusion model, in which the first component (τ_{D1}) was fixed to a three-dimensional diffusion rate of the free-ligand in solution. (f) Deviation of data for CA200645 + A_{2A}R-SMALP from the fitted curve.

the reported affinity of ZM241385 binding to A_{2A}R in the original membranes ($pK_i = 7.95 \pm 0.45$).[11]

The diffusion coefficient of the CA200645:A_{2A}R-SMALP complex ($D = 30 \pm 4$ µm^2 s^{-1}) was used to estimate the hydrodynamic radius of the A_{2A}R-SMALP as calculated by the Stokes–Einstein equation (eqn (4)), with the caveat that SMALPs are disc-shaped rather than spherical. The resulting values of 7–9 nm were consistent with the published values for the SMALP diameter of c.10 nm determined by a wide range of biophysical techniques, including small angle neutron scattering (SANS), electron microscopy (EM), attenuated total reflection Fourier transform infrared spectroscopy (ATR-FTIR), differential scanning calorimetry (DSC) and nuclear magnetic resonance spectroscopy (NMR).[10,37]

Numerous applications of FCS with GPCR-SMALPs can be envisaged. For example, allosteric modulators of GPCRs bind to sites on the receptor discrete from the 'classical' ligand binding site and are of current interest to the pharmaceutical industry as they have therapeutic potential for 'tuning' receptor signalling (up or down).[38] The size differential between

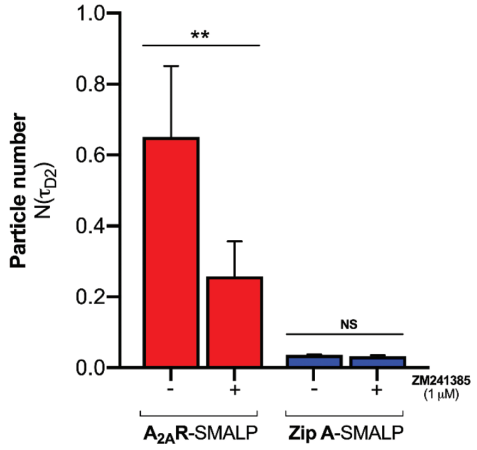

Fig. 3 Specific binding of CA200645 to A_{2A}R-SMALP detected with FCS. The particle number of the (τ_{D2}) component of the autocorrelation curve is shown for CA200645 (25 nM) binding to A_{2A}R-SMALP or to ZipA-SMALP, in the absence (–) or presence (+) of a saturating concentration of competing ligand ZM241385 (1μM). $^{**}p < 0.01$, NS = not significant. Data are mean ± s.e.m. (n = 3).

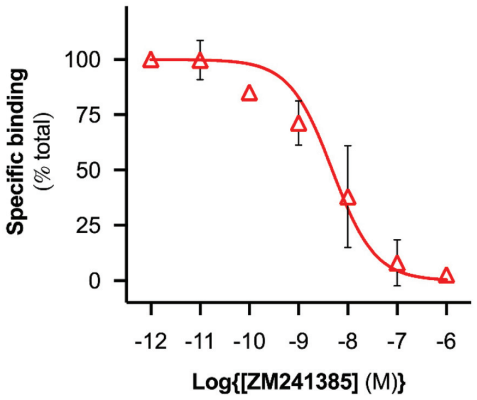

Fig. 4 Competition binding curve derived using FCS with A_{2A}R-SMALP. CA200645 (25 nM) was used as fluorescent tracer ligand in FCS experiments with A_{2A}R-SMALP in the presence of ZM421385 at the concentrations indicated. Data are mean ± s.e.m. (n = 3).

GPCR-SMALPs and fluorescent ligands is sufficiently large that FCS will be a useful tool in the future for investigating potential allosteric modulators as it is compatible with a very wide range of modulator sizes from small molecules to therapeutic antibodies. Of course other approaches for nano-encapsulation of GPCRs, such as reconstituted lipid nanodiscs stabilised by an annulus of membrane scaffolding proteins[39] or the use of recently-reported SMA-like polymers,[28–30] may also be compatible with characterisation using FCS.

The application of SMALPs to studying membrane proteins is expanding rapidly[40] and recently SMALPs have been used to obtain high resolution structures of membrane proteins; including crystallisation of the proton pump bacteriorhodopsin transferred from SMALPs into lipidic cubic phase for *in meso* crystalisation[13] and the cryo-EM structure of bacterial alternative complex III in a super-complex with cytochrome oxidase encapsulated in a SMALP.[14] Combining the technologies of fluorescence imaging and SMALP-solubilisation for studying membrane proteins is becoming increasingly versatile. For example, using proteins fluorescently labelled *via* introduced unnatural amino acids to enable single-molecule fluorescence studies and using FCS to confirm the existence of dimers of the transporter protein ABCG2 and its interaction with substrate.[41,42] This expanding utility of SMALPs has been the driver for developing new amphipathic co-polymers that retain the ability of SMA to solubilise membrane proteins but exhibit different physico-chemical characteristics to SMA. For example, styrene-*co*-maleimide (SMI) is positively-charged and retains functionality at acidic pH, in contrast to the negative charge and alkaline working range of SMA;[28] styrene maleimide quarternary ammonium (SMA-QA) forms relatively large nanodiscs (~30 nm diameter) that remain stable between pH 2.5–pH 10;[29] diisobutylene-*co*-maleic acid (DIBMA) in which the styrene aromatic ring of SMA is replaced by the aliphatic diisobutylene thereby changing how the polymer interacts with the lipid in the nanoparticles[30] and thiolated SMA (SMA-SH) which can be derivatised or immobilised *via* the introduced thiol.[43] All of these 'second generation' polymers generate lipid nanoparticles in the complete absence of detergent so preserve the native lipid in close association with the membrane protein. This is particularly important for GPCRs, as it has been shown that they can be regulated by the juxtaposition of specific membrane lipids. For example, phosphatidylethanolamine and phosphatidylglycerol favour inactive and active conformational states of the β_2-adrenergic receptor (β_2-AR), respectively.[44] Likewise, cholesterol can modulate receptor conformation[45] and function.[46,47] Indeed a specific cholesterol binding site incorporating a 'cholesterol consensus motif' has been proposed for some GPCRs following the identification of cholesterol in GPCR crystal structures.[48] In addition, the selectivity of the β_1-AR for signalling *via* the G-protein Gs, in preference to other G-proteins, is enhanced by the membrane lipid phosphatidylinositol 4,5 bisphosphate (PIP_2) but not by structural homologues. Using engineered 'mini-Gα' constructs, formation of β_1-AR : mini-Gs complex was stabilised by two molecules of PIP_2 whereas PIP_2 did not stabilise coupling between β_1-AR and other mini-Gα subunits.[49] Although the plasma membrane of *P. pastoris* differs from that of mammalian cells, notably in substitution of cholesterol by ergosterol, the major classes of phospholipids are similar and the A_{2A}R was pharmacologically active.[50] Furthermore, phospholipids in SMALPS can also be exchanged,[51] which offers opportunities in the future for modifying the lipid composition following isolation of GPCRs in SMALPs. Overall, the preservation of native lipid encapsulated in GPCR-SMALPs combined with the

advantages of FCS described above, establishes a versatile platform for investigating ligand : GPCR interactions specifically, and membrane protein interactions in general, in the future.

Conclusions

Nanodisc technology is becoming widely adopted as a membrane protein solubilisation strategy due to the benefits provided by SMALPs over other solubilisation approaches. Proteins are directly solubilised from membranes with preservation of the annular lipids thereby maintaining the native environment of the encapsulated protein. This is a notable advantage for research focusing on the large GPCR family of membrane proteins which constitute the primary therapeutic target for drug discovery.[6]

Nano-encapsulation of one of these GPCRs (the $A_{2A}R$) into SMALPs allowed us to report the first use of solution-based FCS to investigate the ligand binding capability of the receptor within the nanodisc particle in real time. Our study established that GPCR-SMALP used in combination with FCS is a powerful approach for characterising ligand : receptor complexes in a nano-scale native environment. It is anticipated that given the versatility and general utility of our strategy, it can be applied to the quantitative investigation of a wide range of target receptors plus their cognate ligands, modulators and interacting protein partners in the future.

Conflicts of interest

There are no conflicts to declare.

Acknowledgements

This work was supported by funding from the Biotechnology and Biological Sciences Research Council (BBSRC: BB/R016615/1 and BB/R016755/1) to MW and DRP and the Medical Research Council (MRC: MR/N020081/1) to SJH and SJB. RLG was supported by a BBSRC-MIBTP award to RLG and MW.

References

1 J.-L. Popot, *Annu. Rev. Biochem.*, 2010, **79**, 737–775.
2 M. Le Maire, P. Champeil and J. V. Moller, *Biochim. Biophys. Acta*, 2000, **1508**, 86–111.
3 M. Wheatley, J. Charlton, M. Jamshad, S. J. Routledge, S. Bailey, P. J. La-Borde, M. T. Azam, R. T. Logan, R. M. Bill, T. R. Dafforn and D. R. Poyner, *Biochem. Soc. Trans.*, 2016, **44**, 619–623.
4 A. J. Venkatakrishnan, X. Deupi, G. Lebon, F. M. Heydenreich, T. Flock, T. Miljus, S. Balaji, M. Bouvier, D. B. Veprintsev, C. G. Tate, G. F. Schertler and M. M. Babu, *Nature*, 2016, **536**, 484–487.
5 M. Wheatley, D. Wootten, M. T. Conner, J. Simms, R. Kendrick, R. T. Logan, D. R. Poyner and J. Barwell, *Br. J. Pharmacol.*, 2012, **165**, 1688–1703.
6 A. S. Hauser, M. M. Attwood, M. Rask-Andersen, H. B. Schiöth and D. E. Gloriam, *Nat. Rev. Drug Discovery*, 2017, **16**, 829–842.
7 K. Sriram and P. A. Insel, *Mol. Pharmacol.*, 2018, **93**, 251–258.
8 T. J. Knowles, R. Finka, C. Smith, Y. P. Lin, T. Dafforn and M. Overduin, *J. Am. Chem. Soc.*, 2009, **131**, 7484–7485.
9 C. Vargas, R. C. Arenas, E. Frotscher and S. Keller, *Nanoscale*, 2015, **7**, 20685–20696.
10 M. Jamshad, V. Grimard, I. Idini, T. J. Knowles, M. R. Dowle, N. Schofield, P. Sridhar, Y. Lin, R. Finka, M. Wheatley, O. R. T. Thomas, R. E. Palmer, M. Overduin, C. Govaerts, J.-M. Ruysschaert, K. J. Edler and T. R. Dafforn, *Nano Res.*, 2015, **8**, 774–789.
11 M. Jamshad, J. Charlton, Y.-P. Lin, S. J. Routledge, Z. Bawa, T. J. Knowles, M. Overduin, N. Dekker, T. R. Dafforn, R. M. Bill, D. R. Poyner and M. Wheatley, *Biosci. Rep.*, 2015, **35**, e00188.
12 S. C. Lee, T. J. Knowles, V. L. G. Postis, M. Jamshad, R. A. Parslow, Y.-P. Lin, A. Goldman, P. Sridhar, M. Overduin, S. P. Muench and T. R. Dafforn, *Nat. Protoc.*, 2016, **11**, 1149–1162.
13 J. Broeker, B. T. Eger and O. P. Ernst, *Structure*, 2017, **25**, 384–392.
14 C. Sun, S. Benlekbir, P. Venkatakrishnan, Y. Wang, S. Hong, J. Hosler, E. Tajkhorshid, J. L. Rubinstein and R. B. Gennis, *Nature*, 2018, **557**, 123–126.
15 S. J. Briddon, B. Kellam and S. J. Hill, *Methods Mol. Biol.*, 2011, **746**, 211–236.
16 L. A. Stoddart, L. E. Kilpatrick, S. J. Briddon and S. J. Hill, *Neuropharmacology*, 2015, **98**, 48–57.
17 L. A. Stoddart, L. E. Kilpatrick and S. J. Hill, *Trends Pharmacol. Sci.*, 2018, **39**, 136–147.
18 S. J. Briddon, L. E. Kilpatrick and S. J. Hill, *Trends Pharmacol. Sci.*, 2018, **39**, 158–174.
19 U. Meseth, T. Wohland, R. Rigler and H. Vogel, *Biophys. J.*, 1999, **76**, 1619–1631.
20 R. Corriden, L. E. Kilpatrick, B. Kellam, S. J. Briddon and S. J. Hill, *FASEB J.*, 2014, **28**, 4211–4222.
21 S. J. Briddon, R. J. Middleton, Y. Cordeaux, F. M. Flavin, J. A. Weinstein, M. W. George, B. Kellam and S. J. Hill, *Proc. Natl. Acad. Sci. U. S. A.*, 2004, **101**, 4673–4678.
22 L. E. Kilpatrick, S. J. Briddon and N. D. Holliday, *Biochim. Biophys. Acta*, 2012, **1823**, 1068–1081.
23 R. Machan and T. Wohland, *FEBS Lett.*, 2014, **588**, 3571–3584.
24 L. E. Kilpatrick and S. J. Hill, *Biochem. Soc. Trans.*, 2016, **44**, 624–629.
25 B. B. Fredholm, A. P. IJzerman, K. A. Jacobson, J. Linden and C. E. Müller, *Pharmacol. Rev.*, 2011, **63**, 1–34.
26 B. B. Fredholm, J. F. Chen, S. A. Masino and J. M. Vaugeois, *Annu. Rev. Pharmacol. Toxicol.*, 2005, **45**, 385–412.

27 M. Wachsmuth, C. Conrad, J. Bulkescher, B. Koch, R. Mahen, M. Isokane, R. Pepperkok and J. Ellenberg, *Nat. Biotechnol.*, 2015, **33**, 384–389.
28 S. C. L. Hall, C. Tognoloni, J. Charlton, E. C. Bragginton, A. J. Rothnie, P. Sridhar, M. Wheatley, T. J. Knowles, T. Arnold, K. J. Edler and T. R. Dafforn, *Nanoscale*, 2018, **10**, 10609–10619.
29 T. Ravula, N. Z. Hardin, S. K. Ramadugu, S. J. Cox and A. Ramamoorthy, *Angew. Chem., Int. Ed.*, 2018, **57**, 1342–1345.
30 A. O. Oluwole, B. Danielczak, A. Meister, J. O. Babalola, C. Vargas and S. Keller, *Angew. Chem., Int. Ed.*, 2017, **56**, 1919–1924.
31 C. A. Schneider, W. S. Rasband and K. W. Eliceiri, *Nat. Methods*, 2012, **9**, 671–675.
32 Y. Cheng and W. H. Prusoff, *Biochem. Pharmacol.*, 1973, **22**, 3099–3108.
33 L. A. Stoddart, A. J. Vernall, J. L. Denman, S. J. Briddon, B. Kellam and S. J. Hill, *Chem. Biol.*, 2012, **19**, 1105–1115.
34 A. J. Vernall, L. A. Stoddart, S. J. Briddon, H. W. Ng, C. A. Laughton, S. W. Doughty, S. J. Hill and B. Kellam, *Org. Biomol. Chem.*, 2013, **11**, 5673–5682.
35 L. A. Stoddart, E. K. M. Johnstone, A. J. Wheal, J. Goulding, M. B. Robers, T. Machleidt, K. V. Wood, S. J. Hill and K. D. G. Pfleger, *Nat. Methods*, 2015, **12**, 661–663.
36 J. R. Keddie, S. M. Poucher, G. R. Shaw, R. Brooks and M. G. Collis, *Eur. J. Pharmacol.*, 1996, **301**, 107–113.
37 S. C. L. Hall, C. Tognoloni, G. J. Price, B. Klumperman, K. J. Edler, T. R. Dafforn and T. Arnold, *Biomacromolecules*, 2018, **19**, 761–772.
38 D. Wootten, A. Christopoulos and P. Sexton, *Nat. Rev. Drug Discovery*, 2013, **12**, 630–644.
39 T. H. Bayburt and S. G. Sligar, *FEBS Lett.*, 2010, **584**, 1721–1727.
40 K. S. Simon, N. L. Pollock and S. C. Lee, *Biochem. Soc. Trans.*, 2018, **46**, 1495–1504.
41 J.-M. Swiecicki, J. T. Santana and B. Imperiali, *Cell Chem. Biol.*, 2020, **27**, 245–251.
42 A. J. Horsey, D. A. Briggs, N. D. Holliday and S. J. Briddon, *Biochim. Biophys. Acta, Biomembr.*, 2020, **1862**, 183218.
43 V. Schmidt and J. N. Sturgis, *Biochim. Biophys. Acta, Biomembr.*, 2018, **1860**, 777–783.
44 R. Dawaliby, C. Trubbia, C. Delporte, M. Masureel, P. Van Antwerpen, B. K. Kobilka and C. Govaerts, *Nat. Chem. Biol.*, 2016, **12**, 35–39.
45 S. Muth, A. Fries and G. Gimpl, *Biochem. J.*, 2011, **437**, 541–553.
46 G. Gimpl, K. Burger and F. Fahrenholz, *Biochemistry*, 1997, **36**, 10959–10974.
47 L. Pang, M. Graziano and S. Wang, *Biochemistry*, 1999, **38**, 12003–12011.
48 M. A. Hanson, V. Cherezov, M. T. Griffith, C. B. Roth, V. P. Jaakola, E. Y. Chien, J. Velasquez, P. Kuhn and R. C. Stevens, *Structure*, 2008, **16**, 897–905.
49 H. Y. Yen, K. K. Hoi, I. Liko, G. Hedger, M. R. Horrell, W. Song, D. Wu, P. Heine, T. Warne, Y. Lee, B. Carpenter, A. Plückthun, C. G. Tate, M. S. P. Sansom and C. V. Robinson, *Nature*, 2018, **559**, 423–427.
50 S. J. Routledge, M. Jamshad, H. A. Little, Y.-P. Lin, J. Simms, A. Thakker, C. M. Spickett, R. M. Bill, T. R. Dafforn, D. R. Poyner and M. Wheatley, *Biochim. Biophys. Acta, Biomembr.*, 2020, **1862**, 183235.
51 G. Hazell, T. Arnold, R. D. Barker, L. A. Clifton, N. J. Steinke, C. Tognoloni and K. J. Edler, *Langmuir*, 2016, **32**, 11845–11853.

Appendix B: Pharmacology 2018 poster prize

The following certificate was awarded for work presented in chapter 3 at The British Pharmacological Society's flagship annual meeting; Pharmacology 2018, London, UK

Appendix C: Pharmacology 2019 poster prize

The following certificate was awarded for work presented in chapter 6 at The British Pharmacological Society's flagship annual meeting; Pharmacology 2019, Edinburgh, UK

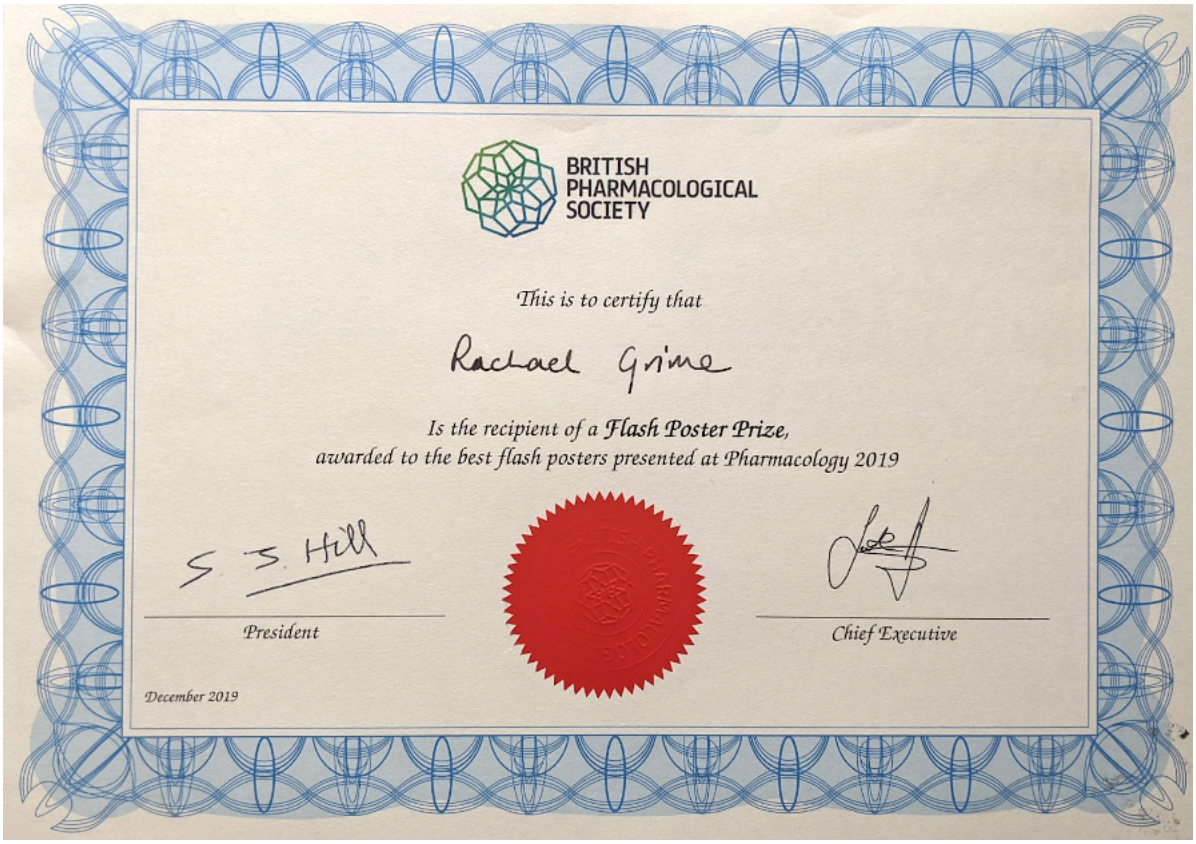

Appendix D: DNA sequencing chromatograms from CLR mutagenesis

Performed at Source Bioscience, UK (orders #443766401; #443735101; #4564490; #456957001)

1 = [$N^{201}\Delta$]CLR

100% sequence coverage + match

859 bp by T7F and 1123 bp by BGHR

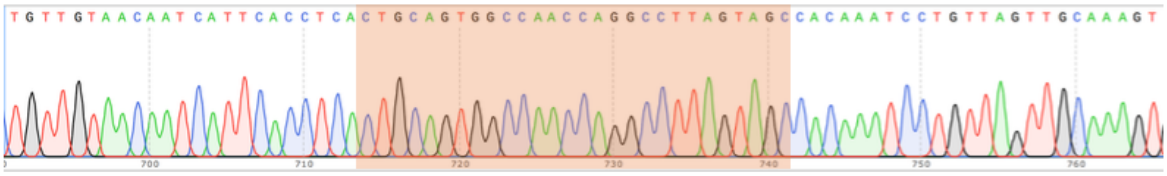

5'-CTGCAGTGGCCAACCAGGCCTTAGTAGC-3'

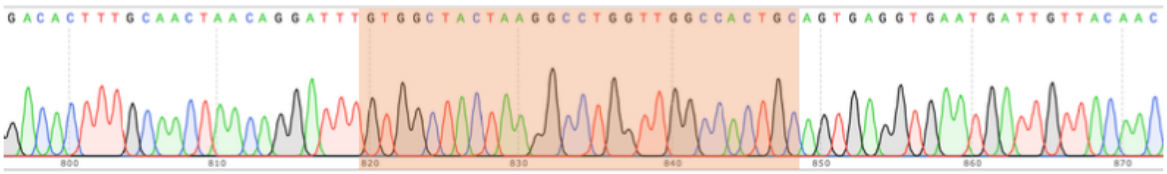

5'-GTGGCTACTAAGGCCTGGTTGGCCACTGC-3'

2 = [$Q^{202}\Delta$]CLR

100% sequence coverage + match

1007 bp by T7F and 1116 bp by BGHR

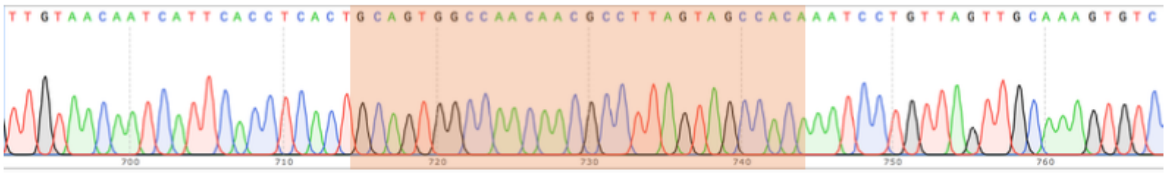

5'-GCAGTGGCCAACAACGCCTTAGTAGCCACA-3'

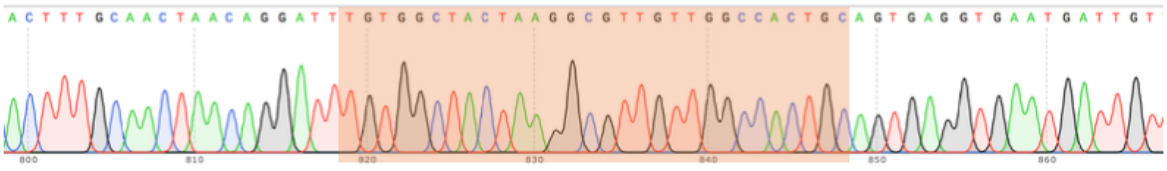

5'-TGTGGCTACTAAGGCGTTGTTGGCCACTGC-3'

3 = [A^{203}Δ]CLR

100% sequence coverage + match

1021 bp by T7F and 1123 by BGHR

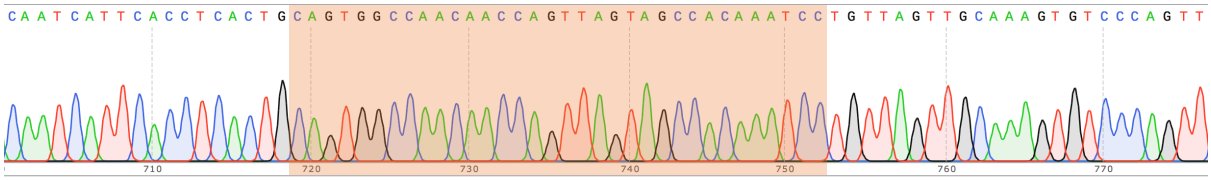

5’-CAGTGGCCAACAACCAGTTAGTAGCCACAAATCC-3’

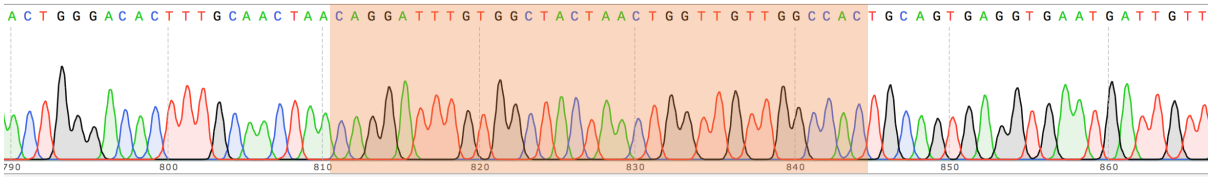

5’-CAGGATTTGTGGCTACTAACTGGTTGTTGGCCAC-3’

4 = [L^{204}Δ]CLR

100% sequence coverage + match

1014 bp by T7F and 1168 bp by BGHR

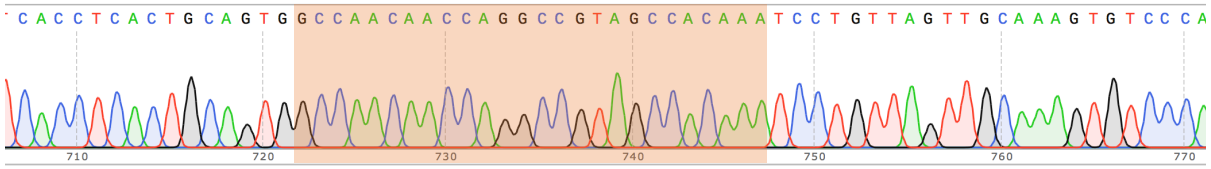

5’-GCCAACAACCAGGCCGTAGCCACAAATCCT-3’

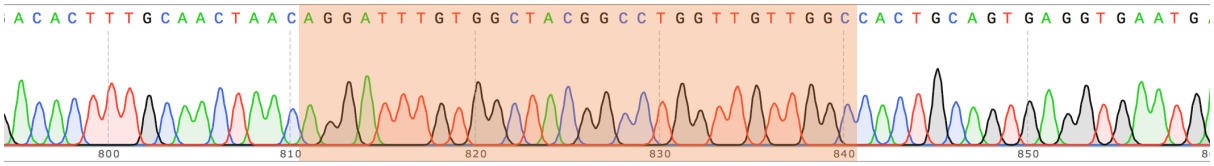

5’-AGGATTTGTGGCTACGGCCTGGTTGTTGGC-3’

5 = [V^{205}Δ]CLR

100% sequence coverage & match

1010 bp by T7F and 1126 bp by BGHR

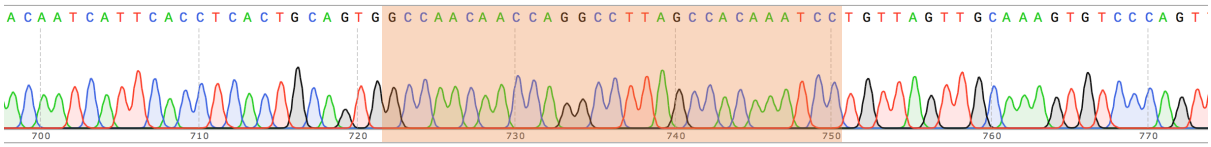

5’-GGCCAACAACCAGGCCTTAGCCACAAATCC-3’

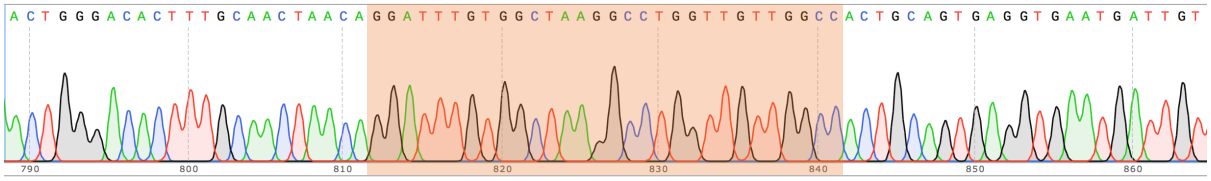

5’-GGATTTGTGGCTAAGGCCTGGTTGTTGGCC-3’

6 = [A^{206}Δ]CLR

100% sequence coverage & match

1017 bp by T7F and 1159 bp by BGHR

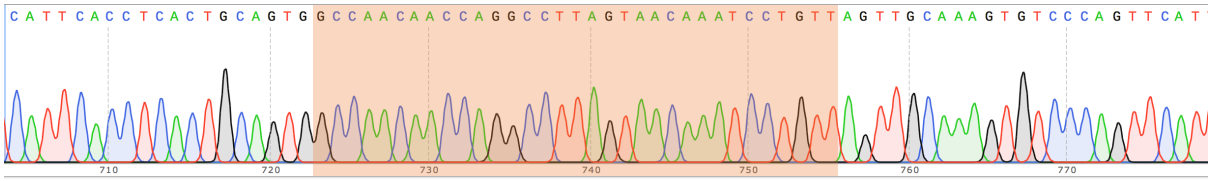

5’-GCCAACAACCAGGCCTTAGTAACAAATCCTGTTAGTT-3’

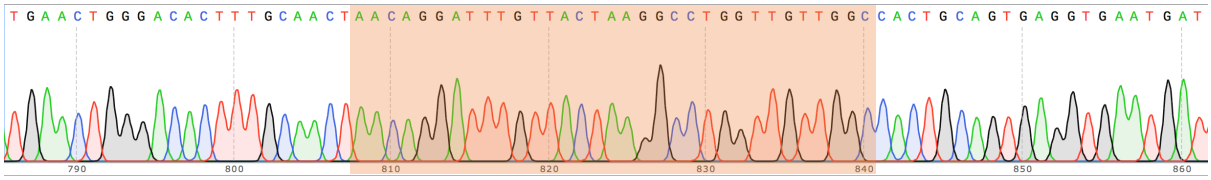

5’-AACTAACAGGATTTGTTACTAAGGCCTGGTTGTTGGC-3’

7 = [T^{207}Δ]CLR

100% sequence coverage & match

862bp by T7F and 1126bp by BHGR

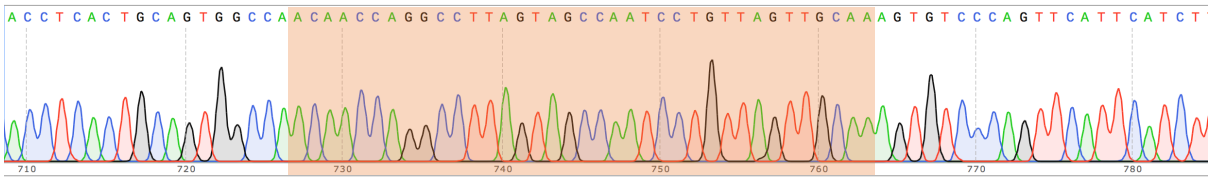

5’-ACCAGGCCTTAGTAGCCAATCCTGTTAGTTGCAA-3’

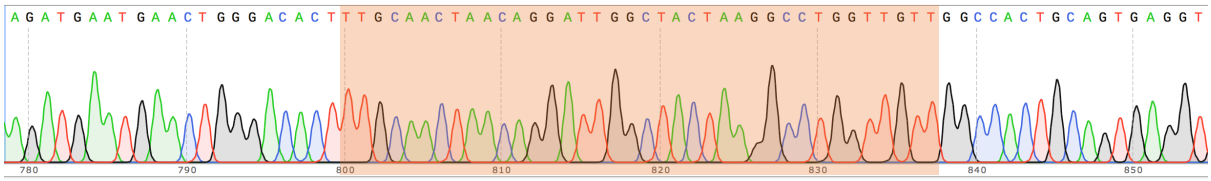

5’-TTGCAACTAACAGGATTGGCTACTAAGGCCTGGT-3’

8 = [N^{208}Δ]CLR

100% sequence coverage & match

1010 bp by T7F and 1168 bp by BGHR

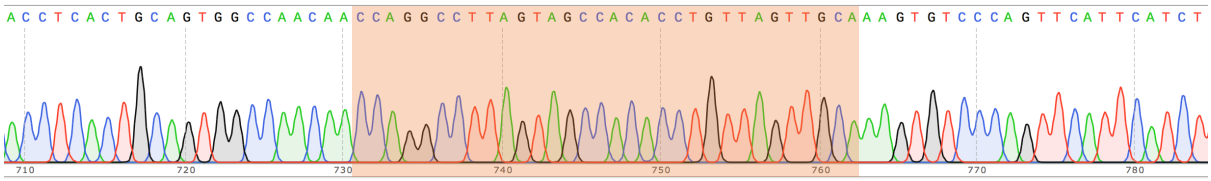

5’-CCAGGCCTTAGTAGCCACACCTGTTAGTTGCA-3’

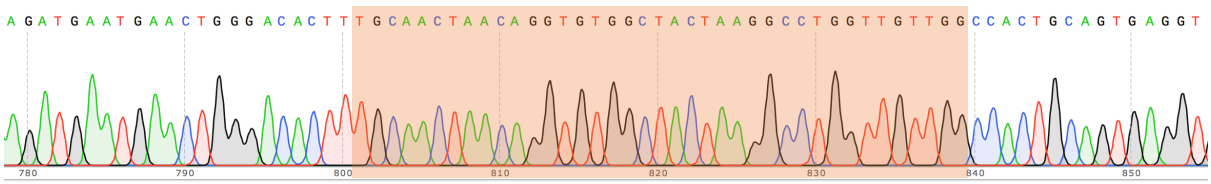

5’-TGCAACTAACAGGTGTGGCTACTAAGGCCTGG-3’

9 = [$N^{200}\Delta$]CLR, [$N^{201}\Delta$]CLR

100% sequence coverage & match

1101 bp by T7F and 1168 bp by BGHR

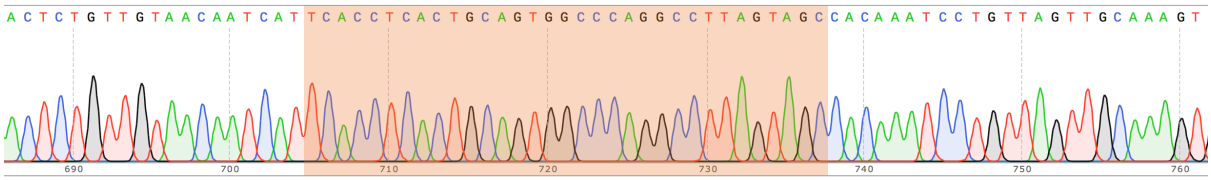

5’-TCACTGCAGTGGCCCAGGCCTTAGTAGC-3’

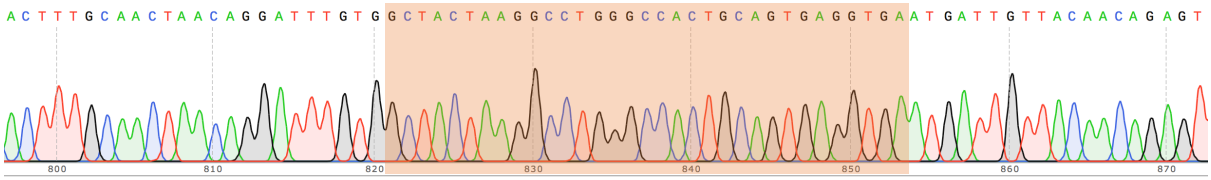

5’-GCTACTAAGGCCTGGGCCACTGCAGTGA-3’

10 = Insertion [N^{200}NN]

100% sequence coverage & match

1010 bp by T7F and 1126 bp by BGHR

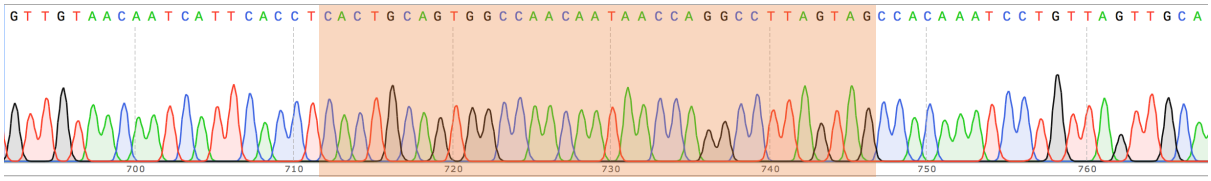

5’-CACTGCAGTGGCCAACAATAACCAGGCCTTAGTAG-3’

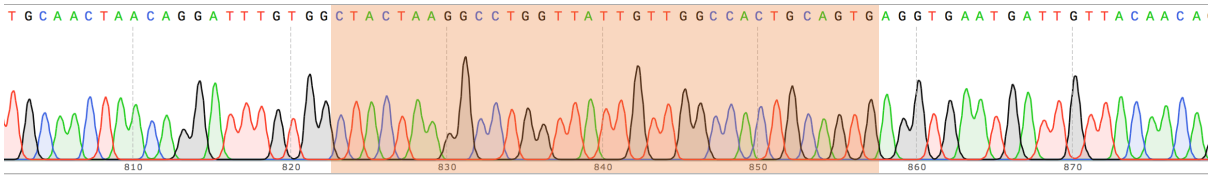

5’-CTACTAAGGCCTGGTTATTGTTGGCCACTGCAGTG-3’

11 = Triple deletion I: [N^{200}Δ]CLR, [N^{201}Δ]CLR and [N^{208}Δ]CLR

100 % sequence coverage & match

1246 bp by T7F and 1286 bp by BGHR

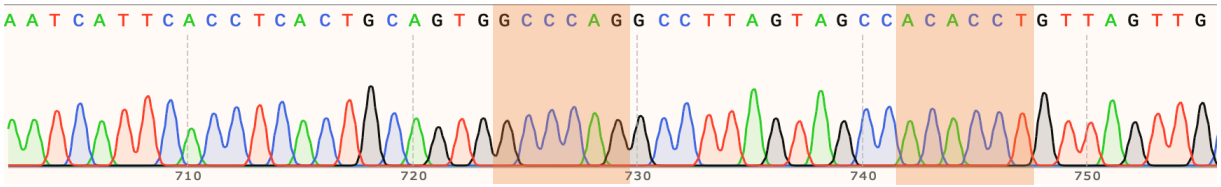

5’ – AATCATTCACCTCACTGCAGTGGCCCAGGCCTTAGTAGCCACACCTGTTAGTTG – 3’

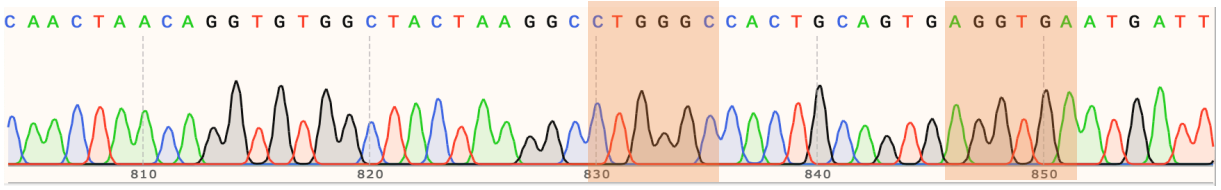

3’ – CAACTAACAGGTGTGGCTACTAAGGCCTGGGCCACTGCAGTGAGGTGAATGATT – 5’

12 = Triple deletion II: [A^{199}Δ]CLR, [N^{200}Δ]CLR and [N^{201}Δ]CLR

100 % sequence coverage & match

1196 bp by T7F and 1138 bp by BGHR

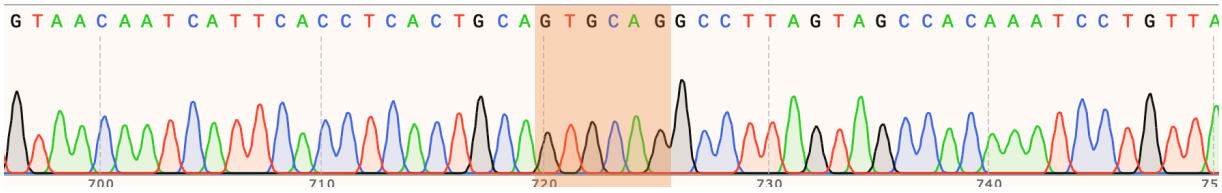

5’ – GTAACAATCATTCACCTCACTGCAGTGCAGGCCTTAGTAGCCACAAATCCTGTT – 3’

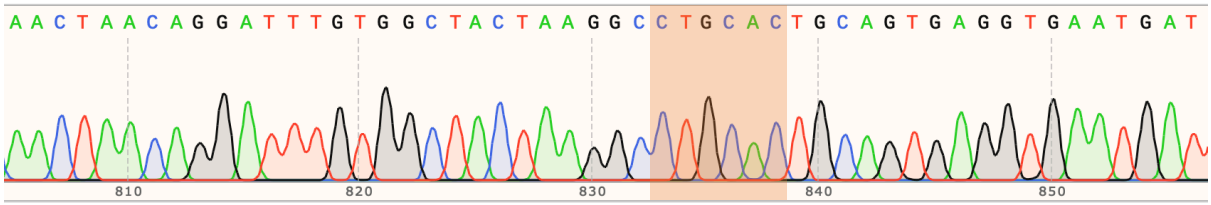

3’ – AACTAACAGGATTTGTGGCTACTAAGGCCTGCACTGCAGTGAGGTGAATGAT – 5’

Appendix E: Receptor constructs used in this study

Adenosine 2A receptor ($A_{2A}R$)

The de-glycosylated human adenosine 2A receptor construct was originally designed by Dr. Niall J. Fraser (University of Glasgow, UK) (Fraser, 2006). DNA sequencing was confirmed in sense and antisense direction by Dr. Sarah J. Routledge (Aston University, UK).

Key

*Eco*RI-START-His-10 TAG-A_{2A}R-STOP-*Not*I

Protein sequence

MHHHHHHHHHHPIMGSSVYITVELAIAVLAILGNVLVCWAVWLNSNLQNVTNYFVVSLAAADIAVGVLAIP
FAITISTGFCAACHGCLFIACFVLVLTQSSIFSLLAIAIDRYIAIRIPLRYNGLVTGTRAKGIIAICWVLS
FAIGLTPMLGWNNCGQPKEGKQHSQGCGEGQVACLFEDVVPMNYMVYFNFFACVLVPLLLMLGVYLRIFLA
ARRQLKQMESQPLPGERARSTLQKEVHAAKSLAIIVGLFALCWLPLHIINCFTFFCPDCSHAPLWLMYLAI
VLSHTNSVVNPFIYAYRIREFRQTFRKIIRSHVLRQQEPFKAAGTSARVLAAHGSDGEQVSLRLNGHPPGV
WANGSAPHPERRPNGYALGLVSGGSAQESQGNTGLPDVELLSHELKGVCPEPPGLDDPLAQDGAGVS

Oxytocin receptor (OTR_{Avi})

Key

KpnI-*Hin*DIII-KOZAK-START-His-10 TAG-TEV-HA TAG-OTR-Linker-AVI TAG-STOP-*Eco*RI-*NotI*

Protein sequence

MHHHHHHHHHHENLYFQSYPYDVPDYAEGALAANWSAEAANASAAPPGAEGNRTAGPPRRNEALARVEVAVL
CLILLLALSGNACVLLALRTTRQKHSRLFFFMKHLSIADLVVAVFQVLPQLLWDITFRFYGPDLLCRLVKYL
QVVGMFASTYLLLLMSLDRCLAICQPLRSLRRRTDRLAVLATWLGCLVASAPQVHIFSLREVADGVFDCWAV
FIQPWGPKAYITWITLAVYIVPVIVLATCYGLISFKIWQNLRLKTAAAAAAEAPEGAAAGDGGRVALARVSS
VKLISKAKIRTVKMTFIIVLAFIVCWTPFFFVQMWSVWDANAPKEASAFIIVMLLASLNSCCNPWIYMLFTG
HLFHELVQRFLCCSASYLKGRRLGETSASKKSNSSSFVLSHRSSSQRSCSQPSTAGGGGSGGGGSGGGGSGL
NDIFEAQKIEWHE

DNA sequence

GGTACCAAGCTTGCCACCATGCACCATCATCACCATCACCATCACCATCACGAGAATCTTTACTTTCAATCT
TACCCCTACGACGTCCCCGACTACGCCGAGGGCGCGCTCGCAGCCAACTGGAGCGCCGAGGCAGCCAACGCC
AGCGCCGCGCCGCCGGGGGCCGAGGGCAACCGCACCGCCGGACCCCCGCGGCGCAACGAGGCCCTGGCGCGC
GTGGAGGTGGCGGTGCTGTGTCTCATCCTGCTCCTGGCGCTGAGCGGGAACGCGTGTGTGCTGCTGGCGCTG
CGCACCACACGCCAGAAGCACTCGCGCCTCTTCTTCTTCATGAAGCACCTAAGCATCGCCGACCTGGTGGTG
GCAGTGTTTCAGGTGCTGCCGCAGTTGCTGTGGGACATCACCTTCCGCTTCTACGGGCCCGACCTGCTGTGC
CGCCTGGTCAAGTACTTGCAGGTGGTGGGCATGTTCGCCTCCACCTACCTGCTGCTGCTCATGTCCCTGGAC
CGCTGCCTGGCCATCTGCCAGCCGCTGCGCTCGCTGCGCCGCCGCACCGACCGCCTGGCAGTGCTCGCCACG
TGGCTCGGCTGCCTGGTGGCCAGCGCGCCGCAGGTGCACATCTTCTCTCTGCGCGAGGTGGCTGACGGCGTC
TTCGACTGCTGGGCCGTCTTCATCCAGCCCTGGGGACCCAAGGCCTACATCACATGGATCACGCTAGCTGTC
TACATCGTGCCGGTCATCGTGCTCGCTACCTGCTACGGCCTTATCAGCTTCAAGATCTGGCAGAACTTGCGG
CTCAAGACCGCTGCAGCGGCGGCGGCCGAGGCGCCAGAGGGCGCGGCGGCTGGCGATGGGGGGCGCGTGGCC
CTGGCGCGTGTCAGCAGCGTCAAGCTCATCTCCAAGGCCAAGATCCGCACGGTCAAGATGACTTTCATCATC
GTGCTGGCCTTCATCGTGTGCTGGACGCCTTTCTTCTTCGTGCAGATGTGGAGCGTCTGGGATGCCAACGCG
CCCAAGGAAGCCTCGGCCTTCATCATCGTCATGCTCCTGGCCAGCCTCAACAGCTGCTGCAACCCCTGGATC
TACATGCTGTTCACGGGCCACCTCTTCCACGAACTCGTGCAGCGCTTCCTGTGCTGCTCCGCCAGCTACCTG
AAGGGCAGACGCCTGGGAGAGACGAGTGCCAGCAAAAAGAGCAACTCGTCCTCCTTTGTCCTGAGCCATCGC
AGCTCCAGCCAGAGGAGCTGCTCCCAGCCATCCACGGCGGGAGGGGGCGGCTCGGGTGGGGGTGGCAGCGGC
GGTGGGGGCTCTGGTCTTAACGATATCTTCGAGGCTCAGAAAATTGAGTGGCATGAGTAGGAATTCGCGGCC
GC

Parathyroid hormone 1 receptor ($PTH1R_{Avi}$)

Key

KPNI-HINDIII-KOZAK-START-HIS-10 TAG-TEV-HA TAG-PTH1R-Linker-AVI TAG-STOP-ECORI-NOTI

Protein sequence

MHHHHHHHHHHENLYFQSYPYDVPDYAGTARIAPGLALLLCCPVLSSAYALVDADDVMTKEEQIFLLHRAQAQCE
KRLKEVLQRPASIMESDKGWTSASTSGKPRKDKASGKLYPESEEDKEAPTGSRYRGRPCLPEWDHILCWPLGAPG
EVVAVPCPDYIYDFNHKGHAYRRCDRNGSWELVPGHNRTWANYSECVKFLTNETRREREVFDRLGMIYTVGYSVSL
ASLTVAVLILAYFRRLHCTRNYIHMHLFLSFMLRAVSIFVKDAVLYSGATLDEAERLTEEELRAIAQAPPPPATA
AAGYAGCRVAVTFFLYFLATNYYWILVEGLYLHSLIFMAFFSEKKYLWGFTVFGWGLPAVFVAVWVSVRATLANT
GCWDLSSGNKKWIIQVPILASIVLNFILFINIVRVLATKLRETNAGRCDTRQQYRKLLKSTLVLMPLFGVHYIVF
MATPYTEVSGTLWQVQMHYEMLFNSFQGFFVAIIYCFCNGEVQAEIKKSWSRWTLALDFKRKARSGSSSYSYGPM
VSHTSVTNVGPRVGLGLPLSPRLLPTATTNGHPQLPGHAKPGTPALETLETTPPAMAAPKDDGFLNGSCSGLDEE
ASGPERPPALLQEEWETVMGGGGSGGGGSGGGGSGLNDIFEAQKIEWHE

DNA sequence

GGTACCAAGCTTGCCACCATGCACCATCATCACCATCACCATCACCATCACGAGAATCTTTACTTTCAATCT
TACCCCTACGACGTCCCCGACTACGCCGGCACCGCCAGGATCGCCCCCGGCCTGGCCCTGCTGCTGTGCTGC
CCCGTGCTGAGCAGCGCCTACGCCCTGGTGGACGCCGACGACGTGATGACCAAGGAGGAGCAGATCTTCCTG
CTGCACAGGGCCCAGGCCCAGTGCGAGAAGAGGCTGAAGGAGGTGCTGCAGAGGCCCGCCAGCATCATGGAG
AGCGACAAGGGCTGGACCAGCGCCAGCACCAGCGGCAAGCCCAGGAAGGACAAGGCCAGCGGCAAGCTGTAC
CCCGAGAGCGAGGAGGACAAGGAGGCCCCCACCGGCAGCAGGTACAGGGGCAGGCCCTGCCTGCCCGAGTGG
GACCACATCCTGTGCTGGCCCCTGGGCGCCCCCGGCGAGGTGGTGGCCGTGCCCTGCCCCGACTACATCTAC
GACTTCAACCACAAGGGCCACGCCTACAGGAGGTGCGACAGGAACGGCAGCTGGGAGCTGGTGCCCGGCCAC
AACAGGACCTGGGCCAACTACAGCGAGTGCGTGAAGTTCCTGACCAACGAGACCAGGGAGAGGGAGGTGTTC
GACAGGCTGGGCATGATCTACACCGTGGGCTACAGCGTGAGCCTGGCCAGCCTGACCGTGGCCGTGCTGATC
CTGGCCTACTTCAGGAGGCTGCACTGCACCAGGAACTACATCCACATGCACCTGTTCCTGAGCTTCATGCTG
AGGGCCGTGAGCATCTTCGTGAAGGACGCCGTGCTGTACAGCGGCGCCACCCTGGACGAGGCCGAGAGGCTG
ACCGAGGAGGAGCTGAGGGCCATCGCCCAGGCCCCCCCCCCCCCGCCACCGCCGCCGCCGGCTACGCCGGC
TGCAGGGTGGCCGTGACCTTCTTCCTGTACTTCCTGGCCACCAACTACTACTGGATCCTGGTGGAGGGCCTG
TACCTGCACAGCCTGATCTTCATGGCCTTCTTCAGCGAGAAGAAGTACCTGTGGGGCTTCACCGTGTTCGGC
TGGGGCCTGCCCGCCGTGTTCGTGGCCGTGTGGGTGAGCGTGAGGGCCACCCTGGCCAACACCGGCTGCTGG
GACCTGAGCAGCGGCAACAAGAAGTGGATCATCCAGGTGCCCATCCTGGCCAGCATCGTGCTGAACTTCATC
CTGTTCATCAACATCGTGAGGGTGCTGGCCACCAAGCTGAGGGAGACCAACGCCGGCAGGTGCGACACCAGG
CAGCAGTACAGGAAGCTGCTGAAGAGCACCCTGGTGCTGATGCCCCTGTTCGGCGTGCACTACATCGTGTTC
ATGGCCACCCCCTACACCGAGGTGAGCGGCACCCTGTGGCAGGTGCAGATGCACTACGAGATGCTGTTCAAC
AGCTTCCAGGGCTTCTTCGTGGCCATCATCTACTGCTTCTGCAACGGCGAGGTGCAGGCCGAGATCAAGAAG

AGCTGGAGCAGGTGGACCCTGGCCCTGGACTTCAAGAGGAAGGCCAGGAGCGGCAGCAGCAGCTACAGCTAC
GGCCCCATGGTGAGCCACACCAGCGTGACCAACGTGGGCCCCAGGGTGGGCCTGGGCCTGCCCCTGAGCCCC
AGGCTGCTGCCCACCGCCACCACCAACGGCCACCCCCAGCTGCCCGGCCACGCCAAGCCCGGCACCCCCGCC
CTGGAGACCCTGGAGACCACCCCCCCCCGCCATGGCCGCCCCCAAGGACGACGGCTTCCTGAACGGCAGCTGC
AGCGGCCTGGACGAGGAGGCCAGCGGCCCCGAGAGGCCCCCCGCCCTGCTGCAGGAGGAGTGGGAGACCGTG
ATGGGAGGGGGCGGCTCGGGTGGGGGTGGCAGCGGCGGTGGGGGCTCTGGTCTTAACGATATCTTCGAGGCT
CAGAAAATTGAGTGGCATGAGTAGGAATTCGCGGCCGC

Calcitonin receptor-like receptor (CLR)

Key

*Afl*II-START-CD8A signal peptide-linker-HA TAG-linker-CLR-STOP-*ECO*RI

Protein sequence

MALPVTALLLPLALLLHAARPDYASYPYDVPDYASLGGPSLEGSAELEESPEDSIQLGVTRNKIMTAQYECY
QKIMQDPIQQAEGVYCNRTWDGWLCWNDVAAGTESMQLCPDYFQDFDPSEKVTKICDQDGNWFRHPASNRTW
TNYTQCNVNTHEKVKTALNLFYLTIIGHGLSIASLLISLGIFFYFKSLSCQRITLHKNLFFSFVCNSVVTII
HLTAVANNQALVATNPVSCKVSQFIHLYLMGCNYFWMLCEGIYLHTLIVVAVFAEKQHLMWYYFLGWGFPLI
PACIHAIARSLYYNDNCWISSDTHLLYIIHGPICAALLVNLFFLLNIVRVLITKLKVTHQAESNLYMKAVRA
TLILVPLLGIEFVLIPWRPEGKIAEEVYDYIMHILMHFQGLLVSTIFCFFNGEVQAILRRNWNQYKIQFGNS
FSNSEALRSASYTVSTISDGPGYSHDCPSEHLNGKSIHDIENVLLKPENLYN

DNA sequence

TTAAGCTTCTTATGGCCTTACCAGTGACCGCCTTGCTCCTGCCGCTAGCCTTGCTGCTCCACGCCGCCAGGC
CGGATTACGCGTCTTACCCGTATGACGTCCCAGATTACGCATCGCTGGGAGGCCCTTCACTCGAGGGATCCG
CAGAATTAGAAGAGAGTCCTGAGGACTCAATTCAGTTGGGAGTTACTAGAAATAAAATCATGACAGCTCAAT
ATGAATGTTACCAAAAGATTATGCAAGACCCCATTCAACAAGCAGAAGGCGTTTACTGCAACAGAACCTGGG
ATGGATGGCTCTGCTGGAACGATGTTGCAGCAGGAACTGAATCAATGCAGCTCTGCCCTGATTACTTTCAGG
ACTTTGATCCATCAGAAAAAGTTACAAAGATCTGTGACCAAGATGGAAACTGGTTTAGACATCCAGCAAGCA
ACAGAACATGGACAAATTATACCCAGTGTAATGTTAACACCCACGAGAAAGTGAAGACTGCACTAAATTTGT
TTTACCTGACCATAATTGGACACGGATTGTCTATTGCATCACTGCTTATCTCGCTTGGCATATTCTTTTATT
TCAAGAGCCTAAGTTGCCAAAGGATTACCTTACACAAAAATCTGTTCTTCTCATTTGTTTGTAACTCTGTTG
TAACAATCATTCACCTCACTGCAGTGGCCAACAACCAGGCCTTAGTAGCCACAAATCCTGTTAGTTGCAAAG
TGTCCCAGTTCATTCATCTTTACCTGATGGGCTGTAATTACTTTTGGATGCTCTGTGAAGGCATTTACCTAC
ACACACTCATTGTGGTGGCCGTGTTTGCAGAGAAGCAACATTTAATGTGGTATTATTTTCTTGGCTGGGGAT
TTCCACTGATTCCTGCTTGTATACATGCCATTGCTAGAAGCTTATATTACAATGACAATTGCTGGATCAGTT
CTGATACCCATCTCCTCTACATTATCCATGGCCCAATTTGTGCTGCTTTACTGGTGAATCTTTTTTTCTTGT
TAAATATTGTACGCGTTCTCATCACCAAGTTAAAAGTTACACACCAAGCGGAATCCAATCTGTACATGAAAG
CTGTGAGAGCTACTCTTATCTTGGTGCCATTGCTTGGCATTGAATTTGTGCTGATTCCATGGCGACCTGAAG
GAAAGATTGCAGAGGAGGTATATGACTACATCATGCACATCCTTATGCACTTCCAGGGTCTTTTGGTCTCTA
CCATTTTCTGCTTCTTTAATGGAGAGGTTCAAGCAATTCTGAGAAGAAACTGGAATCAATACAAAATCCAAT
TTGGAAACAGCTTTTCCAACTCAGAAGCTCTTCGTAGTGCGTCTTACACAGTGTCAACAATCAGTGATGGTC
CAGGTTATAGTCATGACTGTCCTAGTGAACACTTAAATGGAAAAAGCATCCATGATATTGAAAATGTTCTCT
TAAAACCAGAAAATTTATATAATTGAGGAATTC

Receptor Activity Modifying Proteins (RAMPs)

Key: Untagged RAMP

XhoI-KOZAK-START-Signal peptide-RAMP-STOP-*NotI*

RAMP1

MARALCRLPRRGLWLLLAHHLFMTTACQEANYGALLRELCLTQFQVDMEAVGETLWCDWGRTIRSYRELADC
TWHMAEKLGCFWPNAEVDRFFLAVHGRYFRSCPISGRAVRDPPGSILYPFIVVPITVTLLVTALVVWQSKRT
EGIV

RAMP2

MASLRVERAGGPRLPRTRVGRPAALRLLLLLGAVLNPHEALAQPLPTTGTPGSEGGTVKNYETAVQFCWNHY
KDQMDPIEKDWCDWAMISRPYSTLRDCLEHFAELFDLGFPNPLAERIIFETHQIHFANCSLVQPTFSDPPED
VLLAMIIAPICLIPFLITLVVWRSKDSEAQA

RAMP3

METGALRRPQLLPLLLLLCGGCPRAGGCNETGMLERLPLCGKAFADMMGKVDVWKWCNLSEFIVYYESFTNC
TEMEANVVGCYWPNPLAQGFITGIHRQFFSNCTVDRVHLEDPPDEVLIPLIVIPVVLTVAMAGLVVWRSKRT
DTLL

Key: FLAG-tagged RAMP

XhoI-KOZAK-START-Signal peptide-FLAG-tag-RAMP-STOP-*NotI*

FLAG-RAMP2

MASLRVERAGGPRLPRTRVGRPAALRLLLLLGAVLNPHEALADYKDDDKQPLPTTGTPGSEGGTVKNYETAV
QFCWNHYKDQMDPIEKDWCDWAMISRPYSTLRDCLEHFAELFDLGFPNPLAERIIFETHQIHFANCSLVQPT
FSDPPEDVLLAMIIAPICLIPFLITLVVWRSKDSEAQA

Appendix F: 'Snake plot' diagrams of receptors in this study

human adenosine A2 receptor ($A_{2A}R$)

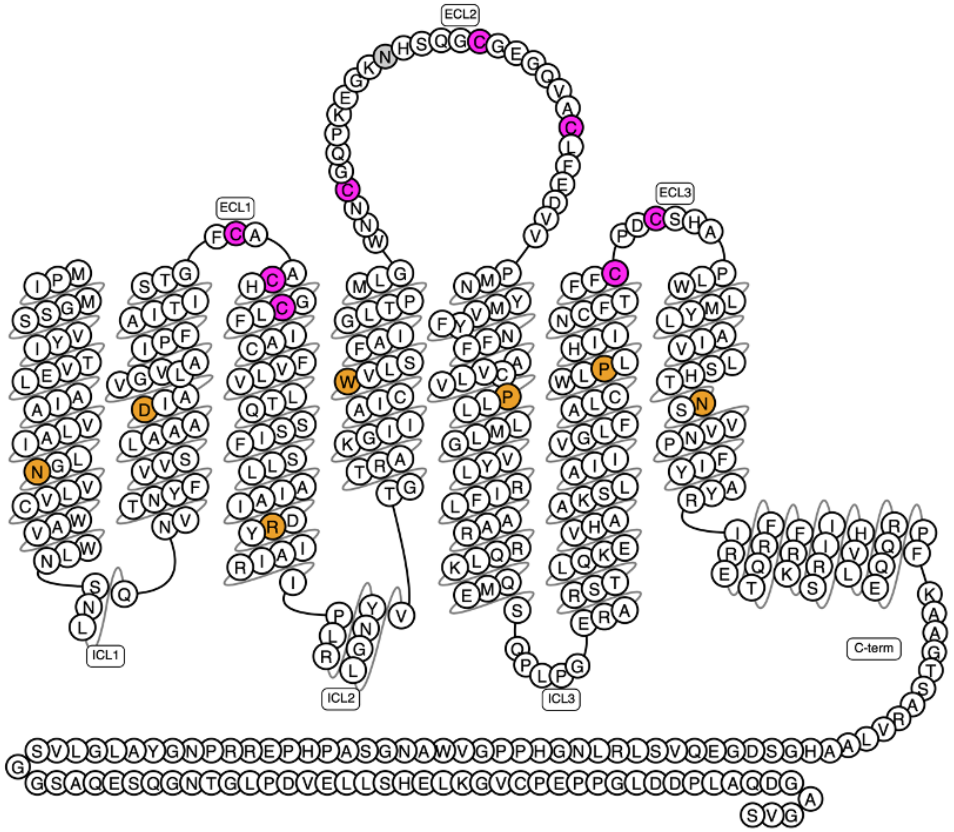

Orange: Ballesteros residues

Pink: Conserved cysteines for disulphide bond formation

Grey: N-link glycosylation (this study utilised $Asn^{154}Gln$ mutation to preclude glycosylation)

bovine rhodopsin

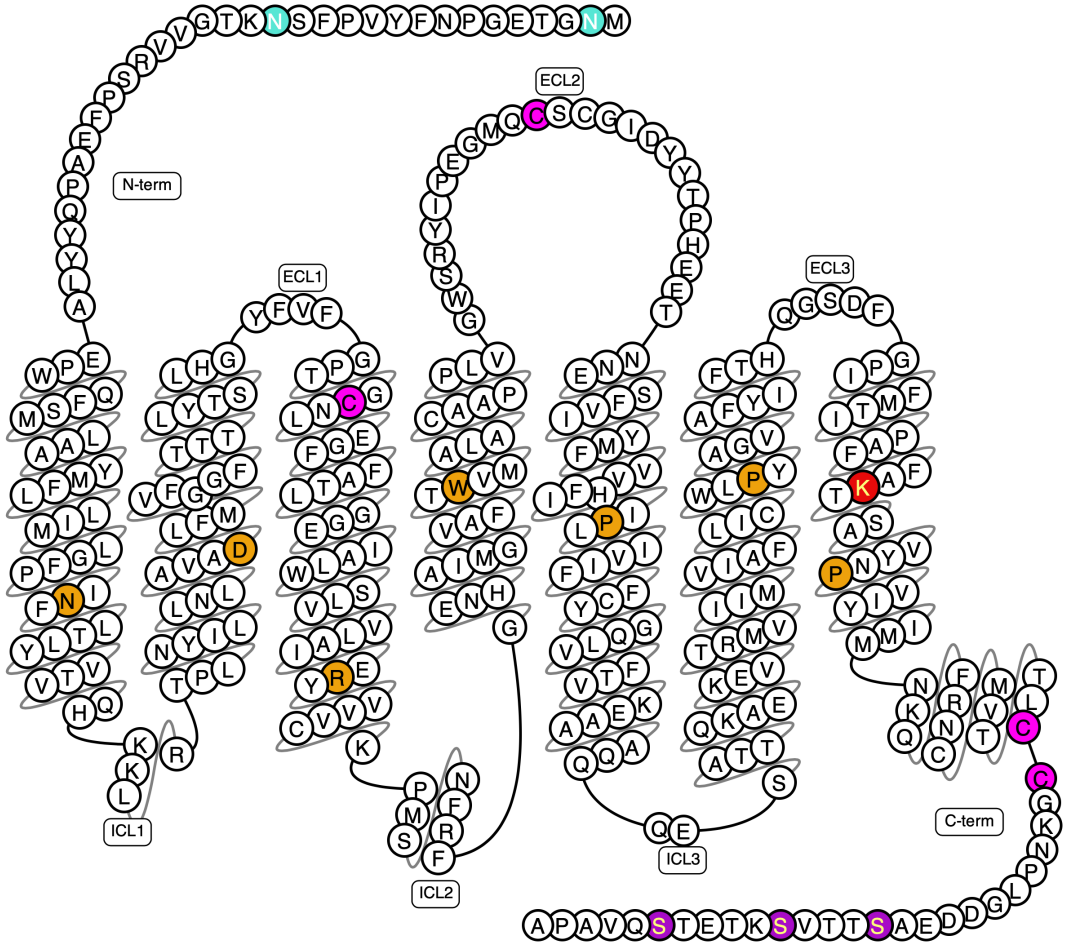

Orange: Ballesteros residues

Red: Schiff base formation at Lys^{296}

Pink: Conserved cysteines for disulphide bond formation, or palmytoilation

Purple: Phosphorylation

Turquoise: N-linked glycosylation

human oxytocin receptor (OTR)

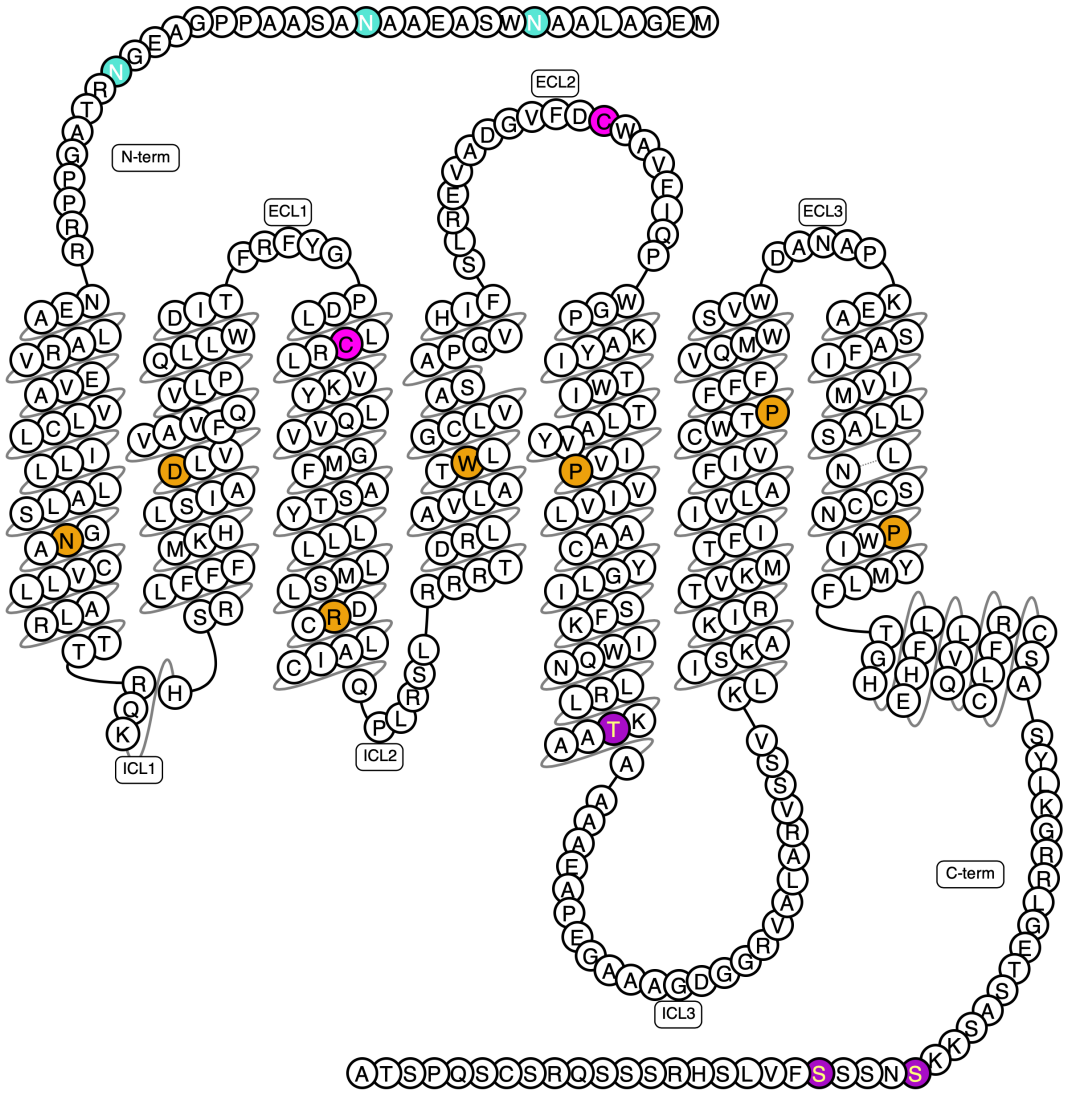

Orange: Ballesteros residues

Pink: Conserved cysteines for disulphide bond formation

Purple: Phosphorylation

Turquoise: N-linked glycosylation

human parathyroid hormone 1 receptor (PTH1R)

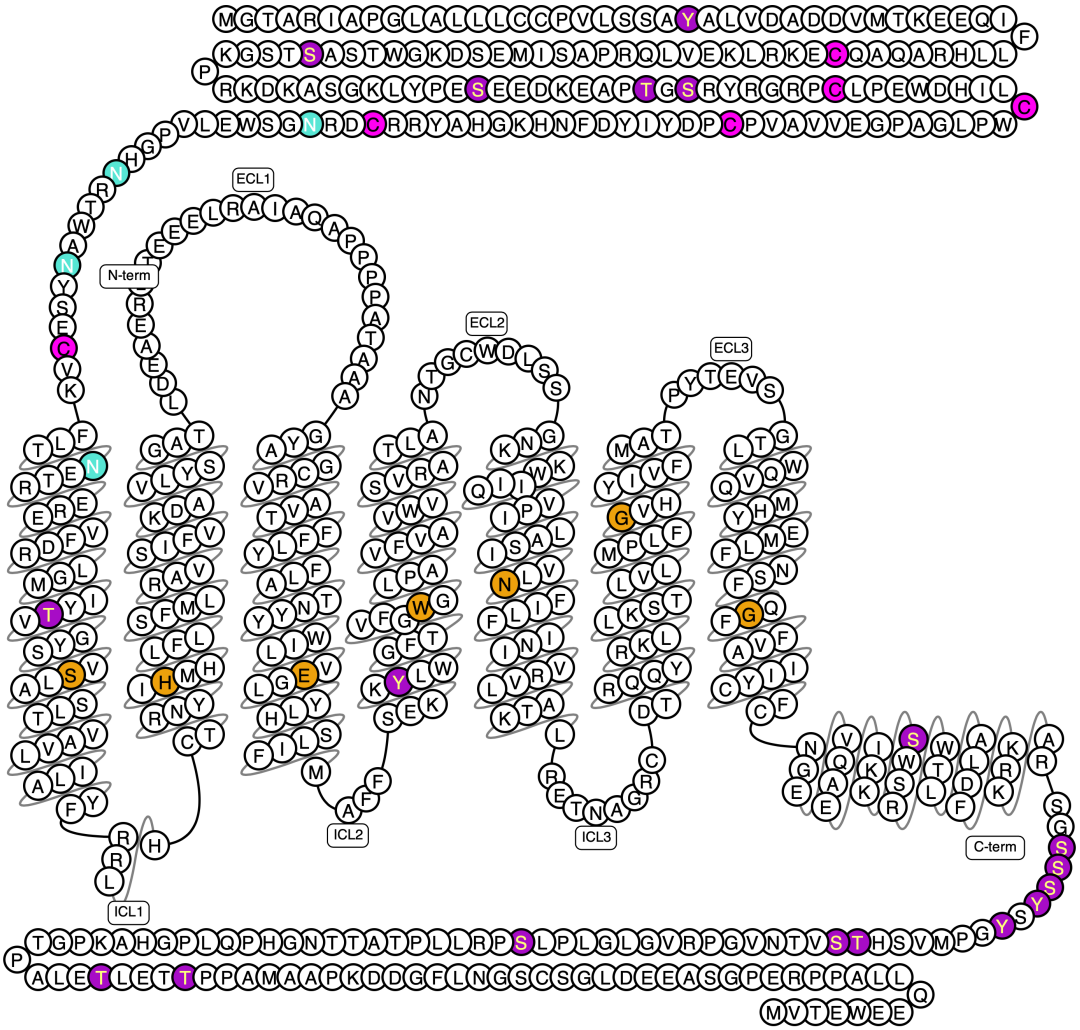

Orange: Ballesteros residues

Pink: Conserved cysteines for disulphide bond formation

Purple: Phosphorylation

Turquoise: N-linked glycosylation

human calcitonin receptor-like receptor (CLR)

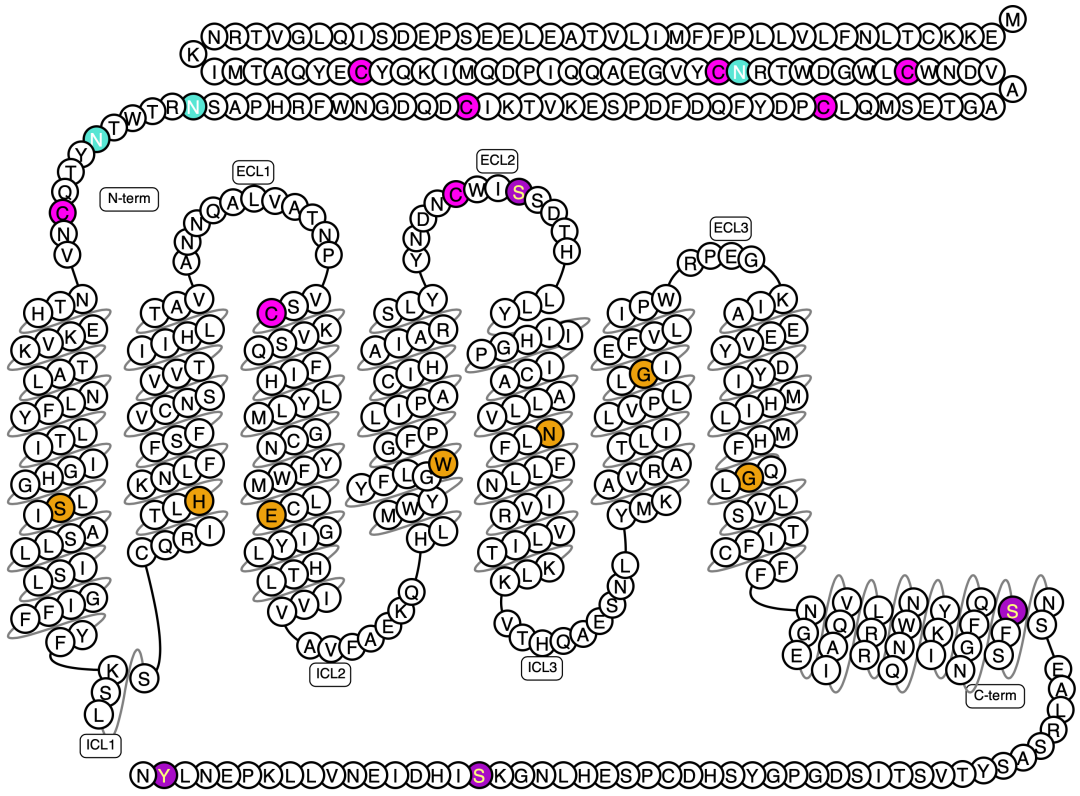

Orange: Ballesteros residues

Pink: Conserved cysteines for disulphide bond formation

Purple: Phosphorylation

Turquoise: N-linked glycosylation